ATOM-ATOM IONIZATION MECHANISMS AND CROSS SECTIONS IN NOBLE GASES AND NOBLE GAS MIXTURES

Thesis by

Arnold James Kelly

In Partial Fulfillment of the Requirements

For the Degree of

Doctor of Philosophy

California Institute of Technology

Pasadena, California

1965

(Submitted May 17, 1965)

ACKNOWLEDGMENTS

It is a pleasure to express my appreciation to Professor Frank E. Marble for the guidance and encouragement he provided during the course of this study. The initial phases of this investigation were conducted under the direction of Professor R. G. Jahn (currently at Princeton University), whose contributions to the success of this endeavor are hereby gratefully acknowledged.

The author is indebted to Mr. Frank "Ty" Linton for the assistance he provided in conducting the experiments and for the many figures he so meticulously prepared. Similarly, a note of appreciation is due to Mrs. Roberta Duffy for her typing of the manuscript.

During the course of this study the author has been employed on a part-time basis at the Jet Propulsion Laboratory in the Propulsion Research and Advanced Concepts Section headed by Donald R. Bartz. A special note of appreciation and thanks is extended to Mr. Bartz for his continuing support and encouragement, and to the JPL tuition support program which helped to make this endeavor financially feasible. A word of well earned recognition is due to Mr. John Nichol of the JPL Computer Applications Section for the development of the computer program used as part of the data reduction procedure.

As in any endeavor of this nature, the unabating support and encouragement received from one's family, while largely unsung, is of incalculable value and can never be properly repaid or acknowledged other than to say thank you with the deepest sincerity that these simple words can convey.

ABSTRACT

An experimental investigation of the initial phase of shock produced ionization in argon, krypton, xenon, and argon-xenon mixtures has been conducted in order to elucidate the atom-atom ionization reaction and to determine the atom-atom ionization cross sections for the gases noted. A high-purity shock tube was employed to heat these gases to temperatures in the range 5000°K to 9000°K at neutral particle densities of 4.41×10^{17} cm^{-3}, 6.96×10^{17} cm^{-3}, and 13.76×10^{17} cm^{-3}, and impurity levels of around 10^{-6}. A K-band (24 gcps) microwave system situated so that the microwave beam propagation direction was normal to the shock tube monitored the ionization relaxation process occurring immediately after the passage of the shock front. Electron density was calculated from the microwave data using a plane wave - plane plasma slab interaction theory corrected for near-field effects associated with the coupling of the microwave energy to the plasma. These data, adjusted to compensate for the effects of shock attenuation, verified that the dominant electron generation process involves a two-step, atom-atom ionization reaction, the first step (excitation to the first excited states) being rate determining. The quadratic dependence on neutral density associated with this reaction was experimentally demonstrated (with an uncertainty of $\pm$ 15 per cent). The cross section, characterized as having a constant slope from threshold (first excited-energy level), represented as the cross-sectional slope constant C , was found to be equal to 1.2×10^{-19} $\pm$ 15 per cent cm^2/ev, 1.4×10^{-19} $\pm$ 15 per cent cm^2/ev, and 1.8×10^{-20} $\pm$ 15 per cent cm^2/ev for argon, krypton, and xenon, respectively. The C factor for argon ionizing xenon

was determined to be equal with an uncertainty of $\pm$ 20 per cent to the xenon-xenon C factor, i.e., 1.8×10^{-20} cm^2/ev. This would imply that, for atom-atom processes in the noble gases at about 1 atmosphere pressure and temperature of about 1 ev, the ionization cross section is independent of the electronic structure of the projectile atom. The electron-atom elastic momentum-exchange cross sections derived from the microwave data correlated quite well with Maxwell-averaged beam data, the agreement for the case of argon being $\pm$ 20 per cent; krypton, $\pm$ 30 per cent; and xenon, within a factor of 2.

TABLE OF CONTENTS

LIST OF FIGURES

CHAPTER I

INTRODUCTION

Although atom-atom ionization processes are an ubiquitous contribution to gas-phase bulk* - thermal** ionization, they are rather inefficient in comparison to electron-atom ionization[1]. Only when ionization is inhibited, by a paucity of free electrons, from the utilization of this more efficient electron-atom process does the atom-atom process become dominant. Such a situation occurs when a volume of un-ionized gas is rapidly heated, for example, by the passage of a shock wave. Here, the enthalpy of the gas immediately after the passage of the shock front is, in many instances, of such magnitude as to permit a sensible level of ionization. Neglecting photo-ionization, a relatively ineffective mechanism[2], diffusion of electrons from more highly ionized regions of the gas, which is proportionately small enough to be ignored[3]; and the action of external agencies†; the only means of generating the necessary free electrons for the ionization to proceed by the preferred electron-atom process is through atom-atom interactions. In this instance, then, the atom-atom process becomes the dominant rate-controlling step and is of singular importance.

---

* Here defined as implying processes uninfluenced by catalytic surfaces.

** The discussion will be restricted to temperatures (kT) on the order of 1 ev.

† Irradiation by ionizing particles produced external to the body of the gas or ionization arising from radioactive decay of components present in the gas.

Two fundamentally different experimental techniques have been employed for the study of the atom-atom ionization process; beam devices and shock tubes. The use of a neutral beam as a means of investigating this inelastic process was employed circa 1930 by a number of workers[4, 5]. The work of Rostagni[4] is particularly noteworthy; his data for the argon-argon ionization are presented in Figure 31. These data probably represent the one-step, direct ionization reaction. It is not possible to make a more definitive statement as to whether the data are truly for a one-step or a two-step* reaction because of the uncertainty associated with the determination of the threshold energy of the interaction. This lack of precision in the determination of threshold energies, which are on the order of 20 ev in the laboratory system, is, in fact, a general feature of virtually all neutral beam devices. A characteristic of these devices that would favor the one-step, as opposed to the two-step, reaction is the low density of the beam and the target gases (around 10^{-2} torr). This low density, necessary for the successful collection of the liberated electrons, enhances the probability that once an atom is raised to an excited state it can successfully radiate its energy to the container prior to suffering a second, ionizing collision with a beam particle.

For these reasons, the beam technique has not been conspicuously successful as a diagnostic tool for the investigation of the atom-atom ionization process near threshold. However, it has provided quite useful information concerning features of the ionization

* Cf. Chapter II.

mechanism at relative particle energies in the kilovolt range, information vital to the development of the theory of high-energy inelastic processes, but of limited use in this study. Recent experiments conducted at these higher relative energies have shown that ionization cross sections determined using ion beams are approximately 30 to 40 per cent larger, because of polarization effects, than those measured using neutral beams[6]; He-He and He-Ne cross sections are smaller than 5×10^{-17} cm^2 (for energies in the range of 40→100 ev); and that ionization cross sections for He-N_2 are measurably different from N_2-N_2 cross sections[7], reflecting the influence of the projectile's internal structure upon the measurement. In addition, Berry[8] has shown that ionization induced by 0.3→3.0 Kev beams of xenon interacting with both xenon and krypton produces free electrons with a broad energy spectrum as well as electrons having quite definite energies indicative of an auto-ionization process. Finally, Russek and Thomas[9] have, on the basis of tests conducted at these higher energies, shown that as the electron clouds of the interaction particles sweep through one another, a friction-like mechanism occurs wherein one cloud can gain sufficient energy that, when statistically redistributed, can cause ionization in a manner quite analogous to evaporation.

While these studies are of intrinsic interest, they have not directly provided information of the details of the thermally-induced, atom-atom ionization process.

Shock tube studies have been somewhat more successful in this regard. Bond[10] was the first (1957) to actively suggest that,

on the basis of his shock tube experiments, atom-atom ionization proceeded by a two-step reaction, the rate-controlling first step being dependent upon the excitation energy. Petschek and Byron, in their now almost classical work[1], showed that the initial (atom-atom) ionization process in argon proceeded by a two-step process, the first, rate-controlling, step being associated with the first excitation energy level. As a result of an analysis of his shock-tube experiments, and of those of others, Weyman[3] (1958) substantiated this conclusion. In the main, these experiments were concerned with the luminosity delay time observed between the passage of the shock front and the onset of luminosity attributed to the electron-atom ionization regime, cf. reference (1). Using microwave absorption techniques, Johnston and Kornegay[11] (1961) apparently were the first to actually demonstrate that xenon-xenon ionization proceeded by a two-step process, the rate-controlling first step being associated with a measured activation energy equivalent to the energy of the first excited levels. Although the cesium data of Haught[12] (1962) (luminosity measurements) shows unmistakable evidence for the existence of a two-step, atom-atom ionization process, he failed to make this observation and was at a loss to explain his results*.

The most recent shock-tube investigation of the atom-atom ionization process, and the one that is of greatest interest insofar as this work is concerned, was initiated by R. G. Jahn. In his 1962

---

* His measured activation energy 1.43 + 0.06 ev) coincides with the known first excitation level of cesium, viz., 1.39 ev.

paper[13], he reviewed the basic details of the application of microwave technique to the probing of shock-produced ionization processes. The microwave probe was shown to be particularly suited to the delineation of the initial (atom-atom) ionization regime occurring immediately behind the shock front. The preliminary results of the application of this technique to the study of the initial ionization process in argon, krypton, and xenon were subsequently reported by Harwell and Jahn[14] in 1964. They demonstrated that atom-atom ionization did indeed proceed by a two-step process; the first, rate-controlling step being characterized by an activation energy equal, within experimental error, to the first excited level of the gases tested. In addition, the quadratic pressure dependence demanded by the theory of the two-step, atom-atom ionization mechanism (cf. Chapter III) was qualitatively verified by their data. Moreover, they showed that the impurity level of the test gas could have a profound effect upon the overall characteristics of the process, as discussed by Petschek and Byron[1].

Using the same basic shock tube and microwave diagnostic system as employed by Harwell and Jahn[14], but with certain essential differences which are discussed in the text, the work reported herein is a continuation of the investigation of atom-atom processes in the noble gases first conceived and initiated by Jahn.

It has been remarked that, with the advent of the Schroedinger equation and the development of quantum mechanics, chemistry had become a "closed" science. While ultimately this is undoubtedly true, there are still a vast variety of problems that, while solu-

ble in principle, are difficult if not impossible of solution in practice. One such problem has been that of the inelastic collision between two atoms where, because of the number of particles involved (electrons plus two or more nuclei), the analysis of any one specific reaction becomes involved to the point of despair without the use of gross simplifying assumptions. For collisions at high relative energies, i.e., well above threshold, a number of analyses based on quasi-classical collision dynamics[15, 16] and statistical electron-cloud models[17] have shown limited success. At lower energies near threshold, these methods are generally inapplicable, the analysis being the more difficult. Rosen of the University of Massachusetts has addressed himself to the problem of collision dynamics at relative energies near the ionization threshold. Using suitable approximated hydrogenic wave functions, he succeeded in calculating the one-step ionization cross section for He-He[18] and Ar-Ar[19]. His results for argon, shown in Figure 31, exhibit reasonable agreement with experiment. The extension of this work to the inelastic, excitation reaction and the collision dynamics of krypton, xenon, and of argon-xenon mixtures is well beyond the scope of this work.

Ideally, one would prefer to have available a well-developed theoretical cross-sectional model against which the experimentally-determined cross section could be compared. As Rosen's cross sections are, as mentioned, for the one-step ionization reaction in helium and argon, and since there are apparently no other, even remotely comparable, works in open literature, any comparison between this theory and experimental results must of necessity be

qualitative.

Statement of the Problem

The primary purpose of this experimental study, evolving around the use of a high-purity shock tube employing microwave techniques as a diagnostic tool, was the determination of the effect that controlled amounts of an impurity, having an excitation level lower than that of the host specie, would have upon the atom-atom ionization process. Of particular interest was the interspecie ionization cross section. Xenon was chosen as the impurity specie, to be used in conjunction with argon as the background specie. This choice was dictated by the convenience with which argon-xenon mixtures could be studied, because the first excitation level of xenon (8.315 ev) is some 3.233 ev below that of argon (11.548 ev), and because of the added information such a study would provide concerning the overall behavior of monatomic gases undergoing atom-atom ionization (excitation).

In order to attain the above goal, it was mandatory that the effects of the intra-specie reactions, that is, argon-argon and xenon-xenon, upon the overall electron generation rate of the shocked argon-xenon mixture be known and be suitably taken into account. Moreover, the influence of extraneous impurity species predominantly from the experimental apparatus had, of necessity, to be effectively eliminated so as not to obscure the argon-xenon reaction.

Once these high purity conditions had been established, and since the pure gas (argon-argon and xenon-xenon), atom-atom exci-

tation reaction cross sections had to be known preliminary to the study of argon-xenon mixtures, a more comprehensive investigation of the pure, noble gases was undertaken. This study had as its goals the determination of the atom-atom excitation cross section for pure argon, krypton, and xenon; the verification of the two-step excitation process, controlled by the rate-limiting first step of excitation to the first excited level; and a demonstration of the quadratic pressure dependence associated with this process.

CHAPTER II

ONE-STEP VERSUS TWO-STEP ATOM-ATOM IONIZATION PROCESS

In the absence of impurities, there are but two possible reaction paths by which atom-atom ionization in monatomic gases (or their mixtures) can occur; the one-step, direct-ionization reaction,

$$A + A \xrightarrow{k_1} A + A^+ + e^- , \tag{1}$$

and the two-step, excitation-ionization reaction,

$$A + A \underset{k'_*}{\overset{k_*}{\rightleftharpoons}} A^* + A \tag{2a}$$

$$A + A^* \xrightarrow{k_+} A^+ + e^- + A \tag{2b}$$

$$A^* \underset{}{\overset{\overline{k_\nu}}{\rightleftharpoons}} A + h\nu \tag{2c}$$

where k_1 , k_* , k'_* , k_+ , $\overline{k_\nu}$ are the reaction rate constants for the processes shown. From the work of Harwell and Jahn[14], where it was demonstrated that the ionization process in argon, krypton, and xenon proceeded by a process which was dependent upon the first excited level, it is clear that the two-step process is dominant, i. e., $k_1 \ll k_*$, as the one-step, direct-ionization process is associated with an activation energy equivalent to the ionization energy.

In the two-step ionization process, a neutral noble-gas atom is elevated, by means of a close encounter (inelastic collision) with a second neutral atom, to the first excited state or to one of the many energy levels between this state and the ionization limit. In the noble gases the first excited state is actually composed of four closely-spaced[20] levels. Two of these are spectroscopically iso-

lated from the ground state, i.e., they are metastable. Transitions between the other two levels and the ground state are permitted by the selection rules, and give rise to the so-called resonance radiation. If collisionally excited into one of the metastable states, the atom will remain in that state for extended periods of time (10^{-4} sec) because of its inability to radiatively transit to the ground state. Therefore, the probability that a second inelastic collision would occur leading to ionization of this atom is greatly enhanced. This second collision need only supply a fraction of the energy required for the initial excitation to cause ionization, e.g., in the case of argon, 11.55 ev is necessary for excitation (lowest metastable state) but only an additional 4.21 ev is required for ionization from this state. Were the atom collisionally excited to one of the resonance levels, which for the noble gases studied lie < 0.3 ev above the lowest metastable level, radiative decay would occur in on the order of 10^{-8} sec. However, since the gas is optically thick for this resonance radiation, the emitted photon would be trapped in the gas[2], individual atoms being alternately collisionally or radiatively excited and radiatively de-excited, the overall population of excited atoms remaining relatively constant. Therefore, the probability of an inelastic, atom-atom collision occurring when one of the collision partners is in an excited state is vastly increased by this mechanism of resonance radiation trapping.

To investigate the various implications of the two-step ionization reaction, it is necessary to develop the kinetic reaction-rate equations describing the population density of the excited state (N_*),

$$\frac{d}{dt}(N_*) = k_* N^2 - (k_+ + k'_*) N N_* - \overline{k_\nu} N_* \qquad (3)$$

and

$$\frac{d}{dt}(N_+) = k_+ N N_* \qquad (4)$$

where $N_+ = N_-$ for the quasi-neutral plasma generated in the shock tube and for the ionization levels attained, the neutral particle density level $N >> N_*$, N_+, and therefore, N can be assumed constant. The solution of equation (3) for N = constant and $N_* = 0$ for $t = 0$, i.e., no pre-excitation, is

$$N_* = k_* a N^2 (1 - e^{-t/a}), \qquad (5)$$

where

$$a = [(k_+ + k'_*) N_+ + \overline{k_\nu}]^{-1}$$

and the ion (i.e., electron) density as a function of time, from equations (4) and (5) and for $N_+ = 0$ for $t = 0$, is written as

$$N_+ = N_- \equiv N_o = k_* k_+ a N^3 [t - a(1 - e^{-t/a})] = \frac{k_* k_+ N^3}{[(k_+ + k'_*) N + \overline{k_\nu}]}$$

$$\left[t - \frac{1 - e^{-t[(k_+ + k'_*) N + \overline{k_\nu}]}}{[(k_+ + k'_*) N + \overline{k_\nu}]} \right] . \qquad (6)$$

It is immediately obvious that for $t >> 1/[(k_+ + k'_*) N + \overline{k_\nu}]$, the quadratic dependence of electron density upon neutral particle density N (note: $N_+ \propto N^2$ for constant temperature, T), which is suggested by the data of Harwell and Jahn[14], is only possible when radiative de-excitation is very much smaller than collisional de-excitation, i.e., $\overline{k_\nu} << (k_+ + k'_*) N$. This is consistent with the arguments advanced

concerning the role of the metastable states and the resonance-radiation trapping mechanism in the two-step ionization process. The electron density relation (6) is consequently rewritten as

$$N_+ = N_e = \frac{k_* k_+ N^2}{(k_+ + k_*')} \left[t - \frac{(1 - e^{-t[(k_+ + k_*')N]})}{(k_+ + k_*')N} \right] . \qquad (7)$$

Were $k_*' \gg k_+$, then $N_+ = N_e \approx k_+ N^2(t)$, and the activation energy would equal the ionization energy, which is at variance with observation. Therefore, $k_*' \ll k_+$, implying that the rate-determining step is the generation of the excited state; the second step in the process, viz., the final elevation of the atom to the ionization level and beyond, occurs with ease. This is physically quite reasonable, as neutral rare-gas atoms have complete p shells and are chemically quite stable; however, when excited, one electron is of necessity displaced into a higher orbit and the atom therefore assumes a larger geometrical collisional cross section.

The electron generation rate is then

$$N_+ = N_e = k_* N^2 \left[t - \frac{(1 - e^{-tk_+ N})}{k_+ N} \right] . \qquad (8)$$

For $t \ll 1/k_+ N$,

$$N_+ = N_e \simeq \frac{k_* k_+ N^3 t^2}{2} - O(t^3 k_+^2 k_* N^4) .$$

Consequently, the two-step, atom-atom ionization process should exhibit an initial phase which is cubic in neutral particle density and quadratic in time.

The microwave diagnostic and recording system has an esti-

mated temporal resolution* of about 4 μsec**. No evidence of the initial inception phase of the atom-atom excitation process has been observed when shock heating argon, krypton, xenon, or argon-xenon mixtures, and it is therefore construed as occurring at times and/or electron densities ($<\sim 2\times10^{10}$) below the limits of resolution of the diagnostic system. Setting $t = 1/k_+N = 20$ μsec, we find that k_+, for the neutral particle densities encountered in this study (i.e., $N \sim 10^{-18}$), is on the order of 10^{-13}. This can be compared to values of k_*, defined as

$$k_* = \frac{C}{2}\frac{2\sqrt{2}}{\sqrt{\pi\mu}}\left[(1/\beta)^{3/2}(2+\beta E_*)e^{-\beta E_*}\right]$$

(cf. Chapter III), which are in the range $10^{-21} \rightarrow 10^{-22}$, thereby lending substantiation to the inequality $k_* \ll k_+$.

Because the metastable states lie somewhat below the resonance levels, the Boltzmann probability factor for a reaction involving the metastable state would be higher than for those involving the resonance states. However, the difference in energy separating these states is commensurate with the experimental uncertainty associated with the determination of these energies. Therefore, it is currently not possible to ascertain which of these two mechanisms, i.e., excitation of the long-lived metastable states or resonance-radiation trapping, is dominant, or indeed, even if they are independent. One can only state that on the basis of Harwell and Jahn's

---

* Largely a function of the spatial resolution of the microwave transmitting and receiving horns, cf. Appendix I.

** 4 μsec in laboratory time coordinates, t, is equivalent to ~ 16 μsec in the particle-time coordinate system, t_p.

work (and the results of the experiments described herein), that the two-step ionization process has been established as the preferred atom-atom ionization path; that the first step of this process, that is, excitation to the resonance and/or the metastable level, is the rate-controlling step; that collisional and radiative de-excitation and recombination have a negligible effect upon the population of the excited state; and that the second step in the process apparently occurs with such alacrity that it need not be considered. This, of course, implies that the cross sections determined for these reactions are in actuality not truly ionization cross sections but rather those of the rate-controlling excitation reaction.

CHAPTER III

ATOM-ATOM ELECTRON GENERATION RATES

In general, a cross section Q is defined by the following relation:

$$dP_j = N_i Q_{ij} dX , \tag{9}$$

where dP_j is the probability that a particle of specie j will interact with a particle of specie i when traveling a distance X in a sea of type i particles having a particle density N_i. The rate of interaction probability, e.g., collision frequency, excitation rate, ionization rate, ... (per unit volume per unit time) is written

$$\left(\frac{dP}{dt}\right)_j = N_i Q_{ij} v_j . \tag{10}$$

This expression is further generalized for the case where two or more classes of particles have different velocity distributions to

$$N_j\left(\frac{dP}{dt}\right)_j = N_i N_j \int_{N_i} \int_{N_j} f(\bar{v}_i) f(\bar{v}_j) Q(|\bar{v}_i - \bar{v}_j|) |\bar{v}_i - \bar{v}_j| \, d\bar{v}_i d\bar{v}_j \equiv \nu . \tag{11}$$

Considering the temperatures and pressures encountered in this study and the low levels of ionization attained, it is warranted to assume that both species are in thermal equilibrium, so that $f(\bar{v}_i)$ and $f(\bar{v}_j)$ are Maxwell-Boltzmann distributions. Note that when $i = j$, implying interaction between atoms of the same specie, it is necessary to apply a multiplicative symmetry factor of 1/2 to the above relation in order to avoid counting the interactions twice.

Following Chapman and Cowling[21], Chapter 5, we shall convert to center-of-mass coordinates. Labeling the reduced mass

$(m_i m_j)/(m_i+m_j)$ as μ_{ij} and the relative velocity $(\bar{v}_j-\bar{v}_i)$ as $\bar{g}$, it is a straightforward, albeit tedious, exercise to show that

$$\nu = \left[\frac{N_i N_j 4\pi}{1+\delta_{ij}}\left(\frac{\mu_{ij}}{2\pi kT}\right)^{3/2}\right]\int_{g_*}^{\infty} \exp\left(\frac{-\mu_{ij}g}{2kT}\right) Q_{ij}(g) g^3 dg \qquad (12)$$

where now g_* is the threshold relative velocity at which the reaction first starts and $1/(1+\delta_{ij})$ is the symmetry factor alluded to above. The relative interaction energy E is related to the relative center-of-mass velcoity g as $E = (\mu_{ij}/2)g^2$, which, for the case of threshold, becomes $E_{*i} = (\mu_{ij}/2)g_{*i}^2$. Substitution of a constant slope ionization (excitation) cross section*, that is, $Q_{ij} = C_{ij}(E-E_{*i})$, into (12) results in an expression for the atom-atom electron generation rate (per unit volume and time):

$$\nu \equiv \dot{N}_e = \frac{N_i N_j}{1+\delta_{ij}} C_{ij} K_{ij} (1/\beta)^{3/2} (2+\beta E_{*i}) e^{-\beta E_{*i}} , \qquad (13)$$

where, for convenience, we have defined

$$\beta = 1/kT \quad \text{and} \quad K_{ij} = \frac{2\sqrt{2}}{\sqrt{\mu_{ij}\pi}} ,$$

and δ_{ij} is the Kronecker delta function.

Single Specie Atom-Atom Ionization Rate

For a single specie, i = j, so that

$$N_e = \frac{N_i^2}{2} C_{ii} K_{ii} (1/\beta)^{3/2} (2+\beta E_*) e^{-\beta E_*} . \qquad (14)$$

---

* Cf. Appendix A for a discussion of the validity of a constant slope approximation to the excitation-ionization cross section. The cross-sectional slope constant C is related to the cross section Q_c which is a constant for all energies greater than threshold ($E \geq E_*$) by the expression

$$Q_c = \frac{C}{\beta}\left(\frac{\beta E_* + 2}{\beta E_* + 1}\right) .$$

Here, E_* is of course the threshold reaction energy characteristic of the specie in question. From this, one concludes that the reaction should proceed as the square of the particle density N_i. Furthermore, taking the natural logarithms of both sides and differentiating with respect to β,

$$\frac{d\,\ell n\,(N_e)}{d\beta} = -\frac{3}{2\beta} + \frac{E_*}{2+\beta E_*} - E_* \quad . \tag{15}$$

We see that the slope of the data presented in the form of an Arrhenius plot, that is, $\ell n\, N_e$ versus β, will equal (to within ~ 5 per cent) the threshold energy E_* of the reaction*. The exact expression for the threshold energy E_* is, in terms of the Arrhenius slope (denoted by ψ),

$$E_* = \frac{(\psi\beta + 5/2) + \sqrt{(\psi\beta+5/2)^2 - 4(3+2\psi\beta)}}{2\beta} \quad . \tag{16}$$

Binary Atom-Atom Ionization Rates

When a binary gas mixture undergoes atom-atom ionization, there are four separate electron generation processes simultaneously occurring; i.e., two intra-specie reactions where, for example, a specie i particle ionizes another i particle (threshold energy E_{*_i}) and two inter-specie reactions, e.g., a specie i particle ionizing a specie j particle (with threshold energy E_{*_j}). The electron generation rate for binary mixtures is, therefore:

* This is true for the values of β ($\gtrsim \frac{1}{2}$ ev) and E_* ($\gtrsim 8$ ev) encountered in this study.

$$\dot{N}_e = \begin{cases} \frac{N_1^2}{2} C_{11} K_{11} \left(\frac{1}{\beta}\right)^{3/2} (2+\beta E_{*1}) e^{-\beta E_{*1}} & \text{specie 1 ionized by specie 1} \\ + N_1 N_2 C_{12} K_{12} \left(\frac{1}{\beta}\right)^{3/2} (2+\beta E_{*1}) e^{-\beta E_{*1}} & \text{specie 1 ionized by specie 2} \\ + N_2 N_1 C_{21} K_{21} \left(\frac{1}{\beta}\right)^{3/2} (2+\beta E_{*2}) e^{-\beta E_{*2}} & \text{specie 2 ionized by specie 1} \\ + \frac{N_2^2}{2} C_{22} K_{22} \left(\frac{1}{\beta}\right)^{3/2} (2+\beta E_{*2}) e^{-\beta E_{*2}} & \text{specie 2 ionized by specie 2} \end{cases} \quad (17)$$

The interpretation of binary gas mixture electron-generation rates requires a knowledge of the pure-gas cross section constants (C_{11}, C_{22}) and the threshold energies, E_{*1} and E_{*2}. It should be noted that the interparticle electron generation rate terms (2nd and 3rd terms) have been written with the implicit assumption that the threshold energies for the reaction are determined by the inherent characteristics of the particle undergoing ionization (excitation) independent of the specie causing the excitation. That is, it is assumed that the threshold energy for an argon atom exciting (ionizing) a xenon atom will be 8.315 ev, the same as observed for a xenon atom exciting (ionizing) another xenon atom. This assumption is reasonable, and is apparently substantiated by experiment (cf. Chapter V). Even with this assumption and a knowledge of the pure-gas cross sections, there are two unknowns, C_{12} and C_{21}. In practice (e.g., argon-xenon mixtures), the difference between the threshold energy of specie 1 (argon) and specie 2 (xenon) is sufficiently large so that, at the temperatures involved, the exponential factors differ by as much as two orders of magnitude. Since the inter-specie cross sections probably do not differ by more than an

order of magnitude, the reaction with the lowest threshold energy is dominant. This is actually observed in the Arrhenius plots of the argon-xenon mixture data, the slopes indicating a threshold energy the same, to within experimental error, as that for pure xenon. Because of these practical considerations, we are restricted experimentally to the determination of only one of the two inter-specie cross sections, the one corresponding to the ionization of the specie possessing the lower threshold energy. In theory at least, it should be possible to determine the other inter-specie cross section constant by conducting two independent experiments and solving for the two unknowns. However, as will be discussed, this is not possible, as the influence of this second reaction is obscured by the data scatter.

CHAPTER IV

DESIGN OF THE EXPERIMENT

Introduction

The shock tube is a well-established research tool particularly suited to the study of gas kinetics*. By its very nature, it provides a means of rapidly** and uniformly heating a body of gas to high, and precisely known (and controlled), temperature levels, and can maintain those levels for periods of time long enough for a wide variety of reactions to occur. In this regard it is especially applicable to the study of the noble gas atom-atom ionization process, for, in the absence of photo-ionization, this reaction is the first to occur after passage of the shock. In addition, it is possible to maintain stringent control over the purity level of the shocked gas, a prime requisite for the successful delineation of the reaction's kinetic properties. For these reasons, the shock tube, to be described in detail later, was designed and employed for the study of the noble-gas initial (atom-atom) ionization rates.

Since the ionization process was of overriding interest, a direct means of monitoring the ion (or electron) generation rate was required which would not significantly alter the process under scrutiny. Jahn[13] has designed and developed a microwave probe system compatible for use with a shock tube and specifically tailored to

---

* Cf. the survey article by Kantrowitz[22].

** For shock strengths and gas pressures of interest, the translational temperature increase across the shock front occurs in on the order of 10^{-8} sec.

monitor the initial phases of the ionization relaxation process occurring immediately behind the incident shock*. While the intensity of the microwave beam generated by this system (which is employed as the primary diagnostic tool in this investigation) can be regulated so as to satisfy the negligible interaction requirement**, its use has influenced the design and operation of the shock tube. The details of the overall shock tube, diagnostic system, and data reduction procedure used in the course of this investigation are described briefly in the following paragraphs, the finer details of these topics being relegated to the appendices.

Shock Tube Design Details

A schematic plan view of the overall shock tube used in these experiments is depicted in Figure 1 (also see the three photographs of the experiment shown in Figure 2 through 4). The conventional shock tube depicted in these figures was constructed of 6066-T5 aluminum tubing having a square internal passage 5 cm by 5 cm and external dimensions of 9 cm by 9 cm. All sections of the tube were sealed with standard Buna N O-rings which were adequate to permit evacuation to pressure levels of approximately 2×10^{-6} torr. The driver section, consisting of a 1.2 M length of tubing, permitted driver pressures of up to 1000 psia to be attained. Using various thicknesses of both copper and aluminum diaphragms, scored in a precisely controlled manner (refer to Appendix C), it was possible

* Cf. also Dickson[23] for a discussion of the relative merits of microwave diagnostics in comparison to other techniques employed for the determination of electron density.

** Cf. Appendix S for a discussion of the influence of a microwave beam upon plasma properties.

to reproducibly generate shock waves in the range $7 \leq M_s \leq 10$ using hydrogen, helium, their mixtures, or helium-argon mixtures as driver gases; and argon, krypton, xenon, and argon-xenon mixtures as the driven gas. The initial driven gas pressure was adjustable, within an error of less than 0.1 torr, to any pressure in the range $\sim$ 1 to 20 torr, experiments being conducted with driven pressures in a limited range of from around 3 to around 10 torr. As shown in the schematic diagram of Figure 1 , the shock tube's basic structure was composed of, in addition to the aluminum tubing, a short (0.3 M) section of pyrex tubing used for the microwave diagnostics and luminosity measurements. This "diagnostics" section was joined to the tube by a special fixture, as seen in Figure 3 . This dielectric section of tubing had, within close limits, the same internal dimensions as the aluminum tubing, and was sealed to the fixture (and the fixture in turn was sealed to the tubing) by O-rings. The dump tank, separated from the diagnostics section by a short (0.6 M) length of aluminum tubing, was used as a means of reducing the post-shock tube pressure, and was isolated from the shock tube proper by a thin (2 mil) aluminum diaphragm. This diaphragm permitted the smaller volume of the shock tube to be treated as separate and apart from the larger dump tank volume, and facilitated the attainment of high shock-tube purity levels. All ports into the tube were standardized 2.5 cm diameter (cf. Figure 7) and were sealed to the tube with O-rings.

In addition to providing a means for the generation of accurately controlled high-strength shocks, the shock tube was specifical-

ly designed to permit operation at gas impurity levels at least equal to those associated with the research-grade gases tested (i.e., impurity levels on the order of one part per million). No effort was made to improve upon the known impurity level of the research-grade gases used in these experiments (see Appendix E). However, considerable effort was devoted to the reduction of the contamination of the test gases caused by outgassing from the shock tube walls and fittings and from leakage into the tube. The combined outgassing and leak rate of the shock tube, a composite of 45 runs*, is shown in Figure 5.

These data were taken by closing the gate valve to the diffusion pump (used to evacuate the shock tube to ultimate pressures in the range 2×10^{-6} to 5×10^{-6} torr) and observing the pressure rise in the tube (as delineated by the two diaphragms) as a function of time. As seen, the tube pressure increases steadily during the first three minutes to $\sim 10^{-4}$ torr and thereafter continues to increase at a much reduced rate, indicative of a leak rate which is very much smaller than the initial outgassing rate**. Mass spectroscopic analysis of the outgassing material (cf. Appendix C) indicated that it had an approximate composition consisting of about 60 per cent H_2O, about 10 per cent N_2, and about 30 per cent hydrocarbons. In order to reduce to as low a level as possible this outgassing rate, the tube, after every two or three shots, was heated (by heating tapes insulated with fibreglass covered in turn by the aluminum foil seen in Figure 4) to

---

* An outgassing rate was measured prior to each run.

** The mean outgassing rate is equivalent to $\sim 3/2\times10^{10}\,cm^{-3}sec^{-1}$.

around 200°C while being continuously exhausted by the diffusion pump.

By flowing the research-grade test gases* through the tube (and thence to atmosphere), it was possible to reduce the impurity level (caused by outgassing) to calculated levels on the order of fractions of a part per million. The calculated impurity level, as a function of time, is presented in Figure 6, and details of the computation in Appendix E. To preclude the possibility of back diffusion of oil vapor from the roughing pump used in the flow system, a cold trap was placed just downstream of the flow-system exit port and upstream of the pump. As a further precaution in preventing oil vapor from entering the tube during rough pumping (wherein the tube is evacuated after a run) and contributing to the outgassing process, a cold trap was provided for this line also. A discussion of the operational procedures employed and the precautions instituted to assure gas purity are to be found in Appendices D and L.

Shock Velocity Measuring System

While small, the impurity level was sufficient to produce shock front luminosity, a phenomenon first reported by Petschek[24] and studied in detail by Turner[25]. This luminosity zone, which extends over the entire cross section of the tube, is quite narrow (~ 0.6 mm) and is seen to be present on every luminosity profile studied**. Occurring as it does in close proximity to the shock front, and be-

* The flow rates used were equivalent to 5.8×10^{16} $cm^{-3}sec^{-1}$ for the 5 and 10 torr shots, and for the 3 torr shots, 3.3×10^{16} $cm^{-3}sec^{-1}$.

** The reproduction of the test record shown in Figure 19 shows a "light spike" at the estimated shock position.

cause of difficulties (due to ionization effects) attendant with the use of thin film gauges at high Mach numbers ($M_s > 8$), a photomultiplier shock-position indicator (SPI) system was devised (cf. Appendix F). This system, the details of which are shown in Figure 7 , was specifically designed to take advantage of this sharp luminosity zone as a means for accurately determining shock passage time. Four shock position indicators, positioned as shown in the sketch on page 124 were used to provide information from which not only the mean shock velocity but also shock attenuation could be calculated (see Appendix M).

The outputs of the SPI's were fed to an amplifier-differentiator flip-flop unit (ADFF unit, described in Appendix G), where the signal arising as a consequence of the luminous shock front was amplified, differentiated, and fed to a flip-flop stage, the output of which was a pulse having an amplitude of about 7 volts, a rise time of about 0.2 μsec, and a decay time of about 10 μsec. The circuitry associated with this unit is shown in Figure 8 . The four "pips" (one for each SPI station) were then displayed on an oscilloscope raster, an example of which is reproduced as Figure 9 . This raster was generated using the components depicted in Figure 10 (and discussed in detail in Appendix H), and permitted the determination of shock passage times accurate to within 0.3 μsec over periods of time up to 2000 μsec. Using this system, mean shock velocities could be determined, in the majority of instances, to within 0.15 per cent accuracy. The translational temperature of the shock-heated gases was then computed from this mean velocity data by the

application of the perfect gas equations which, for the low ionization levels encountered ($< 10^{-4}$), are quite accurate representation of the gas behavior. The shock attenuation data were used directly in the computation of an electron-density correction factor which normalized the electron density profile to temperature conditions existing immediately behind the shock front, thereby permitting the true behavior of the ionization relaxation process to be observed. This correction is discussed in some detail in Appendix W, and its application to the microwave data is explained in the ensuing paragraphs.

Microwave Diagnostic System

The microwave circuitry shown in Figure 11 was employed as the primary diagnostic tool in the experiment. As demonstrated by Jahn[27], providing the so-called effective electron collision frequency ν_c/ω is greater than about 0.07, the measurement of reflected and transmitted signal amplitudes provides as wide an electron density range as would be detected by measurement of the transmitted and reflected phases. As the measurement of signal amplitude necessitates far less sophisticated circuitry than is required for phase determination, and since ν_c/ω is indeed almost consistently greater than 0.07 for the shock-produced plasmas of interest and the microwave frequency employed (24 gcps), the circuit depicted in Figure 11, which monitors the amplitude of the microwave signal transmitted through and reflected from the plasma, was designed. It has been shown (cf. Jahn) that if the dielectric walls, between which a plasma is contained (in this case, the pyrex tubing) and through

which the microwave beam passes, have been matched to the microwaves so that in the absence of plasma no net reflection results from the presence of the walls*, then the walls will continue to be matched when plasma is present; and therefore their presence will not influence the characteristics of the microwave-plasma interaction. In order to satisfy this non-interference criterion, the Rexolite matching structures shown emplaced in the apertures of the transmitting and receiving horns were developed. By trial-and-error variation of the depth and the width of the grooves machined in one surface of the structure, it was possible to match the microwave circuit to the pyrex diagnostic section with a VSWR < 1.05. Therefore, for all practical intents and purposes, the pyrex section is invisible to the microwaves and its presence can be neglected.

Microwave-Plasma Interaction Theory and Corrections

The microwave horns were of special design insofar as they collimate the microwave beam in the vertical (x) dimension by providing a slight degree of focussing, the output of each horn being, in effect, focussed on the aperture of the other. This was done in an effort to simulate, with a plasma of restricted dimensions, the idealized geometry associated with the theory of a plane, plane-polarized monochromatic electromagnetic wave interacting with a plane slab of isotropic, homogeneous plasma whose lateral dimensions are infinite in extent. This theory, developed in detail in Appendix N, is based on the concept of the electromagnetic wave interacting with an

* Therefore, they are invisible to the microwaves for the case of loss-less media, a good approximation for pyrex.

ensembled averaged electron, the plasma being macroscopically characterized by the electron density N_e and the effective electron, heavy component (atom, ion) elastic momentum-exchange collisions ν_c (usually written in the form ν_c/ω, where ω is the microwave frequency). The normalized transmitted signal amplitude ${}_1S_T$ and the normalized reflected signal amplitude ${}_1S_R$ computed using the theory just described, applied to the case of a plasma slab of thickness $4\lambda_o$ (for 24 gcps, $\lambda_o = 1.25$ cm), i.e., 5 cm for various values of ν_v/ω, are shown in Figures 13 and 12 respectively, as a function of the normalized electron density N_e/N_p. The parameter N_p is the electron density which exists when the plasma frequency (ω_p) equals the microwave frequency (ω), or, for the case being discussed, $N_p = 7.14 \times 10^{12}$ cm^{-3}.

As the plane wave, plane plasma-slab interaction theory is an idealization, only incompletely simulated in practice by the microwave circuitry and the shock-tube diagnostic section to which it is matched, a number of corrections were found to be necessary in order to bring the theory and the physical geometry of the diagnostic system into closer correspondence, and thereby permit a more accurate interpretation of the microwaved data (in terms of N_e and ν_c/ω) to be made. As the transmitting and receiving horns are in immediate contact with the pyrex diagnostic section and therefore only a few wavelengths apart, they are effectively within each other's near field pattern. This leads to inhomogeneities in the distribution of the microwave energy in the region where interaction with the plasma occurs. This is at variance with the concept of a plane

electromagnetic wave used in the interaction theory, which, by its very definition, exhibits a spatially-uniform energy distribution in the direction of propagation. In order to account for this inhomogeneity in energy, a simplified one-dimensional model of the radial near-field pattern of the horn system was synthesized. This model correlated surprisingly well* with the observed field pattern. By following the work of Harris[45] and assuming that the normalized separation distance d/d_o is related to the wavelength ratio λ_o/λ_p (λ_p is the wavelength in plasma), i.e., $d/d_o = \lambda_o/\lambda_p$, and introducing the effects of refraction and diffraction, the field-pattern correction factor depicted in Figure 17 was developed. In this figure, the ratio ϵ_s/ϵ_p, i.e., the ratio of the energy received calculated on the basis of the synthesized field pattern to that received in the plane wave case, is plotted as a function of the ratio of the free space to plasma wavelength λ_o/λ_p. The details of the development of this correction factor are presented at length in Appendix P. Also shown in this figure is the actual radial field pattern plotted using the relation $d/d_o = \lambda_o/\lambda_p$, and the so-called mean field-pattern correction factor, derived by taking the mean of the oscillatory radial field pattern and re-normalizing the result. A mean field correction was used by Harwell and Jahn[14] in their data reduction. It is interesting to note that while the mean field correction, when applied to observed microwave interaction data, yields electron-density generation rates only some 20 per cent higher than those computed

* The observed radial field pattern was duplicated precisely, i.e., to within the 0.1 db uncertainty associated with its experimental determination over the range of separation distances of interest.

using the synthesized field-pattern correction, that the data are much harder to interpret, as the mean field correction fails to compensate correctly for the field pattern induced perturbations of the transmitted microwave signal. Moreover, the effective collision frequency calculated from identical data reduced using these two correction factors can differ by as much as fifty per cent.

It was observed that the microwave crystals, used to detect the transmitted and reflected signal amplitudes, did not produce an output linear with the incident energy, thereby necessitating that a crystal correction be applied. Further, it proved necessary to perform a crystal calibration for each of the data runs as the calibration characteristics of these crystals varied slightly but significantly in an unpredictable manner from day to day. A typical example of this correction for the case of a transmitted signal crystal (hence the subscript T) is shown in Figure 18 where the actual normalized energy detected by the crystal, ${}_1S_T$, is plotted as a function of the indicated normalized output ${}_oS_T$. Appendix O should be consulted for a more detailed discussion of the characteristics of these microwave crystals.

The effect of the electron-density boundary layer, in particular the gradient in the direction of propagation, upon the microwave measurement of plasma properties has been investigated (see Appendix Q) and found to be unimportant for the operating regimes of interest. A qualitative discussion of the effects of the lateral electron

density gradient* presented in Appendix R leads to the conclusion that at high Mach numbers, where a significant variation in electron density ($\sim 0.1\ N_p$) can exist over the dimensions of the field pattern, the microwave system will indicate electron generation rates lower than is true, because of diffraction effects.

Interpretation of Microwave Data

To facilitate the accurate, rapid interpretation of the microwave data produced by the system described above (cf. Figure 19 for a typical example of these data), taking into account the field pattern and crystal correction factors, an IBM computer program was developed. The block diagram of the program used for the reduction of the transmitted signal data is shown in Figure 20 and is discussed in Appendix T. A reproduction of the output of this program is presented in Figure 21. This program requires as input data the "raw" transmitted signal data from the oscilloscope trace (Figure 19), an assumed value of ν_c/ω, the crystal correction, the field pattern correction (both in tabular form), and the physical parameters representing the plasma thickness, microwave frequency, etc. Operating on these data, the program automatically determines electron density, the corresponding reflected signal amplitude, reflected and transmitted measurable phases (see Appendix N), and the ratio of free space to plasma wavelengths. The results of the application of this program to the data of Figure 19 are shown in Figure 22 where the calculated electron density (N_e) is plotted as a function

* Lateral in the sense that the gradient considered is due to the ionization process and is therefore lateral to the microwave propagation direction but axial with respect to the shock tube.

of particle time (t_p) for various values of ν_c/ω .

The simplified theory used to describe the electromagnetic wave - plasma interaction was developed around the concept of a plasma characterized, as noted, by two parameters, the electron density and the electron - heavy specie collision frequency ν_c . Therefore, it is necessary to have two independent measurements of the manner in which the electromagnetic wave interacts with the plasma in order to unambiguously determine these two parameters. As noted, two measurements are made, the transmitted and reflected signal amplitudes. However, it was found that a considerable degree of uncertainty could be associated with the determination of ν_c/ω and therefore the electron generation rate, if this parameter were to be determined by matching the transmitted and reflected signal data. A more satisfactory method of determining ν_c/ω involves the use of the transmitted signal data and the so-called hybrid phase or "bump" data (cf. Appendix V for a discussion of the procedure employed to determine ν_c/ω). It was Jahn[13] who first observed that by producing a small mismatch in the stub tuner of the microwave circuit (Figure 11) and then bucking this signal out by adjusting the stub of the transmitted signal crystal mount (so that in the absence of a plasma the reflected signal was negligible), the circuit could be made to produce small-amplitude reflected signals much in the manner of an interferometer. These signals are to be seen on the reproduced test record of Figure 19 as a small-amplitude oscillation of the 5 times amplified reflected signal. An analysis of the hybrid phase process is presented in Appendix U, where it

is shown that these data (the extrema of the oscillatory trace) are relatively weak functions of ν_c/ω. This is evidenced by Figure 23 where the effective collision frequency ν_c/ω is plotted against the electron density level at which the first two maxima and the first two minima occur, using the same slab thickness ($4\lambda_o$, i.e., m = 4) and the same frequency previously used. Referring back to Figure 22, we see that the hybrid phase measurement provides an unambiguous determination of ν_c/ω to be effected.

The collision frequency ν_c can be interpreted in terms of an electron - heavy particle elastic momentum-exchange collision process (cf. Appendix N), so that it provides a unique means by which the basic validity of the simplified microwave plasma theory can be evaluated.

Once ν_c/ω has been determined, it is then possible to plot the electron density versus particle time and attempt to determine the initial slope which, as shown in Chapter II, should be a consequence of the linear (with time) atom-atom ionization process. For the example shown, the determination of the initial slope is a trivial matter. As demanded by theory, the initial portion of the trace is linear, indicating that the effects of shock attenuation upon the electron generate are negligible. For cases where the particle times are longer and/or the shock attenuation factor larger, the electron density exhibits a continuous monotonic increase with time, no portion of the trace being linear. This is caused by variations in the shock speed (i.e., attenuation); gas particles being passed over by the shock wave far from the diagnostic station are hotter, as the

shock was stronger than when it passes over gas particles closer to this station. Therefore, in laboratory coordinates, the particle temperature would indicate a monotonic increase with time from the shock front, if measured directly. This effect is discussed in detail in Appendix W, where the shock attenuation electron-density correction factor (A) is derived as a function of the non-dimensionalized particle time θ. A plot of this correction factor is shown in Figure 24. This factor in essence permits an observed electron-density trace, influenced by shock attentuation, to be reduced to an equivalent constant-temperature case, i.e., it compensates for the attenuation induced temperature variation within the body of the gas.

Once the initial slope, that is, the atom-atom electron generation rate, has been determined, a minor normalization correction is applied. This correction (never exceeding 5 per cent) compensates for the small variations of neutral particle density resulting from variations in the initial pressure or temperature of the shocked gas, assuming the quadratic density dependence of the atom-atom two-step ionization process of Chapter III. The electron generation rate data is finally in a form suitable for presentation on an Arrhenius plot (see Figures 26 through 30).

Luminosity Profile Measurements

In addition to the microwave measurements, the luminosity profile existing behind the shock was monitored by the photomultiplier system depicted in Figure 25 and discussed in Appendix J. This system monitored the total luminosity and simultaneously the

radiation contained within a narrow spectral band centered at 4190 Å*. In the test record of Figure 19, the total luminosity trace is displayed with normal polarity and the filtered light trace with inverted polarity. The primary interest in these measurements was in the determination of the shock position, whose presence is heralded by the shock-front luminosity mentioned previously, and in the information they could convey concerning the behavior of a shock-produced luminosity generated during the atom-atom ionization phase.

---

* This wavelength corresponds to a spectroscopically-observed shock-produced group of transitions in argon.

CHAPTER V

RESULTS

Ionization Cross Sections

Following the data reduction procedures outlined above, the Arrhenius plots for the pure gases, argon (Figure 26), krypton (Figure 27), xenon (Figure 28), and the argon-xenon mixtures (Figures 29 and 30), were developed. The error brackets shown in these figures represent what is considered to be a reasonable estimate of the error involved in the determination of the initial slope of the electron generation rate curve, about $\pm$ 20 per cent, and those errors involved in the determination of the shock velocity and therefore the calculated atom temperature as discussed in Appendix M. It should be pointed out that the effects of lateral electron-density gradients upon the microwave signal and subsequently upon the electron generation rate is not included in the error estimate quoted. As explained in Appendix R, this particular phenomenon becomes manifest at high Mach numbers and low values of β and tends to depress the initial electron generation rate below its true value. This accounts for the almost consistently lower positions of the low β data points in relation to the curve representative of the best fit to the data.

Single Specie

The activation energies and cross-sectional slope constants derived from the data of Figures 26, 27 , and 28 are presented in Table 1.

Because of the error brackets associated with the data on the

Table 1

Single-Specie Activation Energies and Cross-Sectional Slope Constants

Specie	P_1* (torr)	E_* (ev)	C (cm^2/ev)**
Argon	3	11.8 ± 1.1	1.15×10^{-19}
	5	11.2 ± 0.9	1.24×10^{-19}
	10	11.4 ± 1.0	1.04×10^{-19}
Krypton	3	9.6 ± 0.9	1.68×10^{-19}
	5	10.1 ± 0.7	1.29×10^{-19}
	10	10.1 ± 0.7	1.32×10^{-19}
Xenon	5	8.2 ± 0.7	1.90×10^{-20}
	10	8.4 ± 0.7	1.66×10^{-20}

Arrhenius plots, there was some uncertainty accompanying the determination of the slope (ψ) of the best fit line through the data. The uncertainties in E_* shown in the table are representative of the maximum slope (ψ)† variation that the data would allow. As is obvious, these variations amounted to less than 10 per cent of the mean value in all instances. Moreover, the mean values of the excitation energy for each of the species are all within 0.4 ev of the

* "3 torr", "5 torr", and "10 torr" are equivalent to particle densities of $4.41\times10^{17}cm^{-3}$, $6.96\times10^{17}cm^{-3}$, and $13.26\times10^{17}cm^{-3}$, respectively.

** Reduced on the basis of: $E_{*Ar} = 11.548$ ev, $E_{*Kr} = 9.915$ ev, $E_{*Xe} = 8.315$ ev.

† Cf. equation (16), Chapter III, for the expression relating E_* to ψ.

lowest metastable levels listed by Cook[28]. This close correlation between these experimentally-determined activation energies and the lowest metastable excited state provides substantiation of the contention that the ionization process involves two steps; the first, excitation step being rate controlling. This is consistent with the work of Harwell and Jahn[14]. From the work of Ecker and Kröll[29], it is inferred that the apparent ionization energy, and presumably the excitation energy, is lowered, due to the presence of microfields in the plasma, by less than 0.01 ev, an amount which is insignificant in comparison to the experimental error, and consequently need not be considered.

A least squares curve-fitting IBM 7090 computer program was devised* for the purpose of providing an accurate means of interpreting the data of the Arrhenius plots. In this program, the theoretical atom-atom ionization rate equation (equation (14), Chapter III) is fitted, with minimum error, to the data (neglecting the error brackets). This fit is accomplished by varying the cross-sectional slope constant, the activation energy being fixed and specified as input to the program. For the values shown in the table, the activation energy was chosen to be equal to the first metastable energy level, in concordance with the concept of a two-step excitation-ionization process.

The cross-sectional slope constants (C) are seen to be, within an error bracket of $\pm$ 15 per cent, substantially independent of the

---

* This program was developed by Mr. William Thomas and Mrs. Barbara Philpot of JPL.

particle density level (i.e., pressure level). As the data were reduced using the theoretical atom-atom electron generation rate equation, where the generation rate is quadratic in neutral particle density, it can then be stated that the quadratic pressure dependence of the atom-atom, two-step ionization process has been substantiated. To put the $\pm$ 15 per cent uncertainty associated with this statement into proper perspective, it should be realized that if we take as unity the number of electrons generated at a particle density equivalent to "3 torr" (4.41×10^{17} cm^{-3} in this case) and a fixed temperature T, then at "5 torr" there would be about $2\frac{1}{2}$, and at "10 torr" approximately 9, or almost an order of magnitude variation in electron generation rate due to pressure effects.

Weighting the cross-sectional slope constants according to the number of data points available at each pressure, the values for the three species tested are:

Table 2

argon	$C = 1.2\times10^{-19}$ $cm^2/ev \pm 15$ per cent,
krypton	$C = 1.4\times10^{-19}$ $cm^2/ev \pm 15$ per cent,
xenon	$C = 1.8\times10^{-20}$ $cm^2/ev \pm 15$ per cent.

Figure 31 shows a comparison of the experimental work of Rostagni[4], the theoretical computation of Rosen[19], and the results of this study for argon. As explained in the introduction, the work of Rostagni and Rosen was concerned with the one-step process so that the comparison of their results with those of this investigation is, at best, qualitative; but the fact that the argon cross-

sectional slope constant determined in this study fairs quite well into Rosen's theoretical curve, at energies just above threshold, is noteworthy. A more quantitative comparison can be made with the work of Harwell and Jahn. From the data contained in their corrected Arrhenius plots*, the cross-sectional slope constant C was computed to be $\sim 7\times10^{-19}$ cm^2/ev, $\sim 2\times10^{-19}$ cm^2/ev, and $\sim 3\times10^{-20}$ cm^2/ev, for argon, krypton, and xenon, respectively, using the first metastable level as the activation energy. A critical comparison of these results with those of this study is to be found in Chapter VII.

The most singular aspect of the cross-sectional slope constant data presented in Table 1 is that the C factor for xenon appears to be precisely an order of magnitude too small to be consistent with the data for argon and krypton. As there is no theory of the atom-atom excitation-ionization process currently extant which can analytically describe this interaction and predict the behavior of the cross section near threshold, it would be pure speculation to attempt to provide a reason for the relatively diminuitive size of the xenon cross-sectional slope; indeed, it would be just as speculative to try to explain why the argon and krypton slope constants are, to within experimental error, equal. One could only reiterate the precautions used in the experiment and point out that while small ($\lesssim 10^{-6}$), the impurity level was finite, and possibly (but not probably) affected the results. As will be discussed below, the xenon-xenon ionization (excitation) cross section is equal, again to within experimental error, to the argon ionizing xenon cross section, i.e.,

* Cf. Physics of Fluids 7, 214 (1964).

the data are seemingly self-consistent.

The behavior of pure xenon during the initial ionization phase was, at high β ($\gtrsim 2.0$), that is, low temperatures, conspicuously different than that of the other pure gases, argon and krypton, and from the argon-xenon mixtures. This difference was a pronounced increase in electron density to a level between 10^{11} and 2×10^{11} cm^{-3} in times on the order of 100 to 200 μsec* immediately after the passage of the shock. This initial electron-density increase appeared to be almost linear and was followed by what for all intents and purposes was construed as being a normal atom-atom, two-step ionization process, i.e., a slow, linear build-up of electron density. The atom-atom electron generation rate data were computed by first subtracting out this initial "block" of electron density, the results correlating remarkably well with data taken at higher Mach numbers (low β) where this "pre-ionization" phenomenon was not evident.

For temperatures below $\beta > 2.5$, the atom-atom phase was so weak that no useful data could be collected. Initially, it was thought that this precipitous rise in electron density was a manifestation of the preliminary phases of the atom-atom ionization process discussed in Chapter II. On closer scrutiny, the times involved were shown to be too long and the electron density too high for this to be true. Photoionization has been discounted as a possible mechanism because of

---

* Compared to useful electron-density data test times of $\sim$2000 μsec.

the almost complete lack* of visible luminosity** associated with these, and in fact all of the, xenon runs and because of radiation trapping. The most reasonable explanation is that an impurity, perhaps water vapor, is ionized and rapidly attains an equilibrium level of ionization. This level, about 2×10^{11} cm^{-3}, would correspond to an impurity level of around 2×10^{-7} if we assume complete ionization of the impurity. This is surprisingly close to the calculated "uncontrolled" impurity level of the shock tube (see Appendix E, and particularly Figure 6). However, it should be re-emphasized that while the uncontrolled impurity level was, as far as can be determined, consistent from run to run, this behavior was peculiar only to the xenon and not the other gases tested. This would lead one to suspect also the high N_2 impurity level (i.e., 22 ppm, cf. Table page 84) in the xenon received from the supplier. At this time, therefore, no truly definitive statement can be made concerning the anomalous ionization behavior.

Binary Specie

All told, four different argon-xenon mixtures were studied: 0.1 per cent, 0.48 per cent, 5 per cent, and 20 per cent xenon in argon. Because the results from the testing of the 0.1 per cent and 0.48 per cent mixtures were not substantially different from those obtained when testing pure argon, they have not been presented. The Arrhenius plots for the 5 per cent and 20 per cent mixture ratios are

* Using the same amplification of the luminosity signals as used in recording argon data, see Appendix J.

** Except for the ubiquitous light spike marking the shock front.

presented in Figures 29 and 30, respectively. All these data were obtained at a nominal pressure of 5 torr, no attempt being made to investigate pressure dependence as was done in the case of the single specie gas.

As discussed in Chapter III, the atom-atom electron generation rate for binary gas mixtures is ideally* the consequence of four independent reactions. The cross-sectional slope constants for two of these, the intra-specie reactions, i.e., argon-argon (C_{11}) and xenon-xenon (C_{22}), are known from the single specie studies. The other two, the interspecie reactions, i.e., xenon ionizing argon and argon ionizing xenon, whose cross-sectional slope constants are denoted as C_{12} and C_{21} respectively, are of course unknown and the reason for the binary gas mixture experiments. In fact, it is possible to determine, with accuracy, only one of the interspecie cross sections, for reasons which will be explained shortly.

The best fit to the data in both the 5 per cent and 20 per cent cases is obtained by letting C_{21} equal $C_{22} = 1.8\times10^{-20}$ cm^2/ev and, for consistency, C_{12} equal $C_{11} = 1.2\times10^{-19}$ cm^2/ev, with $E_{*1} = 11.548$ ev and $E_{*2} = 8.315$ ev. The extent to which uncertainties associated with both the intra-specie cross-sectional slope constants (C_{11} and C_{22}) and the (unknown) interspecie (xenon ionizing argon) cross-sectional slope constant (C_{12}) would affect the determination of the argon ionizing xenon cross-sectional slope constant (C_{21}) can be readily judged by inquiring as to the relative contribution each of

---

* In the absence of extraneous impurities which would constitute a third specie.

the four reactions makes to the overall, atom-atom electron generation rate. Denoting the reactions by their cross-sectional slope constants, the fractional contribution each makes to the electron population for temperatures representative of the extremes of the range studied, is shown in the following table:

Table 3

Mixture	β	Reaction C_{11}	C_{12}	C_{21}	C_{22}
5% xenon in argon	1.4	0.501	0.042	0.449	0.008
	1.8	0.230	0.020	0.737	0.013
20% xenon in argon	1.6	0.098	0.040	0.794	0.068
	2.0	0.032	0.013	0.881	0.075

At worst, the $\pm$ 15 per cent uncertainty associated with the argon-argon cross-sectional slope constant (C_{11}) will contribute approximately 8 per cent uncertainty to the argon ionizing xenon cross-sectional slope constant (C_{21}). Similarly, the error in the determination of C_{21} due to the uncertainty in the xenon-xenon cross-sectional slope constant (C_{22}) could at most amount to about 1 per cent. Further, it can be appreciated that even if the assumed interspecie, xenon ionizing argon cross section (C_{12}) were to be in error by $\pm$ 100 per cent, the argon ionizing xenon cross section (C_{21}) for the extreme case of low β, 5 per cent xenon in argon, would be affected by $\pm$ 10 per cent. It is obvious then that no reasonable estimate of the xenon ionizing argon cross-sectional slope constant (C_{12}) can be made on the basis of this experimental work, and that

the majority of the generated electrons,for the mixtures studied and the test conditions encountered, arise from the argon ionizing xenon reaction.

The mixture data have associated with them error brackets which are equivalent to those applied to the single specie data. The uncertainty introduced by possible variation from the specified mixture ratio is included in the brackets shown in Figures 29 and 30. Also shown in these figures are dashed lines representing the calculated composite atom-atom ionization behavior for a variation of $\pm$ 20 per cent in the argon ionizing xenon cross-sectional slope constant ($C_{21} = 1.8 \times 10^{-20}$ cm^2/ev). This amount of uncertainty is judged to be a reasonable estimate of the error associated with the determination of this cross section.

Therefore, it is concluded that, within a probable error of about $\pm 20\%$, the argon ionizing xenon cross section is equal to the xenon-xenon ionization cross section.

ν_c/ω Data

By matching the transmitted signal amplitude data to the hybrid phase (bump) extrema, it is possible, for each run, to uniquely determine the electron density (as a function of time) and the effective collision frequency ν_c*. From the simplified theory used to interpret the microwave data in terms of the physical characteristics of the plasma (see Appendix N), it has been shown that collision fre-

---

* Detailed discussions of the hybrid phase (bump) measurement and the matching procedure are to be found in Appendices U and V respectively.

quency ν_c can be written

$$\nu_c = \sum_j N_j \overline{v\Omega_{dj}}$$

where N_j is the particle density of the atoms and ions in the plasma and $\overline{v\Omega_{dj}}$ is the product of the electron velocity and the monoergic beam cross section for elastic momentum exchange, averaged over the electrons' velocity distribution. Since the microwave interaction theory was based on the concept of the ensembled averaged electron and is admittedly approximate*, the following representation of ν_c was used to correlate the data and should be consistent with the basic theory:

$$\nu_c = N \overline{v_e} \Omega_T$$

where $\overline{v_e}$ is the mean electron velocity, that is, $\sqrt{8kT_e/\pi m_e}$, m_e and T_e are the mass and temperature of the electron, and Ω_T is the "total" elastic, electron momentum-exchange cross section. The first hybrid phase maxima, occurring at an electron density of about 0.9×10^{12} cm^{-3}, was employed as the primary agent by which ν_c/ω was determined, subsequent hybrid phase extrema (refer to Figure 23) being utilized, where available, to effect a more accurate determination of this parameter. At an electron density equal to 0.9×10^{12} cm^{-3} (that is, conditions at the first matching point) and temperature in the range 5000 to 10,000°K, the calculated value for ν_c/ω using Spitzer's[30] equation for the electron-ion Coulombic elastic momentum-exchange cross section amounts to slightly less than 10^{-3}. The observed values of ν_c/ω ranged from 0.05 to about

* ν_c is considered to be a constant $\therefore \nu_c \neq \nu_c(T_e)$.

0.25, which permits the conclusion that, for all intents and purposes, Q_T can be identified with the electron-atom elastic cross section, the contribution of electron-ion elastic collisions accounting for less than 1 per cent of the total, while inelastic electron-atom collisions* amounted to another 1 per cent of the total.

The experimentally determined values of Q_T are presented for the single specie gases (argon, krypton, and xenon) in Figures 32 to 34, respectively, and for the argon-xenon mixtures in Figures 35 and 36, as functions of $\beta^{-\frac{1}{2}}$, having employed the assumption that the electron and atom temperatures were equal. In other words, $T_e = T_a$ and $\beta = 1/kT_a = 1/kT_e$ where T_e and T_a are, respectively, the electron and atom temperatures. Since $\overline{v_e} = \sqrt{8kT_e/\pi m_e}$, $\beta^{-\frac{1}{2}}$ is then directly proportional to the mean electron velocity. Comparison of experimental (argon) electron density versus time traces with computed electron-density profiles using the known atom-atom and electron-atom ionization cross sections*, taking shock attenuation effects into account, indicates that the difference between the electron and atom temperatures ($T_a - T_e$) reaches a maximum of about 500°K at an electron density of about 1.2×10^{12} cm^{-3}, that is, between the first hybrid-phase maxima and the first minima. At higher ($N_e > 3 \times 10^{12}$) or lower ($N_e < 0.4 \times 10^{12}$) electron densities, the electron and atom temperatures were found to be equal ($T_a = T_e$) to within experimental error. Therefore, when

* An electron-atom (argon) inelastic (ionization) cross-sectional slope constant equal to 7×10^{-18} cm^2/ev was employed for these calculations, cf. reference 1.

plotted as a function of $\beta^{-\frac{1}{2}}$ ($T_e = T_a$), the values for Q_T are somewhat lower and shifted to somewhat higher values of $\beta^{-\frac{1}{2}}$ than is actually the case if T_e rather than T_a were used to compute $\beta^{-\frac{1}{2}}$. The error brackets accompanying the data are indicative of the uncertainties involved in matching the hybrid phase and the transmitted wave data.

For comparison, Maxwell-averaged beam cross-sectional data, as computed by Heighway and Nichol[31] from data compiled by S. C. Brown[32], are also presented on the Q_T versus $\beta^{-\frac{1}{2}}$ plots, the argon-xenon mixture cross sections being calculated by weighting according to specie concentration, the argon and xenon cross sections.

The Maxwell-averaged beam data denoted as "Heighway, Nichols NASA TN D-2657" on the graphs exhibit quite good agreement with the microwave-determined Q_T data. The agreement is particularly good in the case of argon, virtually all of the microwave data falling (exclusive of the uncertainty brackets) within $\pm$ 20 per cent of the curve. Good agreement is also shown for krypton and for the argon-xenon mixtures. The xenon microwave data are, at low values of $\beta^{-\frac{1}{2}}$, a trifle less than a factor of two lower than the Maxwell-averaged beam data, the disparity decreasing to about 30 per cent at high $\beta^{-\frac{1}{2}}$ values. This discrepancy could be accounted for if the electron temperature were around 1000°K less than the atom temperature. It should be noted that the Maxwell-averaged beam data have associated with them an uncertainty which, although not stated, probably is of the order of $\pm$ 10 per cent[33].

The remarkable thing about the apparent close agreement is the fact that the microwave theory (see Appendix N) employs an equation of motion for the electron which assumes that ν_c is independent of electron velocity and therefore temperature. This might account, at least in part, for the better agreement of the microwave and beam data for argon, where the elastic momentum-exchange cross section in the temperature range of interest is a relatively weak function of temperature, in contrast to the poorer correlation exhibited by xenon and krypton, whose elastic momentum-exchange cross sections are somewhat more temperature dependent.

Luminosity Measurements

Luminosity profiles behind the incident shock wave were monitored using the system shown in Figure 25 and discussed in Appendix J. This system permitted the simultaneous measurement, as a function of time, of both the total (unfiltered) visible light radiated by the shock-heated gases and the emission contained in a narrow wavelength band centered at 4190 Å. This wavelength corresponds to a group of argon lines which were observed to be relatively prominent features of a weak spectra (obtained from a Mach 9.5 shock in "5 torr" of argon).

The luminosity profiles for both the filtered and unfiltered light were observed, in the case of research-grade argon and 0.1 and 0.48 per cent xenon in argon mixtures, to exhibit the same quantitative behavior. A typical example of this behavior is to be seen in the reproduction of a test record shown in Figure 19. In

general, the luminosity from shock-heated krypton and xenon was less intense than for argon, and the data so obtained less amenable to analysis. In addition, fewer data points were available for each of these two gases (Kr and Xe) as compared to argon, so that we shall consider here only the argon data. The behavior of the luminosity associated with argon-xenon mixtures was quite similar to that for pure argon. Since the electron generation rates for the 0.1 per cent and 0.48 per cent xenon in argon gas mixtures were close to that for pure argon, the overall behavior of these two mixtures was expected to be similar to pure argon, and are presented along with the argon data* in Figure 37.

In this figure, the ordinate is the time (t_L in μsec) required for the emitted intensity to reach a pre-selected arbitrary level (200 mv output from photomultiplier no. 1 (unfiltered light) and 4 mv from photomultiplier no. 2 (filtered light)). The data shown were derived from the output of photomultiplier no. 1, as its signal to noise ratio, while poor, was substantially greater than that for photomultiplier no. 2. However, the times for both outputs to reach the arbitrary levels noted (2 cm deflection of the oscilloscope trace) were generally consistent to within approximately 30 per cent. The abscissa of the graph is the inverse atom temperature ($\beta = 1/kT$) compensated for shock attenutation. That is to say, the temperature at particle time t_L was calculated using the ideal gas relationships,

---

* Pure argon was shocked at initial pressures of 3, 5, and 10 torr, whereas the argon-xenon mixtures were tested only at one initial pressure, 5 torr.

and the known shock velocity and attenuation* (cf. Appendix W for a detailed discussion of the effects of shock attenuation upon the atom temperature).

An estimate of the error associated with the determination of t_L and β is shown in the figure. The uncertainty accompanying the shock attenuation factor contributed, in large measure, to the estimated error in β. For comparison, the uncertainty associated with β, as shown in the electron generation rate (i.e., Arrhenius) plots of Figures 26 through 30, is much smaller, because here any error introduced with the shock attenuation factor is manifested as an uncertainty in the electron generation rate rather than as an uncertainty in the inverse temperature β.

In an effort to interpret these data, it was assumed that the observed luminosity was a consequence of a two-step process. In the first, rate-controlling step, an atom is collisionally raised to the first excited level, this step being identical to that of the two-step, excitation-ionization process discussed in Chapter II. The second step is postulated to parallel that of the atom-atom, excitation-ionization process with the essential difference that the energy supplied by the second atom-atom collision (ΔE) is only sufficient to further excite the atom but not ionize it, that is, $\Delta E < E_i - E_*$, where E_i and E_* are the ionization and first excited state energies, re-

* The same attenuation factors as used in the reduction of the microwave data were employed. It should be noted that the data reduced without consideration being given to the effects of shock attenuation were scattered to such a degree as to preclude interpretation. This would indicate that the luminosity is, at least to some extent, a function of the atom temperature.

spectively. The excited atom (upper excited state) then is either further collisionally excited (or ionized) or undergoes radiative de-excitation, returning, via one or more intermediate states (with an attendant production of radiation), to the first excited level. The intensity of radiation emanating from this upper excited state is dependent upon the population density of the state, i.e., $L \propto N_{**}$, where L represents the intensity of radiation from the upper excited state whose population density is N_{**}. Following the same procedure as employed in Chapter II, we write $dN_{**}/dt \propto N_{*}N$ where N_{*} as before is the population density of the first excited state and N is the neutral population density. Using equation (11), Chapter III to calculate the number of collisions per unit time per unit volume, which would impart an energy of ΔE to the excited state, and denoting the cross-sectional slope constant for this process as C_{**}, it is possible to derive

$$\frac{dN_{**}}{dt} = \frac{4\sqrt{2}}{\sqrt{\mu\pi}} C_{**}\left(\frac{1}{\beta}\right)^{3/2} N\left\{2 - \frac{3}{2}(\beta\Delta E)^2 e^{-\beta\Delta E} - 2(1+\beta\Delta E)e^{-\beta\Delta E}\right\}N_{*} .$$

Substituting the known form for N_{*} (equation (12), Chapter III) and integrating, we have

$$L \propto N_{**} = \frac{4}{\pi\mu} CC_{**}N^3\left(\frac{1}{\beta}\right)^3 (2+\beta E_{*})e^{-\beta E_{*}}\left\{2-\frac{3}{2}(\beta\Delta E)^2 e^{-\beta\Delta E} - 2(1+\beta\Delta E)e^{-\beta\Delta E}\right\}t^2 .$$

Numerical evaluation of the terms in the brackets and the pre-exponential terms using temperatures and energies typical of those encountered in this study permits us to write

$$t_L \propto \frac{L_o e^{\beta E_*/2}}{N^{3/2}} ,$$

where t_L is the time required for the luminosity to reach a level L_o.

In other words, the data, when plotted as $\ell n(t_L)$ versus β should exhibit a characteristic slope of $E_*/2$ (for argon, $E_*/2$ = 5.78 ev), and should have an inverse 3/2-power pressure dependence.

Unfortunately, the data exhibit a considerable degree of scatter, making the determination of the slope somewhat difficult. The line marked "5 torr" on the graph was judged as providing the closest fit to the data and has the proper slope (5.78 ev). The lines denoted as "3 torr" and "10 torr" also have a slope of 5.78 ev, and are positioned so as to exhibit a 3/2-power pressure dependence in relation to the "5 torr" line.

Because of the scatter, the limited number of data points available at "3 torr" and "10 torr," and the relatively restricted range of temperatures studied, it is difficult to make a definitive statement concerning the validity of the proposed mechanism other than that the data are not inconsistent with the hypothesis. Weymann[3] has derived a quite similar luminosity time dependence employing as a mechanism a two-body recombination reaction (in the atom-atom ionization regime). However, his atom-atom electron generation rate equation, because of the manner in which the second step of the process is handled, predicts a quadratic rather than the observed linear time dependence. Therefore, the similarity of form must be construed as being accidental.

CHAPTER VI

CRITICAL DISCUSSION OF THE RESULTS OF HARWELL AND JAHN*

The pronounced discrepancy between the pure gas (Ar, Kr, and Xe) collision cross-sectional slope constants determined from the data of Harwell and Jahn** and those determined during the course of this investigation, led to an attempt to reconcile the two sets of results. In particular, the cross-sectional slope constant estimated from Harwell and Jahn's data for argon is some five times larger than that derived from the data presented in Figure 26. The krypton and xenon data exhibit a disparity amounting approximately to a factor of two, in the same direction as noted for the argon case. The attempted reconciliation involved an evaluation of the effects that differences in both the data reduction procedure and the experimental technique might have upon the final result, i.e., the cross-sectional slope constant.

Besides the manner in which the microwave crystal calibration was handled (Harwell and Jahn used a fixed calibration curve for all their data rather than a separate calibration for each data point as used here), they employed a different field-pattern correction function. The mean field-pattern correction curve of Figure 17 was inferred to be similar to the function they applied to their data in

---

* In their investigation of the atom-atom ionization process in the pure (single specie) noble gases, Harwell and Jahn[14] employed the same basic shock tube and microwave circuitry used in this study. The details of their experiment are to be found in reference 53.

** Cf. Physics of Fluids 7, 214 (1964); also Chapter V.

contrast to the synthesized correction curve used in this study, which is shown on the same figure (labeled $\nu_c/\omega = 0.30$), and is discussed in Appendix P. To ascertain just what influence the choice of a field-pattern correction function would have upon the final result, all of the "5 torr" argon data shown in Figure 26 were re-reduced using the mean field-pattern correction function. Even though the data reduced in this manner were somewhat difficult to interpret because of uncompensated field pattern-induced perturbations of the transmitted signal, the resultant cross-sectional slope constant was only some 20 per cent higher than the value deduced using the synthesized field-pattern correction function*. Therefore, this difference in the data reduction procedure is inadequate to account for the observed discrepancy in the results. Similarly, estimates of the effect of variations in the crystal calibration characteristics and the matching procedure, wherein ν_c/ω is determined, can at most account for a factor of two. Clearly, the discrepancy (for the case of argon) does not arise from the peculiarities of the data reduction scheme employed.

In order to duplicate as closely as possible the experiments conducted by Harwell and Jahn[14], the mechanical refrigeration system discussed in Appendices D and L, and shown schematically in Figure 1, was turned off. This means that if back diffusion of pump oil (from the mechanical vacuum pump in the flow system)

* The values of ν_c/ω computed for the same runs using the two different correction factors differed, however, by as much as 50 per cent; the uncertainty in the determination of this parameter was greater when using the mean rather than the synthetic field-correction function.

were to be present during the flow period preceding the shot, oil vapor could enter the tube unhindered by the cold-trapping effect of the jacketed flow line. In addition, because the rough pumping line (used to evacuate the tube after a run) were no longer acting as a cold trap, contamination of the tube walls could occur, leading to an increase in the outgassing rate. Also, to further duplicate the operational procedure employed by Harwell and Jahn, no effort was made to "dump" the gases trapped around the barrel and/or O-rings of the 6 mm (1/4") Circle Seal valve interposed between the shock tube and the 0→20 torr Wallace and Tiernan gauge used to sense pre-shock gas pressure. As discussed in Appendix L, this valve was normally* activated a number of times prior to activation of the flow system so that the trapped gases could be evacuated. This procedure prevented these gases from entering the test gas when, just prior to the shock, the Circle Seal valve is shut, thereby isolating the gauge from the potentially deleterious effects of the shock and post-shock high-pressure (> 20 torr) tube environment.

Six shots were made in 5 torr of argon under the conditions discussed, the resulting data from these experiments being reduced precisely the same way as all the other data presented (cf. Appendix X, etc.). The results of these tests are presented in Figure 38.

It is obvious that the absence of the cold traps and the precautionary dumping of the gas trapped in the pressure-gauge valve did indeed lead to gross changes in the ionization rate, particularly

---

* This procedure was followed in the collection of all the data presented in Chapter V.

at high values of β. At the time these tests were conducted, the refrigeration system had been off for about 41 hours. Outgassing rates taken during this test series were not significantly different from previous test series where the refrigeration system was operating; any increase in the rate could have very well been obscured by the scatter associated with the measurement (cf. Figure 5). Similarly, the ultimate tube pressure remained within the range normally encountered (around $2 \rightarrow 5 \times 10^{-6}$ torr).

In addition to the ionization rates increasing , there was a marked increase in the visible (filtered and unfiltered) luminosity associated with these shots* as compared to similar argon shots taken under almost identical conditions of Mach number and initial pressure, employing the full operational procedures of Appendix L. From past experience, such an increase in luminosity has been associated with contamination of the test gas. It should be mentioned that the research grade gas used for this test series was from the same cylinder as used in gathering part of the data of Figure 26.

These facts would strongly suggest that the test gas of this series was contaminated, either by back diffusion of oil vapor from the flow-system pump and/or contamination released from the protective valve leading to the pressure gauge. The data, although limited in number, are consistent with this hypothesis, a contami-

---

* The values of Q_T for these data, when plotted as a function of $\beta^{-\frac{1}{2}}$, were found to be consistently above (by as much as 30 per cent) the argon data presented in Figure 32. Because of their sparse number and the relatively large uncertainty associated with their determination, it was felt that not too much significance could be attributed to this observation.

nant of lower ionization potential than the host gas tending to influence the low temperature (high β) ionization rates more than those taken at high temperature (low β), cf. the discussion of Chapter V concerning the binary specie ionization rate.

The fact that there is less of a differential between the two sets of cross-sectional slope constants (i.e., between Harwell and Jahn's and this work) for krypton and xenon lends credence to this supposition, as these gases have lower ionization (excitation) potential than does argon, and their behavior would be less affected by a contaminating impurity specie having an ionization (or excitation) potential somewhat lower than that of argon. Therefore, one is led to the tentative conclusion that the estimated impurity levels quoted by Harwell and Jahn could very well be in error, that is, lower than actually was the case.

CHAPTER VII

CONCLUSIONS AND RECOMMENDATIONS

Conclusions

On the basis of the experiment discussed in the preceding chapters (and in the Appendices), it is possible to arrive at a number of conclusions concerning the atom-atom ionization process in the noble gases and their mixtures. In addition, it is possible to draw certain inferences relevant to the evaluation of the microwave diagnostic system, to wit:

(1) The two-step, atom-atom ionization process, wherein the first step (the elevation of the target atom to the first excited level) is rate controlling, has been shown to be the dominant ionization path, immediately after the passage of the shock and prior to the electron-atom ionization process.

(2) As a corollary, the atom-atom ionization process has been shown to exhibit an electron generation rate which has a quadratic dependence on pressure, that is, neutral particle density (within an experimental error of 15 per cent), to have an activation energy equivalent to the lower excited energy levels, and to be independent of time.

(3) The use of an approximate form of the atom-atom ionization cross section (wherein the cross section Q near threshold, E_*, is characterized by a linear dependence on relative energy, i.e., $Q = C(E-E_*)$, C being the cross-sectional slope constant) has been experimentally verified (within about 15 per cent) as being an entirely adequate representation for use in formulating low tempera-

ture ($\beta \equiv \frac{1}{kT} \approx 1\ ev^{-1} < E_* \sim 10$ ev) kinetic reactions.

(4) The atom-atom ionization cross-sectional slope constants for three pure, noble gases have been determined as having the following values:

argon: $C = 1.2 \times 10^{-19} \pm 15$ per cent cm^2/ev,

krypton: $C = 1.4 \times 10^{-19} \pm 15$ per cent cm^2/ev,

xenon: $C = 1.8 \times 10^{-20} \pm 15$ per cent cm^2/ev.

(5) The cross-sectional slope constant for argon ionizing xenon has been determined to be (within an experimental uncertainty of $\pm$ 20 per cent) equal to the xenon-xenon ionization cross-sectional slope constant, that is, $C = 1.8 \times 10^{-20}$ cm^2/ev (see Figures 29 and 30).

(6) While it is somewhat dangerous to generalize on the basis of a single correlation, the argon-xenon mixture results suggest that, at least for the low energies at which the tests were conducted $kT < 1$ ev, the projectile atom (argon for the binary specie tests, xenon for the single specie tests) behaves as a structureless particle, this in spite of their relatively involved electronic structures.

(7) The Maxwell-averaged elastic momentum-exchange cross sections for argon, krypton, and xenon, as determined from the microwave data (ν_c/ω), exhibit (particularly for the case of argon) remarkable agreement with Maxwell-averaged beam data. The agreement for argon is within about 20 per cent; krypton, about 30 per cent; and xenon, variable from a factor of 2 at the low end of the temperature range to about 30 per cent at the high end (see Figures 32 to 34).

(8) Such excellent agreement as exhibited by the argon elastic cross-sectional data (the beam data for argon presumably is more reliable than for krypton or xenon) would suggest that the simplified model of microwave-plasma interaction based upon the concept of an ensembled averaged electron (and the associated assumption of an energy-independent elastic momentum cross section, that is, $\nu_c \neq \nu_c(E)$ is an entirely valid representation of the interaction of electromagnetic waves with moderate pressure (about 1 atmos.), moderate temperature ($kT \sim 1$ ev) magnetically unbiased plasmas.

(9) A limited evaluation of the earlier atom-atom ionization rate work of Harwell and Jahn indicates that their results were affected by impurities, the impurity level of their test gas being higher than quoted.

(10) An evaluation of the luminosity profiles associated with the atom-atom ionization process suggests that it is primarily composed of line radiation, the monitoring system being too imprecise and, as a consequence, the data too scattered, for a more definitive statement to be warranted at this time.

Recommendations

(1) Because the major proportion of the test-gas impurity level is caused by the known impurities associated with the research grade gases (cf. Appendix E), as purchased from the vendor, it is recommended that a limited series of tests be conducted using test gases having lower (known) impurity levels (on the order of 10^{-7}).

(2) It is recommended that a series of tests be conducted using krypton-xenon mixtures to determine the krypton ionizing xe-

non cross-sectional slope constant and to further substantiate that the cross section is not affected by the structure of the projectile particles (for energies on the order of 1 ev).

(3) It is recommended that an analytical study of the idealized interaction of a plane, plane-polarized monochromatic electromagnetic wave with an isotropic slab of plasma, infinite in lateral extent, having an arbitrary electron density distribution in one lateral direction (the density being uniform in the direction of propagation), be made. This would permit a more realistic assessment of the effects of lateral electron-density gradients to be made and facilitate the interpretation of the shock-tube microwave data.

(4) It is recommended that the work of Petschek and Byron[1] be expanded to include the effects of the atom-atom ionization process. This would permit realistic estimates of the electron-atom ionization cross section to be made and allow the electron temperature to be calculated relatively accurately, thereby improving the interpretation of the elastic momentum-exchange cross sectional data (i.e., the interpretation of ν_c/ω in terms of Q_T).

APPENDIX A

DISCUSSION OF THE CONSTANT SLOPE APPROXIMATION OF THE ATOM-ATOM IONIZATION CROSS SECTION

Rosen has computed the one-step, atom-atom ionization cross section for argon[18] and for helium[19] and compared his results with the experimental work of Rostagni[4]. This comparison for the case of argon is shown in Figure 31. Rostagni's data show a virtually linear cross-sectional dependence on relative energy for relative energies up to the limits of the comparison (250 ev), while the computed cross section of Rosen has a monotonically increasing slope. In general, inelastic collision cross sections exhibit a characteristic dependence on relative energy wherein the cross section increases almost linearly from threshold to some maximum value and then decreases slowly over a range of energies considerably larger than the range over which the increase occurred.*

It can be inferred, then, that the atom-atom ionization (or more properly, excitation) cross section would in all probability have an energy dependence similar to that described above. Ideally, such a cross section could be represented by an analytical relation having three adjustable parameters. These parameters would specify the initial behavior of the cross section from the threshold to the maximum energy (e.g., the slope of the initial portion of the cross-section

* Cf. Chapter 4 of Basic Data of Plasma Physics, by S. C. Brown[32] for many examples of this type of behavior. Also, the work of Geltman[34] and Foner and Nall[35], who demonstrate that the initial rise in cross action as a function of energy above threshold is quite linear for one-step ionization of He, Ar, Kr, Xe by electron impact, should be consulted.

curve), the maximum point, and the characteristic manner in which the cross section decreased with increasing energy. A comparison of the atom-atom electron generation rate, calculated on the basis of this cross section with the experimentally observed rate, would then provide a means of determining the proper numerical values for the three factors characterizing the cross section. This is feasible only insofar as the experimental data are sufficiently precise so as to permit these parameters to be evaluated unambiguously.

The uncertainties associated with the experimental determination of electron generation rates were found to be of sufficient magnitude as to preclude the use of the three-parameter cross section representation. Because of this, it was decided to characterize the cross section by one parameter. Weymann[3], in his work, has employed a one-parameter cross-sectional model where the cross section is assumed to be a constant for all energies above threshold. In this study, it was deemed to be more realistic to assume that the cross section could be adequately represented by the initial phase of the three-parameter model, that is to say, the cross section Q is taken to be a linear function of the relative interaction energy above threshold, i.e., $Q = C(E-E_*)$, where E_* is the threshold (excitation energy) and C, the slope factor, is the adjustable parameter which is to be experimentally determined. This method of approach is identical to that used by Harwell and Jahn[14].

It is obvious that this form of cross-sectional dependence on energy will weigh too heavily those collisions which occur at relative energies higher than that at which the peak actually occurs. As we

are experimentally generating gases with temperatures equivalent to about 2/3 ev and the threshold energy in all instances is above 8 ev, it is only those relatively few atoms which occupy the exponentially decreasing (with increasing energy) tail of the Boltzmann distribution that have sufficient energy to interact. Therefore, one would anticipate that the constant-slope cross section should be a quite accurate approximation. In order to set some bounds on the inaccuracies introduced by this assumption, it would be of interest to determine the fraction ($\mathfrak{F}$) of reactions which occur for all relative energies above a lower value, E_f, where $E_f \geq E_*$ and $\mathfrak{F} = 1.0$ for $E_f = E_*$. Following the calculations described in Chapter III, it is a straightforward exercise to show that

$$\mathfrak{F} = \frac{\left[\left(\frac{E_f}{kT}\right)^2 + \left(\frac{E_f}{kT} + 1\right)\left(2 - \frac{E_*}{kT}\right)\right] e^{-\left(\frac{E_f - E_*}{kT}\right)}}{\left(2 + \frac{E_*}{kT}\right)} .$$

For argon ($E_* = 11.55$ ev) at a temperature equivalent to 2/3 ev, direct computation shows that $\mathfrak{F} = 0.015$ for $E_f = 16$ ev, i.e., approximately 1.5 per cent of all ionizing (excitation) reactions are a result of encounters where the relative energy was 16 ev or greater. Stated in another way, for every 1000 electrons generated (per unit time and volume) in argon at 2/3 ev, 985 are a result of reactions involving relative energies such that $11.55 \leq E \leq 16.00$, and 15 arise from interactions $E \geq 16.00$. In light of the known experimental and calculated argon cross-section behavior*, it is anticipated that the

---

* For the one-step process discussed earlier.

peak of the cross-section curve would occur at energies on the order of 100 ev. From this, one is lead to the opinion that the constant-slope cross section is an excellent approximation to the actual cross section, the inaccuracies associated with its use being negligible in comparison to those associated with the determination of the electron generation rate.

APPENDIX B

BASIC SHOCK TUBE DESIGN DETAILS

The overall layout of the conventional shock tube used in this experiment can be discerned from the photograph of Figure 2 . In this photograph, the dump tank and diagnostic sections are in the foreground; the driver section and the refrigerated portions of the flow system are in the background. A clearer view of the driver section end of the shock tube, and of the portion wherein most of the diagnostics are performed, is presented in the photographs of Figures 4 and 3, respectively. In addition to these photographs, the schematic plan view of the shock tube presented in Figure 1 should be consulted.

The shock tube proper is constructed from specially extruded aluminum (6066-T5) tubing. This tubing, supplied by the Alcoa Company in 3 meter (10') lengths, has a square internal passage 5 cm by 5 cm*, and walls about 2 cm (3/4") thick (corresponding to external tube dimensions of 9 cm by 9 cm). The selection of the square geometry and the internal dimensions noted was predicated by the dielectric, microwave-diagnostic section. This section, a length of Fischer-Porter pyrex tubing about 25 cm long (10"), has internal dimensions which are precisely (to within <0. 1 mm) those of the aluminum tubing.

A 1. 2 M(4') length of aluminum tubing, both ends of which have been machined to accept a standard Buna N O-ring, is used as a driver section. One end is sealed with a steel cover plate through

---

* The corners of the square are "filled," the fillet being some 3 mm wide.

which the driver gases are admitted; the other end seals against the diaphragm. Although proof-tested to 2000 psi, driver-gas pressures have been restricted to the range below 1000 psia. Standard CIT bottled gases, supplied by the Linde Company, with an impurity level of approximately 50 ppm, were used as driver gases. These gases, suitably regulated, flowed from the cylinders into a flow-control manifold and thence into the driver section via an $\sim$ 1 cm (3/8") flexible line. A Heise 0 - 1000 psia gauge with an indicator needle was used to monitor the maximum (i.e., diaphragm burst pressure) manifold pressure for each run. At any one time, a maximum of two cylinders could be used to supply the driver section, permitting gas mixtures such as H_2 + He and He + Ar to be used. Variation of the mixture ratio, for a given diaphragm bursting pressure, provided a precise means of controlling the test Mach number. The dual supply feature also permitted, for those cases where a single specie and not a mixture was used as the driver gas, complete utilization of these gases. By using a cylinder in which the pressure was higher than the diaphragm bursting pressure, in conjunction with one whose pressure was lower, it was possible to completely exhaust the lower pressure bottle.

Diaphragms cut from copper or aluminum sheeting (in the fully annealed state) were used to separate the driver section from the rest of the tube. Aluminum diaphragms ranged in thickness from 0.25 mm (0.010") to 0.65 mm (0.026") in increments of about 0.13 mm (0.005"); the copper diaphragms ranged from 0.28 mm (0.011") to 0.43 mm (0.017") in increments of 0.076 mm ($\sim$ 0.003"). To ensure reprodu-

cible burst pressures, the diaphragm scorer shown in Figure 39 was designed and fabricated. The diaphragms were scored in directions coincident with the diagonals of the tube passage so that the four petals formed when the diaphragms burst would conform to the inside of the tube and not obstruct the flow. A "Red Devil" glass cutter provided the scoring action under a force of about 6 lb. from the off-set weight. From tests it was determined that a minimum of 4 passes (for each of the two diagonal score marks) was required to prevent the diaphragms from bursting in such a manner that pieces of the petals entered the tube. Most runs were made with diaphragms scored by 12 passes (in each of the two directions) of the glass cutter, the remainder of the runs being made with diaphragms scored only 4 times. For the same diaphragm material, a consistent bursting pressure differential of about 50 psia could be expected between those scored 4 times and those scored 12 times. It was possible then, by judicious choice of diaphragm material, thickness, and scoring procedure, to reproducibly* select any one of 13 driver pressures (i.e., bursting pressures) in the range between 90 psia and 970 psia so that a required shock strength could be readily produced.

Two 3M (10') lengths of aluminum tubing separate the driver section from the pyrex, microwave diagnostic section, the joints again being sealed by O-rings. All openings into the tube, save one, have a

---

* The vast majority of the diaphragms burst within $\pm$ 5 per cent of their experimentally-determined nominal pressure levels. In some instances, where variations in Mach number were generated by altering driver-gas mixture ratio, a series of similar diaphragms were observed to burst within $\pm$ 2 per cent of their nominal value.

standardized 2.5 cm (1") diameter, great care being exercised to ensure that the shock-tube wall thickness at these port stations was uniform to within less than 0.04 mm. A set of interchangeable port plugs was fabricated, to the same tolerance limits as noted, to mate with the wall ports. These plugs, sealed to the tube with an O-ring, were then modified for use as view ports (see Figure 7), film gauges, or flow ports, their dimensions ensuring that the inside surface of the shock tube would be free from discontinuities greater than ~ 0.04 mm.

Immediately downstream ($\sim$15 cm) from the diaphragm station, a 5-cm diameter port was machined. This relatively large diameter opening was required to assure efficient pumping action from the 5-cm (2") diffusion pump* used to evacuate the tube below the limits of the mechanical pumps, i.e., below 10^{-3} torr. The diffusion pump was connected to a dry ice - acetone cold trap, which in turn was connected via 5-cm stainless-steel tubing to the 5 cm (2") gate valve affixed directly on the shock tube. A cavity, 5 cm in diameter by $\sim$8 cm high, was therefore present when the gate valve was in the closed position preparatory to the passage of a shock wave. However, since shock formation takes place over a distance on the order of $\frac{1}{2}M$ in front of the diaphragm, this cavity apparently is not detrimental to its proper formation.

Two standard plugs, positioned about 25 cm and 32 cm from the diaphragm station, modified as $\sim$17 mm I.D. flow ports, are used respectively for rough pumping and for the flow system. Two other

---

* A Cenco model PCM 115 diffusion pump operating on Dow-Corning DS 705 silicone fluid was used.

standard ports have been included in this first section of the shock tube. One at about 10 cm from the diaphragm station accepts a plug modified as a safety valve to prevent the tube from being accidentally pressurized above 50 psi. The other, some 10 cm from the joint separating the two 3M sections, is used to mount a CEC model GPH-100A cold-cathode pressure gauge.

The second 3M length of tubing has three pairs of ports positioned as shown in the sketch on page 124. The steel yoke used to support the pyrex diagnostic section is sealed to this section of tubing with an O-ring, the pyrex tube in turn being sealed to the yoke in the same manner.

A 60 cm (2') length of aluminum tubing separates the yoke from the dump tank. In addition to the two pair of ports shown in Figure an additional port, used to admit both the research-grade test gases and the CIT argon, post run, pressurizing gas is present. A special flange is affixed to the downstream end of this section of tubing which mates with a similar flange on the dump tank. A 0.05 mm (2 mil) annealed aluminum diaphragm is sealed between these flanges by O-rings, thereby isolating the shock tube from the dump tank, which need not be evacuated to as low a pressure level as the shock tube proper.

The dump tank used to eliminate strong reflected shock waves (which could interfere with the processes under study) and to reduce the post-shock pressure level in the tube,* is a modification of a surplus Air Force breathing oxygen tank. With dimensions of ~60 cm diameter by ~ 120 cm length (2' diameter by 4' long), the included vol-

* Post-shock pressure levels in all cases were less than 500 torr.

ume of this tank, $\sim 0.3\ M^3$ (18,000 cu. in.), is some 16 times that of the shock tube.* A single opening into this tank permits evacuation by a Hypervac 25 pump to pressure levels on the order 100μ.

The details of the instrumentation, particularly those used for the diagnosis of the shock-produced plasma, will be discussed in Appendices F through K.

---

* The estimated total volume of the shock tube + lines (to closed valves) is 18,200 cm^3.

APPENDIX C

SHOCK TUBE OPERATIONAL CHARACTERISTICS

The chock tube just described was used to generate shock waves in the range $7 \leq M_s \leq 10$. This range was delineated by two considerations; the limitation of driver pressures to below 1000 psia, and the necessity for interaction of the K-band (24 gcps) microwaves with the shock-produced plasma. The only instance where the driver pressure limitation became manifest was encountered when shock heating argon at higher tube pressures. It was just possible, within the driver pressure limitation, to produce a full range of microwave-plasma interactions* in 10 mm of argon. Attempts to secure data at higher initial pressures in argon, to further substantiate the theoretically predicted pressure dependence of the atom-atom ionization process, were thwarted by this restriction. Except for this case, limitations associated with the interaction of the microwave beam with the shock-produced plasma served to restrict the operation of this shock tube to the range noted.

Experimentally-determined test times, defined as the time interval ($\Delta\tau$), in laboratory coordinates, between the shock front (as evidenced by the light spike) and the occurrence of the cold front which was assumed to be manifested by a drop in electron density (and a subsequent precipitous rise in the transmitted microwave signal), agreed

---

* The determination of the atom-atom ionization rates was limited, in the strong interactions limits, by diffraction effects (cf. Appendix R), and in the weak interaction case by the occurrence of the cold front prior to the generation of an electron density level sufficient to interact with the microwave beam.

well with theory[36]. For argon, testing times for all Mach numbers and pressures encountered were in the range 230 μsec to 320 μsec. Similarly, for krypton, the testing times ranged from 410 μsec to 560 μsec; and for xenon, from 570 μsec to 680 μsec.

As a point of reference, the equilibrium translational gas temperature, as calculated using the ideal shock relations, a ratio of specific heats (γ) of 5/3 (corresponding to the noble gases), and an unshocked gas tempe rature of 20°C, is 4653°K behind a Mach 7 shock, and 9417°K behind a Mach 10 shock. In terms of electron volts (ev), these temperatures correspond to 0.4009 and 0.8114 ev, respectively.

One other characteristic of the shock tube which is of pertinent interest is its outgassing characteristics, which, as discussed in Appendix E, influence the purity level of the test gases being shocked. Figure 6 represents the data from 45 outgassing tests. As described in Appendix L, an outgassing rate is taken prior to each run. This is accomplished by slowly closing the gate valve to the diffusion pump over a period of about 10 sec, starting at time $t = 0$ and observing, via the output of the cold-cathode gauge, the pressure rise in the isolated shock tube.* As the gate valve is closed, the tube pressure is observed to increase from its ultimate pressure, $\sim 2.5 \times 10^{-6}$ torr, to a value of $\sim 9 \times 10^{-6}$ torr. This observation is borne out by zero time intercept of the initially linearly-rising mean pressure curve, Figure 5 . The pressure increases almost linearly for approximately two

---

* The portions of the shock tube thus isolated included all portions between the driver and dump tank diaphragms, an included volume of $\sim 18,200$ cm^3 .

minutes, and then begins to level off. Thereafter, it increases slowly, apparently as a linear function of time. After 5 minutes, the mean pressure typically was of the order of 10^{-4} torr. Outgassing tests continued for $\frac{1}{2}$ hour showed that the pressure rose to between 1.5×10^{-4} and 3.0×10^{-4} torr. This is indicative of an exceptionally small leak rate, so small that for the purposes of these tests the leak rate has been taken to be completely negligible in comparison to the outgassing rate. An interesting effect was occasionally noticed when the outgassing tests were continued for 10 minutes or longer. Presumably because of pumping action induced by the operation of the cold-cathode pressure gauge, the indicated pressure would drop slightly for a period of a minute or so (starting at about 10 minutes) and then continue its almost linear rise.

A CEC type 21-611 mass spectrometer was installed on the shock tube, the Diatron unit mounted via a short (about 6 cm) tube with a diameter of about 2 cm (3/4") at the first port position downstream of the pyrex diagnostic section. A survey of the mass spectrum from mass number 10 to 77 was manually undertaken with the tube under normal pumping operation, i.e., at its ultimate pressure level of $\sim2.5\times10^{-6}$ torr, the gate valve to the diffusion pump being open. Using the total integrated output over the indicated mass range as a normalization factor, the mass spectrum was interpreted as indicating the definite presence of the following species:

water vapor	$\sim$ 63 per cent
nitrogen	$\sim$ 12 per cent
argon	$\sim$ 4 per cent

oxygen ~ 1 per cent

In addition, broad peaks in the mass spectrum centered at 43, 57, and 70 mass units accounted for an additional 11 per cent in the proportion 3, 5, 3, respectively. The broad peaks at 43 could possibly be due to the presence of CO_2, but, as with the other two broad peaks and the numerous smaller peaks occurring throughout the spectrum (accounting for some 9 per cent of the total), it is just as probable that complex hydrocarbons are also present.

Therefore, taking into account the inaccuracies inherent in the mass spectrometer (about $\pm$ 1 mass unit uncertainty above ~ 40 mass units), one can only state that the majority of the outgassing material is composed of water vapor, with nitrogen the next most prevalent specie definitely established as being present, and that approximately one-quarter of the outgassing material is composed of a mixture of argon, oxygen, and most probably hydrocarbons.

Outgassing rates taken after the mass spectrum was recorded were normal in all respects, the tube having undergone a heating cycle initiated some 18 hours previously.

APPENDIX D

SHOCK TUBE RESEARCH-GAS FLOW SYSTEM

The material outgassing from the walls of the shock tube into the gas being tested represents a source of uncontrolled impurity. This impurity is uncontrolled in the sense that its composition, and to a lesser extent its rate, is dependent upon factors over which little direct control can be exercised. In an effort to mitigate the influence that the introduction of this unwanted specie would have upon the reaction rates under study, a flow system was developed. This system, first used by Harwell and Jahn[14] and applied in a modified form in this work, uses the research-graded gases which are being tested as a diluent for the outgassing material and thereby permits the uncontrolled impurity concentration to be reduced to any level, consistent with the known impurity level of the test gases and economic considerations. The analysis of the flow system and the estimated uncontrolled impurity levels attained by its use are presented in Appendices C and E.

Figure 1 depicts the essential features of this system. Commercially available research gases are regulated to pressures on the order of 2 atmospheres (absolute) by a Matheson model 19-580 diffusion-resistant pressure regulator. Although the diaphragm of this regulator is metal, some diffusion apparently occurs. This was evidenced by an increase in the atom-atom ionization rates for those few runs where the research-grade gas was permitted to remain locked in the regulator for extended periods of time (> 100 hrs) as compared to

runs made under similar conditions where the gas was in the regulator for 24 hours or less. Since the flow system from the bellows control valve immediately downstream of this regulator to the shock tube was helium leak-tested and found to be tight, diffusion of air and/or water vapor through the regulator diaphragm was indicted as the most probable cause of the spurious reaction rates noted. To circumvent this problem, it was standard operating procedure to discard* any gas which remained in the regulator for more than 24 hours and to repressurize the system with fresh gas.

A Heise 10", 0 to 500 cm Hg absolute-pressure gauge was used to monitor the flow system pressure just upstream of the Mathieson model 603 ball-float flowmeter. This flowmeter was utilized to monitor the flow rate of the test gas and provided a reproducible and accurate means to rapidly establish a given initial test pressure in the shock tube during a run. The test-gas flow rate was controlled by a Mathieson model 657-L bellows needle valve. A check valve interposed between this needle valve and the shock tube prevented the high-pressure driver, driven-gas mixture from entering the flow system upon passage of the shock. All lines in this system were 6 mm (1/4") O. D. copper, and all junctions were soldered. To eliminate possible outgassing from the walls of the flow-system tubing, all segments except the pyrex flowmeter and the Heise gauge were heated with an acetylene torch. Heating, starting from the regulator and progressing

* This was accomplished by permitting the gas in the flow system, up to the research-grade cylinder valve (which was firmly closed between shots) to be exhausted into the shock tube and thence to atmosphere. The flow system during this operation was reduced to $\sim 10^{-4}$ torr or less in pressure.

slowly toward the open needle valve, was continued until the shock tube, which was being pumped on by the diffusion pump, remained at its ultimate pressure level (about 3×10^{-6} torr).

The test gas introduced into the shock tube close to the rear diaphragm flowed the length of the tube and was exhausted through a 2 cm (3/4") Circle Seal valve. A check valve immediately downstream of this valve prevented the shocked gases from being vented. The check valve, actuated by the passage of the shock wave, did not significantly impede the flow of the test gas prior to the occurrence of the shock. Once past the check valve, the gases proceeded to flow through a cold trap. This cold trap, whose function it was to prevent back-diffusion of oil vapors from the Hypervac 25 pump into the shock tube, consisted of a length of 69 cm, 2 cm-diameter tubing. A jacket surrounding the length of this tube acted as an evaporator for the 1/4-ton mechanical refrigeration unit. The full capacity of this unit was used to cool this line to temperatures $< -40^{\circ}C$, the great majority of data being taken with temperatures in the range of -42 to $-45^{\circ}C$. For reference, at $-40^{\circ}C$, the vapor pressure of mechanical pump oil is on the order of 10^{-8} torr. After the gas passed through the cold trap, it entered a 34,500 cm^3 settling tank employed to suppress any flow pulsation induced by the mechanical pump. Upon exiting the tank, and prior to its ultimate exhaustion outside the laboratory by the Hypervac 25 pump, the test gas flowed through another 2 cm (3/4") Circle Seal valve. This valve was carefully calibrated so that it was possible to make runs at initial tube pressures of 10 torr using the same flow rate, as indicated by the flowmeter, as was employed for the 5 torr

shots. This was done in an effort to conserve the expensive research-grade test gases, and to maintain the same impurity level for the 10-torr tests as was obtained in the 5-torr series.

The employment of a cold trap to prevent back-diffusion of pump oil, the use of a bellows-type, high-vacuum valve on the regulator (rather than a packing-type valve which had previously been used and was shown to leak), the operational procedure of dumping gas locked in the regulator for extended periods of time, and the calibration of the 2 cm (3/4") flow valve to permit constant purity level operation, are the primary features which distinguish this flow system from the one (denoted as flow system no. 3) used by Harwell and Jahn[14] in their work.

APPENDIX E

TEST GAS IMPURITY LEVEL CALCULATION

As an idealization of the flow system and outgassing process, the following simplified model will be used.

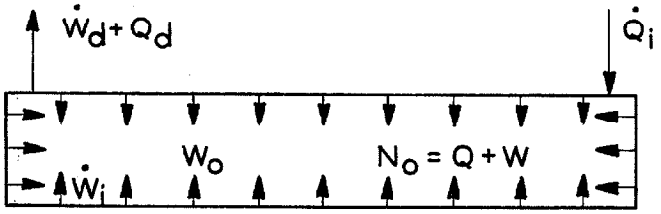

Here, $\dot{Q}_i$ represents the flow rate, in particles per second, of the research-grade test gas entering the shock tube; $\dot{W}_i$, the rate of evolution of gases from the tube wall, i.e., outgassing rate* (particles per second); N_o, the particle density under steady-state conditions, composed of pure gas Q and the impurity W; W_o, the initial impurity level present in the tube at time zero, that is, when the flow rate Q_i is initiated; and $\dot{W}_d+\dot{Q}_d$ is the rate of efflux from the tube, a mixture of impurity plus pure gas.

The quantity of interest is W/N_o, the ratio of the impurity particle density to the overall particle density of the tube as a function of time. It will be assumed that perfect mixing of the outgassing impurity with the flowing pure gases occurs so that at any instant the ratio of the impurity efflux to the pure efflux is the same as the ratio of impurity to pure particle density occurring in the tube, i.e., $Q_d/W_d = Q/W$. This assumption should be an adequate representa-

---

* The measured outgassing rate is a combination of the outgassing and leak rates. The leak rate, as determined by experiment, is quite negligible compared to the outgassing rate, and is therefore neglected.

tion of the actual mixing process because of the time scale (about 1 minute) and the low particle densities involved. Implicit in the perfect mixing assumption is the neglect of concentration gradients and the implication that all portions of the interior surface of the shock tube have the same outgassing characteristic. It will further be postulated that the tube pressure is instantaneously established, that is, for $t < 0$ the particle density is W_o, and for $t \geq 0$, N_o. It usually requires 10 to 20 seconds to reach the approximate pressure desired for a given run, the remainder of the flow time being devoted to the fine adjustment and stabilization of the pressure. Therefore, this latter assumption is not unrealistic and permits the following expressions to be written describing the steady-state character of the flow:

$$\dot{Q}_i + \dot{W}_i = \dot{Q}_d + \dot{W}_d$$

$$\dot{N}_o = \dot{Q} + \dot{W} = 0 \Longrightarrow \dot{Q} = \dot{Q}_i - \dot{Q}_d \quad \text{and} \quad \dot{W} = \dot{W}_i - \dot{W}_d$$

As the shock tube pressure is assumed to be instantaneously established, it is obvious that Q_i = constant = K (particles/cm^{3}sec). Consideration of the outgassing characteristics of the constant volume, constant temperature shock tube (cf. Figure 1) reveals that it is justified, for flow times $< \sim 120$ seconds, to set W_i = constant $\equiv \varkappa$ (particles/cm^3 sec).

From the above expressions we can write

$$K + \varkappa = \dot{Q}_d + \dot{W}_d = \left(\frac{Q+W}{W}\right)\dot{W}_d = \frac{N_o}{W}\dot{W}_d .$$

But $\dot{W}_d = \varkappa - \dot{W}$, so $K + \varkappa = \frac{N_o}{W}(\varkappa - \dot{W})$, and

$$\dot{W} = \varkappa - \frac{(K+\varkappa)W}{W_o} \quad , \quad \text{or} \quad \int_0^t dt = \int_{W_o}^{W(t)} \frac{dW}{\varkappa - \frac{(K+\varkappa)W}{N_o}} \; .$$

Performing the indicated integration, the desired result is obtained, viz.,

$$\frac{W(t)}{N_o} = \left(\frac{\varkappa}{K-\varkappa}\right)\left(1 - e^{-\left(\frac{K+\varkappa}{N_o}\right)t}\right) + \frac{W_o}{N_o} e^{-\left(\frac{K+\varkappa}{N_o}\right)t} \; .$$

This expression is graphically represented in Figure 6 for the three pressure levels encountered in this study. The curves are representative of the calculated impurity levels associated with all of the data presented in Chapter V. The great perponderance of data was taken under conditions where the flow time t was 60 sec or longer. In a few instances, it was possible to shorten this time, 40 sec being the shortest (for one shot). Using the 40 sec case as an extremum, it is seen that the maximum calculated impurity levels (W/N_o) for shots having initial pressures of 3, 5, and 10 torr are 0.47×10^{-6}, 0.26×10^{-6}, and 0.26×10^{-6}, respectively.

These impurity concentrations compare quite favorably with the known impurity levels of the assayed research-grade test gases used in this study. The table below is a compilation of the gas analysis supplied by the vendor with each of the research-grade test gases tested. The impurity levels of the mixed gases were calculated from the analyses supplied for each constituent*.

---

* In all cases the gas analysis accompanying the cylinder of test gas was that of the larger batch from which the cylinder was filled. To ensure contamination-free filling, an oxygen trace analysis was requested and performed on every cylinder purchased.

TABLE E-1. Impurity* - Parts per Million

Test Gas			O_2	H_2	N_2	H_2O	N_2O	CO_2	HC**	Rare
Argon	1.		0.5	-	4	-	-	-	0.4	-
	2.		<5	<1	<10	<3	-	-	< 5	-
	3.		0.6	1	< 4	-	-	1.8	1.2	-
Krypton			<5		<100(N_2+CO)	<4	⟵ <25 ⟶		<25	<10Ar <10Xe
Xenon			-	-	22	-	-	-	-	<20Kr
Ar + 5% Xe	1.	Ar	<1	-	< 1	-	< 1	< 1	< 1	-
		Xe	<5	-	-	-	-	-	-	-
		Mix	<1	-	< 1	-	< 1	< 1	< 1	-
	2.	Ar	<1	-	2	1.5	-	< 1	< 1	-
		Xe	<5	5	50	3	-	-	12	10Kr
		Mix	<1	.25	4.5	1.6	-	< 1	< 1.6	0.5Kr
Ar + 20% Xe		Ar	2.1	<1	2.8	0.3	-	-	< 1	-
		Xe	2.0	<5	<30	<2	-	-	<15	<10Kr
		Mix	2.1	<1.8	< 6.3	<7	-	-	< 4	< 2Kr

* The batch analyses for the individual gases are listed as quoted by the supplier. The overall impurity level of a mixture is calculated by weighing the impurity level of the constituent gases of the mixture according to their concentration.

** Hydrocarbons, usually CH_4.

APPENDIX F

DETAILS OF THE PHOTOMULTIPLIER SHOCK-POSITION INDICATORS

The typical thin-film heat gauge used for the purpose of indicating the passage of a shock front consists of a platinum film about 1 mm wide and 1 cm long deposited on a glass or quartz substrate. This film, mounted flush with the shock tube wall, its long axis parallel to the shock front, has a resistance on the order of 100 → 200 ohms. Theoretically[37], the temperature of the film, and therefore its resistance, will respond to an instantaneous change in gas temperature, e. g., to the passage of a shock front, in less than a microsecond. By connecting the film in series with a battery and a ballast resistor, as shown in the accompanying diagram, it is then possible, in principle, to use the AC-coupled output of this device as a shock position indicator, or as a side wall heat-transfer indicator. The diagram shows

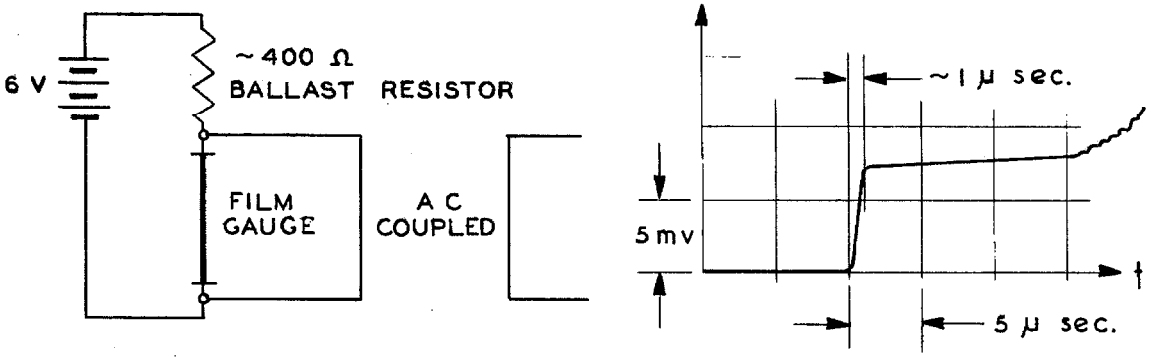

how the gauge ideally responds to the passage of the shock front, the laminar boundary layer, and then the turbulent boundary of the shock heated gases.

Numerous experiments conducted in argon at 5 torr indeed corroborate the behavior described above for shock strengths below

approximately Mach 8. However, above Mach 8, presumably because of ionization effects[38, 39], the response of these gauges to the passage of the shock front appeared as follows:

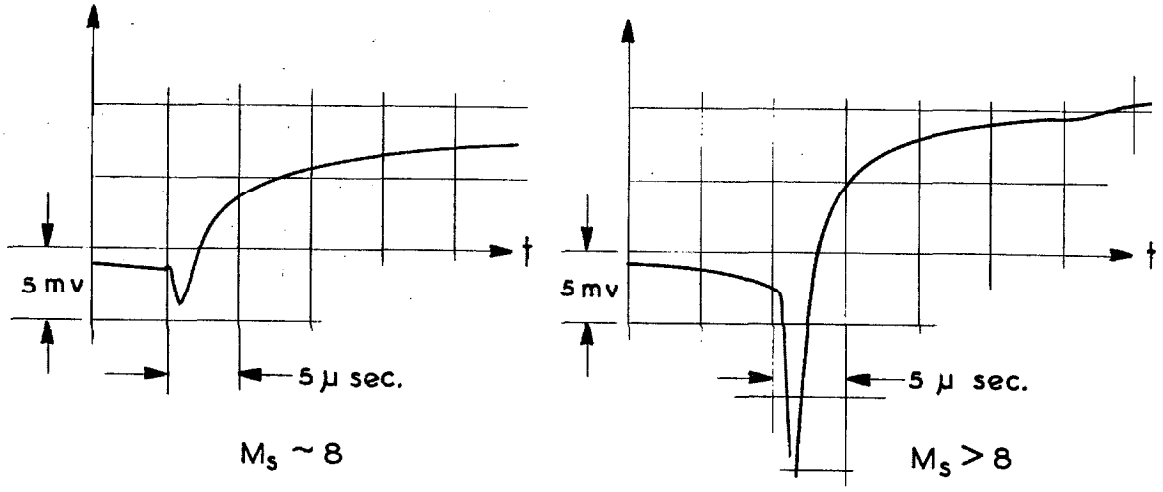

For Mach numbers on the order of 9, the amplitude of the negative portion of the signal far exceeded the positive signal level. What is more significant, the initial signal level change preceding the negative spike and the signal's behavior after the spike became progressively more gradual, extending over some few microseconds, the stronger the shock strength. To discount the possibility that this effect was due to the circuit design, the battery and the ballast resistor were removed from the circuit,leaving only the film. The response of this modified circuit (i. e., the film) to a Mach 9 shock into 5 torr of argon is depicted below.

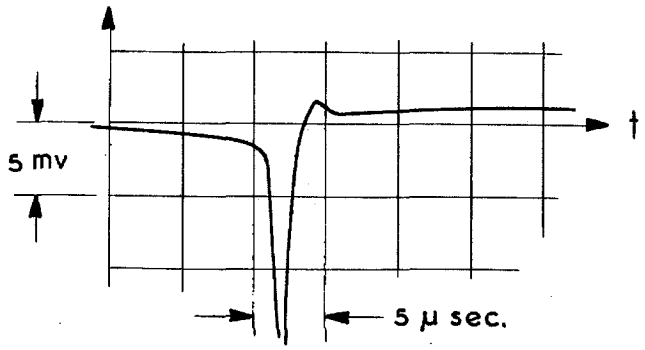

Clearly then, the use of the thin-film gauge as a shock position indicator leaves much to be desired for the accurate determination of mean shock velocity in the range $7 \leq M_s \leq 10$. Ideally, one would like a signal with a rise time on the order of one microsecond or less whose amplitude and basic characteristics were but a weak function of Mach number (for the range noted) and initial gas pressure for the test gases of interest (i.e., noble gases and their mixtures). Fortunately, there is a characteristic feature of the shock front, besides its temperature differential, which can be made to yield a signal possessing the desired attributes noted above.

This feature, the shock front luminosity, was first reported by Petschek[24] and spectroscopically studied by Turner[25]. These studies demonstrated that for Mach numbers above about 6 in ~ 5 torr of argon (and krypton), the luminosity zone was quite narrow, being on the order of 0.6 mm, and became narrower the higher the Mach number of the shock. Further, it was shown that this luminosity was due to non-equilibrium excitation of N_2 and/or CN (present in small amounts in the test gas) extending across the entire shock front rather than arising in the boundary layer from impurities scraped from the shock tube walls. Every luminosity profile taken during the course of this experiment shows the presence of shock front luminosity. In Figure 19, this phenomenon appears as a sharply rising signal, the form of which is somewhat obscure because of the manner in which it was recorded (i.e., a chopped signal of 1 μsec duration displayed every 4 μsec, characteristic of the type M plug-in used as a preamplifier for

the photomultiplier output, see Appendix J). For Mach 7 shocks, the shock front luminosity, which we shall hereafter refer to as a "light spike," rises to a maximum in between 1 and 2 μsec, decaying over a period of 20 or so μsec to a low luminosity level characteristic of the atom-atom ionization regime immediately behind this front. For higher Mach numbers, the amplitude of the "light spike" is somewhat higher, and both the rise time and the decay time are shorter (around 1 μsec and 10 μsec, respectively). These observations are directly comparable to those made by Petschek and by Turner when consideration is given to the spatial resolution employed in these tests*. For all gases considered, all Mach numbers, and all initial pressures encountered in this study, the "light spike" was present as an ubiquitous and highly reproducible feature. As will be recognized, the presence of this luminosity is indicative of nitrogenous and/or carbonaceous impurities in the test gas, which, as shown in Appendix E, are present in concentrations of less than a few parts per million.

In order to take advantage of the sharply defined shock-front luminosity zone to the fullest extent, the photomultiplier shock-position (SPI) system diagrammed in Figure 7 was designed and fabricated. Since the shock-front luminosity zone has a thickness of on the order of $\frac{1}{2}$ mm, and it was desired to measure shock passage times with an accuracy of at least 0.4 μsec and preferably 0.2 μsec, th PI optical system was designed to have a maximum breadth of vi n

---

* Cf. Appendix J for the details of the instrumentation us In particular, Figure 25 should be consulted, where a diagram the actual gas volume observed is shown.

the shock propagation direction) of about $\frac{1}{2}$ mm. As shown, this maximum occurred at the far wall of the shock tube, the field of view being only 0.35 mm wide at the near wall*.

The light port through which the shock front is observed is a standard plug modified as shown. The scratch-free, optically flat (and clear) pyrex disk is sealed to the plug by epoxy resin. Great care was exercised in mounting the pyrex window in the plug so that when installed in the tube its surface would be flush (to within < 0.04 mm) with the plug and the shock tube proper. To eliminate reflection from the walls of the plug, an insert of 100-grit aluminum-oxide cloth (spray-painted flat black) was installed. This proved to be an entirely effective reflection suppressant.

The light pipe was electrically isolated from the plug, and therefore the body of the shock tube, by a micarta sleeve. The use of this sleeve was dictated by the occurrence of some rather severe ground-loop induced noise whenever the SPI's were placed in contact with the shock tube. On either end of the light pipe (16 cm long by 2.5 cm diameter) thin disks (0.3 mm thick) were mounted. Each disk had a slit 0.24 mm wide by 1.6 cm long machined coincident with a diameter. These slits, as shown in the ray system depicted in the figure, defined a field of view having the desired characteristics. Internal reflections in the light pipe were eliminated, as in the case of the view port, by the insertion of a liner of aluminum-oxide cloth which extended the whole length of the tube, with the grit side in. This method

* Neglecting diffraction effects. Diffraction of the luminosity by the slits increases the effective view width to $\sim 3/4$ mm at the far shock-tube wall.

of reflection suppression proved to be as effective as the use of coiled pipe cleaners (cf. Appendix J) and had the advantage of being simpler to accomplish.

As in the case of the luminosity monitoring system (discussed in Appendix J), RCA type 6655A photomultiplier tubes were used to detect the shock-generated light. No special tube shield was found to be necessary in this application; a simple, well-grounded section of steel tubing (3 mm wall thickness) forming the outer casing at the SPI body proved to be quite adequate as a shield. The circuitry of the SPI photomultiplier tubes was virtually identical to that used in PM nos. 1 and 2 with the notable exception that,in order to be compatible with the amplifier-differentiator unit (pulse box), the output was positive and the amplification factor variable. Power (-950 v) was supplied to the bleeder chain of each of the SPI's by a John Fluke model 412A regulated power supply through shielded RG 55/U cabling, the four SPI's being wired in parallel. Each of the SPI units was connected to an input of the amplifier-differentiator flip-flop unit (ADFF unit) by 2 M lengths of RG 62/U cabling.

The output signal level of all four SPI units was adjusted so as to be equal for a constant (fixed intensity amplitude) input. This constant input was supplied by the calibration unit shown in Figure 7 . Under typical operating conditions, the SPI's would be adjusted (i.e., the miniature potentiometers varied) to yield an output of $\sim$ 1 mv, corresponding to a potentiometer resistance on the order of 20 Ω*.

* Because of variation in the amplification factor among the photomultiplier tubes used in the SPI units, the individual potentiometer readings for 1 mv output were $9\frac{1}{2}$, 13, 15, and 36 Ω .

Because of the low output resistance level, the output signal was found to be virtually free of internal, tube-generated noise.

In order to be assured of the highest degree of precision in the determination of shock passage time, the SPI output level and the triggering level of the ADFF unit were adjusted so as to yield a pip when the light spike signal was increasing most rapidly as a function of time. From tests this was found to consistently occur when the signal was between 1/3 and 2/3 of its maximum amplitude. Monitoring the output of one SPI unit in response to shocks of various strengths permitted the selection of those potentiometer settings which would yield a signal level just sufficient to trigger the pulse box as the light spike reached about half of its peak intensity. In turn, the output of the same SPI in response to the fixed intensity calibration unit was determined. This output (in response to the calibrator) was then used as a means of standardizing the output for all four SPI's.

APPENDIX G

DESCRIPTION OF THE AMPLIFIER-DIFFERENTIATOR FLIP-FLOP UNIT

Previous to the use of the photomultiplier shock position indicator (SPI), thin film-gauge heat gauges were utilized to sense the passage of the shock front. Since these indicators produce an output on the order of one, or at best a few, millivolts, it is necessary to amplify the output to at least 200 mv, or preferably several volts, in order to provide an adequate signal level suitable for triggering the recording instruments. This function was superbly performed by a highly reliable, three-transistor amplifier-differentiator unit, the details of the genesis of which have been lost to posterity.

In the design of the shock-velocity determination system used throughout the experiments reported herein, it was decided to use a combination of film gauge and photomultiplier shock-position indicators. Because of its availability and simplicity, a film gauge was employed to trigger the "raster scope." In this application, the vagaries attendant with its spurious reaction to high Mach number shocks (as described in Appendix F) were small compared to the time available for the "raster scope" to trigger and record the outputs of the succeeding, more precise, photomultiplier shock-position indicators. Therefore, since a reliable amplifier-differentiator circuit design was available, and since it was a trivial matter to design a photomultiplier SPI circuit to produce output signals comparable to those produced by the film gauges (that is, in the low mv range), the so-called amplifier-differentiator flip-flop (ADFF) unit was designed to be

suitable for use with both these devices. As is recognized, the requirement for compatibility of the ADFF circuitry for use with the film gauges established a far more rigorous, but simply satisfied, performance criteria than if it were designed for use solely with photomultiplier SPI's.

A circuit diagram of the ADFF unit is shown in Figure 8 . In the amplifier-differentiator portion of this circuit, the mv range signal from film-gauge or photomultiplier SPI's is differentiated and amplified to approximately 15 v. The amplifier has a constant gain of approximately 15000 for inputs below about 1 mv. For input levels above 1 mv, the output is maintained at about 15 v. Differentiation of the input signal ensures that the output signal will have uniformly short rise times. Rise times, to maximum, as short as 0.1 μsec are characteristic of this design. The output of the amplifier-differentiator unit is fed to a flip-flop circuit where, once a pre-set level is exceeded, a "pip" having a rise time on the order of 0.2 μsec, an amplitude of from 4 to 7 volts, and an exponential decay time of about 10 μsec is produced. No further output from the flip-flop is possible until it is manually re-set. A re-set indicator circuit is also shown in the figure. The re-set indicator circuit is tied directly to the outputs of the flip-flop units. Whenever one of the units produces a pip, the event is marked by the indicator light. Since the ADFF units and the shock-position indicator units were to operate in an electrically noisy environment where spurious triggering of the slip-flops would be expected, this indicator feature was particularly useful. In order to obviate the need for continually checking the viability of 30-volt

batteries, as were used to power the original amplifier-differentiator units, the power supply shown in the figure was incorporated in the overall design.

Six of these amplifier-differentiator flip-flop units, the power supply, and the reset indicator circuit* have been integrated into a single unit. Six independent inputs can therefore be individually handled. For each input there are two output terminals, one for the output from the amplifier-differentiator circuit (prior to the flip-flop) and the other for the output at the flip-flop unit (the so-called "pip" output). All six of the pip outputs are internally connected via switches to a single UHF output terminal. This feature permits any combination of the pips to be "added," as is necessary for the production of a raster display.

Because of the electrically noisy environment in which this unit was employed, it was necessary to extensively shield the entire unit with "mu" metal. Meticulous care was also exercised in providing adequate grounding for the circuits and the "mu" metal shields. As a result of these procedures, the incidence of spurious triggering of the flip-flop units was reduced to an acceptable level. With no power to the photomultiplier SPI units, triggering would occur on the average of once every 20 minutes or so. With power to the (4) photomultiplier SPI units, the time interval between incidents of unwanted triggering of one or another of the six units was approximately 4 minutes, a quite acceptable level.

---

* The author is indebted to Mr. Rex Hafer of JPL for the design of the flip-flop unit, the power supply, and the reset indicator circuits.

APPENDIX H

DESCRIPTION OF THE RASTER SHOCK-POSITION RECORDING SYSTEM

The essential features of the raster system circuitry, which has demonstrated a high degree of reliability in over 250 runs, are illustrated in Figure 10.

A Hammer Electronics Co. model H-106 regulated power supply is used, in accordance with specifications, to power the Radionics, Inc. model TWM-2a timing generator*. Two outputs are available from the timing generator; a highly accurate, linear triangular wave having a frequency of 1, 2, 10, or 20 kcps with a peak-to-peak amplitude variable from 0 to 2 volts; and a marker pulse suitable for z axis (i.e., intensity) modulation of an oscilloscope CRT intensity, at frequencies precisely ten times that of the triangular wave. The 20 kcps output was used exclusively in these studies. At this frequency, the elapsed time from peak to peak (maximum to minimum) is 25 μsec, and therefore a marker pulse occurs every 5 μsec.

The output of the marker-pulse circuit was fed directly into the CRT cathode jack on the back of the Tektronix 535 oscilloscope (the "raster" scope) to modulate the signal trace in such a manner that every 5 μsec the trace was intensified for ~ 0.1 μsec. The dots on the trace seen in Figure 9 are a result of this marker signal. The triangular wave output was, as shown, fed into the "Trigger or Ext Sweep In" input terminal of the oscilloscope. The ~ 2v peak-to-

* For proper operating, the timing generator requires a 200 v, 135 ma supply having less than 100 μv of ripple and hum, and a filament supply of 6.3 v at 6.8 amperes.

peak amplitude of this signal served to drive the oscilloscope trace horizontally so that it extended over the central 8 cm of the display. The oscilloscope's saw-tooth main sweep output was used to supply an accurately-controlled vertical displacement of the trace. This was accomplished by externally connecting the main sweep generator to one channel of a Tektronix CA type plug-in, operated in the "added algebraically" mode. The other channel received the pulses produced by the four photomultiplier SPI units, the presence of an SPI pulse serving to displace the trace abruptly in the vertical direction, making it easy to accurately position the occurrence of the event in time.

A pip from the first channel of the ADFF unit, initiated by the output of the film gauge, is used as a trigger signal. Upon receipt of this signal, the display is unblocked, that is, the trace intensity becomes visible, and the main sweep saw-tooth output voltage starts to increase linearly with time, thereby driving the trace up the face of the CRT. The triangular wave generator is running continuously; therefore, the horizontal position at which the trace starts is variable. This uncertainty in trace starting position is of no consequence and can be ignored.

Modifications* to the oscilloscope's basic circuitry were necessary before it could be operated in the manner just described. These were effected by Mr. Charles Mullett, the local Tektronix field engineer. In its modified form, it is not possible to operate the oscilloscope in the single-sweep mode, wherein the trigger circuit

* Resistor R17, in the main-sweep trigger circuit, was shunted with a 15K resistor and the delaying sweep unblanking signal was grounded.

would operate once on the first appropriate signal and thereafter remain insensitive to all others until manually re-set. This restriction offered no difficulty because, as mentioned, a pip from the ADFF box was used as a trigger signal, the ADFF box thereby acting as an extension of the triggering circuitry, permitting single-sweep operation.

In the raster display depicted in Figure 9 , it can be seen that the marker dots, excluding those at the left and right hand extremes of the trace, do not form individual columns but rather delineate two vertical, closely spaced columns. This is indicative of a slight amount of horizontal amplifier distortion caused by the high frequency of the triangular wave signal. This distortion is of no consequence as the time interval between successive marker dots was shown to be accurate to 0.1 μsec or better. This was demonstrated by displaying precisely-generated marker signals from a Tektronix type 180 A time-base generator on the raster and directly effecting a comparison. On the basis of these tests, it is reasonable to anticipate measurement accuracies on the order of 0.1 μsec for signals spaced over an interval of up to 2 millisec or more*.

The raster display presented on the oscilloscope's CRT was recorded on Polaroid type 46-L transparencies; the oscilloscope camera being opened just prior to the shot and closed immediately thereafter. To facilitate precise reduction of these raster data, $8\frac{1}{2}'' \times 11''$ photographic enlargements were made from the transparencies.

---

* The raster shown in Figure 9 exhibits a time-base length of ~ 1 millisec. By the simple expedient of altering the frequency of the time-base generator, it is possible to expand the display so that more triangular waves could be displayed, a total time base of ~ 2 millisec being a reasonable practical limit.

APPENDIX I

DESCRIPTION OF THE MICROWAVE DIAGNOSTIC SYSTEM

The microwave circuit used as the primary diagnostic tool in this experiment was designed to provide as close an approximation to a plane wave beam as possible within the context of component availability, simplicity, and reliability of operation. The basic intent in mating this circuitry to the shock tube was to physically duplicate, as closely as possible, the conditions prevailing when a plane, plane-polarized monochromatic beam of electromagnetic energy interacts with an infinite plane slab of isotropic, homogeneous plasma. The underlying philosophy then was to employ the simplest possible microwave circuitry to simulate this analytically unsophisticated but physically relevant microwave - plasma interaction.

The details of the analysis of plane plasma-slab microwave interaction and the corrections necessary to bring this theory into closer correspondence with reality are discussed, at length, in subsequent appendices. For the idealized interaction described, there are four measurable quantities, viz., the phases and magnitudes of the microwave signal transmitted through and reflected from the plasma slab. The circuit employed and schematically shown in Figure 11 measures the magnitude of these two signals. For the values of ν_c/ω associated with the shock-heated plasmas studied in this experiment ($\nu_c/\omega \sim O(0.1)$), the measurement of signal amplitudes permits as large a range of electron densities to be detected as could be accomplished with phase measurements[26] but with far fewer components.

The Bendix (Red Bank Division) 2K50 reflex klystron used as the microwave generator supplies up to 8.5 mw of coherent microwave energy in the frequency band from 23.50 gcps to 24.46 gcps. Nominal operation at 24.00 gcps is maintained by thermal tuning of the klystron cavity. A Dressen-Barnes model 10-30 (0.5→30 v DC) regulated power supply connected to the tuning grid of the tube permits the frequency to be adjusted to any value within the range specified. Another Dressen-Barnes regulated power supply (a model 62-109) is used to supply the cathode (6.3 v), the repeller (-90 v), and the cavity (+300 v). Because the shell of the klystron is also at 300 v, and in addition becomes thermally hot from operation, a protective shield in the form of a coil was installed surrounding the tube to prevent accidental contact. This coil can be seen in Figure 3 .

A DeMornay-Bonardi model DBE-979 E/H plane tuner attached to the klystron by a short wave-guide adaptor provides a means to maximize the power output at a given frequency. In essence, this component behaves as if it were part of the resonating cavity, permitting the klystron to be optimally "matched" to the rest of the circuit. The 15-cm (6") section of flexible wave guide separating the E/H plane tuner from the Uniline compensates for physical misalignments in the circuit components and serves to protect the klystron from shock-induced vibration. Since the frequency and power output characteristics of most klystrons are sensitive to the load into which they are delivering power, a narrow-band (23→25 gcps) ferrite isolator (Monogram Precision Industries, Inc., Uniline) is employed to

prevent plasma-induced reflections from reaching the klystron. This particular device has 21.2 db reverse attenuation and 0.6 db forward attenuation at the nominal test frequency of 24 gcps. A DeMornay-Bonardi model DBE-410 precision-calibrated attenuator, attached directly to the Uniline, is used to adjust the power level reaching the crystal detectors and as a means to calibrate conveniently these crystals (cf. Appendix O).

Frequencies in the range from 18 to 26.5 gcps (K-band) can be measured by the Microwave Associates, Inc. model MA 588 absorption type cavity wave meter, positioned immediately after the attenuator. Frequency measurements made with this instrument close to the nominal frequency of 24 gcps were found to be accurate to around $\pm$ 7 Mcps, which is an adequate level of accuracy for the purposes of this experiment.

A Hewlett-Packard model K752A, 3 db, multi-hole directional coupler is mounted immediately forward of the cavity wave meter. The DeMornay-Bonardi model DBE-319 tunable crystal mount mounted directly on the "side" leg of the directional coupler detects the microwave signal reflected from the plasma and converts it, via a 1N26 crystal, to an output voltage. This crystal mount has been adjusted for minimum VSWR (that is, VSWR $\sim$ 1.03), and therefore acts as a blackbody inasmuch as virtually all microwave energy incident on the input flange is absorbed, only a very small and inconsequential percentage being reflected back into the system.

Interposed between the transmitting horn and the directional coupler is a DeMornay-Bonardi model DBE-919 variable stub tuner.

This device is used in the dual capacity of bucking out any small mismatch resulting from the horn's being "matched" to the pyrex test section and to introduce a small mismatch for the purpose of creating hybrid phase "bumps" (cf. Appendix U). The receiver tunable crystal mount affixed directly to the receiver horn was initially adjusted for minimum VSWR in a similar manner to the reflected signal crystal detector mount. In order to provide a compensating-bucking signal to offset the controlled mismatch of the stub tuner, the receiver crystal mount was purposefully mismatched by a small amount.

The transmitting and receiving horns supplied by DeMornay-Bonardi were of special design, insofar as the beam pattern they radiated was restricted in the vertical (E) plane and the horns when mounted on the pyrex test section, as shown in Figure 11, had their focal points adjusted to coincide with the aperture plane of the facing horn. The Rexolite insert in the mouth of these horns served as a matching structure. Following a trial-and-error procedure, various combinations of slot width and depth machined in the Rexolite were tested until a minimum VSWR of ~ 1.05 was attained with the horn mounted to the pyrex test section. For all intents and purposes, then, the pyrex test section was non-existent insofar as the microwaves were concerned*.

After an initial warm-up period of approximately twenty minutes, the klystron's power output and frequency were found to remain quite stable for extended periods. Variations in power level on the

* Jahn[27] discusses the matching of multi-interface, dielectric slab structures, and shows that, when properly matched, such structures could be made "invisible" to the microwaves.

order of 5 to 7 per cent were observed from run to run (klystron turned off between runs) and random slow drifts in a band about $\pm$ 3 per cent wide around a nominal value were prevalent during any one run. These output power-level shifts were random and occurred over a long enough time scale so that crystal calibrations taken approximately 5 minutes after the shot indicated power levels which agreed to within 2 per cent of those recorded at the time of the shock. The frequency of the output signal exhibited the same general characteristics as the power level, slow random drifts over a range of around 26 Mcps being typical for a time span of about $\frac{1}{2}$ hour. Differences in the frequency checked just before the shock and checked again during the crystal calibration some 5 minutes later usually amounted to less than 15 Mcps. These small variations in frequency made no observable change in the crystal calibration characteristics or in the matching characteristics of the circuit to the pyrex test section.

All microwave data were recorded using a Tektronix type M four-trace plug-in unit to modeulate one beam of a Tektronix model 551 dual-beam oscilloscope. The received signal was displayed at 20 mv/cm (DC) on one trace. The reflected signal modulated two traces: one trace had an amplification factor of 100 mv/cm (DC); and the other had 5 times this amplification, i.e., was displayed at 20 mv/cm. The fourth, remaining, trace was used to display the output, at 100 mv/cm amplification, of the photomultiplier tube monitoring the unfiltered luminosity at the horn station. The second beam displayed the output of another photomultiplier tube sensing the horn station luminosity occurring in a narrow spectral band. These lumi-

nosity measurements are discussed in Appendix J. The time base generated by the oscilloscope was found to be (by comparison with a Tektronix model 180A time-base generator signal) accurate to within 1 per cent over the central 8 cm of the CRT display.

Figure 19 is a reproduction of the microwave data from a typical run displaying the three microwave and two photomultiplier signal traces. It is apparent from this figure why the reflected signal is displayed at two amplifications. The hybrid phase data ("bumps") are quite pronounced when displayed at 20 mv/cm, but the majority of the reflected signal is "off-scale." The reverse is true of the same signal displayed at 100 mv/cm, that is, the "bumps" can hardly be discerned, but the complete history of the reflected signal is exhibited. All data shown on the oscilloscope CRT face were recorded by a projected graticule Tektronix C-12 camera on Polaroid type 46-L transparency film to facilitate enlargement. The projected graticule eliminates completely all parallax with the trace and therefore permits a higher level of accuracy to be attained than was possible with the standard illuminated graticule typical of these oscilloscopes. This oscilloscope was triggered by the amplified output of the first photomultiplier SPI at a position some 46.21 cm upstream of the horn station.

APPENDIX J

DESCRIPTION OF THE SHOCK LUMINOSITY MONITORING SYSTEM

In addition to the microwave diagnostic circuitry used to monitor electron density behind the shock, the visible luminosity as a function of time was also measured.

After considerable difficulty, a faint spectra of the luminosity from a Mach 9.5 shock in 5 torr of argon was obtained using a small Hilger prism spectrograph and Royal Pan X film. Besides hydrogen Balmer lines (from the hydrogen driver gas) there appeared a group of closely spaced lines centered around 4190 Å. These lines were subsequently identified as arising from transitions between upper excited states in argon. In particular, the following transitions were involved:

$5P \rightarrow 4S$	4181, 4191, 4200 Å ,
$4P \rightarrow 4S$	4198 Å .

Because a knowledge of the intensity of radiation occurring at these wavelengths, as a function of time, would provide an insight into the population levels (in argon) of the states involved, it was decided to measure not only the intensity of the total visible light emanating from the shocked gases but also the intensity of radiation occurring in a narrow spectral region centered around 4190 Å.

The optical system depicted in Figure 25 was used to sense the total and filtered shocked-gas luminosity. A spatial resolution of 2 mm was selected as providing adequate time resolution (about $1 \rightarrow 2$ μsec) and a sufficient volume of gas (about 4.0 cm^3) for reasonable

response levels from the detectors. The slit system shown, composed of two 0.71-mm wide by 2-cm high slits separated by 21 cm and positioned as indicated, delineates a trapezoidal field of view having the desired dimension in the direction of gas flow. Light from the glowing shock-heated gases passes normally through the top of the clear pyrex test section. Affixed to the top of this section and centered on the microwave horns is a light-tight box supporting a front-surfaced mirror. This mirror is used to turn the light path from a vertical to a horizontal position. To prevent extraneous outside light from entering the test section, its surface is covered completely (except under the mirror box) by a layer of opaque, black vinyl electrician's tape. Upon being reflected from the mirror, the light passes through the first slit and into the "light pipe." To suppress reflection of non-axial light rays, the inside of this pipe has been painted flat black. In addition, a coil of pipe cleaners also painted flat black and closely conforming to the inside surface has been inserted. These measures ensure that all light emanating from the second slit has come directly from the first slit, in conformity to the ray diagram shown in the figure.* Once through the second slit, the light ray is split into two portions by a half-silvered mirror having neutral spectral characteristics, i.e., transmission and reflection are constant throughout the visible spectral region. When adjusted for maximum reflection (at 90° to the incident beam path), approximately 30 per cent of the incident energy is transmitted and the same amount re-

* Diffraction effects associated with this slit system are quite small and can be neglected.

flected in the 90° direction. The light transmitted through this half-silvered mirror proceeds directly to the photocathode surface of a RCA model 6655A, 10-dynode photomultiplier tube (labelled as photomultiplier no. 1). This photomultiplier therefore responds to the complete visual spectrum of the shocked gas. The light reflected at 90° from the half-silvered mirror passes through a 2.5 cm by 2.5-cm Baird Atomic model B-1 visible, dielectric-interference filter prior to entering a second RCA 6655A photomultiplier (labelled as photomultiplier no. 2). The spectral characteristics of this filter were evaluated using a 3.4 M Jerald Ash spectrograph. Maximum transmission occurs at 4190 Å, 50 per cent transmission between 4170 and 4240 Å, and 10 per cent transmission between 4132 and 4288 Å. This spectral spread amply covers the observed argon lines. As far as can be determined, no other species are present in the shocked gas which could contribute to the radiation in this wavelength range; therefore, photomultiplier no. 2 monitors only the narrow group of argon transitions lines centered at 4190 Å.

Both photomultipliers nos. 1 and 2 used the circuitry shown in the figure. A John Fluke model 412A regulated power supply was used to supply about 950 v to these tubes*. At no time did the anode current of either tube exceed 0.2 ma. This compared to a bleeder current of about 1 ma. Therefore, since the ratio of the bleeder to the anode currents was at least five, the tubes were operating within

---

* The same power supply also supplied ~950 v to the four photomultiplier SPI's, cf. discussion in Appendix F.

the linear portion of their input-output characteristic curve*. The response time for the circuitry used was calculated to be < 1 μsec, their observed behavior substantiating this value.

The output of photomultiplier no. 1, as described in Appendix I, was fed into one channel of a type M plug-in and displayed (at an amplification of 100 mv/cm DC) as one of the four chopped upper-beam traces on a Tektronix 551 dual-beam oscilloscope. The output of photomultiplier no. 2 was fed into a type D plug-in to modulate the lower beam of this oscilloscope at an amplification of 2 mv/cm DC. The polarity of the two traces (photomultipliers 1 and 2) is opposite. Starting from a common zero level, for increasing luminosity the output from photomultiplier no. 1 drives the trace upwards on the CRT face, while that from photomultiplier no. 2 proceeds downward. This was done to facilitate data interpretation.

Some noise will be seen on the highly amplified output from photomultiplier no. 2, shown in Figure 19. It was impractical to cool these tubes, a measure that would have undoubtedly eliminated this noise. However, various other strategems were employed to ensure that noise was held to a minimum. The tubes used were selected for their low noise levels. Both photomultipliers nos. 1 and 2 were encased in "mu" metal shields floating at the same potential (~ 950 v) as the photocathode. In addition, the tube and shield are surrounded by an electrostatically-grounded, light-tight steel shell. These measures reduced the noise to as low a level as practicable

---

* Cf. RCA 6655A data bulletin.

without resorting to cooling to temperatures below the 20°C of the laboratory in which they were used.

APPENDIX K

SHOCK TUBE PRESSURE AND TEMPERATURE MONITORING INSTRUMENTATION

Pressure

A Wallace and Tiernan 0→20 torr pressure gauge was used to monitor the gas pressure existing in the tube prior to a shot. Connected by 6 mm (1/4") O. D. tubing to the shock tube at the last port position (46. 21 cm downstream of the microwave horn), the gauge was protected from the high pressure behind the shock by a 6 mm (1/4") Circle Seal valve. This valve was closed, isolating the gauge, just prior to the shock, and remained closed whenever the tube pressure was over 20 torr. At all other times the valve was left open, the gauge and its line therefore being exposed to the hard vacuum existing in the tube. Isolating the gauge from rapidly changing pressures was deemed necessary to preserve its calibration characteristics.

Two careful calibrations of this gauge, the second some 11 months after the first, were performed by the Standards Laboratory of JPL, with accuracies on the order of 0. 01 torr. These tests were in consistent agreement and showed that the dial reading was almost 0. 50 torr lower throughout the full range of the instrument than the actual pressure to which the gauge was exposed. Armed with these calibrations, it was a trivial matter to convert the indicated dial readings to the actual readings being sensed. No effort was made to readjust the dial so that it would yield correct readings, as this would have been too expensive and time consuming a procedure to be warranted. Throughout this work, whenever reference is made to

data taken at "5 torr" initial gas pressures, the actual pressure was 5.50 torr, this latter value being used in the data reduction calculations. Similarly, the actual pressures at which the "3 torr" and "10 torr" data were taken are 3.50 torr and 10.48 torr, respectively.

A Consolidated Vacuum Company model GPH-100A discharge vacuum gauge ("cold-cathode" pressure gauge) was used to measure shock tube pressure in the regime below 25×10^{-3} torr and above 10^{-7} torr. This gauge, positioned approximately 3 M downstream of the driver section (cf. Appendix B) and connected to the tube by a short (about 8 cm) length of 2 cm (3/4") tubing, was of sufficiently rugged construction so that it was not necessary to isolate it from the passage of the shock or from pressures exceeding its operating range. The gauge was simply shut off whenever one of these conditions was about to occur. Calibration of this gauge using a large, accurately-calibrated McLoud gauge as a standard* indicated that it was accurate to within 10 per cent at 5×10^{-5} torr, the midpoint of the pressure range most often measured (that is, 10^{-5} to 10^{-4} torr was the normal range encountered during outgassing tests).

In addition, besides the 0→1000 psia gauge used to monitor the driver diaphragm bursting pressure, four other pressure gauges were employed on the shock tube. A Consolidated Electrodynamics Corp. type GTC-100, 1→1000 μ thermocouple gauge was used to monitor the pressure just downstream of the diffusion pump (upstream of the backing pump). A 0→50 torr Wallace and Tiernan pressure gauge

---

* The author is indebted to Dr. Bradford Sturtevant of C. I. T. for performing this calibration.

was connected to the line leading from the dump tank to the Hypervac 25 pump used solely to evacuate this tank. This gauge was used to verify, prior to a shot, that a suitably low pressure had been obtained in the dump tank (about 100 μ). A second gauge in this line, a 10-cm (4") diameter, 30" Hg to 30 psia range Bourdon tube gauge was employed for the purpose of indicating when atmospheric pressure was reached during the post-run pressurization procedure (using CIT argon). As soon as the indicated tube pressure was above atmospheric, the tube could be "opened" and the diaphragms changed without danger of having atmospheric air contaminating the shock tube. A 0→500 cm Hg Heise gauge is used in conjunction with the research-gas flow system flowmeter, as previously discussed in Appendix D.

Temperature

The shock tube was situated in a completely air-conditioned laboratory. With the laboratory thermostats set at 20°C, it was observed that the mean air temperature usually fluctuated, on a day to day basis, within the range 19.5 to 22.5°C. Temperature variation during the course of a run, i.e., over a period of approximately one hour, rarely exceeded 1/2°C and never was greater than 3/4°C.

Temperature was monitored at a number of points along the shock tube by precision mercury-bulb thermometers. A 0→50°C thermometer, graduated every 0.1°C, was mounted on the shocktube just upstream of the diagnostic section; the pre-shock gas temperature was taken to be equal to the temperature indicated by this thermometer. Two -20°→+110°C thermometers (graduated every 1°C),

one on the shock tube at the driver section and the other immediately upstream of the joint separating the two 3 M sections of the shock tube, were used primarily during the heating cycle. Because of possible damage to the Buna-N O-rings located at these stations, if their temperature were to exceed 100°C, a careful check on these thermometers was maintained during and immediately after a heating cycle. A 0→360°C (1°C graduations) thermometer was located midway along the first 3 M length of the shock tube. The bulb of this thermometer was inserted through the fiberglass insulating layer and made intimate contact with the shock tube's outer surface, thereby accurately reflecting the maximum temperature condition attained during a heating cycle. Three -100°→+50°C (1°C graduations) thermometers were used in conjunction with the refrigeration system. These thermometers were located on the refrigerated line from the roughing pump (Hypervac 25) to the shock tube; on the jacketed, refrigerated flow line from the shock tube to the settling tank; and on the 5-cm (2") diameter cold-trap manifold line between the gate valve and the diffusion pump.

APPENDIX L

EXPERIMENTAL PROCEDURE

Having discussed the shock tube and its associated instrumentation and subsidiary accoutrements (Appendices B through K), we shall now document the manner in which they are used. This is best accomplished by describing the various steps involved in making a run, i.e., collecting one data point.

Pre-Run Conditions

The mechanical roughing pump (Hypervac 25) is used to "back up" the 5-cm (2") diffusion pump (PCM no. 115 using Dow Corning DS705 fluid). These two pumps are in continuous operation and, except for servicing, have been since installed on the tube. Also in continuous operation is the 1/4-ton refrigeration system which is, between runs, used to cool the 5-cm (2") line between the gate valve (on the shock tube) and the dry-ice cold trap connected to the diffusion pump. The rough pumping line between the 2-cm (3/4") Circle Seal valve (near the gate valve) and the Hypervac 25 is also cooled by this refrigeration system (cf. Figure). The diffusion-pump, dry-ice (plus acetone) cold trap was always at least partially full, the mechanical refrigeration system serving to reduce the consumption of dry ice by the cooling it provides. To ensure uniformly low outgassing rates and ultimate tube pressure, the laboratory was thermostatically maintained at 20°C, no shots being made when, for various reasons, the ambient temperature exceeded 23°C.

The ultimate pressure in the tube was, for the first run after a heating cycle, in the range $2.0 \rightarrow 2.6 \times 10^{-6}$ torr. For the second or

third run* after a heating cycle, this pressure rises somewhat to $2.5 \rightarrow 5.0 \times 10^{-6}$ torr. This is attributed to contamination** of the walls of the tube by the shock and the shorter pumping time (about 3 hours) between the first and second (and second and third) run as compared to at least 16 hours of pumping the tube undergoes while being heated and then cooled prior to the first run.

Sequence of Preparatory Events

The first operation involves switching the cold-cathode gauge on and allowing it to warm up, the warm-up time being some 5 to 10 minutes. Immediately after having turned on this gauge, the valves in the refrigeration system are manipulated so that the refrigerant is no longer permitted to cool the 5-cm (2") gate-valve line or the 2-cm (3/4") line to the Hypervac 25, but rather the full capacity of the system is used to cool down the jacketed, 2-cm (3/4") I. D. line in the flow system. As seen in Figure 1 , this line is connected to the tube via a check valve and a 2-cm (3/4") Circle Seal valve. Gases flowing through this line enter a settling tank, which serves to reduce flow pulsation, and thence to the Hypervac 25 pump (which is also used in the flow system). As it usually requires some 25 minutes for this line to reach a desired temperature of at least -42°C, it is essential that the switchover of the mechanical refrigeration system occur as a first step in the initiation of a run.

---

* A maximum of three runs could be made in any 24-hour period, the pumping time between runs and the outgassing rate being the limiting factors.

** That is, gases driven into the shock-tube walls by the passage of the shock wave.

As soon as the refrigeration system has been adjusted, the power to both oscilloscopes (551 and 535), the raster unit, sawtooth generator unit, the photomultiplier, power supply, and the klystron power supply is turned on. After a suitable warm-up period (~ 20 sec), all of these instruments, except for the klystron power supply, automatically come up to voltage and start to stabilize. In an effort to prolong the life expectancy of the 2K50 reflex klystron, the klystron power supply is allowed to "idle" under no load conditions for a few minutes. During this time, only the klystron filament and cavity heater* are drawing power. While this process is occurring, the square wave output from the microwave scope (Tektronix no. 551) is used to check the reset level of the ADFF box. All amplifiers are adjusted so that when a $\frac{1}{2}$-mv square-wave input is applied, the re-set light remains off, indicating that the flip-flops associated with each of the amplifiers have not produced a pip. When a 1-mv square wave is used as an input to the individual amplifiers, the adjustment is such that the re-set light comes on and a pip is produced by the flip-flop unit. By this procedure, which requires about 4 minutes, all told, one is assured of consistent, uniform performance from the ADFF box. As soon as this check is completed, the klystron reflector and beam voltages are adjusted to their operating levels and the klystron begins to oscillate. At this point, approximately 5 minutes have elapsed since operations were commenced. Approximately 10 to 15 minutes are required for the klystron to stabilize in power output and

* The Bendix 2K50 klystron can be electrically tuned over a narrow frequency range by means of thermal expansion or contraction of its cavity.

frequency.

The photomultiplier calibration unit, cf. Figure 7 , is applied successively to each of the four photomultiplier shock-position indicators (SPI's). By adjustment of the variable output resistor, the output of each of the SPI's, in response to the calibrator, is made equal to some pre-selected value. The SPI outputs are observed on the Tektronix 551 scope. Prior to connecting the outputs of the SPI to the ADFF box, a 1-mv amplitude square wave is fed to the two amplifiers, whose outputs are used, in part, to trigger the two oscilloscopes. This provides assurance that the oscilloscopes will trigger correctly. Upon connecting the SPI's and the film gauge (used to trigger the raster scope) outputs to the ADFF box, the SPI's are placed in their pre-positioned mountings and adjusted so that their collimating slits are vertical and therefore parallel to the shock front as it passes.

For the next 5 minutes, during which the Megavac back-up pump has been turned on and is pumping down, an outgassing rate is recorded. This is accomplished by closing the gate valve and observing the rise in tube pressure via the cold-cathode gauge. At the close of the 5-minute period, with the gate valve still closed, the valve connecting the Megavac pump to the diffusion pump is opened. With both the Megavac and the Hypervac pumps backing up the diffusion pump, the gate valve is opened and the tube reduced from around 10^{-4} torr, the pressure level reached at the end of the outgassing, to its ultimate pressure of about 2×10^{-6} torr. This requires about 3 minutes, during which time the 6 mm (1/4") valve which isolates the Wallace and

Tiernan pressure gauge from the tube is actuated a number of times. This serves to dump any gas that may be trapped around the barrel of the valve into the tube, where it is exhausted. By doing this, extraneous gas is prevented from contaminating the test gas, when just before the shot, this valve is closed to protect the Wallace and Tiernan gauge from the high pressure existing behind the shock.

As the tube is once again at its ultimate pressure level, a valve between the Hypervac 25 and the diffusion pump is closed. The diffusion pump is now being "backed up" solely by the Megavac pump, and the Hypervac pump can be used for the flow system. At this time the Hypervac 25 pump is used to evacuate the driver section of any gas which might have leaked in since it was initially evacuated after the previous test run. Once this is completed, the tube is nearly in a state where data can be taken.

The output frequency of the klystron is checked and adjusted if necessary. Approximately 25 minutes have elapsed since the procedure was initiated, and the refrigerated flow line from the shock tube to the Hypervac 25 is at its equilibrium temperature of approximately $-43^{\circ}C$. In preparation for the shock, the valve on the research-grade gas bottle is opened, as is the diaphragm valve on the regulator. The research gas is prevented from entering the tube by another diaphragm control valve in the line from the regulator, which is located immediately adjacent to the shock tube proper.

Just prior to the introduction of the research-grade gas into the shock tube, the ultimate shock-tube pressure is recorded and the cold-cathode pressure gauge electronics are turned off. No attempt

is made to isolate the gauge element from the shock-heated gases. The construction of the gauge is rugged enough to permit this, no damage or alteration in performance being evidenced in nearly 400 runs while using this procedure.

Immediately after this, the temperature of the refrigerated flow line to the Hypervac 20 is noted, as is the klystron output frequency. The oscilloscope displays are checked, the oscilloscopes being then set for triggered operation. The battery box supplying power to the film gauge is turned on and the re-set button depressed, thereby returning all the flip-flop units in the ADFF box to a "pre-fire" condition.

Shock

Because of the dispersed positions of the flow control valves (being located at both ends of the tube, about 10 M apart) and the desire to utilize most effectively the expensive research-grade gases, the actual firing of the tube requires two operators*. One operator is stationed at the driver section, the other at the diagnostic section. While the oscilloscopes are made ready to trigger, etc., some of the driver gas is admitted to the driver section, until the pressure is approximately 1/3 of the predicted bursting pressure.

The shot can now be made. At a signal, the operator at the driver end slowly closes the gate valve to the diffusion pump. The gate valve is closed** in the same manner, i.e., in the same length

---

* The author is indebted to Frank "Ty" Linton, who has assisted in the collection of all the shock-tube data contained herein.

** The gate valve is closed over a period of approximately 10 seconds.

of time, as when the outgassing rate was taken. This ensures that the outgassing rate will be a meaningful measure of the contaminant level of the test gases*. Immediately upon complete closure of the gate valve, the research-grade gas is introduced into the tube and a stop watch is started to record the length of time between closure and shock passage, therefore permitting an estimate of purity level to be made. When the tube pressure reaches about 3 torr, the 2-cm (3/4") valve to the refrigerated flow line is opened. The research-grade gas flow rate is adjusted to give a desired tube pressure. It requires approximately 40 seconds for the pressure to be "fine" adjusted to a pre-determined level, at which time the flowmeter reading and the flowmeter input pressure are recorded. During this time the driver pressure has been allowed to slowly increase to from 60 to 80 per cent of bursting pressure. Once the tube pressure has stabilized, the 6 mm (1/4") Circle Seal valve to the Wallace and Tiernan 0→20 mm pressure gauge used to monitor the tube pressure is closed. The electronics (oscilloscopes and amplifier box) are re-set if they have spuriously triggered, the oscilloscope cameras' shutters opened, and the command to fire given. To ensure uniformity of operation, the driver pressure is then allowed to increase at a uniform rate of ~ 30 psi/sec until the diaphragm bursts. This usually occurs within 5 seconds of the command to fire. The driver-gas control valves are closed immediately upon the occurrence of the shot.

---

* It has been observed that the slower the gate valve is closed the lower the pressure will be immediately upon closure. With a 10 sec closure time, the observed pressure at the instant of complete closure is $\sim 9 \times 10^{-6}$ torr.

Post-Shock Events

Immediately after the passage of the shock, the research-grade gas flow-control valve is closed, the stop watch stopped, and the cameras closed. The Polaroid film is pulled through the cameras initiating the development process, and if this is the last shot of the day, all the electronics are shut off except the klystron power supply and the microwave scope (551). If other shots are to follow, only the film-gauge battery box is shut off, the rest of the electronics remaining on. The research-grade cylinder's valve and the valve on its regulator are securely closed and the pressure indicated by the Wallace and Tiernan gauge is recorded. Immediately thereafter, the refrigeration system is returned to its initial state, that is, the flow of refrigerant to the jacketed flow line is stopped and the valves to the cooling coils on the 5-cm (2") gate-valve line and the 2-cm (3/4") line from the shock tube to the Hypervac 25 pump are opened. The 2-cm (3/4") valve to the jacketed (refrigerated) flow line is closed at this time, the shocked gases being prevented from leaving the tube by a shock-actuated check valve in this line.

The temperatures existing at various stations along the tube now are recorded and the klystron frequency is rechecked and recorded, as is the flow time from the stop watch. By this time (about 2 minutes after the shock), the Polaroid 46-L transparencies have developed and are removed from the cameras. The microwave crystals are now calibrated, a procedure requiring approximately 8 minutes. During this time, the refrigeration system has reduced the temperature of the 2-cm (3/4") line between the tube and the Hyper-

vac 25 to an equilibrium value of about -35°C. Once this temperature is attained, the tube can be pumped out without contamination from the pump oil occurring. It is necessary to evacuate* the tube because either hydrogen or a hydrogen-helium mixture is the usual driver gas. This gas is exhausted through a line which terminates well outside of the laboratory, a purge of nitrogen gas being used to dilute the efflux as a safety measure. When helium or a combination of helium and argon is used as the driver gas, the tube need not be evacuated and can be immediately brought up to atmospheric pressure.

Dry argon (99.995 per cent pure) is used to pressurize the tube. When the tube pressure is up to atmospheric pressure, the rear diaphragm (2 mil aluminum) separating the dump tank from the shock tube is changed and the dump tank resecured to the shock tube. As soon as the diaphragm is secured in place, a separate Hypervac 25 pump situated near the dump tank is used to evacuate it. The driver diaphragm is removed and a new pre-cut and pre-scribed diaphragm emplaced. When the driver section is tightly clamped in position, the shock tube and driver section are evacuated by the Hypervac 25 pump used in the flow system. Here again, the line from the shock tube to this pump is refrigerated (around -32°C). It requires only 3 minutes for the shock tube to be pumped to 10^{-3} torr. When this pressure is attained, the shock tube and the driver section are isolated from the Hypervac and the valve between this pump and the diffusion pump opened. With both the Megavac and the Hypervac pumps now backing up the diffusion pump, the gate valve is opened.

* Rough pumped to about 10^{-1} torr.

The tube pressure now drops quite precipitously, reaching 2×10^{-5} torr some 10 minutes after the gate valve to the diffusion pump is opened. It requires some 15 minutes for the dump tank to attain $\sim 10^{-1}$ torr, at which time pumping is stopped and the tank isolated. The Megavac pump is now stopped, the Hypervac continuing to back up the diffusion pump. The tube is once more in a pre-run condition.

It requires 1 1/4 to 1 1/2 hours for the complete sequence of operations involved in collecting one data point to be completed.

Heating Cycle

Portions of the shock tube are heated. Five 380-watt heating tapes are wrapped around the tube and are covered with a layer of fiberglass insulation, this in turn being covered with aluminum foil, as seen in Figures 2 and 4. These tapes are usually in operation for approximately 70 minutes, during which time the diffusion pump continues to evacuate the tube. A maximum temperature of 200°C* is reached at the center of the tape-wrapped regions; the tube joint, the driver end, and the shock-position indicator and film-gauge portions of the tube being maintained at temperatures below 85°C. This is mandatory in order to prevent the O-rings in these positions from decomposing.

At the close of the heating period, the pressure in the tube rises to about 5.5×10^{-5} torr, the pressure dropping as the tube cools, until around 12 hours after the heating cycle, ambient temperature is again reached and the ultimate tube pressure reattained. Heating

---

* The tube elongates some 2.2 cm after about 70 minutes of heating.

usually occurs after the last run of the day, so that by the next morning the tube is once again ready to resume normal operation.

APPENDIX M

INTERPRETATION OF SHOCK-POSITION DATA

The details of the shock velocity determination instrumentation system are discussed at length in Appendices F through H. The raison d'etre of this elaborate system is, of course, the production, for each shot, of a permanent record of the times at which the shockfront passed accurately known stations in its flight along the shock tube. A reproduction of an example of such a record, i.e., the output of the "raster scope", is shown in Figure 9 . We shall now discuss the procedure involved and the assumptions employed in the extraction of mean shock velocity and shock attenuation information from these data.

To facilitate this discussion and to codify the symbols used herein, reference should be made to the accompanying schematic diagram showing the arrangement of the shock-position indicators (SPI) in relation to the shock-tube diagnostic test section.

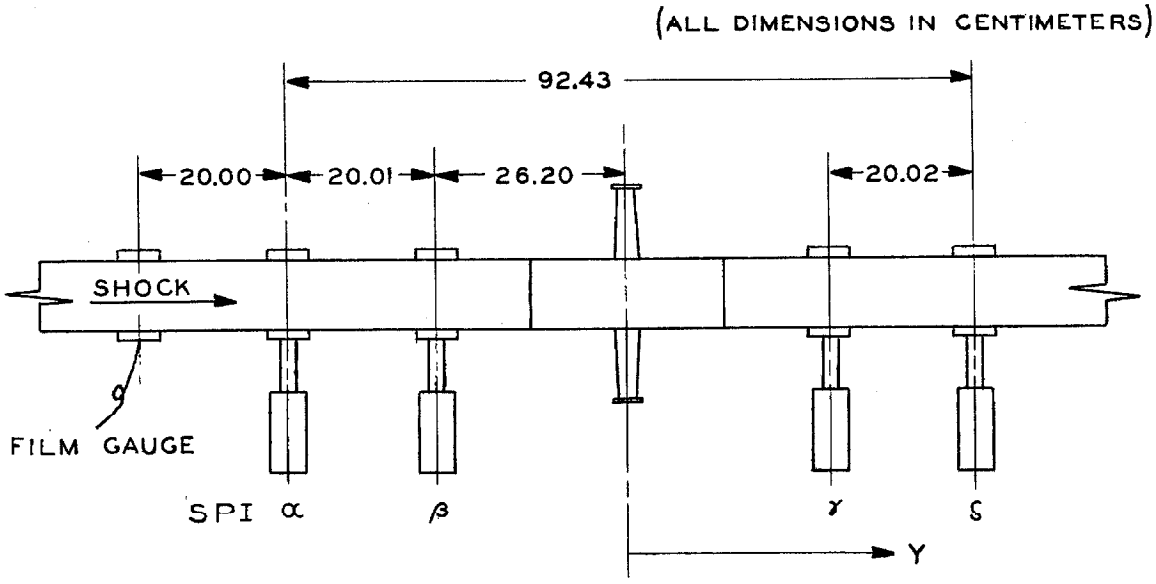

Mean Shock Velocity at Y = 0

Considering that the distance between SPI α and δ is less than one meter, it is not unreasonable to assume that the shock velocity, U_s, can be represented as

$$U_s = U_o(1+\alpha Y),$$

where $\alpha(M^{-1})$ is the constant attenuation factor ($\alpha < 0$ for attemuation). The time increment required for the shock front to traverse the distance between any two SPI stations is

$$t_{ji} = \int_{Y_i}^{Y_j} \frac{dx}{U_{\overline{ji}}(1+\alpha Y)}$$

where $i = \alpha, \beta, \gamma$, $j = \beta, \gamma, \delta$; $t_{\beta\alpha}$ being the time of flight for passage from SPI α to SPI β, Y_β, Y_α their respective positions, and $U_{\overline{ji}}$ the mean velocity of the shock wave, i.e., the indicated shock velocity at the position $(Y_j - Y_i)/2$ *.

Performing the indicated integration, we have

$$t_{ij} = \frac{1}{\alpha U_{\overline{ji}}} \ell n \left(\frac{1+\alpha Y_j}{1+\alpha Y_i}\right) .$$

Expanding the logarithmic term and recognizing that $Y_\delta = -Y_\alpha$, $Y_\gamma = -Y_\beta$ **, then

$$t_{ji} = \frac{Y_j - Y_i}{U_{\overline{ji}}} \left[1 + \sigma \left(\frac{\alpha^2}{3} \frac{Y_j^3 - Y_i^3}{Y_j - Y_i}\right)\right] .$$

---

* When $j = \delta$ and $i = \alpha$, or $j = \gamma$ and $i = \beta$, $U_{\overline{ij}} = U_o$, the indicated average velocity of the shock front at the horn station ($Y = 0$).

** The adoption of this equality introduces an error of, at most, 1 part in 2600.

For the extreme case where $\alpha = 0.05$, $Y_j = -Y_i = 0.462$, the second term in the bracket amounts to 1.8×10^{-4} and can be neglected, so that

$$U_o = \frac{0.9243}{t_{\delta\alpha}} \quad \text{or} \quad \frac{0.5240}{t_{\delta\beta}} \quad \text{M/sec.}$$

In all instances, the mean velocity (U_o) used in the calculation of the horn station Mach number ($M_s = M_o$ at $Y = 0$) was computed using the data from SPI α and δ (i.e., $U_o = 0.9243/t_{\delta\alpha}$). The mean velocity computed using the shorter base line (i.e., $U_o = 0.5240\ t_{\gamma\beta}$) was utilized solely as a check. In this regard, the velocities calculated using these two independent sets of data were in quite reasonable agreement. Using a sampling consisting of 154 of the most recent runs, virtually all (94.8 per cent) exhibited agreement to within one per cent; some 62 per cent of the sample were within 0.4 per cent, and of these 53 per cent were within 0.2 per cent. An agreement of 0.2 per cent in velocity for a Mach 8 shock in argon corresponds to a difference in velocity of about 5 M/sec.

Coincidence tests were conducted wherein two SPI's were positioned on opposite sides of the shock tube so that each would monitor the same station. The results of these tests indicated that shock passage time could be determined with an accuracy of some 0.3 μsec. Again using the example of a Mach 8 shock in argon, the 0.3 μsec uncertainty in shock passage time corresponds to about 0.12 per cent error in velocity calculated using data from SPI α and δ, and some 0.21 per cent uncertainty in velocity computed on the basis of SPI β and γ data. For this case, the two velocities could therefore be ex-

pected to agree within a RMS uncertainty of some 1/4 per cent, or about 6 M/sec, which is in reasonable agreement with observation. From this it is straightforward to demonstrate that approximately 2/3 of all mean velocity data calculated using SPI α and δ are accurate to within 0.15 per cent, and the remainder to within 1/2 per cent.

Shock Attenuation Calculations

As with the estimation of the mean shock velocity, shock attenuation was computed in two different ways. For all the data analyzed, the shock attenuation factor was first computed by comparing the mean shock velocity between SPI α and β with its indicated velocity between SPI γ and δ. For comparison, the shock attenuation factor α was then computed by comparing the velocities between SPI α and γ with that between β and δ. This comparison was performed more as a means for checking the validity of the numerical computation than as a determination of the accuracy of the system. This is necessarily the case, as both procedures use the same sets of data and therefore are not independent determinations of the attenuation factor α.

The mean velocity of the shock in the interval between SPI α and β can be written

$$U_{\overline{\beta\alpha}} = \frac{Y_\beta - Y_\alpha}{t_{\beta\alpha}} \left[1 - \frac{\alpha(Y_\beta^2 - Y_\alpha^2)}{2(Y_\beta - Y_\alpha)} + \frac{\alpha^2}{3} \frac{Y_\beta^3 - Y_\alpha^3}{Y_\beta - Y_\alpha} \cdots \right] .$$

Similarly, the mean velocity for the interval $Y_\gamma \rightarrow Y_\delta$ is

$$U_{\overline{\delta\gamma}} = \frac{Y_\delta - Y_\gamma}{t_{\delta\alpha}} \left[1 - \frac{\alpha}{2} \left(\frac{Y_\delta^2 - Y_\gamma^2}{Y_\delta - Y_\gamma} \right) + \frac{\alpha^2}{3} \left(\frac{Y_\delta^3 - Y_\gamma^3}{Y_\delta - Y_\gamma} \right) - \cdots \right] .$$

Recognizing that, to a high degree of accuracy, $Y_\alpha = -Y_\delta$ and $Y_\beta =$

$- Y_\gamma$, the velocity difference (ΔU) between the mean positions $(Y_\alpha + Y_\beta)/2$ and $(Y_\gamma + Y_\delta)/2$ is then

$$\Delta U = U_{\overline{\beta\alpha}} - U_{\overline{\delta\gamma}} = (Y_\beta - Y_\alpha)\left(\frac{1}{t_{\beta\alpha}} - \frac{1}{t_{\delta\gamma}}\right) - \frac{\alpha(Y_\beta^2 - Y_\alpha^2)}{2}\left(\frac{1}{t_{\beta\alpha}} - \frac{1}{t_{\delta\gamma}}\right) + \frac{\alpha^2(Y_\beta^3 - Y_\alpha^3)}{3}\left(\frac{1}{t_{\beta\alpha}} - \frac{1}{t_{\delta\gamma}}\right) \cdots .$$

Retaining only the first term and neglecting the remainder introduces no more than 2 per cent error (for the extreme case of $\alpha = 0.05$) in the estimation of α.

Therefore, the shock attenuation factor α, defined as $\frac{\Delta U}{\Delta Y}/U_o$, can be written in terms of the known passage time and SPI separation distances as:

$$\alpha = (0.2986)\left(\frac{t_{\delta\alpha}}{t_{\delta\gamma}} - \frac{t_{\delta\alpha}}{t_{\beta\alpha}}\right).$$

For a Mach 8 shock in argon, where the attenuation factor $\alpha = 0.035$, it is straightforward to demonstrate that a 0.3 μsec uncertainty in the shock passage time could lead to indicated values for α from 0.014 to 0.057, i.e., a range of $\pm$ 60 per cent about the true value. This is due largely to the relatively close spacing of the SPI's, a factor which was fixed by prior decision.

Calculation of Mach Number (at the Horn Station Y = 0)

Having determined the mean velocity at Y = 0 (U_o), the corresponding Mach number (M_o) can be calculated once the acoustic velocity is known. Using the values of acoustic velocity presented by Cook[28] for the pure noble gases, the following formulas, corrected for temperature variation in the range from 18°C to 23°C, were

derived:

$$a_{ar} = 318.94 + 0.5439\,\Delta T \ \text{M/sec}$$

$$a_{kr} = 220.7 + 0.376\,\Delta T \ \text{M/sec}$$

$$a_{xe} = 174 + 0.296\,\Delta T \ \text{M/sec}$$

where $\Delta T = T - 293.16^{\circ}K$. The small variation in velocity due to pressure variation (in the range 3 to 10 torr) was neglected as being negligible.

Using the perfect gas law and the known pure-gas acoustic velocities for argon and xenon, the appropriate velocity of sound for mixtures of argon and xenon was calculated from the expression

$$a_{\substack{\text{mixture} \\ ar+xe}} = a_{ar}\left\{1 + \frac{N_{xe}}{N_{xe}+N_{ar}}(2.2871)\right\}^{-\frac{1}{2}}$$

where N_{ar}, N_{xe} are the particle densities of argon and xenon, respectively. In the limit $N_{ar} = 0$, the velocity of sound calculated using this relationship yields a result about one per cent higher than the accepted value for pure xenon. Since the largest ratio of xenon to total gas used as a test gas was 0.20, the above expression was deemed to be sufficiently accurate, considering that the acoustic velocity of xenon is only known to three place accuracy.

During any one run, a number of temperatures along the shock tube were recorded (cf. Appendix K). Because of the relatively well-regulated temperature condition prevailing in the laboratory, the precision mercury-bulb thermometer ($0.1^{\circ}C$ graduations) used to monitor the shock-tube temperature at a station just upstream of the pyrex diagnostic section was assumed to also provide an accurate measure

of the test gas temperature.

Translational Temperature of the Shocked Gases

For an ideal un-ionized polytropic gas, the ratio of the temperature (T_2) immediately behind a shock of strength M_o to that of the quiescent gas in front of the shock (T_1) is, from the Rankine-Hugoniot relation,

$$\frac{T_2}{T_1} = \frac{1}{M_o^2}\left[\left(\frac{\gamma-1}{\gamma+1}\right)(M_o^2-1)+M_o^2\right]\left[\left(\frac{\gamma-1}{\gamma+1}\right)(M_s^2-1)+1\right] \quad .$$

For a monatomic gas, the ratio of specific heats (γ) is equal to 5/3, and the temperature of the shock-heated gases can then be written as

$$T_2 = T_1\left(\frac{5}{16}\right)\frac{(M_o^2-0.2)(M_o^2+3)}{M_o^2} \quad .$$

The energy absorbed by a monatomic gas when shock heated is manifested as an increase in the translational temperature and an increase, if any, of the internal energy of the atoms which have undergone inelastic collisions (i.e., excitation and ionization). In all instances encountered, the relative ionization level of the gases being scrutinized never exceeded 10^{-4}. Furthermore, the exceptionally small amounts of visible radiation associated with the atom-atom ionization process leads one to assert that the above relation represents to a high degree of accuracy the translational temperature of the shocked monatomic gases used in this study.*

---

* This is true insofar as the Rankine-Hugoniot relations can be considered to be valid. There is a vast body of literature substantiating their validity, in particular, the paper by Clauston, Gaydon, and Glass, "Temperature Measurements in Shock Waves," Proc. Roy. Soc. London A 248, 429 (1958), should be consulted.

If we realistically assume that the quiescent gas temperature T_1 can be measured with an error of $\pm$ 0.1°C, and that the mean shock velocity (U_o) has an uncertainty of approximately $\pm$ 10 M/sec associated with its measurement, then for a Mach 8 shock in argon, the post-shock gas temperature is determined to within about 0.8 per cent, i.e., 6120 $\pm$ 50°K. In terms of $1/kT_2$, this uncertainty is expressed as $1.8967 \, ^{+0.0141}_{-0.0135} \, ev^{-1}$.

APPENDIX N

THEORY OF MICROWAVE INTERACTION WITH A PLASMA SLAB

We shall consider the interaction of a plane, plane-polarized monochromatic electromagnetic wave, incident normally on a homogeneous, isotropic plasma slab as an idealization of the shock-tube microwave diagnostic system described in Appendix I. The design of this system was indeed dictated by a desire to simulate, as closely as possible, the theoretical model we have outlined. This model is analytically quite tractable and well documented in the literature*, it being one of the most straightforward instances of electromagnetic wave - plasma interaction presenting some semblance of physical reality. In the ensuing development, the work of Jahn[26, 27] will be followed, these references being at once concise and completely applicable to the problem at hand. While repetitious of the earlier work cited, the following discussion is presented not only to ensure some degree of completeness but also to stress the various assumptions implicit in the theory and to present a basis for the development of various corrections to the theory, which make it a more faithful replica of the actual physical situation.

Because of the large mass differential existing between electrons and ions, an electromagnetic wave will interact virtually exclusively with the free electrons present in a plasma. We are implying

---

* E. g., Tevelow, Curchack, "Shock Tube Microwave Propagation Measurements Using the Dielectric Slab Approximation," Diamond Ordnance Fuze Labs, TR-962 (1961).

here a magnetically unbiased (isotropic), "quasi-neutral"* plasma media. For plasmas of interest ($kT \sim 1$ ev), the mean velocity of the electron will be very much less than the velocity of light; therefore[26] the electric field (E) of the wave will be the primary agent by which interaction with the electron occurs. Having restricted our discussion to non-relativistic plasmas we can write, employing MKSQ units throughout, for the electronic equation of motion, the following:

$$m_e \dot{\underline{v}}_d + m_e \nu_c \underline{v}_d = e \underline{E} e^{-i\omega t} \quad . \qquad \text{(N-1)}$$

In this equation, we are essentially considering not an individual electron but rather an "ensembled averaged" electron. Accordingly, $\underline{v}_d$ is taken to be the averaged directed drift velocity from which we may define the averaged current associated with the particle. The electric field of the electromagnetic wave is, as assumed, harmonic, and together with the electronic charge e forms the forcing function shown on the right hand side of the relation. As is usual, m_e represents the electronic mass. The quantity ν_c, or effective collision frequency, can be taken as defined by this expression. It represents the damping of the (ensemble averaged) electron's motion due to momentum exchange collisions with the more massive constituents of the plasma, i.e., atoms and ions. An extensive discussion of this equation and the attendant quantity ν_c is found in Ginzburg's[40] book, Chapter II. For the purposes of this development, ν_c can be viewed as an experimentally determinable quantity, i.e., a quantity which is

---

* As defined by Ginzburg[40], i.e., total overall electrical neutrality.

to be determined along with the electron density, the primary parameter of interest. Nevertheless, it should be noted that from kinetic theoretical considerations the effective collision frequency can be approximately related to the single particle momentum-transfer cross section Q_d averaged over an appropriate electron distribution function, viz.,

$$\nu_c \simeq \sum_j N_j (\overline{Q_{d_j} v_e}) \qquad \text{(N-2)}$$

where we specify N_j as the number density of the j^{th} specie of heavy particles present in the plasma.

Recognizing that although equation (N-2) is only an approximation to the equation of motion of an electron under the action of an electromagnetic field and possesses only limited validity, there is sufficient justification to be found in the references cited to state that, for the purposes for which we shall now apply it, no significant advantage could be accrued from the use of a more elaborate representation.

Writing Ohm's law as $\underline{J} = \sigma^* \underline{E}$, here defining σ^* as a scalar complex conductivity, and recognizing that from the steady-state solution of (N-1) the current density ($\underline{J}$) can be written as $J = -N_e e \underline{v}_d$, N_e being the electron density, we write:

$$\sigma^* = \frac{N_e e^2}{m_e(\nu_c - i\omega)} = \left(\frac{\omega_p}{\omega}\right)^2 \frac{\epsilon_o(\nu_c + i\omega)}{1 + (\nu_c/\omega)^2} , \qquad \text{(N-3)}$$

where ω_p is the electron plasma frequency* defined by $\omega_p = \left(\frac{N_e e^2}{m_e \epsilon_o}\right)^{\frac{1}{2}}$,

---

* That frequency at which an isolated electron would oscillate if displaced and released from its "mean" position within the plasma.

ε_o is the permittivity of free space, and ω is the frequency of the electromagnetic wave.

The wave equation in phasor notation ($\underline{E} = \underline{\tilde{E}} e^{-i\omega t}$) for the propagation of a monochromatic electromagnetic wave in an isotropic, quasi-neutral, sourceless media having finite conductivity (σ^*) is written as

$$\nabla^2 \underline{\tilde{E}} + k_o^2 \left(1 + \frac{i\sigma^*}{\omega\varepsilon}\right) \underline{\tilde{E}} = 0 \ .$$

Here, k_o represents the propagation constant of vacuo, $= 2\pi/\lambda_o$, λ_o being the free space wavelength of the wave.

Defining the propagation constant in plasma as $k^* = k_r + ik_i$, we have

$$(k^*)^2 = (k_o)^2\left(1 + \frac{i\sigma^*}{\omega\varepsilon_o}\right) \ . \qquad \text{(N-4)}$$

For future convenience, we further define a relative propagation constant n^* as k^*/k_o and $n_r \equiv k_r/k_o$, $n_i = k_i/k_o$. Carrying through the albegra, we can cast the real (n_r) and imaginary (n_i) components of the relative propagation constant in terms of the parameters ω_p/ω and ν_c/ω as follows:

$$n_r = \frac{k_r}{k_o} = \left| \left\{ (1-P) + \left| \left[(1-P)^2 + P^2 (\nu_c/\omega)^2 \right]^{\frac{1}{2}} \right| \right\}^{\frac{1}{2}} \right| \qquad \text{(N-5)}$$

$$n_i = \frac{k_i}{k_o} = \left| \left\{ -(1-P) + \left| \left[(1-P)^2 + P^2 (\nu_c/\omega)^2 \right]^{\frac{1}{2}} \right| \right\}^{\frac{1}{2}} \right| \qquad \text{(N-6)}$$

where

$$P \equiv (\omega_p/\omega)^2 \Big/ (1 + (\nu_c/\omega)^2) \ . \qquad \text{(N-7)}$$

It should be recognized that the ratio $k_r/k_o = n_r$ is equivalent to λ_o/λ_p, the ratio of free space to plasma wavelengths.

We now consider a plasma slab (isotropic and homogeneous) extending over the region $0 \leq z \leq m\lambda_o$ (where m is a positive integer, 1, 2, ...), of infinite lateral extent ($-\infty \leq x, y < \infty$), and irradiated, for convenience, by a monochromatic wave propagating from $z \rightarrow -\infty$ in the positive z direction, the E vector of magnitude E_o lying in the x, z plane. It is a straightforward, albeit tedious, exercise to derive the following expressions for the plane waves reflected from and transmitted through the slab:

$$\frac{E_R}{E_o} = |R| e^{i\varphi_R} = \frac{(1-n^{*2})(e^{i2\pi mn^*} - e^{-i2\pi mn^*})}{(1+n^*)^2 e^{i2\pi mn^*} - (1-n^*)^2 e^{-i2\pi mn^*}} , \qquad \text{(N-8)}$$

$$\frac{E_T}{E_o} = |T| e^{i\varphi_T} = \frac{4n^* e^{i2\pi m}}{(1+n^*)^2 e^{i2\pi mn^*} - (1-n^*)^2 e^{-i2\pi mn^*}} . \qquad \text{(N-9)}$$

In principle, then, there are four detectable (measurable) quantities, the relative amplitudes of the reflected and transmitted signals, $|R|$ and $|T|$, respectively, and the relative phases of the reflected and transmitted signals, φ_R and φ_T.

The actual quantity measured is the output of a detector. At the frequencies involved in these studies (K band), and because of the necessity for rapid response, it is necessary to use so-called "square law" crystal detectors. These devices respond to the incident electromagnetic wave by producing a voltage which is essentially proportional to the square of the wave's electric field and therefore linearly with the energy of the wave. For convenience, we shall introduce the following definitions

$$_1S_R \equiv |R|^2 \qquad \text{(N-10)}$$

$$_1S_T \equiv |T|^2 \qquad \text{(N-11)}$$

These quantities can range between 0 and 1 , having been normalized to the maximum signal measured. The reflected crystal detector output is a maximum for a completely saturated plasma, i.e., $\omega_p >> \omega$, while the transmitted crystal detector output is a maximum for the case of no plasma as $\omega_p << \omega$.

Rather than measuring the phases φ_R and φ_T directly by use of a bridge circuit, it is more convenient from a practical standpoint to add (or interfere) the transmitted and reflected waves with a reference signal and detect the resultant output from a crystal detector in response to these composite waves. We call these "the measurable phase quantities" P_R and P_T where

$$P_R = 1 + S_R + 2\sqrt{S_R}\cos\varphi_R \ , \qquad \text{(N-12)}$$

$$P_T = 1 + S_T + 2\sqrt{S_T}\cos\varphi_T \ . \qquad \text{(N-13)}$$

Figures 12 , 13 , 14 , and 15 represent the quantities $_1S_R$, $_1S_T$, P_R , P_T , respectively as a function of N_e/N_p for various values of the parameter ν_c/ω and $m = 4$. Here, N_p is the electron density at which $\omega = \omega_p$, N_p equalling 7.14×10^{13} cm^{-3} for a frequency of 24,000 GCPS.

Any two of these detectable quantities, when simultaneously measurable, will suffice to unambiguously determine the two unknowns of interest, viz., N_e and ν_c . Primary among the considerations influencing the selection of which of the four quantities to be measured was a desire for as wide a range of detectable electron density consistent with an unsophisticated circuit design so as to permit reliable

operation.

Jahn[27] has shown that, for m = 4 and values of ν_c/ω greater than approximately 0.07, the range of electron densities detectable by measuring ${}_1S_R$ and ${}_1S_T$ is equal to or larger than that detectable by measuring P_R and P_T. The circuitry necessary to measure P_R and P_T is more involved than one designed to measure ${}_1S_R$ and ${}_1S_T$ because of the need in the latter instance for a reference signal and means for adding the reference wave to the waves that have interacted with the plasma. It is only for values of ν_c/ω less than approximately 0.07 that the use of P_R and P_T would allow a larger range of electron density, as contrasted to the range detectable by ${}_1S_R$ and ${}_1S_T$ measurements, to be made.

Virtually all of the plasmas observed in the shock tube experiments have exhibited values of ν_c/ω of 0.07 or greater, therefore justifying the a priori choice of the simple microwave diagnostic circuitry shown in Figure 11. This circuit was specifically designed to measure the quantities ${}_1S_R$ and ${}_1S_T$ as discussed previously. In addition to these two measurements, a third, the so-called hybrid phase or "bump", measurement can be made to yield a definitive measure of electron density (N_e). The basis for this measurement is discussed in Appendix U.

APPENDIX O

MICROWAVE CRYSTAL DETECTOR CHARACTERISTICS

An extensive series of IN26 crystal detector calibrations were conducted both at the Jet Propulsion Laboratory[41] and with the shock tube microwave circuitry at the California Institute of Technology. In both instances, the same frequency, 24 gcps, was used and the output of the crystal correlated to the setting of a precision-calibrated attenuator (DeMornay-Bonardi model DBE-410). The precision attenuator was calibrated, in turn, with a compensated thermistor head (FXR model no. K218AF), the two agreeing to within 3 per cent over the range of the attenuator.

Although the IN26, K band, crystal detectors used in the shock tube microwave circuit are called square law detectors, implying an output linear with the magnitude of the incident microwave energy, it was found that their behavior is only approximately square law, and then only for output levels less than around 400 mv. Above this level, which corresponds, by actual comparison to a matched calibrated thermistor head, to an input microwave power of 0.16 mw, significant deviations from "square law" behavior are to be expected.

A typical calibration chart is shown in Figure 18. The data shown are for a transmitted (i.e., received) signal detector, hence the subscript T. The VSWR of all detectors so calibrated was on the order of 1.05 or less. On this plot, the normalized crystal output, typically terminated in the 1 megohm impedance characteristic of a Tektronix letter-series oscilloscope plug-in unit, is denoted by $_{o}S_{T}$. The corresponding "actual" normalized energy, read from the cali-

brated precision attenuator, is denoted by ${}_1S_T$.

It was found that these calibration data could, in general, be empirically represented by a bi-linear curve on a log-log scale, each segment of the curve being representable as

$$ {}_1S_T = A_T \, ({}_oS_T)^{K_T} $$

where both A_T and K_T are constants. A_T is, of course, unity for the upper segment in all cases. Values of K_T were found to vary between 0.8 and 1.5 for outputs below 400 mv, with the usual range of K_T being from 0.9 to 1.2. Values of K_T varied from one calibration to the next for the same crystal and environmental conditions, sometimes by as much as 0.15 or more.

It has been shown[42] that for the IN23B crystal detector (which is quite similar to the IN26 but operated at a lower frequency, 2→11 gcps), the application of a constant reverse bias applied to the crystal would greatly enhance the crystal's "square law" behavior. Rather than do this, it was decided that calibration of the crystal for each test run would be advisable. It should be mentioned that various devices were used to record crystal output. These included Speedomax recorders, galvanometers, and oscilloscopes. In all cases, the impedance seen by the crystal was at least 10^4 ohms. The type of recording device used apparently had no measurable effect upon the crystal's calibration behavior, thereby providing assurance that the characteristics discussed are truly associated with the crystal and not with the method of recording its output.

It is assumed that the calibration characteristics of these

crystals under dynamic conditions, where the signal varies rapidly with time, are the same as under static conditions. Tests conducted at the Jet Propulsion Laboratory [41] using a mechanical chopper to modulate the input microwave power to the crystal detector undergoing test indicated that there was no measurable (3 per cent accuracy) change in the calibration behavior for modulation frequencies up to 10 kcps.

Numerous instances have been recorded where the crystal output in response to a shock-wave generated plasma has varied over 50 per cent in less than 4 microseconds, with no evidence of capacitive effects. For these tests, the crystal output was fed directly into a Tektronix type M plug-in via approximately 6 feet of RG 58/ U cable. Modulation of the klystron's reflector voltage by a signal having a rise time to maximum of approximately 1 microsecond produces a crystal output having the same rise time. From these tests then, we conclude that the crystal response is less than 1 μsec.

These tests lend credence to the assumption that the steady-state crystal calibration is representative of the device's input - output characteristics under the dynamic conditions encountered in this study.

APPENDIX P

ANALYSIS OF MICROWAVE FIELD PATTERN EFFECTS

In the basic theory of electromagnetic wave interaction with a weakly ionized plasma developed previously, the electromagnetic field was characterized as being a plane wave. Such waves, by their very definition, have surfaces of constant phase which are planar, normal to the direction of propagation, and infinite in lateral extent. This carries the implication that the source of these waves is at infinity or, at the very least, at a sufficient distance (in terms of wavelength λ) from the point of observation that, for limited regions of interest, the wave fronts can be considered planar.

In the vast majority of experiments (and the one considered here is no exception), where microwaves are used for the investigation of plasma properties, the plasma under scrutiny at any one instant possesses dimensions comparable with the free space wavelength of the probing microwave beam. Therefore, in order to duplicate the conditions of the idealized theory, particularly the assumption of an infinite plasma slab, the microwave energy has to be suitably constrained so that the majority of the beam energy is restricted to pass through an area whose dimensions are equal to or smaller than those of the plasma under study. By use of quasi-optical techniques[43, 44] it has recently been shown to be possible to focus a microwave beam so that its lateral dimensions in the focal region are on the order of $1\lambda_o$, the wave front in this region being almost plane. The stratagem of producing a relatively plane wave over a small area was applied to a limited extent in the design of the antennae used in this experiment.

Each of the horns (cf. Figure 11) was adjusted to have its focal point coincident with the aperture plane of the other when separated by the shock-tube pyrex diagnostic section. Estimates of the wave front curvature indicate a $1/16\lambda_o$ deviation from planarity in the x-z plane.

Due to their close proximity, which is required for efficient coupling of the microwave energy to the plasma, the transmitter and receiver horns are within each other's near fields.* Even though the horns and the dielectric (test section) were matched so that only negligible reflection occurs when no plasma is present, there is considerable internal reflection of energy between the horns. That this is so is shown quite conclusively in Figure 16. Here we see the output of the receiver crystal detector versus horn separation distance along an axis coincident with the centerline of both horns. For this test, the horns were covered by quartz plates having the same electrical characteristics as the pyrex channel, and the crystal output has been normalized to the value existing at nominal channel separation, 5 cm. The existence of the standing wave pattern is indicative of the internal reflections existing between the transmitter and receiver horns and the adjacent portion of the channel. By way of comparison, one would expect no interference pattern for a pure plane wave, i.e., the trace would be constant (unity) for all channel widths.

---

* The region in which effects due to the finite dimensions of the aperture are significant. The near field is commonly taken as extending from the plane of the aperture (of characteristic dimension ℓ), a distance $(2\ell^2)/\lambda_o$. For our case, the near field extends $\sim$ 10 cm from the horn's aperture.

As the electron density increases in the channel, the wavelength of the microwaves in the plasma also increases (cf. eq. (N-4), Appendix N). As a consequence, if we were to follow a suggestion by Harris[45] and scale the field pattern in terms of λ_o/λ_p *, that is to say the apparent horn separation distance varied in proportion to λ_o/λ_p, we would expect to observe evidence of this oscillatory behavior on the transmitted signal. Close perusal of numerous records similar to that shown in Figure 19 does indeed show some influence of the field pattern. While it is hard to discern an oscillatory contribution to the general ${}_oS_T$ versus τ test record, undoubtedly because of attenuation effects, the first peak of the pattern occurring at $d/d_o = \lambda_o/\lambda_p \approx 0.95$ is evident on the trace as a "hump" in the region $25 \leq \tau \leq 50$. Since this "hump" occurs at almost precisely the same time as the first bump** appears, it was at first stipulated that the mismatch purposely put into and bucked out of the microwave circuit (for the express purpose of causing the "bumps"), while small, was affecting the transmitted signal. Approximately ten test shots were made where no measurable mismatch was present, the "hump" in the transmitted signal remaining very much in evidence. Because it does occur coincidentally with the first "bump," it is reasonable to stipulate that the "hump," like the "bump," is caused by interference effects.

---

* This is consistent with the analysis of T. Soejima[46], who treats the case of the gain of two horns in each other's near field. For typical rectangular horns, and for the dimensions of our apparatus, he shows that the gain is an almost linear function of a parameter δ where $\delta = \lambda d/\text{aperture area}$, d being the horn separation distance.

** Cf. Appendix U.

The problem of a uniform plasma slab being irradiated by the far field of an antenna has been investigated[47]. However, the more realistic problem of near field irradiation of a plasma slab even without the presence of a second horn (the receiver) is not to be found in the literature. A cursory examination of this problem reveals its great complexity, and an attempt at solution would not be warranted within the context of this endeavor.

The approach that is pursued is based primarily on the observation that the interference effects are apparently small, i.e., the "hump" amplitude is small compared to the mean signal level over which it is superposed. Because of this, we shall postulate that the interference effects can be treated as a perturbation on the transmitted signal,as little if any interference effect is to be noticed on the reflected signal because of attentuation effects and because reflection occurs primarily at the first plasma-surround interface. Also, the transmitted signal is used as our primary measurement (cf. Appendix V).

Since the interference effects are relatively small, it should be possible to construct a crude theoretical model having the essential features of the actual physical situation and apply the result as a correction to the idealized theory of Appendix N. This is precisely the approach employed. We first seek to construct a simple one-dimensional model of the two horns such that we can approximate the radial field pattern shown in Figure 16. We when will introduce a plasma between the horns. To this one-dimensional representation we add, in an approximate fashion, multi-dimensional effects such as refrac-

tion and diffraction. The result of this is a correction factor labeled $\varepsilon_s/\varepsilon_p$, the ratio of the received energy calculated on the basis of the synthetic field pattern (ε_s) to that calculated assuming plane waves, etc. (ε_p). The application of this correction factor will be described in Appendix T.

The one-dimensional model used to synthesize the field pattern is shown below:

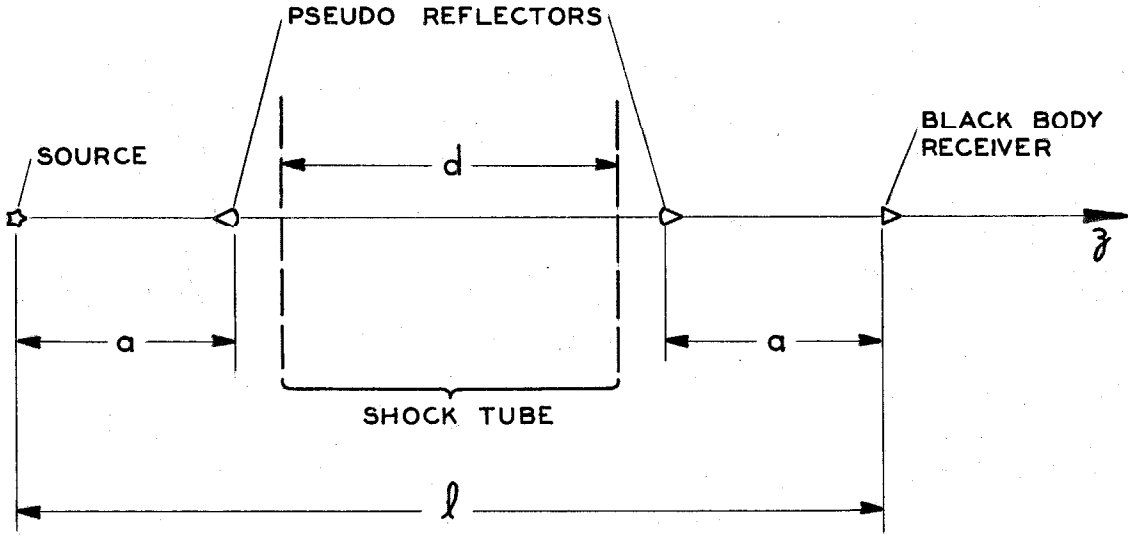

In order to simplify the analysis, but not to the exclusion of essential features, a number of assumptions were made. Because the radial field pattern was taken along an axis coincident with those of the horns, we have restricted out attention to the one-dimensional case. The source is assumed to be a simple dipole whose radiation field is postulated to consist only of transverse E and H components, i.e., we consider only the far-field radiation pattern along the z axis. It would be straightforward to carry along the effects of the radial field components, but this added complication is not warranted a posteriori by the results we derive from this crude model or by the use to which

these results will be applied.

In phasor notation, the E field along the z axis from this dipole can be written as

$$\tilde{E} = \frac{-E_1 k_o^2 e^{ik_o z}}{\epsilon_o z}$$

where E_1 is the dipole strength $P^{(1)}$ divided by 4π (cf. Stratton, pg. 434 ff[48]).

The two pseudo-reflectors are assumed to be symmetrically placed with respect to the dipole and the receiver, which is consistent with the symmetry inherent in the actual microwave transmitting and receiving horn arrangement. The reflectors are called pseudo-reflectors insofar as they reflect only a portion of the energy incident upon them with no phase change and no absorption. For instance, the E field incident on the first reflector from the left (from the dipole) is of magnitude E_1. The wave that is reflected has an electric field strength of magnitude ρE_1 and the transmitted wave of magnitude $(1-\rho)E_1$. Here, ρ denotes the reflectivity factor of the pseudo-reflector. In keeping with the approximate nature of our model, we further assume that multiple reflections beyond the first are negligible. In other words, we only take into account the wave that gets to the receiver via a route that involves being partially reflected four times and which traverses a path length of $3\ell-4a$ and neglect, as being negligible, those contributions due to waves partially reflected 6, 8, or more times.

In keeping with the meticulous manner in which the receiving crystal detector mount was tuned for minimum VSWR, we assume

that the receiver is a blackbody, i.e., all incident energy is absorbed. Consequently, there can be no reflected signal from this station.

By dividing through the by free space wavelength λ_o, we can define the following dimensionless quantities:

$$a/\lambda_o \equiv \gamma \quad , \quad \ell/\lambda_o \equiv \Lambda \quad , \quad d/\lambda_o \equiv \delta \quad ,$$

where d is the channel width. Furthermore, we postulate that $\delta+2\gamma \leq \Lambda$, i.e., the pseudo-reflectors cannot be positioned within the region occupied by the plasma. It is straightforward to write the following expression for the z component of the Poynting's vector of the wave incident on the receiver:

$$\frac{1}{2}\sqrt{\frac{\epsilon_o}{\mu_o}}\left[\frac{(1-\rho^2)E_1 k_o^3}{2\pi\epsilon_o\Lambda}\right]^2\left\{1+\left(\frac{\rho^2\Lambda}{3\Lambda-4\gamma}\right)2\cos[4\pi(\Lambda-2\gamma)]+\left(\frac{\rho^2\Lambda}{3\Lambda-4\gamma}\right)^2\right\} \quad \text{(P-1)}$$

The normalized receiving power, denoted by ϵ, is derived by dividing (P-1) by the received power when $\Lambda = \Lambda_o$, the normalized separation distance between transmitted and receiver when $\delta = \delta_o = m\lambda_o$, $m = 1, 2, \ldots$, the nominal channel width. For the shock tube, $m = 4$. In addition, from the experimental radial field pattern data we know that because the system has been matched for minimum reflectivity when no plasma is present in the test section (nominal width), the nominal point will occur at a maxima in the pattern. Therefore, we specify that the quantity $\cos 4\pi(\Lambda_o-2\gamma) = +1$ at this nominal point. As a consequence:

$$2(\Lambda_o-2\gamma) = s \quad , \quad s = 0, \pm1, \pm2, \ldots \cdot \qquad \text{(P-2)}$$

It should be noticed that if the pseudo-reflectors are positioned immediately adjacent to the sides of the channel, then $\Lambda_o-2\gamma = 4$. In gener-

al, there are only a limited number of discrete positions (values of γ) at which the pseudo-reflectors can be placed in order to satisfy condition (P-2). For example, if $\lambda_o = 10$, then $20 \geq s \geq 4$.

Applying this condition, the normalized received power can be represented as

$$\varepsilon = \left(\frac{\Lambda_o}{\Lambda}\right)^2 \frac{\left\{1 + 2\left(\frac{\rho^2\Lambda}{3\Lambda-4\gamma}\right)\cos[4\pi(\Lambda-2\gamma)] + \left(\frac{\rho^2\Lambda}{3\Lambda-4\gamma}\right)^2\right\}}{\left\{1 + \frac{\rho^2\Lambda_o}{3\Lambda_o-4\gamma}\right\}^2} \quad . \qquad \text{(P-3)}$$

Inspection of this expression reveals that there are three parameters which we are at liberty to adjust so as to duplicate a given radial field pattern, viz., the transmitter-receiver spacing, Λ_o, the positions of the pseudo-reflectors, γ, and the reflectivity factor, ρ.

The normalized mean field line shown in Figure 17 was generated, as the name implies, by constructing a line that was midway between the curves representing the loci of the extrema of the plot and then normalizing the result. This line should then correspond to equation (P-3) when $\rho = 0$, i.e., ε should exhibit an inverse squared dependence on distance. The correspondence between the theoretical ($\rho = 0$) dependence, $(\Lambda_o/\Lambda)^2$, and the experimentally determined mean curve is excellent when $\Lambda_o = 8.55$, this value being selected on the basis of exact agreement at the nominal channel width $d/d_o = 1$ and at zero channel width $d/d_o = 0$*. The maximum divergence between the

---

* The following relation exists between the normalized channel width and Λ: $\Lambda = \Lambda_o - 4(1 - d/d_o)$ or $\Lambda = 4.55 + 4d/d_o$; in terms of δ, $\Lambda = \Lambda_o - 4 + \delta$ for $d_o = 4\lambda_o$.

experimental and theoretical mean curves using this value for Λ_o is less than 2 per cent within the range of values of d/d_o noted. For comparison, the physical distance from the flange of the transmitting horn to that of the receiver horn is, in terms of wavelength, approximately 38.

Having determined Λ_o, a trial-and-error procedure is used to determine which one of the discrete γ values and its corresponding ρ value will provide the closest fit to the complete field pattern curve. Using the analogy between d/d_o and λ_o/λ_p discussed earlier, a "matching" point was chosen at $d/d_o = 0.813$*, the theoretical curve being made to have exact agreement with the experimental data at this point. This particular value was chosen for two reasons; it is an extremum of the experimental curve, the value of ρ for a given γ being more accurately determinable the further from unity the match point is; also, $d/d_o \Rightarrow \lambda_o/\lambda_p = 0.813$ corresponds to an electron density level near the upper range of useful values, i.e., $N_e \simeq 2.4\times10^{12}$ (cf. Appendix V).

By trial solutions it was determined that of the ten γ values possible, the one corresponding, interestingly enough, to a pseudo-reflector position coincident with the plasma boundary gave the closest fit to the experimental data in the range $0.813 \leq d/d_o \leq 1.000$. Accordingly, $\gamma = 2.275$ and $\rho = 0.3095$ are the values that most closely represent the radial field pattern. The synthesized radial field pattern calculated on the basis of these parameters is shown in Figure 16. For values of $d/d_o \lesssim 0.8$, the synthetic pattern system-

* $d/d_o = 0.813$ corresponds to a Λ value of $\Lambda_o-(1-0.813)4 = 7.90$.

atically lags behind the actual pattern for decreasing values of the independent parameter, the amplitude of the extrema being lower than are observed. This can be attributed to the neglect of the near field, radial components of the radiation field which become increasingly important the closer the horns are made to approach one another.

In general, agreement between the synthesized and actual radial field patterns, in the region of concern, is quite satisfactory considering the simplifying assumptions incorporated in the analysis. Having restricted our discussion to the one-dimensional case (radial field pattern), we can make no general statement concerning the actual three-dimensional field pattern. However, it appears, from the quantitative agreement between the results of the model and experiment, that the essential factors characterizing the near field interference phenomena have been properly taken into account and that the model can be used to describe, at least crudely, higher dimensional effects.

Continuing, for the moment, to confine our attention to the one-dimensional case, we shall now modify the theory to take into account a slab of homogeneous, isotropic plasma, characterized by a complex propagation constant, k^*, in the region from γ to $\gamma+\delta_o$. As mentioned, the pseudo-reflectors were positioned at the edge of the plasma slab, i.e., at γ and $\gamma+\delta_o$. It will be assumed that the plasma, now in juxtaposition to the reflectors, does not influence their reflectivity. That is, the value of ρ (0.3095) determined for the free space case is applicable in the presence of plasma, the reflectors being viewed as just outside the plasma.

A wave that is reflected from the plasma boundary will be composed of two components, one due to the discontinuous change in constitutive properties and one arising from the reflector. For values of $\lambda_o/\lambda_p \gtrsim 0.7$* and $\frac{\nu_c}{\omega} \lesssim 0.4$, the reflected signal from the plasma interface is so small as to be beyond the limits of detectability of the microwave circuit used. For all intents and purposes, this contribution to the reflected signal can be ignored. Therefore, the reflected wave will be postulated as emanating solely from the pseudo-reflectors.

Any wave traversing the region between γ and $\gamma+\delta_o$ will have a propagation constant equal to k^* rather than k_o as was used in the free space case. Waves outside the plasma region will continue to be governed by the free-space propagation constant. Having already nondimensionalized the spatial coordinates by dividing by $\lambda_o = 2\pi/k_o$, it turns out that all that is necessary in order to account for the presence of the plasma, under the assumption made above, is to apply the multiplicative factor $k^*/k_o = n_r + in_i$ to the exponential factors representing wave propagation in the plasma region.

It is propitious now to account for one of the higher dimensional effects alluded to earlier. As indicated, Harris[45] has shown that in the near field of an antenna the radiation intensity is a function of the parameter u, the product of the wavelength and the distance from the antenna aperture to the field point. As postulated by Jahn and Harwell[14], but applied not without error to the mean field curve, μ will be taken to be a constant representative of the geometry of the system. The scaling parameter is then

---

* This corresponds to $N_e \sim 3\times10^{12}$ cm^{-3}.

$$\mu = \text{constant} = \lambda_o d_o = \lambda d \quad . \tag{P-4}$$

Writing $\lambda = \lambda_p$, then $\lambda_o/\lambda_p = n_r = d/d_o = \Lambda_o - 4 + \delta$ for $d_o = 4\lambda_o$. Physically, this implies that the field pattern (in three dimensions) remains invariant as a function of wavelength. In other words, since the plasma wavelength λ_p is always equal to or less than the free space wavelength λ_o for a fixed actual separation distance between transmitter and receiver horn, the apparent separation distance with regard to the field pattern, i.e., in terms of wavelength, will decrease with increasing λ_p. Were the plasma lossless and refraction effects negligible, the normalized transmitted signal detector output would appear, as a function of λ_o/λ_p, precisely the same as if the source and receiver were physically brought closer together as $d/d_o = \lambda_o/\lambda_p$.

Accepting the validity of the aforementioned postulate which in reality is simply a restricted statement of Huygens' principle and should be adequate for its intended application, we can write the following expression for ϵ_s'. We define ϵ_s' as the received power calculated on the basis of the synthetic field pattern but neglecting refraction effects, to wit:

$$\epsilon_s' = \frac{1}{2}\left[\frac{(1-\rho^2)E_1}{\lambda_o}\right]^2\left[\frac{1}{\Lambda_o+(n_r-1)\delta_o}\right]^2 \omega^3 \mu_o k_o e^{-4\pi n_i \delta_o} \left\{1 + 2\Omega' \cos(4\pi n_r \delta_o) + (\Omega')^2\right\} \tag{P-5}$$

where Ω' has the form

$$\frac{e^{-4\pi n_i \delta_o} \rho^2 (\Lambda_o + (n_r - 1)\delta_o)}{\Lambda_o + (3 n_r - 1)\delta_o} \tag{P-6}$$

Prior to the introduction of refraction effects, we shall normalize this expression to the received power calculated on the basis of a plane wave interacting with a plane plasma slab, etc. To be consistent, and because the restriction is warranted, in the electron density and collision frequency regime under study, we shall once more neglect reflection effects at the boundaries. Denoting the plane wave, received power by ϵ_p, we have

$$\epsilon_p = \tfrac{1}{2}\sqrt{\epsilon_o/\mu_o}\, E_p^2\, e^{-4\pi n_i \delta_o} \qquad \text{(P-7)}$$

where E_p is the magnitude of the plane-polarized E field vector. Dividing (P-5) by (P-7) and specifying E_1 and E_p such that the ratio ϵ_s'/ϵ_p is unity for the absence of plasma, i.e., $k^* = k_o \Longrightarrow n_r = 1$, $n_i = 0$, we derive the following:

$$\frac{\epsilon_s'}{\epsilon_p} = \left[\frac{\Lambda_o}{\Lambda_o+(n_r-1)\delta_o}\right]^2 \frac{\{1+2Q'\cos(4\pi n_r \delta_o)+(Q')^2\}}{\left\{1+\frac{\Lambda_o \rho^2}{\Lambda_o+2\delta_o}\right\}^2} \,. \qquad \text{(P-8)}$$

We shall now introduce refractive effects into the analysis. The refraction calculation will proceed by two steps which are assumed independent. We first consider the effects of refraction of the waves reflected from the pseudo-reflectors into the plasma. Secondly, we study the effect of the plasma, free space (surround) interface upon the non-axial rays of the incident wave.

The model used as a basis for the calculations of the effects of refraction upon the reflected waves is diagrammed below.

We shall postulate that the pseudo-reflectors are endowed with the ability to collect energy over an aperture of characteristic half

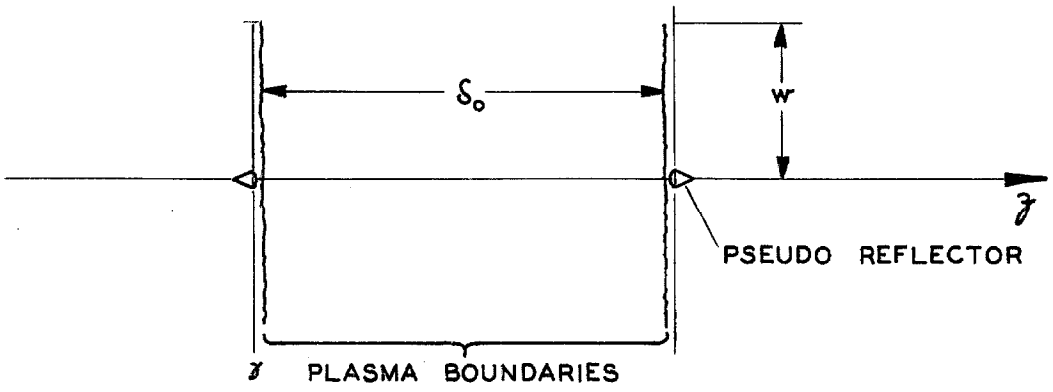

width w and to re-radiate the reflected portion of the wave as a point source (a dipole). This is, of course highly fictitious, but should serve to permit order-of-magnitude estimates of the refraction effect to be made. In keeping with the spirit of this postulate is the further presumption that geometrical, i.e., ray, optics is applicable. Recall that the pseudo-reflectors are situated just outside the plasma slab.

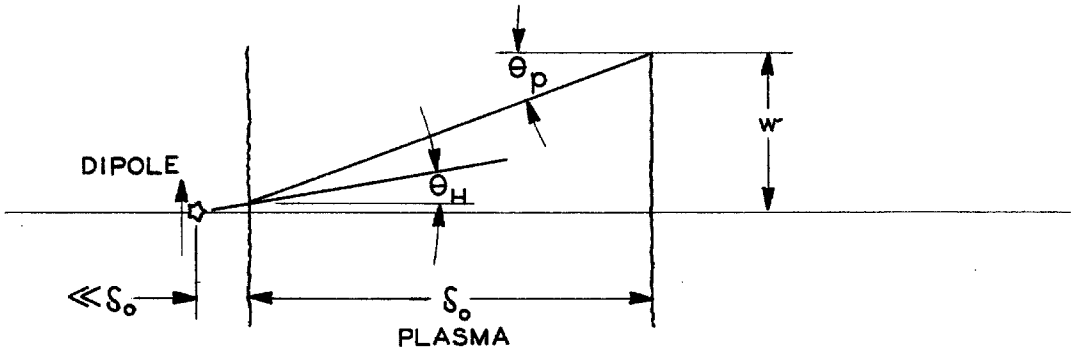

The averaged $\tilde{E}$ field from the dipole can be written as

$$\tilde{E} = \chi_1 \int_0^{\theta_H} \cos\theta \, d\theta = \chi_1 \sin\theta_H$$

where χ_1 is a constant and θ_H is the maximum angle a ray can have and still intercept the collection aperture. We apply Snell's law, i.e.,

$$\left(\frac{\sin\theta_H}{\sin\theta_p}\right) = \frac{k_r}{k_o} = \frac{\lambda_o}{\lambda_p} \quad . \qquad \text{(P-9)}$$

Then

$$\overline{\tilde{E}} = \chi_1 (\lambda_o/\lambda_p)\sin\theta_p \quad . \tag{P-10}$$

A word of explanation is called for insofar as equation (P-9) is Snell's law for non-conductive media. In the regime where $n_i << n_r$ and n_r is of order unity, i.e., plasmas of interest, Snell's law for conductive media[47] can be approximated by the form shown to a high degree of accuracy (much higher accuracy than is consistent with the other assumptions).*

The correction factor which we shall apply to account for the refraction effects of the reflected waves will be written as the ratio of the average $\tilde{E}$ field received with plasma present to that when no plasma is present, or simply

$$\frac{\overline{\tilde{E}}_{plasma}}{\overline{\tilde{E}}_{vacuo}} = \frac{\chi_1(\lambda_o/\lambda_p)\sin\theta_p}{\chi_1(1)\sin\theta_p} = \lambda_o/\lambda_p \quad .$$

It is easily demonstrated that we need only multiply Q' by the square of λ_o/λ_p to account for refraction. The resultant quantity is denoted as Q :

$$Q = (\lambda_o/\lambda_p)^2 Q' \quad . \tag{P-11}$$

The square in this expression arises because the correction is applied twice, once for each reflection in the plasma, the refraction of the initial incident wave being considered below.

There is one further consequence of the refraction phenomena that should be considered; the increased attenuation of the wave due to the added path length of the refracted wave. To account for this

* Cf. Stratton[47], § 9.8.

diminution in signal strength, we should properly write

$$\overline{\tilde{E}} = \chi_1 \int_0^{\theta_H} e^{-2\pi n_i \delta_o \left(\frac{1}{\cos\theta} - 1\right)} \cos\theta d\theta \qquad \text{(P-12)}$$

rather than equation (P-10). This integral is quite involved, and since w , upon which the path length is dependent (through θ_H), is to a large extent indeterminate and subject to whimsey, the following procedure, which is quite in keeping with this analysis, will be used. We define an incremental, averaged additional path length as $\sigma\delta_o$, where now

$$\overline{\tilde{E}} = \chi_1 e^{-2\pi n_i \sigma \delta_o} \sin\theta_H \qquad \text{(P-13)}$$

and σ is an adjustable parameter. The length w is, of course, fictitious and related loosely to the actual physical dimensions of the horn aperture. The vicinity of the horn aperture is the most probable source of the interference reflection; accordingly one could surmise that $0 \leq \sigma \leq \frac{1}{2}$. From a practical point of view, it was found, when applying the field pattern correction formula to the interpretation of test data, that it was more convenient to set $\sigma = 0$ and to vary the quantity n_i. This was done by selecting an appropriate value for ν_c/ω. Whereas the test data indicated values of ν_c/ω in the range of $0.07 \rightarrow 0.15$ as being representative of the gases tested, a value of $\nu_c/\omega = 0.30$ when applied to the calculation of the field pattern correction appeared to be most satisfactory. Figure 17 illustrates the relatively small difference in form between the field correction curves calculated using $\nu_c/\omega = 0.15$ and 0.30. In all that follows, we shall therefore assume $\sigma = 0$.

The last effect we shall take into account is that associated with the incident wave. The model applicable to this investigation is diagrammed below.

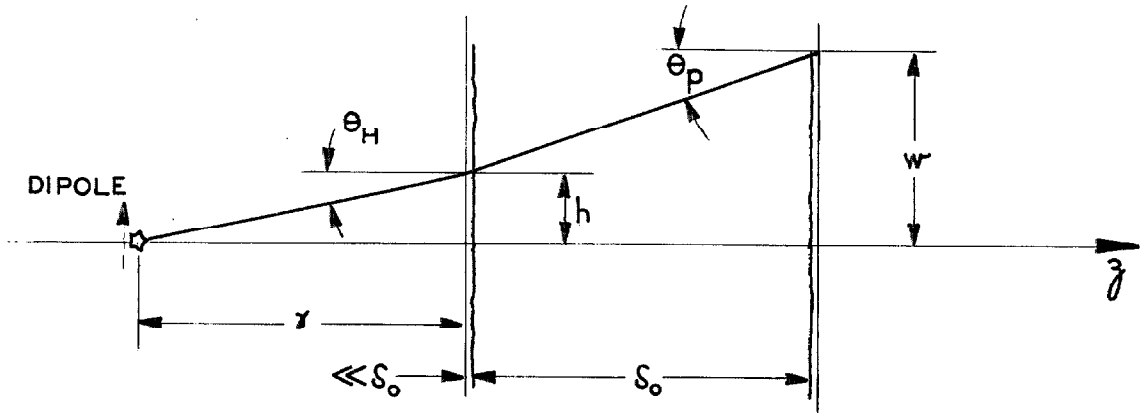

Writing Snell's law again

$$\sin\theta_H/\sin\theta_p = \lambda_o/\lambda_p \quad ,$$

where

$$\sin\theta_H = \frac{h}{\sqrt{\gamma^2+h^2}} \quad \text{and} \quad \sin\theta_p = \frac{w-h}{\sqrt{(w-h)^2+\delta_o^2}} \quad . \qquad \text{(P-14)}$$

As λ_o/λ_p decreases (N_e increasing), there is a corresponding decrease in θ_H. For physically realistic values of w, e.g., $w \leq 2$, a reasonable approximation is to let $\sin\theta_H \approx h/\gamma$. For convenience, we let $U = (w^2+\delta_o^2)^{\frac{1}{2}}$, and write:

$$h = \left\{\left(\frac{U}{\gamma}+\frac{\lambda_o}{\lambda_p}\right) - \sqrt{\left(\frac{U}{\gamma}+\frac{\lambda_o}{\lambda_p}\right)^2 - 4\frac{\lambda_o}{\lambda_p}\frac{w^2}{\gamma U}}\right\} \Big/ \left(\frac{2w}{\gamma U}\right) \qquad \text{(P-15)}$$

where the sign preceding the radical was selected so that as $\lambda_o/\lambda_p \to 0$, $h \to 0$. The averaged $\tilde{E}$ field is then

$$\overline{\tilde{E}} \simeq \chi\left(\frac{h}{\gamma}\right) = \frac{\chi\left[\left(\frac{U}{\gamma}+\frac{\lambda_o}{\lambda_p}\right) - \sqrt{\left(\frac{U}{\gamma}+\frac{\lambda_o}{\lambda_p}\right)^2 - 4\frac{\lambda_o}{\lambda_p}\frac{w^2}{\gamma U}}\right]}{\frac{2w}{U}} \quad . \qquad \text{(P-16)}$$

Normalizing to 1 at $\lambda_o/\lambda_p = 1$, we derive the correction factor $\mathcal{G}$ which represents the effects of refraction upon the initial incident wave, i.e.,

$$\mathcal{G} = \frac{\left(\frac{U}{\gamma} + \frac{\lambda_o}{\lambda_p}\right) - \sqrt{\left(\frac{U}{\gamma} + \frac{\lambda_o}{\lambda_p}\right)^2 - 4\frac{\lambda_o}{\lambda_p}\frac{w^2}{\gamma U}}}{\left(\frac{U}{\gamma} + 1\right) - \sqrt{\left(\frac{U}{\gamma} + 1\right)^2 - \frac{(2w)^2}{\gamma U}}} \quad . \tag{P-17}$$

Expanding the radicals and retaining only the first two terms, the accuracy of this procedure being consistent with the preceding steps, we write:

$$\mathcal{G} = \frac{\left(\frac{U}{\gamma} + 1\right)}{\left(\frac{U}{\gamma} + \frac{\lambda_o}{\lambda_p}\right)} \frac{\lambda_o}{\lambda_p} \quad \text{or} \quad \left(\frac{U + \gamma}{U + \gamma n_r}\right) n_r \quad . \tag{P-18}$$

This correction factor is applied as follows:

$$\frac{\epsilon_s}{\epsilon_p} = \mathcal{G}^2 \left(\frac{\epsilon'_s}{\epsilon_p}\right) , \tag{P-19}$$

where now ϵ_s/ϵ_p is the complete field pattern correction factor to be applied to the normalized transmitted signal, and ϵ'_s/ϵ_p is the field pattern correction factor (equation (P-8)), wherein the refraction of the initial incident wave was not taken into consideration.

The field pattern correction factor $\mathcal{G}$ is a weak function of the magnitude of the parameter w, the characteristic width of the apparent receiving aperture. A constant value of $w = 3/2$ was selected as being the most realistic and consistent with the assumptions of the analysis. All data have been subsequently reduced using this value for w. The application of the complete field pattern correction factor, ϵ_s/ϵ_p, is discussed in Appendix T.

APPENDIX Q

DISCUSSION OF THE INFLUENCE OF BOUNDARY LAYER EFFECTS UPON MICROWAVE MEASUREMENTS

In the microwave-plasma theory developed in Appendix N, the plasma slab was considered to be homogeneous and isotropic. Consequently, a sharp, discontinuous transition in electron density between the plasma and the surrounding space was implied. In reality, rather than a discontinuous electron density profile at the plasma-surround interface, an transition region (where the electron density varies continuously from essentially zero at the shock-tube wall to some large value in the "core" of the flow) will exist. Because the plasma generated by the shock tube is of finite extent not only in a direction normal to the plasma flow direction and parallel to the microwaves' propagation direction (z), but also in a direction mutually perpendicular to both of these directions (that is, in the x direction), the microwave beam will propagate parallel to the boundary layer gradients in the z direction and perpendicularly through those existing in the x direction.

In addition to these two electron density gradients, there is a third that should be considered, viz., the electron density gradient that exists normal to the microwaves' propagation direction but parallel to the plasma flow direction. This gradient exists as a consequence of the ionization relaxation effects dominant in the shock-heated gas and will be considered in Appendix R.

Because of the symmetry of the cross section of the shock tube that exists in the x and z directions, and therefore of the plas-

ents. As a matter of reference, for $\nu_c/\omega = 0.10$ and $m = 4$, S_R, S_T, P_R, and P_T can be measured simultaneously for only a very limited range[27] of electron densities, about $0.60 \leq N_e/N_p \leq 0.67$. Having restricted our experimental program to the determination of ${}_1S_R$ and ${}_1S_T$, we shall therefore estimate the electron density gradients existing under typical shock-tube conditions. From these estimates, the effect of the boundary layers upon the microwaves can then be approximated.

As part of his study of heat transfer from ionized argon behind a shock wave, Jukes[50] considered the form of the argon positive-ion concentration profile near the shock tube wall. Since the approximate equilibrium model he developed to portray conditions far from the shock front assumed quasi-neutrality, the positive ion and electron profiles are identical. He concludes that far from the shock* the ion (electron) boundary layer has a characteristic thickness (δ_s) which is independent of distance behind a shock and can be written as

$$\sqrt{\mathcal{D}_{iA}/G}$$

where $\mathcal{D}_{iA}$ is the argon positive-ion diffusion coefficient, and G is the ratio of ion concentration (in the core) to ion generation rate.

The shock tube, as discussed in Appendix C, can generate shock waves having Mach numbers from approximately 7 to 10 when heating 5 torr of argon. For these two extreme Mach number conditions, using the observed electron-generation rates and the electron

---

* Defined as the distance behind the shock front $\ell \gg U_s/G$, U_s being the shock velocity and G as defined above. In terms of particle time t_p, we have $t_p \gg 1/G$.

densities occurring either when the electron-atom regime becomes dominant (for $M_s \sim 10$) or the cold front occurs ($M_s \sim 7$), coupled with appropriate values of $\mathcal{D}_{iA}$, we find:

$$\delta_s \simeq 1/3 \text{ mm for } M_s \simeq 10 \text{ for } t_p \gg 100 \ \mu\text{sec},$$

and

$$\delta_s \sim 2\tfrac{1}{2} \text{ mm for } M_s \simeq 7 \text{ for } t_p \gg 10,000 \ \mu\text{sec}.$$

For comparison, for the strongest shock strengths generated ($M_s \sim 10$), the atom-atom regime is completely dominated by the electron-atom ionization process for values of $t_p > 80$ μsec. For the weakest shocks, the cold front influences the ionization process when $t_p \sim 1000$ μsec.

From this we can conclude that under the most adverse conditions the electron-density boundary layer would at most be about 2 mm thick. As is discussed in Appendix V, the correct value of ν_c/ω was determined by matching the transmitted data S_T to the hybrid phase ("bump") data, to the exclusion of the use of S_R data. As the S_R data were rarely used (the atom-atom regime invariable being completed prior to the reflected signal becoming detectable), and then only as an added check of the data, we need not consider the effects of the boundary layer upon it.

Referring to Albini and Jahn's[49] study of trapezoidal electron density gradients, we find that for the case where the ramps extend over a distance of some 0.25 λ_o (λ_o = 1.25 cm at 24 gcps), the transmitted signal will differ from the corresponding discontinuous interface plasma slab by two to three per cent. This is true even for electron density profiles that deviate from being linear ramps. This

estimate was made using a value of $n_r + in_i$ (corresponding to Albini's parameter K) equal to $0.8 + 0i$. This value is consistent with an electron density of 2.6×10^{12} and $\nu_c/\omega = 0.10$, under the not unrealistic approximation that the imaginary part n_i (which equals 0.022 for this case) can be satisfactorily taken as zero.

It should be remarked that the electron density level quoted corresponds approximately to the third matching "bump," and is therefore representative of the maximum electron-density level used in the determination of electron generation rates.

From these considerations, we conclude that the electron-density boundary layer present when 5 torr of argon is shock heated by M_s 7 to 10 shock waves will not significantly affect the interpretation of the experimental data. As a general truism, the closer to the shock front one makes observations, the less significance the boundary layer will have. In all cases then, data were taken as close to the front as was possible consistent with desired levels of accuracy.

APPENDIX R

DISCUSSION OF THE INFLUENCE OF LATERAL ELECTRON DENSITY GRADIENT EFFECTS UPON MICROWAVE MEASUREMENTS

The microwave horns used in this experiment were specifically designed to produce a field pattern that is well collimated in the vertical (x), i.e., polarization, direction. This design, while ensuring that the majority of the microwave energy would pass through the plasma (whose x dimension is 5 cm), has relatively poor collimation characteristics in the y direction, i.e., in a direction transverse to the plane of polarization but parallel to the axis of the shock tube. Measurements made inside the pyrex test section indicate that the radiated field pattern sensibly extends over a distance of some 7 cm in the y direction. Clearly then, the changes in the microwave signals attributable to the presence of a plasma in the diagnostic section, are averaged quantities that arise from interaction of the microwave field with a volume of plasma whose x, y, z dimensions are approximately 5 cm × 7 cm × 5 cm. The values of electron density and effective collision frequency calculated from these signals must also, of necessity, be "volume" averaged quantities. We shall attempt here to evaluate, in a most qualitative manner, the effect an electron density gradient in the y direction would have on the transmitted microwave signal, assuming that gradients in the x and z directions (due to boundary layer effects, discussed in Appendix Q) can be neglected.

The y gradient in electron density is the very factor that this experiment was designed to measure, that is, the electron generation

rate occurring behind the shock wave. The tacit assumption has been made that the electron generation rate is sufficiently low so that while an electron density gradient does exist in the y direction, the actual variation of electron density over the 7 cm breadth of the field pattern is small enough to be neglected. For example, experiments with 5 torr of argon involved shocks having Mach numbers ranging from 7.9 to 9.4. The electron density differential existing across the 7 cm of the field pattern, for a shock near the midpoint of this Mach number range ($M_s \sim 8.6$), was found to be about 0.07×10^{12} * cm^{-3}, or approximately one per cent of the electron density level at which "cut-off"** of the transmitted microwave signal would occur. For runs conducted at higher Mach numbers, i.e., $M_o \sim 9.4$, the electron density differential calculated from the data increased to about 0.6×10^{12} cm^{-3}, or just about 10 per cent of the cut-off electron density level. The 3-torr argon shot shown in Figure 19 had a differential amounting to about 6 per cent of the saturated electron density level. Even in the extreme case of an electron density differential of around 10 per cent of the saturation level, the transmitted signal strength differential for a typical value of ν_c/ω, i.e., 0.10, would be only about one per cent†,

---

* We are discussing here conditions which occur immediately after the passage of the front, i.e., the atom-atom regime wherein the electron density, in the absence of shock attenuation, increases linearly with time.

** "Cut-off" occurs when the so-called plasma frequency (ω_p) equals the probing microwave frequency ($\omega = 2\pi \times 24 \times 10^9$); e.g., for this experiment, $\omega = \omega_p$ when $N_e = 7.14 \times 10^{12}$ cm^{-3}.

† Based on computations made assuming a homogeneous, isotopic plane slab, cf. Figure 13 and $N_e \sim 0.3 \times 10^{12}$. For $N_e \sim 3 \times 10^{-12}$, the signal strength differential due to the gradient would be around 20 per cent.

which would appear to be acceptable. However, a curious effect, which was observed to be associated with high electron density gradients, indicated that the effect of these gradients possibly was greater than the calculated change in signal strength quoted above would imply. This effect, a momentary rise in the transmitted signal strength to levels above 100 per cent, taking place near the shock front, is to be seen in the figure noted. The amplitude of the rise in this example is not as great as those observed in other instances where the electron density differential was higher(e. g., around 10 per cent of the saturated electron density level rather than about 6 per cent for the case shown). The details of this anomaly were somewhat difficult to observe because the transmitted signal was displayed as a chopped trace (one channel of a type M plug-in, 1 μsec display every 4 μsec). In spite of this difficulty, it was possible to establish the gross characteristics of this phenomenon. These are presented in the sketch below.

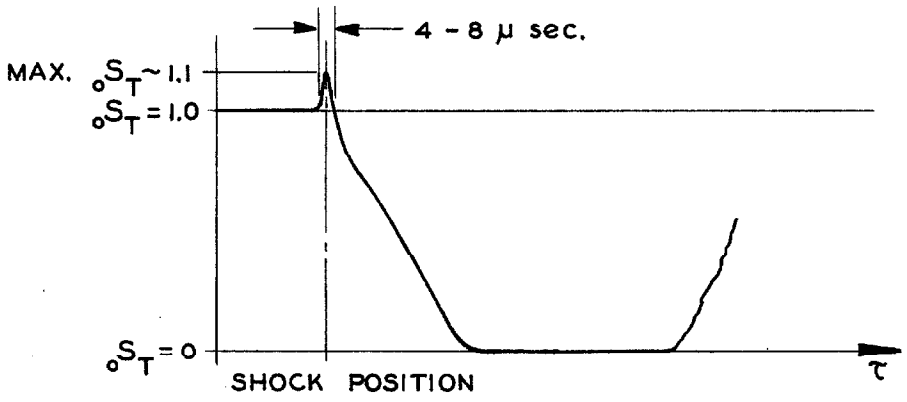

A literature survey was conducted to determine whether the idealized problem of a plane wave incident on a plasma slab possessing a lateral electron density gradient had been solved for the characteristics of the shadow zone, i. e., the near-field diffraction pattern

of the transmitted radiation. While futile, the search did reveal the great inherent complexity of the problem and showed that a meaningful solution would require more effort than was warranted within the context of this study. The problem that came closest to representing the rudiments of the phenomenon was Sommerfeld's[51] analysis of electromagnetic wave diffraction by a perfectly conducting wedge. Geometrical optics were employed in this analysis to represent the diffraction of plane electromagnetic waves by the edge of the wedge, the far-field diffraction pattern being determined. The use of geometrical optics for the solution of the idealized inhomogeneous plasma-slab, plane electromagnetic wave problem is, of course, not warranted; none the less, the characteristic features of Sommerfeld's solution, shown in the sketch below, bear a striking similarity to the anomaly observed.

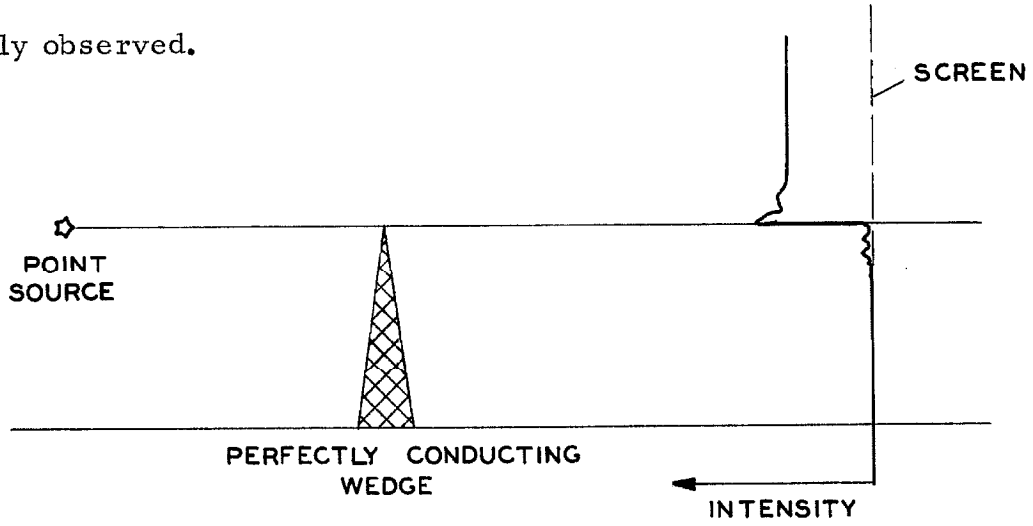

From this, the assertion is made that the anomalous behavior of the transmitted microwave signal, occurring at high Mach numbers, is due to the lateral electron-density gradient that exists across the field pattern of the horn. This explanation is consistent with another

observation. The atom-atom electron generation rates determined from high Mach-number shots are uniformly lower than they should be to be consistent with the large bulk of data taken at lower Mach numbers (cf. the Arrhenius plots of Chapter V). This depression of the data points is explainable in terms of the intensity overshoot in that the higher the value for ${}_{o}S_{T}$ the lower the corresponding indicated N_e value. Consequently, the indicated electron generation rate should be lower than is actually the case. In these instances, the normal* electron density versus time plot, wherein the electron density rises linearly (atom-atom regime) and then (as the electron-atom regime)** is seen to be modified somewhat. The trace exhibits a slight undulation for electron density levels from about 0.5×10^{12} to about 0.8×10^{12}, a region where the electron density gradient has a more pronounced effect upon the transmitted signal than it does at the lower electron density levels associated with the region closer to the shock.

---

* As observed at medium or low Mach numbers.

** This is modified by the shock attenuation effects. When shock attenuation is present, the electron density rises smoothly and monotonically with time.

APPENDIX S

DISCUSSION OF THE INFLUENCE OF MICROWAVES UPON PLASMA PROPERTIES

In order to experimentally determine plasma properties, it is a truism to say that one must physically interact in some manner with the plasma or its emanations. Microwaves, used as a plasma diagnostic device, interact almost exclusively with the free electrons present in the plasma. Therefore, one is led to question the manner in which this interaction occurs and to inquire as to whether the interaction affects those quantities being measured to the extent that the results could be spurious.

In the absence of the microwave diagnostic signal, we shall assume that the free plasma electrons have a Maxwellian velocity distribution, and we shall seek to determine the maximum microwave signal level which, while interacting with these electrons, will not significantly distort their velocity distribution.

Margenau[52] has studied this problem and has established the following criterion:

$$kT \geq \frac{M(eE/m)^2}{6\omega^2}$$

where T = plasma temperature, M = mass of gas atom, m = mass of the electron; E, ω are the amplitude of the electric field and the frequency of the incident electromagnetic wave, and k and e have their usual meanings, i.e., Boltzmann's constant and electric charge of the electron. For typical shock-tube conditions, that is, $kT \sim 2/3$ ev, M = mass of the argon atom, and $\omega = 2\pi \times 24 \times 10^9$, we find that for the

Maxwellian velocity distribution of the electron gas to remain unaffected, it is necessary to restrict the intensity of the electromagnetic wave such that $E \leq 27$ volts/meter.

The model 2K50 klystron used as a microwave generator in these experiments generated up to 8 milliwats of useful power (cf. Appendix I). Taking into account the 3 db loss of power in the directional coupler and the 6 db power loss in the attenuator* but neglecting losses in the ferrite isolator, stub- and E/H plane-tuners, wave guides, and the flanges, it is not unrealistic to assume that the total power emanating from the transmitting horn is, at most, one milliwatt. The physical aperture of the transmitting (and receiving) horn is rectangular, 2 cm by 5 cm. Again being conservative, it will be assumed that the microwave energy does not diverge but rather traverses the diagnostic section as a tightly-collimated beam having the same cross-sectional area (10 cm^2) as the horn aperture. Therefore, the energy per unit area per second, i.e., Poynting's vector, would be 1 watt/m^2, corresponding to an amplitude of the electric field vector of about 20 volts/meter.

Clearly then, the criterion established by Margenau is satisfied, and the microwave diagnostic beam used in these experiments will not significantly alter the characteristics of the electron velocity distribution. As a point of reference, the mean thermal velocity of a free electron in a plasma of temperature $\sim 2/3$ ev is approximately

---

* The nominal attenuator setting corresponded to -6.00 db, which limited the received crystal detector output level to the desired level, that is, about 70 mv.

0.5×10^6 M/sec, while the maximum directed velocity of these electrons interacting with the 20 volt/meter electric field of the microwave beam is only about 22 M/sec.

APPENDIX T

DESCRIPTION OF THE MICROWAVE DATA-REDUCTION COMPUTER PROGRAM

Three separate but related IBM 7090 data-reduction programs have been written to provide an accurate, rapid means of interpreting the shock-produced microwave crystal-detector data in terms of electron density (N_e) and effective collision frequency (ν_c/ω). Three programs were initially thought to be necessary because of the various electron density regimes wherein either the transmitted and reflected signals are both simultaneously observable, the transmitted signal, or only the reflected signal is detectable. These programs were denoted as Plasma I, Plasma II, and Plasma III, respectively. In Plasma I, the transmitted and reflected signals are both used as input data, electron density and effective collision frequency being calculated. In Plasma II, the transmitted signal plus an assumed value for ν_c/ω are used as inputs and the electron density is calculated. Plasma III essentially is identical to Plasma II in that the reflected signal, in addition to an assumed value of ν_c/ω is utilized as input and the electron density is calculated as output.

Only the details of Plasma II will be discussed, as all of the shock tube data were reduced using this program. It should be noted that Plasma II and Plasma III are identical except for the field-pattern correction subroutine required for the interpretation of the transmitted signal data (Plasma II) but not for reflected signal data (Plasma III). At the relatively high collision frequencies encountered in the shock tube, there was no observable overlap of the transmitted and

reflected signals[27], therefore obviating the need for the Plasma I program. Because of this, we shall restrict our discussion to the details of the Plasma II program.

Perhaps the most straightforward way to describe this program is to discuss the input, the operations performed on these data, and the resultant output.

Input

For each run, the following data are supplied as input: the transmitted signal data normalized but uncorrected for vagaries in the crystal calibration characteristics ($_oS_T$) is listed, in tabular form, as a function of a so-called indepepdent parameter. The independent parameter is the particle time (t_p), that is, the point in shock coordinate time at which $_oS_T$ was measured. In order to account for the crystal calibration characteristics, a table of $_oS_T$ versus $_1S_T$ is also supplied as input. This table can have up to 80 entries and is but one of two ways this correction factor can be fed into the program. The alternative method is by way of the empirical, bilinear (on log-log scale) representation of the calibration characteristics (cf. Appendix O). In the latter case, a short table consisting of two values of A_T, two of K_T, and the value of $_oS_T$ at which the two linear segments of the calibration curve join, is used as input. The field-pattern correction factor is also supplied as a table. In this table, the factor $\varepsilon_s/\varepsilon_p$ (see Appendix P) is listed, in one-to-one correspondence with values of λ_o/λ_p. In addition to these data, the free space wavelength, λ_o, the corresponding microwave probe frequen-

cy, ω, and the plasma slab thickness factor, m (slab thickness in terms of λ_o), are supplied. Furthermore, an assumed value of ν_c/ω is specified, together with appropriate alphanumeric information to adequately identify the data being reduced. An initial value of electron density (N_e), the utility of which will be described below, is also specified.

Basic Block Diagram

Figure 20 represents, in block diagram form, the basic operational features of the Plasma II program. Because of the complexity of the theoretical expression relating the ideal (plane wave, plane plasma slab, ...) normalized transmitted signal, here denoted as $_1\hat{S}_T$, to the properties of the plasma slab and microwave probe (i.e., N_e, ν_c/ω, m, ω)*, an iterative method of solution was deemed preferable. To start the iteration, a small value of N_e** is introduced as input, this value being selected to be less than the least value of N_e anticipated. Using this value and the assumed value of ν_c/ω, the corresponding "ideal" magnitude of the transmitted signal is calculated by using eqn. (N-9), Appendix N. The machine simultaneously computes λ_o/λ_p, using the same values for N_e and ν_c/ω, etc., via eqn. (N-5), Appendix N. From this value for λ_o/λ_p, a value of the field-pattern correction factor, ϵ_s/ϵ_p, is interpolated from the tabulated field-correction factor which is supplied

---

* Cf. Appendix N.

** The initial value of N_e was specified as 0.5×10^{10} cm^{-3}, a level so low as to be undetectable by the K-band (24 gcps) microwave probe.

as input. As diagrammed, the "ideal" transmitted signal ${}_1\hat{S}_T$ is multiplied by the field correction factor ϵ_s/ϵ_p to yield the "actual" normalized transmitted signal denoted as ${}_1\tilde{S}_T$. That is, ${}_1\tilde{S}_T = \epsilon_s/\epsilon_p \, {}_1\hat{S}_T$.

Having calculated the "actual" normalized transmitted signal that one would expect to observe from a plasma having the initial assumed electron density and the specified effective collision frequency, it is, of course, necessary to effect a comparison with the experimental data used as input (symbolically written as ${}_oS_T$). Before making the comparison, the cyrstal-calibration characteristics have to be taken into account. The given value of ${}_oS_T$, for which we are computing N_e, is fed into the crystal calibration block. We shall discuss only the case wherein the crystal calibration data is in tabular form, i.e., ${}_oS_T$ versus ${}_1S_T$, where ${}_1S_T$ is the true normalized magnitude of the transmitted signal. Because the calibration data in all instances was such as to loosely define one (or two continuous) straight lines on a plot of $\log {}_oS_T$ versus $\log {}_1S_T$, it was decided to apply this fact to the interpolation of the tabular crystal-correction input data. On the log-log calibration plot (cf. Figure 18), the interpolation would appear to be linear, i.e., a straight line being constructed between the bracketing calibration points. Analytically, this was performed by using the bracketing points to define the coefficients A_T and K_T in the expression ${}_1S_T = A_T({}_oS_T)^{K_T}$. Were the value of ${}_oS_T$, for which a value of ${}_1S_T$ is desired, to fall below the lowest value in the calibration table, K_T was taken as unity. That is, a truly linear interpolation was effected for values of ${}_oS_T$ from zero

to the lowest value on the table. This introduced negligible error, as the calibration typically extended over a sufficiently large range so that such values of ${}_oS_T$ would correspond to N_e values outside the realm of interest (or utility).

Having determined the true normalized transmitted signal, ${}_1S_T$, for which the appropriate N_e value is sought, the program can now proceed with the comparison. The sign of the quantity $({}_1S_T - {}_1\tilde{S}_T)/{}_1S_T$ is determined. For the initial iteration, the sign is negative. This then triggers the increment block where, for a negative comparison sign, the electron density used for the next iteration is incremented so as to be ten times as large as the previous level.

This procedure continues until the sign of the comparison becomes positive, indicating that the desired value of N_e has been surpassed. At such time, the electron density level of the previous iteration (wherein the comparison sign was negative) is again applied; however, it is now incremented by 1/10 the previously used value. This increment in N_e is applied for successive iterations until the sign again becomes positive, the increment for the next round of iterations being further reduced by a factor of ten.

The process continues through successive iterations and is terminated when the incremental change in N_e (i.e., ΔN_e) is some small fraction of N_e*, or 40 iterations have occurred. By way of reference, the desired level of accuracy was usually attained, on the average, in about 25 and seldom required more than 35 iterations.**

* $\Delta N_e/N_e$ was arbitrarily chosen to be ≤ 0.0001.

** When using the field-pattern correction curve denoted as corresponding to $\nu_c/\omega = 0.30$ on Figure 17.

Instances where the result failed to converge were rare, occurring in about 0.7 per cent of the cases run. In such circumstances, the value of N_e corresponding to the last (40th) iteration is printed out.

Although indirect, this method of solution was remarkably fast, requiring on the average* 0.195 seconds per case.

In addition to the calculation of N_e, the Plasma II program was written in such a manner that the corresponding values of the normalized reflected signal, ${}_1S_R$, and the two measurable phases, P_T and P_R, were also computed for each input value of ${}_oS_T$. This provided an added degree of flexibility insofar as interpretation of the reduced data was concerned.

Output

Figure 21 is a reproduction of one page (one run, one value of ν_c/ω) of output print-out from the Plasma II program. As this program was developed prior to the codification of the symbols used in this work, we shall briefly discuss the various quantities shown whose meaning may not be self-evident.

In the first line, besides the run number and test gas, is printed the field-correction table number (FCT 430) used in the data reduction. Field-correction curve no. 430 is seen in Figure 17; here, diffraction and refraction effects have been taken into account, the value of ν_c/ω selected to be 0.30 as discussed in Appendix P. Under the input parameter heading is listed the microwave probe frequency denoted as W (rad/sec), the factor M (plasma slab thick-

* Defined as the number of cases (1 value of ${}_oS_T$ and ν_c/ω) divided by the computation time, which includes input read-in and output write-out.

ness in terms of wavelength λ_o), and the free space wavelength λ_p in centimeters. Under "Table Values for Xtal Calibration" is the input transmitted-signal crystal-calibration data OST and IST , denoting ${}_oS_T$ and ${}_1S_T$, respectively.

The first column (index) here shows the run number, the added flexibility it provides for labeling individual data points not being utilized. Column 2, labeled T2(O), denotes the uncorrected normalized data (${}_oS_T$). The next column, T2, represents the quantity (from the final iteration) we have previously labeled ${}_1S_T$, the normalized transmitted signal from a plane slab irradiated by a plane wave, etc. The meaning of the heading VC/W is obvious (ν_c/ω), as is the one to its right, NE (N_e). R2 is the calculated normalized reflected signal to be expected from the idealized plane-wave interaction with a plasma slab having the indicated values of N_e and ν_c/ω . Theta T and Theta R correspond to the measurable transmitted and reflected phases, again for the idealized case, which have been previously labeled as P_T and P_R , respectively. The ratio of the free space to plasma wavelength is labeled Lambda O/P ; again, the value shown is for the final iteration. The column labeled F lists the numer of iterations required for the computation of N_e to converge to within the limit specified earlier. As mentioned, the independent parameter here is the time in particle coordinates (t_p) at which the measurement of T2(O) (or rather, ${}_oS_T$) was made. The last column is used as a convergence indicator. A zero denotes convergence of the value of electron density,to within the desired accuracy level, occur-

ring in less than 40 iterations. A one in this column shows that convergence failed to occur in 40 iterations; the values shown for N_e, etc., are then those associated with the 40th iteration.

APPENDIX U

DISCUSSION OF THE MICROWAVE HYBRID PHASE (BUMP) MEASUREMENTS

Background

The microwave diagnostic circuitry used in this study was specifically designed to generate and to detect the amplitude of the electromagnetic waves transmitted through and reflected from the shock produced plasma. As has been discussed in Appendix I, the measurement of the signal amplitudes requires less sophisticated circuitry than would be required for the measurement of relative phases (interferometric techniques) or the measurement of a combination of an amplitude and a phase. Furthermore, it has been shown that for the relatively high values of the effective collision frequency encountered in the experiments, the range of detectable electron density using this circuit is equal or superior to that which can be sensed by the necessarily more elaborate circuitry required for phase determination.

Jahn[27] was the first to observe that this simplest of microwave diagnostic systems had the ability of providing a third measurement, the so-called "hybrid phase" or "bump" signal. The hybrid phase signal arises from an interference effect, and while it does not extend the range of electron densities which can be measured, it does provide a unique determination of electron density in the range where the transmitted signal is fast approaching zero and the reflected signal is just beginning to become evident. In addition to bridging these two signal ranges, the hybrid phase, as we shall see, provides a

measure of electron density which is a relatively weak function of the effective collision frequency. It thereby allows this parameter to be determined accurately. This is particularly true for low temperature plasmas where the cold front occurs before the electron density has increased sufficiently to yield a measurable reflected signal.

In his thesis Harwell[53], following Jahn's analysis, presented an approximate relationship governing the position of the extremum of the hybrid-phase bump signal and the parameters of interest, viz., N_e, ν_c/ω. Heretofore, the quantity ν_c/ω was determined by matching the N_e versus t_p data, as determined from the transmitted data (for a fixed ν_c/ω), to the data, at higher values of N_e, derived from the reflected signal (for the same ν_c/ω). The hybrid phase measurements were used in a subsidiary capacity as a check. An independent evaluation of this procedure revealed that in general, for those portions of the shock-produced plasma where the reflected signal is becoming prominent, the transmitted signal being saturated, the electron density increases so rapidly* as to make the unambiguous determination of ν_c/ω unreliable. As a reasonably accurate determination of ν_c/ω is necessary for the evaluation of initial ionization rates, it was therefore necessary to rely upon the hybrid phase (bump) data to be used in concord with the transmitted signal information. The ensuing analysis was conducted to provide a reliable basis for the in-

---

* This electron density regime ($> \sim 3\times10^{12}$) apparently corresponds, for the gases of interest and under the temperature and pressure conditions prevalent, to ionization rates dominated by the electron-atom ionization process[1].

terpretation of these bump data.

Theory

The transmitter and receiver horns are meticulously matched to the pyrex test section of the shock tube so that the microwaves are essentially unaffected by the presence of the dielectric slabs through which they propagate. A small reflected signal is generated by mismatching the tunable crystal detector affixed to the receiver horn, cf. Figure 11. A bucking signal of equal amplitude but opposite phase is provided by the stub tuner, immediately preceding the transmitter horn. These two signals, in the absence of a plasma between the horns, are such as to just cancel, the net reflected signal being once again negligible. When plasma is present, the small mismatch wave reflected from the receiver crystal mount is attenuated and its phase altered so that it is no longer precisely cancelled by the small but invariant bucking signal reflected from the stub tuner. A series of low amplitude interference "bumps" can then be observed superimposed, as a perturbation, on the reflected signal which, in the range where the bumps are dominant, is just barely detectable. Figure 19, a reproduction of an actual test record, clearly shows these interference bumps on the 5-times amplified reflected signal trace. In essence, then, the circuit acts as a crude interferometer in a narrow electron density range ($\sim 0.7\times10^{12} \lesssim N_e \lesssim 4\times10^{12}$ for $\omega = 2\pi\times24\times10^{9}$ sec^{-1}).

An idealization of the portions of circuitry involved in the generation of the hybrid phase signal is shown below, where the various plane waves assumed present are labeled by the magnitude of their

associated electric field vectors.

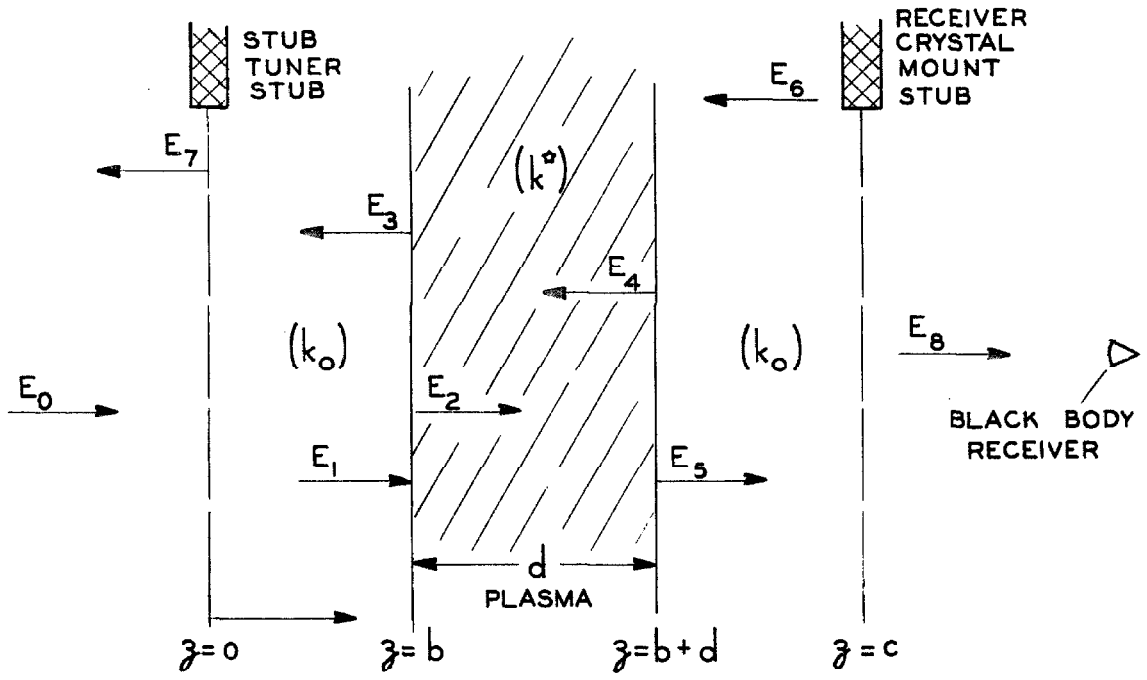

As is implied by the diagram, we shall consider the one-dimensional problem of an incident plane, plane-polarized wave interacting with two idealized stubs and a plasma slab having the same characteristics as assumed for the analysis of Appendix N.

Adjustment of the position and insertion depth of the stub incorporated in the tunable receiver crystal mount permitted its VSWR to be reduced to about 1.02. In the idealization, then, the receiver is considered to be a blackbody, i.e., reflectionless, the stub here representing the additional length of insertion necessary to produce the intentional mismatch discussed above. Because of the excellent match of the horns to the test section, the stub of the stub tuner is inserted only for the purpose of generating the bucking signal.

For convenience, we shall neglect the higher order modes which are generated by the presence of the stub in the wave guide.

These would undoubtedly contribute to the signal level at the detectors, but it is assumed that their contribution is small in comparison to the dominant TE10 mode in the wave guide. It should be noted that the indicated positions of the stuby ($z = 0, c$) have very little relationship with their actual position, as free space is assumed to exist between the outer surface of the plasma and the stubs in this analysis. In actual fact, the test section, horns, and wave guide possess propagation characteristics which, while different from those of free space, should be adequately represented by the model chosen.

The idealized stubs are assumed to be characterized by a reflectivity factor, α, for the stub at $z = 0$ and β for one at $z = c$. These factors are defined as the positive real ratio of the magnitude of the reflected signal's E field to that of the incident signal at the stub point, i.e., $\alpha = (E_7/E_o)_{z=0}$ and $\beta = (E_6/E_5)_{z=c}$. The 180° phase shift occurring when an electromagnetic wave is reflected by an excellent conductor, such as the silver plating on the stubs, is taken into account by the minus sign in equations (U-2) and (U-4) below.

A further simplification is introduced into the analysis by restricting the reflectivities α and β to small values, i.e., $\alpha, \beta < \theta(10^{-1})$. This restriction, in effect, allows us to ignore all secondary reflections and is in keeping with reality. We shall, for example, neglect the small fraction of E_3 reflected from the stub at $z = 0$ as being negligible in comparison to the wave E_7.

Phasor notation will be employed, the suppressed time dependence being understood to be $e^{-i\omega t}$. The E field vector is as-

sumed parallel to the x axis and the H field vector to y , for all waves considered.

We shall now seek to determine the composite reflected signal field strength $\tilde{E}_R$, here defined as $\tilde{E}_3 + \tilde{E}_7$ *. From the definitions we write

$$\underline{\tilde{E}}_0 = E_0 \underline{e}_x e^{ik_o z} e^{-i\omega t} = \underline{\tilde{E}}_0 e^{-i\omega t} = \tilde{E}_0 \underline{e}_x e^{-i\omega t} \qquad \text{(U-1)}$$

at the first stub, $z = 0$, then

$$\tilde{E}_7 = -\alpha E_o e^{-ik_o z} \qquad \text{(U-2)}$$

and, considering the reflection process at the stub surface to be ideally lossless,

$$\tilde{E}_1 = \sqrt{1-\alpha^2}\, E_o e^{ik_o z} \quad . \qquad \text{(U-3)}$$

Similarly, for the stub at $z = c$,

$$\tilde{E}_6 = -\beta E_5 e^{i2k_o c} e^{-ik_o z} , \qquad \text{(U-4)}$$

and

$$E_8 = \sqrt{1-\beta^2}\, \tilde{E}_5 . \qquad \text{(U-5)}$$

At the first plasma-surround interface, $z = b$, satisfying the requirement that the tangential E and H fields be continuous, we write

$$\sqrt{1-\alpha^2}\, E_0 e^{ik_o b} + E_3 e^{-ik_o b} = E_2 e^{ik^* b} + E_4 e^{-ik^* b} , \qquad \text{(U-6)}$$

---

* The microwave reflected-signal crystal detector mounted on the 3-db directional coupler produces an output which is proportional to the energy of the wave incident upon it, i. e.,

$$(\tilde{E}_3 + \tilde{E}_7) \times (\tilde{H}_3 + \tilde{H}_7)^\dagger ,$$

where the dagger here denotes a complex conjugate quantity.

$$\sqrt{1-\alpha}\, E_0 e^{ik_o b} - E_3 e^{-ik_o b} = n^* E_2 e^{ik^* b} - n^* E_4 e^{-ik^* b} , \qquad \text{(U-7)}$$

where, as before (Appendix N), we have defined $n^* \equiv k^*/k_o$. At the second plasma-surround interface, $z = b+d$, we can similarly write

$$E_2 e^{ik^*(b+d)} + E_4 e^{-ik^*(b+d)} = E_5 [e^{ik_o(b+d)} - \beta e^{i2k_o c} e^{-ik_o(b+d)}] \qquad \text{(U-8)}$$

and

$$n^* E_2 e^{ik^*(b+d)} - n^* E_4 e^{-ik^*(b+d)} = E_5 [e^{ik_o(b+d)} + \beta e^{i2k_o c} e^{-ik_o(b+d)}] . \qquad \text{(U-9)}$$

It should be recognized that for physical situations of current interest the plasma thickness (d) is typically restricted to an integral number of free space wavelengths. This is done to facilitate the interpretation of the microwave data. Therefore, we let

$$d = m\lambda_o \quad \text{or} \quad d = \frac{2\pi m}{k_o} \quad \text{where } m = 1, 2, 3, \ldots . \qquad \text{(U-10)}$$

Consequently,

$$e^{\pm ik_o d} = e^{\pm i2\pi m} = +1 .$$

Since the quantities b and c are essentially arbitrary, we can, in keeping with the symmetrical* placement of the stubs in the microwave circuit used in this experiment, specify that

$$c = d + 2b . \qquad \text{(U-11)}$$

Rewriting equations (U-8) and (U-9) using (U-10) and (U-11), we have

$$E_2 e^{ik^*(b+d)} + E_4 e^{-ik^*(b+d)} = E_5 [1 - \beta e^{ik_o 2b}] e^{ik_o b} \qquad \text{(U-12)}$$

and

$$n^* E_2 e^{ik^*(b+d)} - n^* E_4 e^{-ik^*(b+d)} = E_5 [1 + \beta e^{ik_o 2b}] e^{ik_o b} . \qquad \text{(U-13)}$$

* Symmetrical with respect to the centerline of the plasma slab.

Eliminating E_5 from (U-12) and (U-13), we can relate E_2 to E_4:

$$E_2 = -E_4 e^{-2k^*(b+d)} \frac{[(1+n^*)+\beta e^{i2k_o b}(1-n^*)]}{[(1-n^*)+\beta e^{i2k_o b}(1+n^*)]} \quad . \tag{U-14}$$

Substituting equation (U-14) into equations (U-6) and (U-7) permits us to express E_3 in terms of the constant incident signal strength E_0:

$$E_3 = \frac{\sqrt{1-\alpha^2}\, e^{2ik_o b}(A+n^*B)}{(A-n^*B)} \tag{U-15}$$

where

$$A \equiv [(1-n^*)+\beta e^{i2k_o b}(1+n^*)]-e^{-i2k^*d}[(1+n^*)+\beta e^{i2k_o b}(1-n^*)], \tag{U-16}$$

$$B \equiv [(1-n^*)+\beta e^{i2k_o b}(1+n^*)]+e^{-i2k^*d}[(1+n^*)+\beta e^{i2k_o b}(1-n^*)]. \tag{U-17}$$

Finally, we can express the composite reflected signal (normalized to the incident signal) and evaluated for convenience at $z = 0$ as

$$\frac{\tilde{E}_3+\tilde{E}_7}{\tilde{E}_0} = \frac{\sqrt{1-\alpha^2}\, e^{2ik_o b}(A+n^*B)-\alpha(A-n^*B)}{(A-n^*B)} \quad . \tag{U-18}$$

In the absence of plasma, i.e., $k^* = k_o$ or $n^* = 1$, the composite reflected signal, as represented by equation (U-18), has to be zero. Setting $n^* = 1$, we can write

$$\left.\frac{\tilde{E}_3+\tilde{E}_7}{E_0}\right|_{n^*=1} = \sqrt{1-\alpha^2}\,\beta e^{i4k_o b}+\alpha = 0 \quad . \tag{U-19}$$

Having specified that the reflectivities α, β are positive real quantities, we conclude that

$$e^{i4k_o b} = -1 \, ,$$

or

$$b = \frac{(2s+1)\lambda_o}{8} \qquad \text{where } s = 0, \pm 1, \pm 2, \ldots \tag{U-20}$$

and

$$\beta = \alpha/\sqrt{1-\alpha^2} \quad . \tag{U-21}$$

The separation distance between the stubs is then, in terms of free space wavelength, $2b+d = \left(\frac{2s+1}{4} + 2m\right)\lambda_o$. The wave that is reflected from the receiver crystal mount stub and travels back to the first (stub-tuner) stub, traverses a distance of $2(2b+d) = \left(\frac{2s+1}{2} + 2m\right)\lambda_o$. In other words, its phase is shifted exactly 180^o with respect to the wave reflected at the first stub. Since each wave, upon reflection by the highly conductive stub, undergoes a phase shift of 180^o, there is no net effect due to this reflection process.

For complete reflection at the receiver stub, i.e., $\beta = 1$, the maximum corresponding value of α is $1/\sqrt{2}$; therefore,

$$\begin{aligned} 0 \le \beta \le 1 \ , \\ 0 \le \alpha \le 1/\sqrt{2} \ . \end{aligned} \tag{U-22}$$

There is a slight ambiguity in the application of condition (U-20), i.e., $e^{i2k_o b} = \pm i \cdot \begin{cases} +, & s \text{ even} \\ -, & s \text{ odd} \end{cases}$. Since the final result should be invariant as to whether s is odd or even, we shall use $e^{i2k_o b} = +i$, that is, s even.

We can now rewrite (U-16), (U-17), and (U-18) in terms of these parameters:

$$\frac{\tilde{E}_3+\tilde{E}_7}{\tilde{E}_0} = \frac{i\sqrt{1-\alpha^2}\,(A+n^*B)-\alpha(A-n^*B)}{(A-n^*B)} \tag{U-23}$$

where now

$$A \equiv \left[(1-n^*)-(1+n^*)e^{-i4\pi mn^*}\right] + \frac{i\alpha}{\sqrt{1-\alpha^2}}\left[(1+n^*)-(1-n^*)e^{-i4\pi mn^*}\right] \tag{U-24}$$

and

$$B \equiv \left[(1-n^*)+(1+n^*)e^{-i4\pi mn^*}\right] + \frac{i\alpha}{\sqrt{1-\alpha^2}}\left[(1+n^*)+(1-n^*)e^{-i4\pi mn^*}\right] . \tag{U-25}$$

In the limit $\alpha \to 0$, i.e., no mismatch, equation (U-23) reduces* to equation (N- 8), Appendix N, the expression for the reflected signal from a plane slab of plasma, etc., as indeed it should.

As mentioned, the bump signal actually observed is proportional to $(\tilde{E}_3+\tilde{E}_7)(\tilde{E}_3+\tilde{E}_7)^\dagger$. In practice, the extrema of this signal are used as data points. These maxima and minima of the signal are relatively easy to discern and to correlate with the time base. Therefore, one would ideally like to have an analytic expression for the derivative

$$\left.\frac{\partial\left\{\left(\frac{\tilde{E}_3+\tilde{E}_7}{\tilde{E}_0}\right)\left(\frac{\tilde{E}_3+\tilde{E}_7}{\tilde{E}_0}\right)^\dagger\right\}}{\partial N_e}\right|_{\nu_c/\omega} = 0$$

and thereby be able to correlate the various maxima and minima with electron density (N_e) for various values of ν_c/ω . Because of the involved nature of n* (cf. equation (N- 4), Appendix N), the evaluation of the derivative was not pursued but rather the values of N_e corresponding to the first two maximums and the first two minimums were numerically determined for values of ν_c/ω between 0 and 0.4 . The same physical parameters characterizing the plasma slab and the

---

* To within an arbitrary phase factor which is of no consequence.

microwave, as previously used, that is, $m = 4$, $\omega = 2\pi \times 24 \times 10^9$, ... , were employed. The results of these computations* are shown graphically in Figure 23.

We commented earlier that the bump points were relatively weak functions of the parameter ν_c/ω. As shown in the figure, this is particularly true for values of ν_c/ω less than ~ 0.15, which happily coincides with values encountered when shock heating most gases of interest.

---

* Mr. Gary Clinard carried out these tedious calculations.

APPENDIX V

PROCEDURE USED TO DETERMINE ν_c/ω FOR EACH RUN

As a first step in the reduction of the data taken during any one run, $8\frac{1}{2}$"x11" photographic enlargements are made of the Polaroid 46-L transparencies used to record the outputs of the "raster" and "microwave" oscilloscopes. A reproduction of one set of such enlargements is shown in Figures 9 and 19. In order to reduce the microwave data to a form suitable for use with the IBM 7090 computer program described above, it is necessary to "digitize" the transmitted signal, i.e., reduce the continuous trace of the record to a table of discrete values of ${}_oS_T$.

The shock front, as evidenced by the leading edge of the light spike on the photomultiplier traces, is taken as the origin of the time (τ) base*. Errors associated with the establishment of the position of the shock front are unimportant insofar as the determination of ν_c/ω is concerned, as both the transmitted and reflected microwave signals use the same time reference. Were the shock position to be incorrectly chosen, it would have the effect of displacing the initial, linear (atom-atom regime) portion of the N_e versus τ (or t_p) curve so that it would fail to pass through the origin. This is simply correctable and in no way affects the accuracy of the data.

Once the time base is established, it is necessary to determine the zero level of the transmitted signal. For the particular run depicted in Figure 19, the transmitted signal becomes saturated (0 per cent transmission) well before the occurrence of the cold front,

* Refer to the discussion of the "light spike" in Appendix F.

the zero level of the signal thereby being directly established. For those data where, because of weak interaction, the transmitted signal does not saturate prior to the occurrence of the cold front, the crystal calibration data is used to establish this datum*. As no use (outside of the interference bumps) is made of the reflected signal, it is not necessary to determine the saturated (100 per cent) amplitude of this trace**.

Lines parallel to the zero (and 100 per cent) transmitted signal level, spaced at convenient intervals (usually 5 per cent) of the total signal level, are overlayed on the enlargement. The horizontal distance of the points of intersection of these lines with the signal trace from the estimated shock-front position is then measured with dividers and referred to the closest (of the two) horizontal time-base graticules. Using a linear interpolation, the time (τ) corresponding to a particular value of ${}_{o}S_{T}$ can then be determined to within $\pm$ 1 μsec. This procedure reduces to a minimum the effects of scale distortion introduced by the film and the enlargement process.

From the reduction of the raster data, the Mach number is de-

* In all instances where the transmitted signal has "cut off," the amplitude as determined from the enlargement has agreed to within 2 per cent of the value derived from the post-run crystal calibration.

** This is easily done, however, by inserting a metallic reflector into the wave guide and correlating the signal which is reflected to that which would be reflected by a fully saturated (${}_{o}S_{R} \sim 100$ per cent) plasma. It has been determined that the completely cut-off plasma (100 per cent ${}_{o}S_{R}$) reflects ~ 65 per cent of the energy reflected by an aluminum plate covering the wave guide at the transmitting horn flange. To within experimental error, the same result is attained if a metal bar having the same cross section as the shock tube and a few wavelengths in extent is inserted into the test section.

termined. The ratio of t_p/τ is calculated (see Appendix W) and the data put in the form of a table of ${}_oS_T$ versus t_p, suitable for machine reduction. The output of the computer program is shown in Figure 21.

The same procedure as outlined for the determination of ${}_oS_T$ as a function of t_p is followed in the reduction of the interference "bump" data. Using an assumed value of ν_c/ω and Figure 23, a short table of N_e versus t_p is constructed for these data.

Figure 22 is a plot on log-log paper of both the transmitted microwave data reduced for various values of ν_c/ω and the interference bump data. A value of $\nu_c/\omega = 0.08$ apparently gives the closest fit to the "bump" points, the estimated uncertainty in this quantity, $\Delta(\nu_c/\omega)$, being $\pm$ 0.01. The use of log-log paper for the presentation was dictated by a desire to accurately represent the full range of variation of N_e and t_p on one graph and the fact that(in the absence of shock attenuation) the data points corresponding to the atom-atom ionization regime ($N_e \propto t_p$) should lie on a straight line of slope 1. As can be seen, the data do indeed exhibit this characteristic, the electron-atom ionization phase for the run in question becoming dominant for $N_e \sim 10^{12}$ cm^{-3}.

The effective collision frequency ν_c can be interpreted in terms of a cross section Q_t, representing the total elastic momentum exchange of the electron with the neutral specie*, i.e., we write

---

* The effect of ions is neglected, as their calculated contribution to this collision frequency is approximately two orders of magnitude smaller than the observed value, cf. Chapter V.

as an approximation to the interpretation of ν_c presented in Appendix N,

$$\nu_c = N \bar{v}_e Q_t \ .$$

Since the neutral particle density and the atom temperature (T_a) and presumably* the mean electron velocity $\bar{v}_e$ are virtually constant throughout the portion of the plasma being investigated, the use of a constant value of ν_c here is entirely justified.

Appropriate values of ν_c/ω and therefore Q_t are determined for all runs of a given gas mixture wherein "bump" signals are present. These data are then plotted as a function of $\beta^{-\frac{1}{2}} = (kT_a)^{\frac{1}{2}}$ (which is proportional to $\bar{v}_e$ under the assumption of $T_e = T_a$), cf. Figs. 32 to 36 and Chapter V. A line representing the most probable behavior of Q_t versus $\beta^{-\frac{1}{2}}$ is drawn through the data points. This serves to reduce some of the uncertainty associated with the determination of Q_t, as witnessed by the relatively large error brackets accompanying the data, and permits reasonable estimates of Q_t to be made for those lower Mach-number runs where "bump" points were not in evidence. Again applying the equation for Q_t and using the inferred relation between Q_t and $\beta^{-\frac{1}{2}}$ as a guide, the appropriate value of ν_c/ω for each run of the series is calculated.

Once the above has been accomplished, it is possible to pursue the final goal of this analysis, the determination of the initial, atom-atom ionization rates as a function of temperature, cf. Appendix X.

---

* We are here assuming that the electron temperature equals the atom temperature.

APPENDIX W

DISCUSSION OF THE SHOCK ATTENUATION CORRECTION FACTOR

N_e Versus t_p -- Corrected for Shock Attenuation

For any given test gas, once the empirical relationship between Q_T and $\beta^{-\frac{1}{2}}$ has been established, one can proceed directly to the construction of N_e versus t_p plots (on linear graph paper) for the individual runs comprising the test series.

For many tests there occurred a pronounced monotonic increase in the N_e versus t_p trace, no portion of the curve exhibiting the linear time dependence demanded by the atom-atom ionization process of Chapter II. The cause of this anomaly, shock attenuation, was first correctly explained by Jahn[14]. Therefore, before one can proceed with the determination of an initial electron generation rate, it is necessary to develop a correction factor which will adequately compensate for this effect.

Shock Attenuation Correction

As shown in Chapter III, the atom-atom ionization rate is exponentially dependent upon the temperature at which the process is occurring, that is, $\dot{N}_e \sim e^{-E_*/kT}$. The larger the ratio of the "activation" energy of the process, E_*, is in comparison to the energy at which the reaction is occurring, kT, the more pronounced the effect of variations in the reaction temperature will be upon the reaction rate. For a given relative variation in temperature, $\Delta T/T$, where $\Delta T/T \ll 1$, the variation of the relative reaction rate, $\Delta\dot{N}_e/\dot{N}_e$ can be approximately represented as:

$$\frac{\Delta \dot{N}_e}{\dot{N}_e} \sim e^{\frac{E_*}{kT}\frac{\Delta T}{T}} - 1 \ .$$

For the gases and the temperatures attained in the shock tube used in these studies, $E_* \sim 10$ ev , $kT \sim 2/3$, and $E_*/kT \sim 15$. Consequently, if $\Delta T/T \sim 0.01$, then $\Delta \dot{N}_e/\dot{N}_e \sim 0.16$. The temperature of a mass of shock-heated gas is, in the strong shock limit, approximately proportional to the square of the Mach number. Therefore, it is quite obvious that for even modest variation in the Mach number of a shock wave traversing a body of gas, relatively large variations in the reaction (i.e., ionization rate) could be anticipated. Consequently, it is necessary to consider, in detail, the effect of variations in Mach number, that is, shock attenuation effects, upon the observed ionization rate.

The familiar "y-τ" diagram for an attenuating shock wave is shown below.

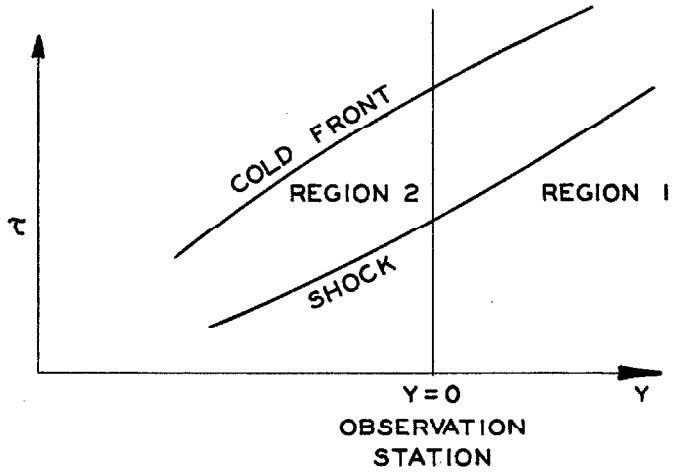

It is easily seen that for an attenuating shock, the temperature of the gas immediately behind the front, as viewed at the observation station (at laboratory time $\tau = 0$) will be lower than that of the gas

viewed at succeeding instances ($\tau > 0$). These latter portions of the gas flow have been passed over further upstream (in the shock tube), and because of attenuation effects the Mach number and therefore the temperature were higher. We have neglected, and shall continue to neglect, the effect of heat transfer to the walls of the tube and longitudinally within the body of gas.

Referring to Chapter III, the electron generation rate for single specie atom-atom ionization is written as

$$\dot{N}_e = N^2 C \sqrt{\frac{2}{\pi\mu}} \left(\frac{1}{\beta}\right)^{3/2} (2+\beta E_*) e^{-\beta E_*}$$

where the symbols have the same connotation as previously defined. Considering an incremental volume of gas at a time t_p (particle coordinates), after the passage of the shock, and which initially ($t_p = 0$) possessed an electron density $N_e(0)$*, we can write

$$N_e(t_p) - N_e(0) = \left[N^2 C \sqrt{\frac{2}{\pi\mu}} \left(\frac{1}{\beta}\right)^{3/2} (2+\beta E_*) e^{-\beta E_*}\right] t_p \ .$$

It has been implicitly assumed, in the derivation of this equation, that not only is there no heat transfer but that there is no flow of electrons due to the electron concentration gradient into or out of the gas volume being considered. Further, no attempt has been made to take into account the slight variation in neutral particle density N that would occur due to Mach number variation along the volume of shocked gas.

The shock velocity U_s is assumed to exhibit the following linear dependence on distance (y) as measured from the observation sta-

* This factor is included for completeness. An initial electron-density level could be due to photoionization at the shock front or electron diffusion ahead of the shock. In all the work that follows, $N_e(0)$ is considered negligibly small in comparison with $N_e(t_p)$ for the values of t_p used.

tion (y = 0):

$$U_s = U_o(1+\alpha y)$$

where U_o = shock velocity at the observation station; and α = attenuation coefficient, M^{-1} ($\alpha > 0 \Rightarrow$ acceleration; $\alpha < 0 \Rightarrow$ attenuation).

The assumption of a linear velocity profile is consistent with the manner in which the shock attenuation was experimentally determined (see Appendix H), the application of a more sophisticated profile being unwarranted. Precautions were taken to ensure that those portions of the unshocked gas in which the ionization process would be observed were at a uniform temperature*. Consequently, the acoustic velocity (a_o) is a constant, and

$$M_s = M_o(1+\alpha y), \text{ where } \quad M_o = U_o/a_o \ . \qquad (W-1)$$

It is now necessary to relate the position y at which a given volume of gas was initially heated by the shock wave to the time, t_p, associated with its passage to the observation station. The ideal shock relationships will be assumed to be valid and adequately precise representation of the behavior of the shock wave. Furthermore, since we have restricted our experimental program to the study of the noble gases and their mixtures, in all that follows it will be understood that the ratio of specific heats γ will be equal to 5/3. Since the ionization level in those regions of the gas of interest did not exceed 10^{-4}, using this value for γ is completely justified. From the ideal shock relations[54], the bulk gas velocity behind the shock front and before the

* The initial unshocked gas temperature (T_1) was uniform to within 3°C along the portion of the shock tube where the observed ionization process was initiated, i.e., over a distance extending ~ 3 meters upstream of the observation station.

cold front, U_2, is

$$U_2 = \frac{3}{4}\left(\frac{M_s^2-1}{M_s}\right) a_o \qquad \text{(W-2)}$$

and the time of flight of the heated gas between the station -y and the observation station y = 0 is

$$\int_{-y}^{0} \frac{dy}{U_2(y)} \quad t_p \ .$$

Substituting the equation relating U_2 to M_s, and using the assumed expression relating M_s to M_o, it is straightforward to demonstrate that

$$y \simeq -\frac{3}{4} t_p U_o \left(\frac{M_o^2-3}{M_o^2}\right)\left[1-\alpha U_o t_p \left(\frac{M_o^2+3}{M_o^2}\right)\right] \qquad \text{(W-3)}$$

where terms of order $\alpha^2 U_o^2 t_p^2$ * or smaller have been neglected in comparison to unity. Once again applying the ideal shock relations, the functional dependence of particle time t_p on laboratory time τ is, to the same level of approximation as applied above, written as:

$$t_p = \left(\frac{4M_o^2}{M_o^2+3}\right)\tau \ .$$

For an ideal shock in a monatomic gas of low ionization level, the ratio of the temperature behind the shock front T_2 to that of the quiescent gas into which the front is propagating T_1, is

$$\frac{T_2}{T_1} = \frac{5}{16}\frac{(M_s^2-0.2)(M_s^2+3.0)}{M_s^2}$$

---

* For cases of interest, $\alpha \sim 0.02$, $U_o \leq 3000$, $t_p \leq 2\times10^{-3}$, $\alpha U_o t_p \leq 0.1$, and $(\alpha U_o t_p)^2 \sim 0.01$.

which can now be written as

$$\frac{T_2}{T_1} \simeq \frac{5}{16}\left[M_o^2 - \frac{3}{2}\alpha U_o t_p M_o^2 + 2.8 - \frac{0.6(1+\frac{3}{2}\alpha U_o t_p)}{M_o^2} + \sigma(\alpha U_o t_p)^2\right] . \tag{W-4}$$

Recognizing that, for $M_o \geq 7$, which is consistent with the operational regime in which all experiments were conducted $\frac{\alpha U_o t_p}{M_o^2} \ll \alpha U_o t_p M_o^2$, and is of order $(\alpha U_o t_p)^2$, we write

$$T_2 = \frac{5}{16} T_1\left[M_o^2 - \frac{0.6}{M_o^2} + 2.8 - \frac{3}{2}\alpha U_o t_p M_o^2\right] .$$

We wish ultimately to normalize all data (i.e., N_e as a function of τ, t_p) so that the effects of shock attenuation are removed, permitting the "true" electron generation rates of the shocked gases to be observed. This is accomplished by referring all conditions to those prevailing immediately behind the shock front as it passes through the observation station, i.e., at $\tau = t_p = 0$. As the increase in gas temperature with time (at the observation plane) due to shock attenuation will be accompanied by an increase in electron density, as previously described, we in essence normalize to the temperature existing at $\tau = 0$, $M_s = M_o$. To this end, we define the correction factor a as follows:

$$\frac{N_e(T_2(o)) - {}_oN_e}{N_e(T_2(t_p)) - {}_oN_e} = a(t_p) \text{ , where } a \leq 1 \text{ for } \alpha \leq 0 .$$

Multiplication of the observed electron density at time τ (or t_p) by this factor then effects the normalization to constant temperature, zero shock attenuation conditions.

By use of the previously derived relationships, it is possible, to a level of approximation consistent with these expressions, to cast

$a(t_p)$ into the following form:

$$a = \left[1 + \frac{\frac{3}{4}\alpha U_o t_p M_o^2}{\left(M_o^2 - \frac{0.6}{M_o^2} + 2.8\right)}\right] \exp\left[\frac{4.8E}{kT_1} \frac{\alpha U_o t_p M_o^2}{\left(M_o^2 - \frac{0.6}{M_o^2} + 2.8\right)^2}\right] \quad . \quad \text{(W-5)}$$

For convenience, the dimensionless quantity (non-dimensional particle time)

$$\theta = \frac{E_*}{kT_1} \alpha a_o t_p$$

will be used rather than t_p as the independent parameter. As the second term in the pre-exponential factor is small in comparison to unity (but not so small as to be neglected), it is possible to make a further approximation when converting the expression for a to a function of θ. For the cases of experimental interest, $8 \leq E_a \leq 12$ and $292 \leq T_1 \leq 296^{\circ}K$. Then, for the second term in the pre-exponential factor, it is justified to set $E_* = 10$ ev and $T_1 = 293^{\circ}K$.

The final result is

$$a \simeq \left[1 + 1.8947 \times 10^{-3} \frac{M_o^3 \theta}{M_o^2 - \frac{0.6}{M_o^2} + 2.8}\right] \exp\left[\frac{4.80\ M_o^3 \theta}{\left(M_o^2 - \frac{0.6}{M_o^2} + 2.8\right)^2}\right]. \quad \text{(W-6)}$$

In Figure 24 we see a graphical representation of this expression, where a is plotted, for various values of the initial ($t_p = \tau = 0$) Mach number M_o, as a function of the dimensionless particle time θ.

APPENDIX X

PROCEDURES USED IN THE DETERMINATION OF INITIAL ELECTRON GENERATION RATES

For the test case used as an example (cf. Figure 19), the relatively minor influence of shock attenuation effects, due largely to the low values of t_p involved, makes the determination of the initial slope virtually a trivial matter. For runs where the data have been more clearly influenced by shock attenuation effects, a trial-and-error procedure is applied. Various shock attenuation factors (a) corresponding to assumed values of the shock attenuation parameter ($-\alpha$) are applied to the data. In all instances, the value of α which corrected the data so that the linear dependence of electron density on time was exhibited was less than or equal to, but never greater than, the value of α determined by the shock-position indicator data. It appears that heat transfer and electron diffusion effects, the former being the most probable, are responsible for this consistent disparity between the two values of α.

Upon application of the appropriate shock-correction factor, it was found that the majority of data intersected the abscissa within about 15 μsec (t_p, which corresponds to around 4 μsec in laboratory time τ) of the origin. For the run exhibited, the shock position was assumed to be coincident with the peak of the light spike, the initial linear slope intersecting the origin.

The slight undulatory behavior of the electron density versus particle time trace in the range $80 \leq t_p \leq 200$ μsec exhibited by the test case, i.e., during the initial stages of the electron-atom ioniza-

tion regime, is attributed to the approximate manner in which the field-pattern correction factor compensates for the effects of three-dimensionality of the actual microwave field pattern. Below about 80 μsec and above about 200 μsec, this correction appears to be quite adequate. In the region noted, $0.97 \leq \lambda_o/\lambda_p \leq 0.91$, the radial field pattern exhibits a pronounced minimum (cf. Figure 19). The field-pattern correction factor, as described earlier, was computed on the basis of a value of $\nu_c/\omega = 0.30$, this value being chosen for its ability to eliminate the undulatory behavior of the observed N_e versus t_p data in the vast majority of cases. In a few instances, for high Mach number runs where lateral diffraction effects (see Appendix R) presumably are of importance, as apparently they are in the case under discussion, the depression of the calculated electron-density trace is observed. Because of this, only those data wherein $\lambda_o/\lambda_p \geq 0.97$ are considered for use in the determination of the initial slope.

Because of variations in particle density due to variation of the temperature (from $20^{\circ}C$) of the unshocked gas, initial gas pressures somewhat higher or lower than planned, and the slight change in density ratio as a function of Mach number, all ionization rate data were normalized to particle density of 4.414×10^{17}, 6.957×10^{17}, or 13.256×10^{17} cm^{-3}, depending upon whether the initial nominal pressure was 3 torr, 5 torr, or 10 torr, respectively. This was done by assuming that the quadratic relationship between electron generation rate ($\dot{N}_e$) and neutral particle density (N^2), predicted by theory (Chapter III), was valid. This is justified by the uniformly small magnitude of the correction required: it never exceeds 5 per cent of the

uncorrected* initial ionization rate, and by the fact that the data does indeed exhibit the required quadratic pressure dependence.

The contribution of the electron-atom ionization process to the initial electron-generation rate has been estimated by using the same cross-sectional slope constant employed by Petschek and Byron[1], viz., 7×10^{-18} cm^2/ev. These estimates were made by neglecting the elastic-energy exchange processes postulated by Petschek and Byron, and therefore overestimate the effect of this process. Even so, the influence that the electron-atom ionization process has upon the ionization rates for the times and conditions studied in all instances amounted to less than 5 per cent of the electron density observed.

---

* Uncorrected for particle density variation.

REFERENCES

1. Petschek, H. E., and Byron, S., Ann. Phys. (N. Y.) 1, 270 (1957).

2. Holstein, T., Phys. Rev. 72, 1212 (1947).

3. Weymann, H. D., "On the Mechanism of Thermal Ionization Behind Strong Shock Waves," University of Maryland Technical Note BN-144 (July 1958).

4. Rostagni, A., Nuovo Cimento 11, 621 (1934).

5. Varney, R. N., Phys. Rev. 50, 159 (1936).

6. Sluyters, Th. J. M., DeHass, E., and Kistemaker, J., Physica 25, 1376 (1959).

7. Utterback, N. G., Proc. of Third Inter. Conf. on the Physics of Electronics and Atomic Collisions, North Holland Press (1963).

8. Berry, H. W., Phys. Rev. 127, 1634 (1962).

9. Russek, A., Thomas, M. Tom, Phys. Rev. 109, 2015 (1958).

10. Bond, J. W., Jr., Phys. Rev. 105, 1683 (1957).

11. Johnston, H. W., Kornegay, W., Trans. Faraday Soc. 57, 1563 (1961).

12. Haught, A. F., Princeton University Physics Dept., Technical Report II-30 (February 1962).

13. Jahn, R. G., Phys. Fluids 5, 678 (1962).

14. Harwell, K. E., and Jahn, R. G., Phys. Fluids 7, 214 (1964).

15. Bates, D. R., Massey, H. S. W., and Steward, A. L., Proc. Roy. Soc. London A 216, 437 (1953).

16. Vainshtein, L., Presnyakon, L., and Sobel'man, I., Soviet Physics, JETP, 16, 370 (1963).

17. Russek, A., Phys. Rev. 132, 246 (1963).

18. Rosen, P., Phys. Rev. 109, 348 (1958).

19. Rosen, P., Phys. Rev. 109, 351 (1958).

20. Phelps, A. V., and Molnar, J. P., Phys. Rev. 89, 1202 (1953).

21. Chapman, S., and Cowling, T. G., The Mathematical Theory of Non-Uniform Gases, Cambridge University Press (1960).

22. Kantrowitz, A., "Shock Tubes for High Temperature Gas Kinetics," AVCO Everett Research Laboratories, Research Report No. 141 (October 1962).

23. Dickson, L. D., "Survey of Diagnostic Techniques Used to Determine Temperature and Density in Plasmas," The Johns Hopkins University Rad. Lab., Technical Report No. AF-95 (May 1962).

24. Petschek, H. E., Phys. Rev. 84, 614 (1951).

25. Turner, E. B., "The Production of Very High Temperatures in the Shock Tube with an Application to the Study of Spectral Line Broadening," Engineering Research Institute, The University of Michigan (May 1956).

26. Jahn, R. G., "Interaction of Electromagnetic Waves with Slightly Ionized Gases, I. Uniform Media," Tech. Note No. 2, Daniel and Florence Guggenheim Jet Propulsion Center, California Institute of Technology (August 1960).

27. Jahn, R. G., "Microwave Probing of Ionized Gas Flows," Tech. Note No. 5, Daniel and Florence Guggenheim Jet Propulsion Center, California Institute of Technology (February 1962).

28. Cook, G. A., Ed., Argon, Helium, and the Rare Gases, Vol. 1, Interscience Publishers, New York (1961).

29. Ecker, G., and Kroll, W., "Lowering of the Ionization Energy for a Plasma in Thermodynamic Equilibrium," Phys. Fluids 6, 62 (1963).

30. Spitzer, L., Jr., Physics of Fully Ionized Gases, Interscience Tracts on Physics and Astronomy, No. 3, Interscience Publishers, New York (1956).

31. Heighway, J. E., Nichols, L. D., "Brayton Cycle MHD Power Generation with Non-Equilibrium Conductivity," NASA TN-D-2651 (February 1965).

32. Brown, S. C., Basic Data of Plasma Physics, The Technology Press, John Wiley and Sons, New York (1959).

33. McDaniel, E. W., Collision Phenomena in Ionized Gases, John Wiley and Sons, New York (1964).

34. Geltman, S., Phys. Rev. 102, 171 (1956).

35. Foner, S. H., and Nall, B. H., Phys. Rev. 122, 512 (1961).

36. Mirels, H., Phys. Fluids 6, 1201 (1963).

37. Chabai, A. J., "Measurement of Wall Heat Transfer and of Transition to Turbulence During Hot Gas and Rarefaction Flows in a Shock Tube," Lehigh University, Technical Report No. 12 (September 1958).

38. Jahn, R. G., and Weimer, D., J. Appl. Phys. 29, 741 (1958).

39. Jahn, R. G., and Grosse, F. A., Phys. Fluids 2, 469 (1959).

40. Ginzburg, V. L., Propagation of Electromagnetic Waves in Plasma, Gordon and Breach, Russian Monographs and Texts on Advanced Mathematics and Physics, Vol. VI (1961).

41. Kelly, A. J., Jet Propulsion Laboratory Space Programs Summary 37-24, Vol. IV, pp. 114-121 (September 1, 1963 to November 30, 1963), Propulsion Division, Plasma Diagnostics.

42. Staniforth, A., and Craven, J. H., I. R. E. Trans. Microwave Theory and Techniques, 111 (1960).

43. Primich, R. I., and Northover, F. H., "Use of Focussed Antenna for Ionized Trail Measurements," Defense Research Telecommunications Establishment, Electronics Laboratory, Report No. 1076, Ottawa, Canada (October 1961).

44. Northover, F. H., "The Incidence of Focussed Microwaves Upon Ionized Distributions. Part I. Plane Distributions," General Motors Defense Research Laboratories, Santa Barbara, California, TR 62-209N (December 1962).

45. Harris, F. B., Jr., "Prediction of Radiation Intensities in the Fresnel and Near-Zone Regions of Microwave Aperture Antennas," Rome Air Development Center, ARDC, Report RADC TN-58-252 (October 1958).

46. Soejima, T., "Fresnel Gain of Aperture Antenna," Harvard University Croft Laboratory, Scientific Report No. 13, Series 2 (May 21, 1962).

47. Stratton, J. A., Electromagnetic Theory, McGraw-Hill Book Co., New York (1941).

48. Jacavanco, D. J., "Plasma Produced Antenna Pattern Distortion," Air Force Cambridge Research Laboratories, Physical Sciences Research Papers No. 28 (June 1964).

49. Albini, F. A., and Jahn, R. G., J. Appl. Physics 32, 75 (1961).

50. Jukes, J., "Heat Transfer from Highly Ionized Argon Produced by Shock Waves," Master of Aero. Eng. Thesis, Cornell University (1956).

51. Sommerfeld, A., Optics, Academic Press, New York (1954).

52. Margenau, H., Phys. Rev. 69, 508 (1946).

53. Harwell, K. E., "Initial Ionization Rates in Shock-Heated Argon, Krypton, and Xenon," Ph. D. Thesis, California Institute of Technology (1963).

54. Bradley, J. N., Shock Waves in Chemistry and Physics, John Wiley and Sons, New York (1962).

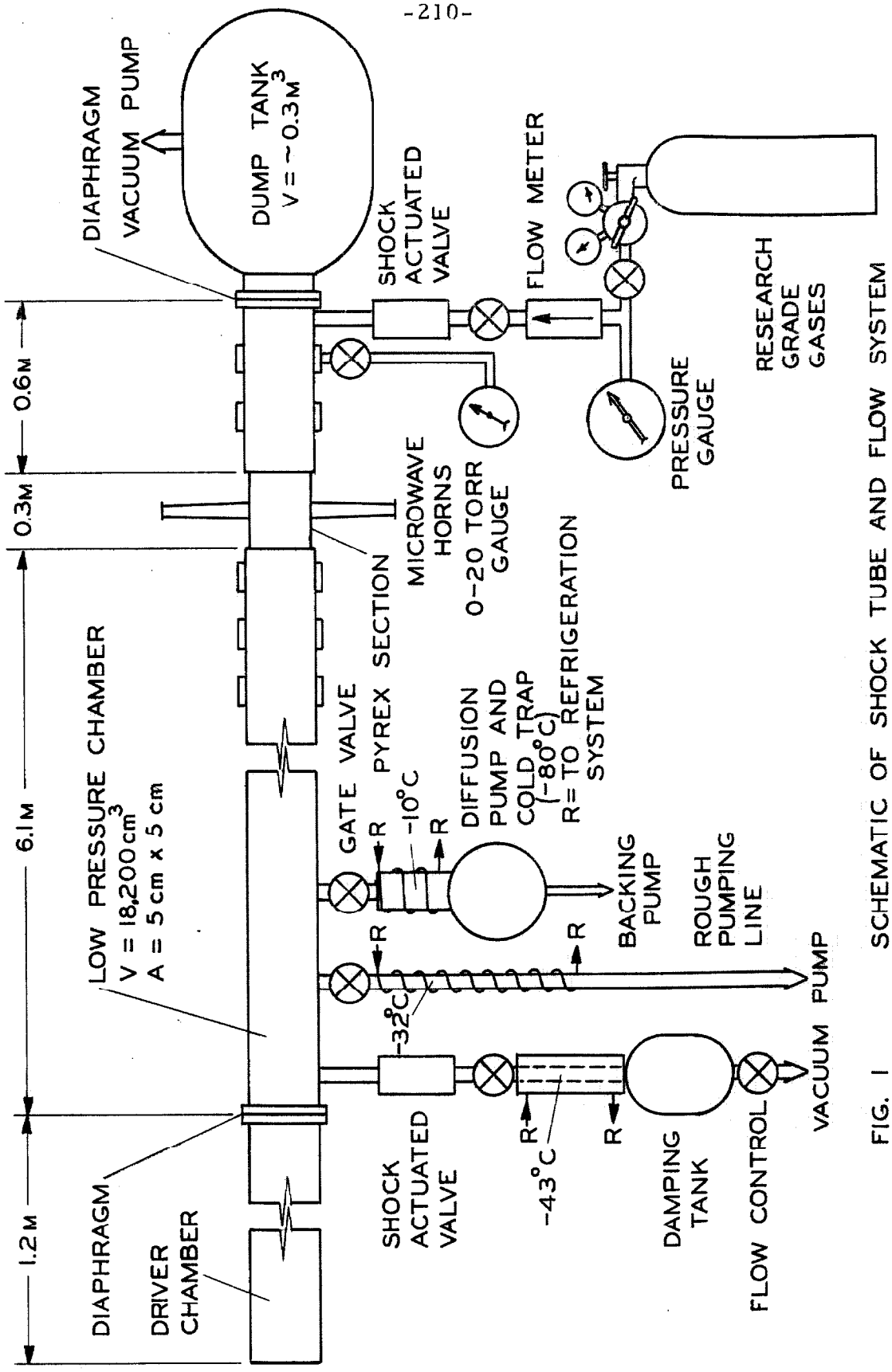

FIG. 1 SCHEMATIC OF SHOCK TUBE AND FLOW SYSTEM

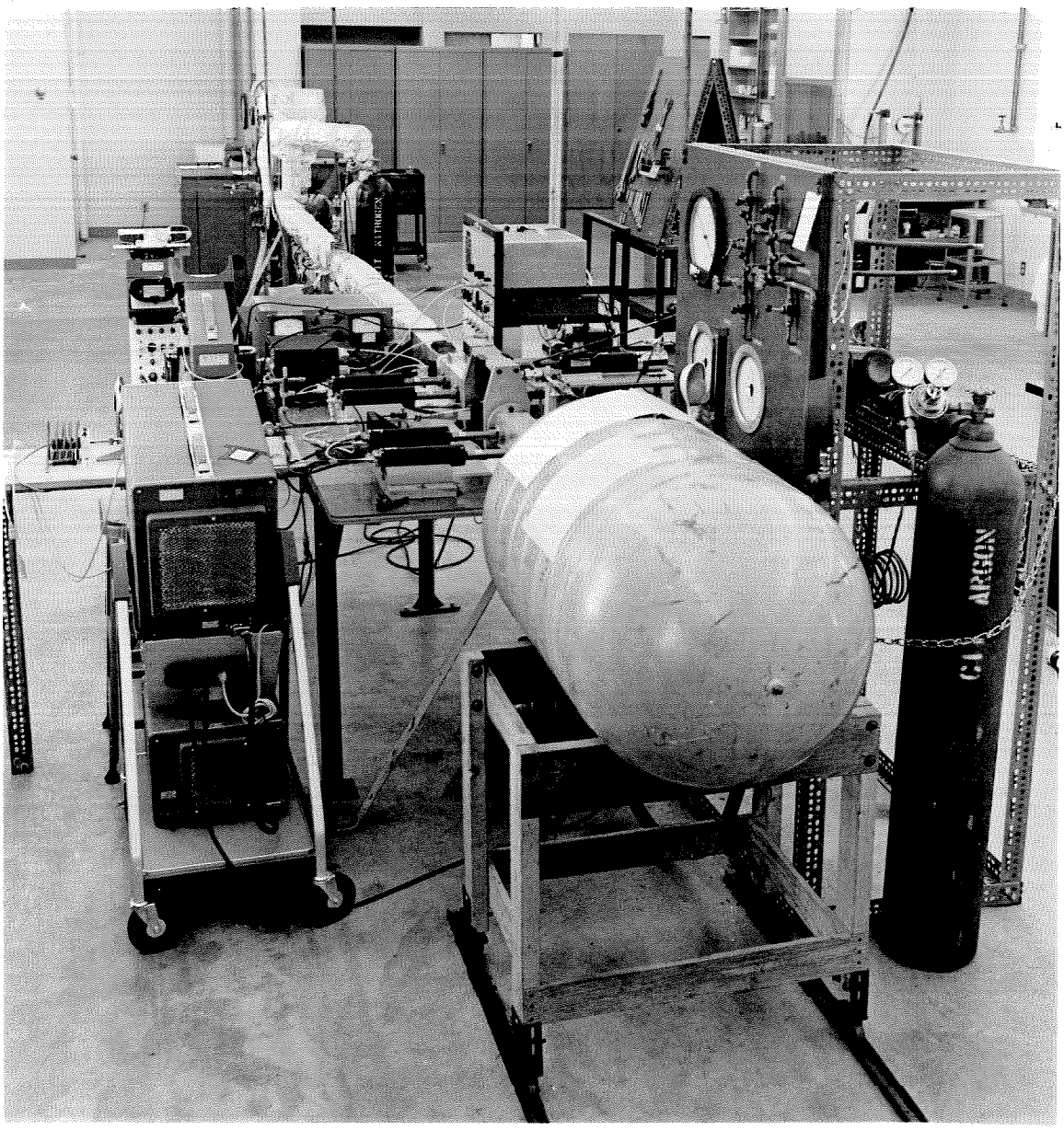

Fig. 2. The Shock Tube Viewed from Dump Tank End

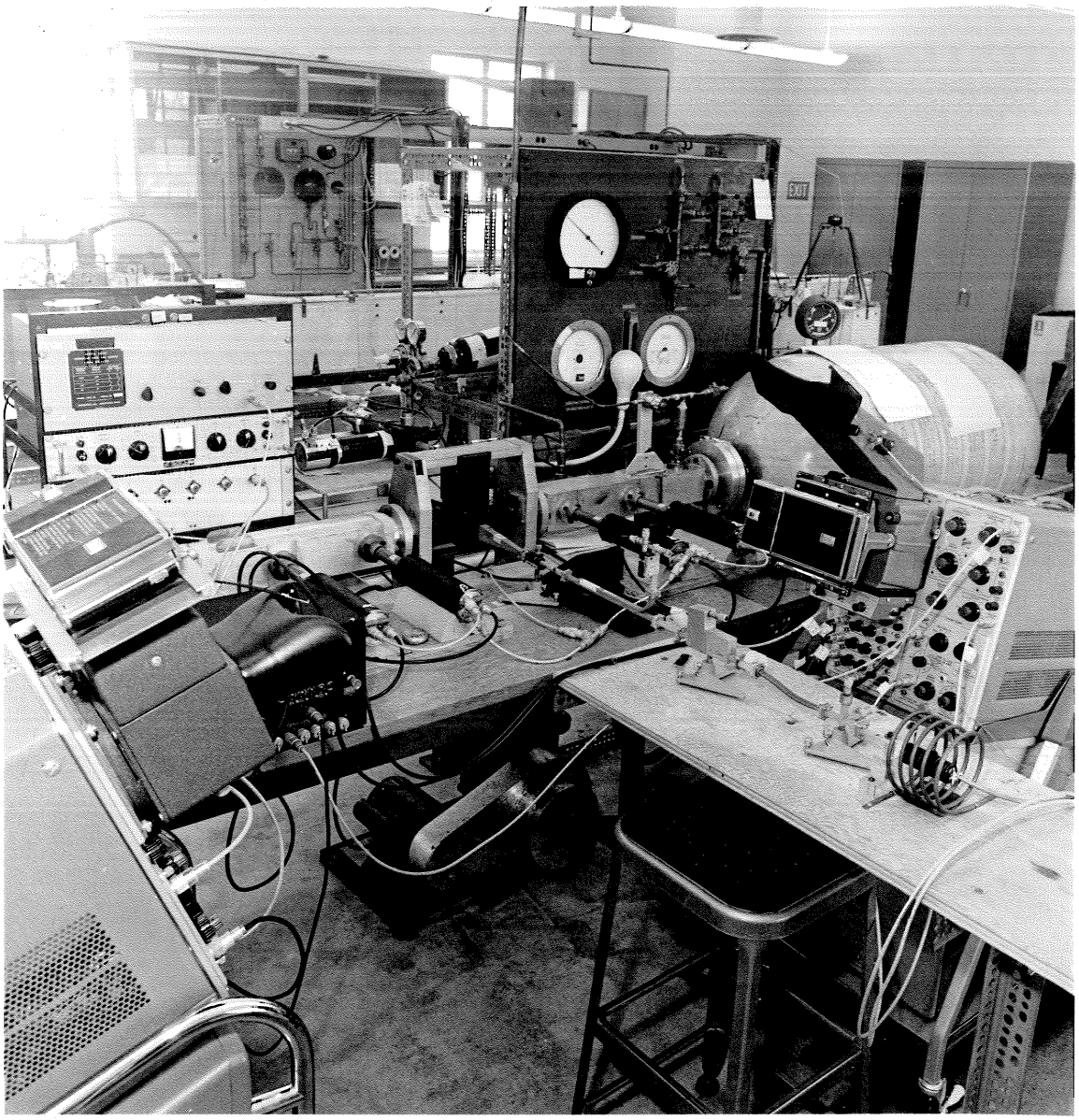

Fig. 3. A View of the Diagnostics Section of the Shock Tube

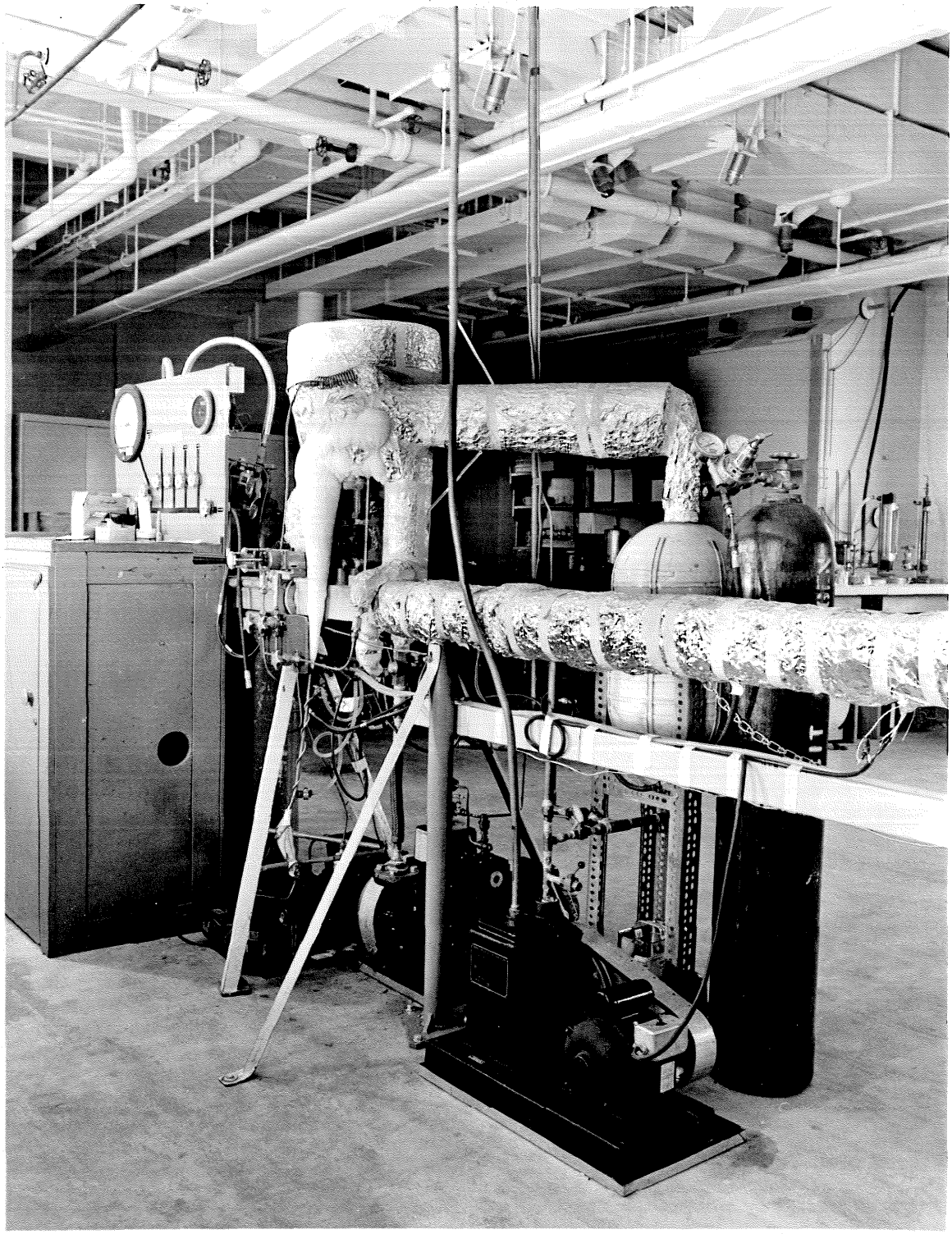

Fig. 4. A View of the Driver Section End of the Shock Tube

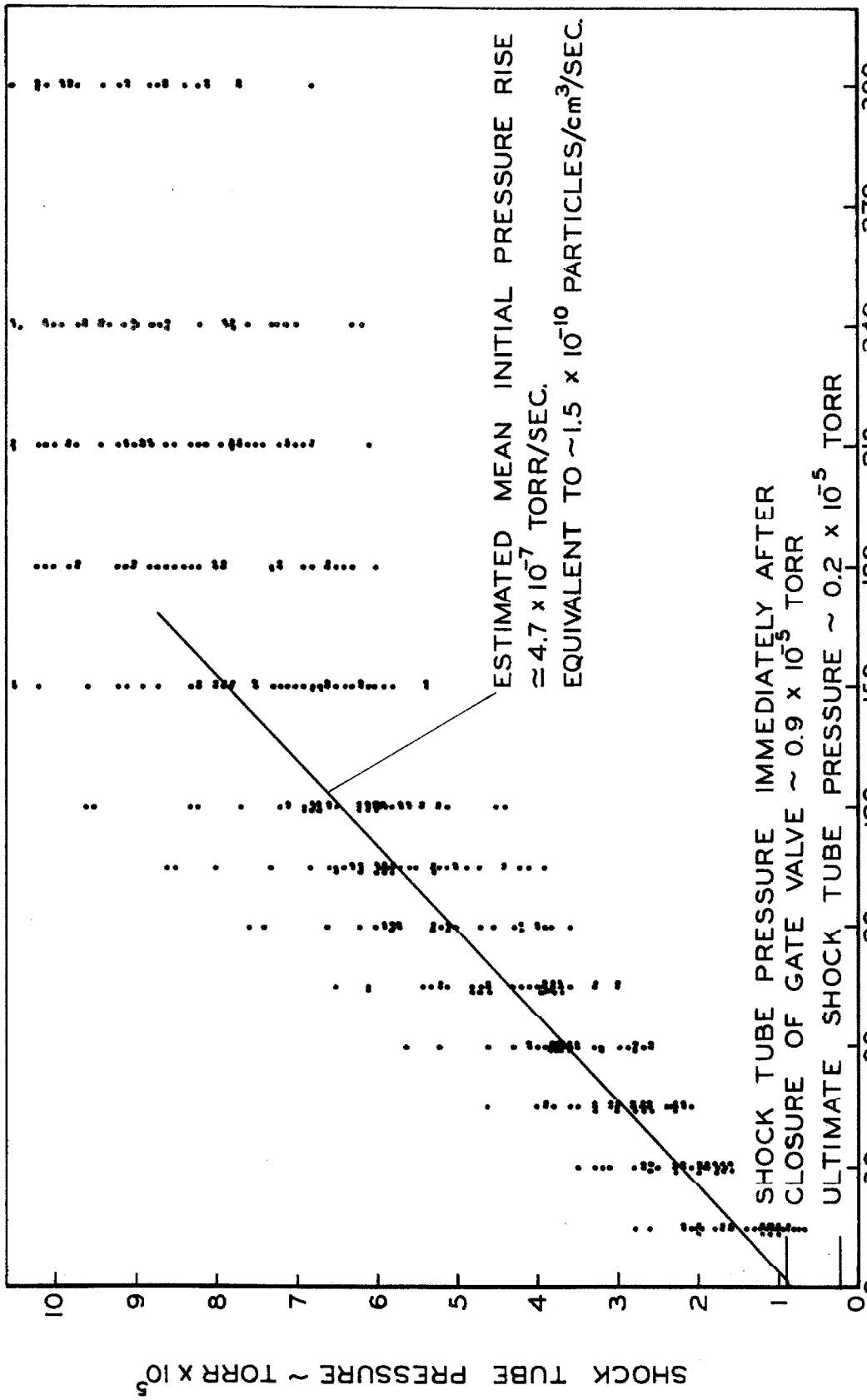

FIG. 5 SHOCK TUBE OUT-GASSING CHARACTERISTICS (COMPOSITE OF 45 RUNS)

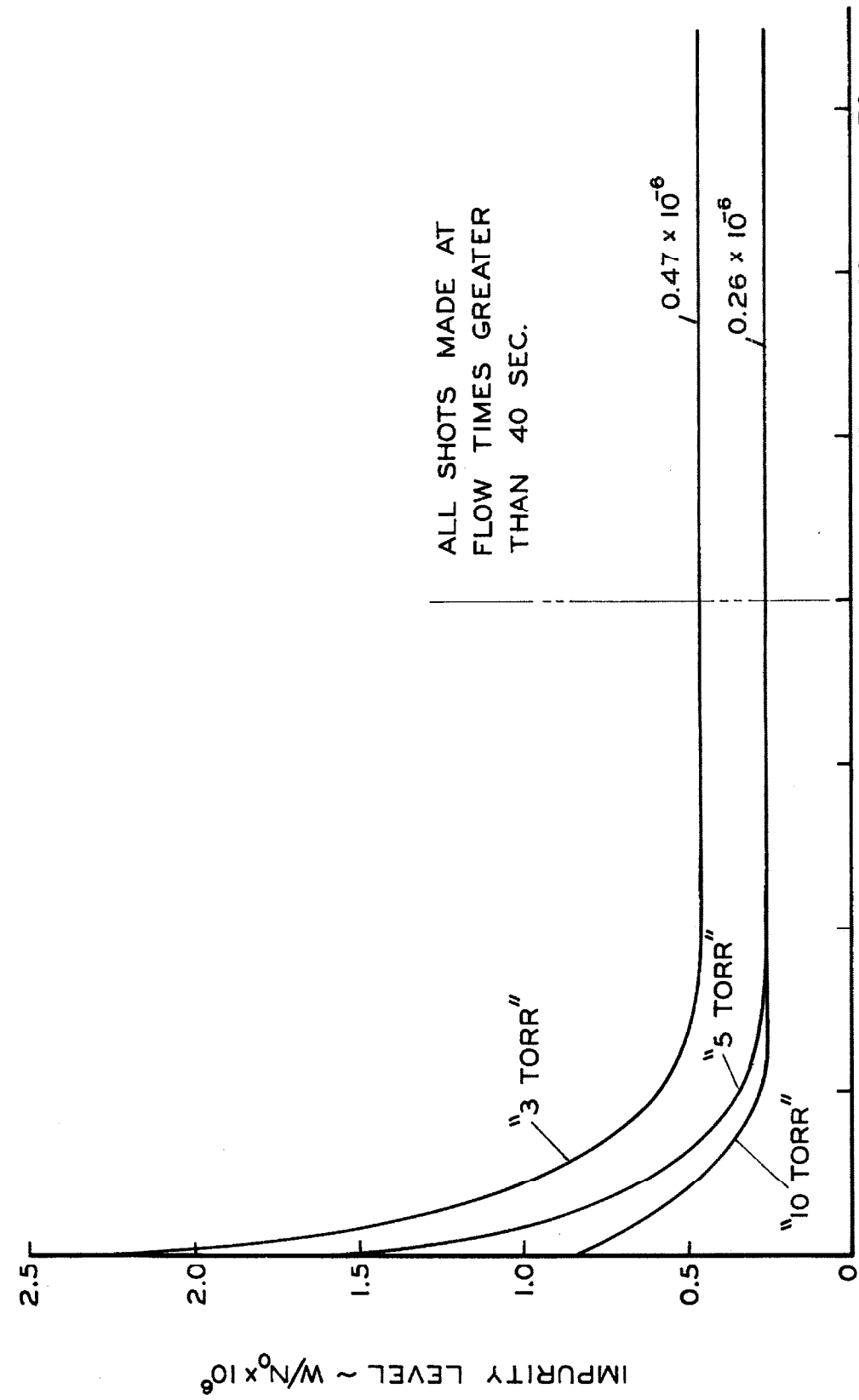

FIG. 6 ESTIMATE OF UNCONTROLLED (OUT-GASSING) IMPURITY LEVEL VS. FLOW TIME

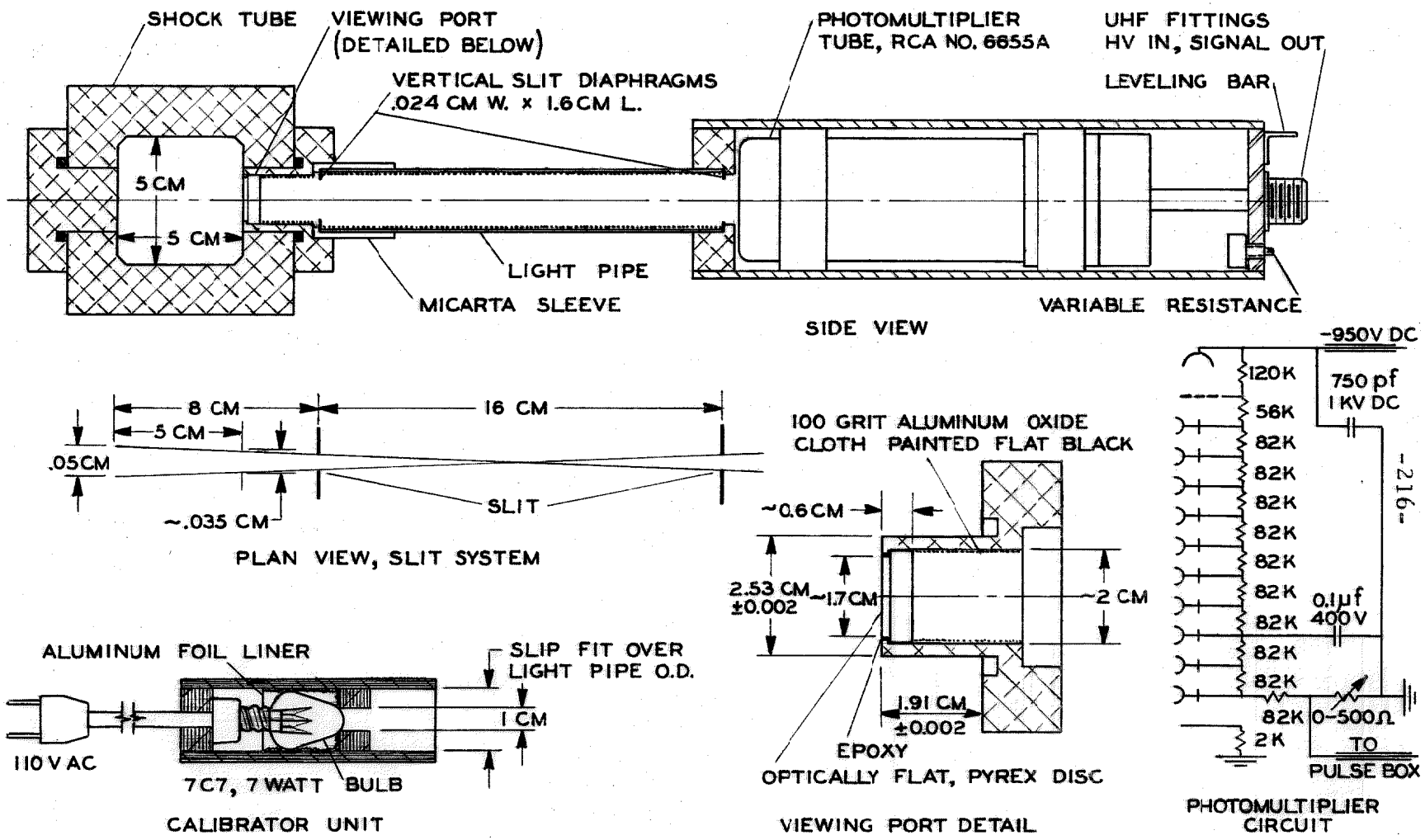

FIG. 7 PHOTOMULTIPLIER SHOCK POSITION INDICATOR SYSTEM

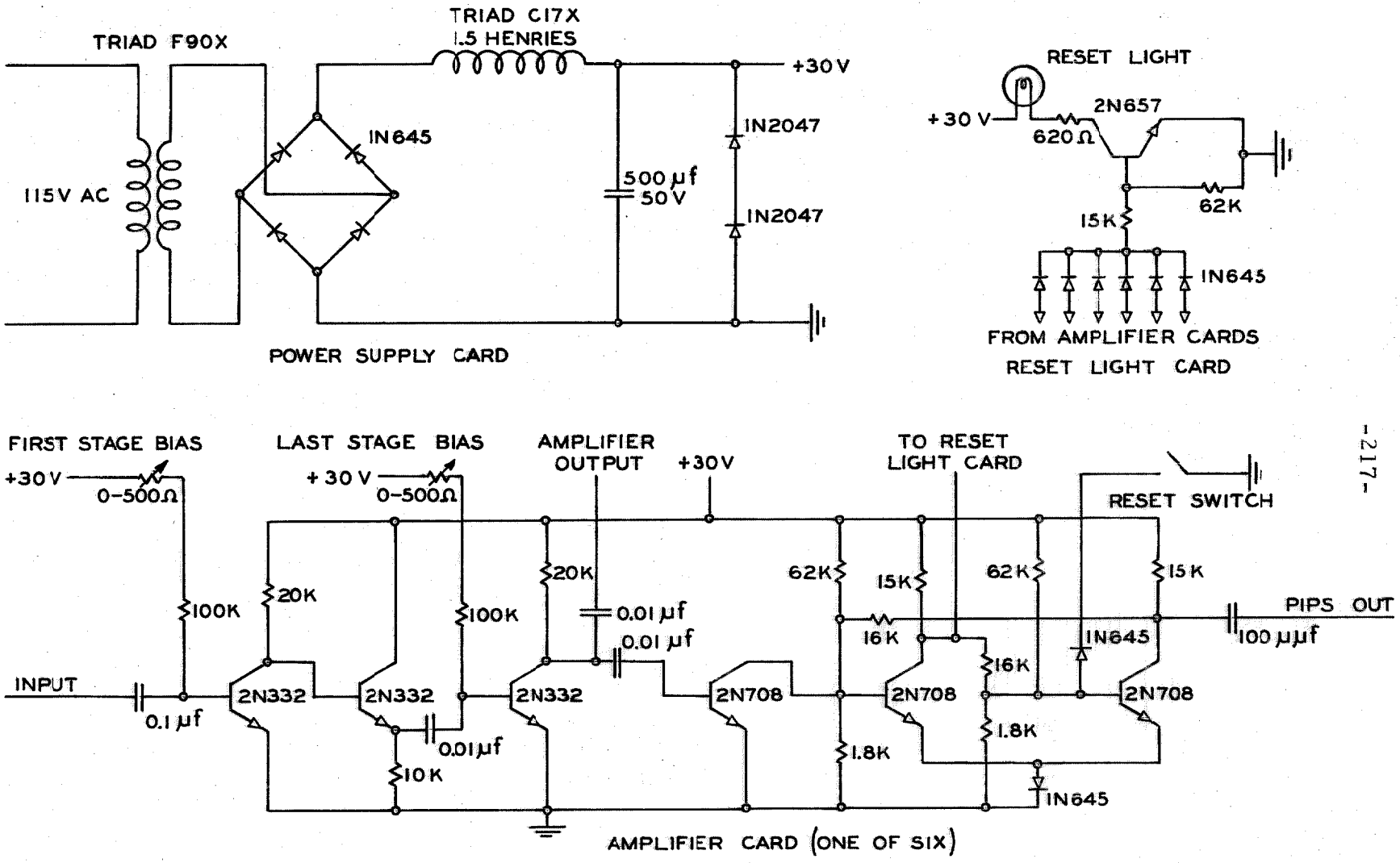

FIG. 8 CIRCUIT DIAGRAM OF AMPLIFIER-DIFFERENTIATOR-FLIP-FLOP UNIT

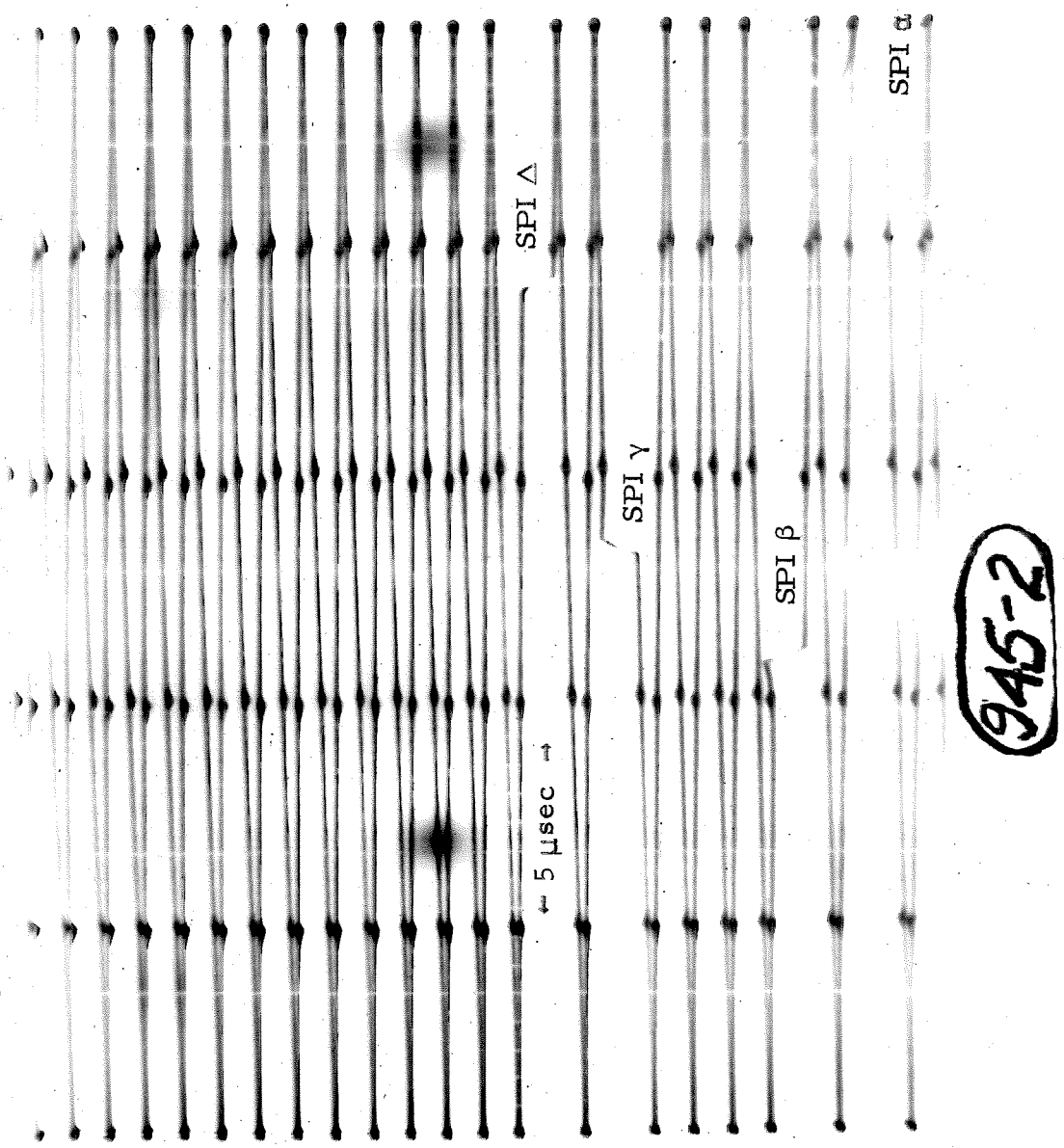

Fig. 9. Photographic Enlargement of a Typical Oscilloscope Raster

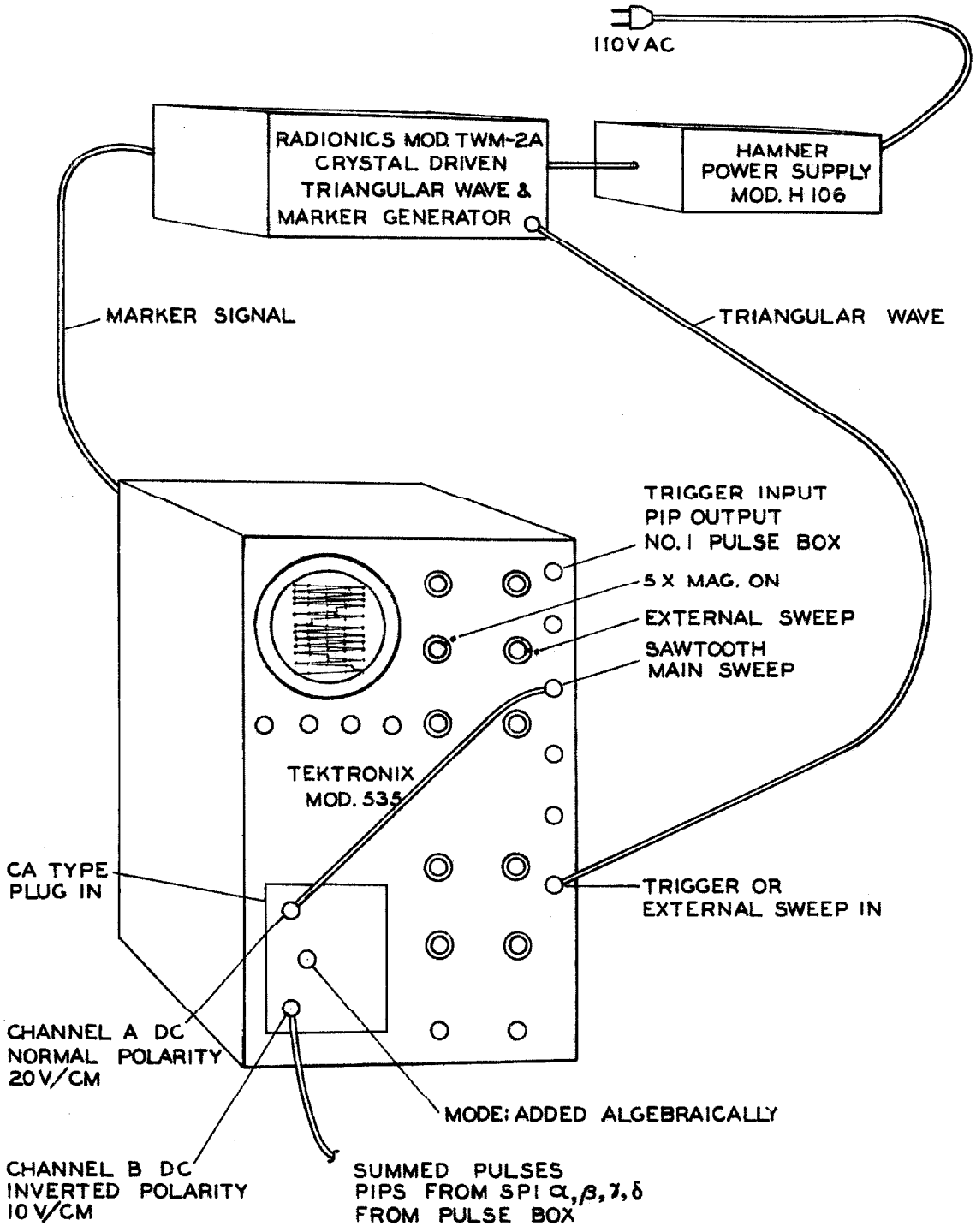

FIG. 10 RASTER ELECTRONICS SYSTEM

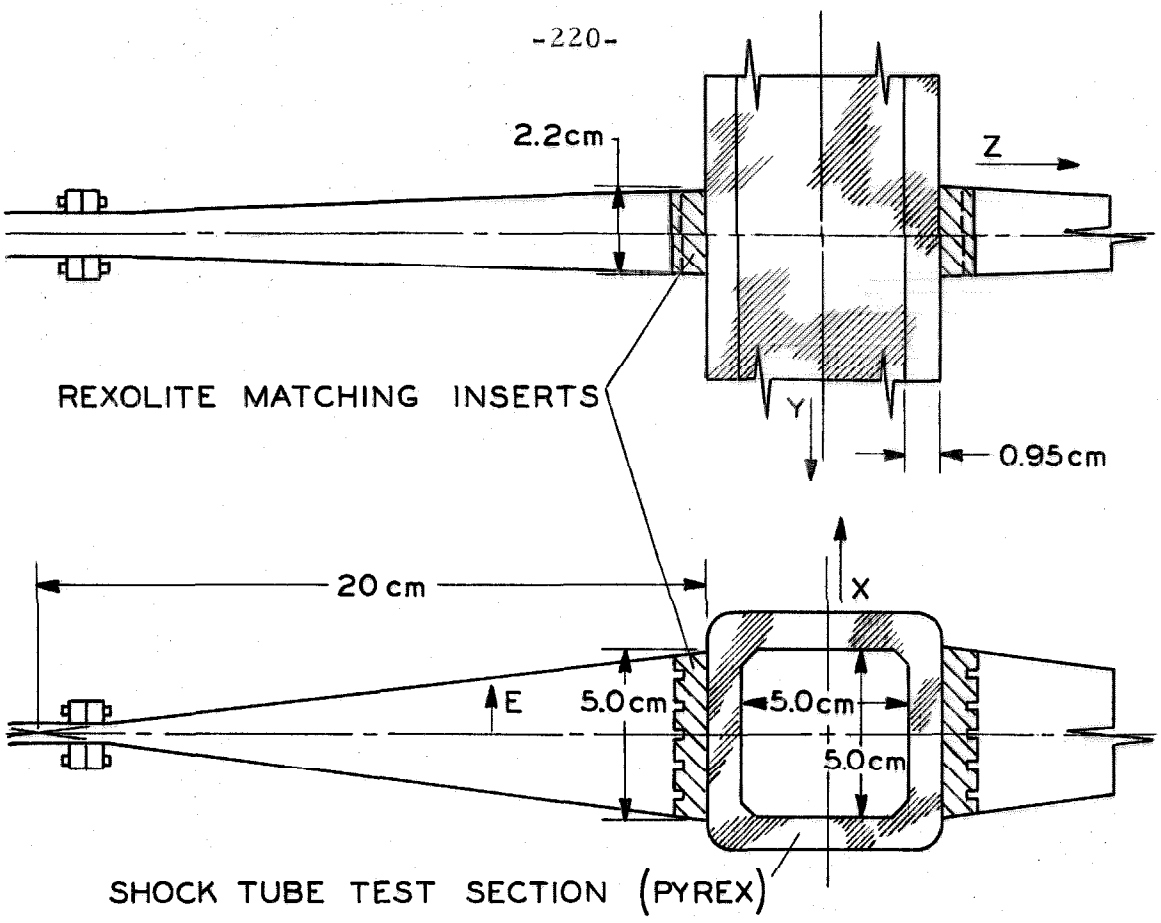

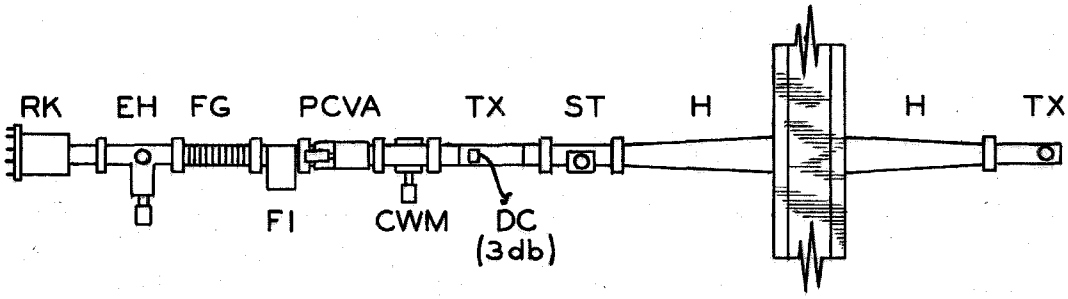

Fig. 11. Microwave Diagnostic System. Nomenclature: RK, 2K50 Reflex Klystron; EH, E and H Plane Tuner; FG, Flexible Waveguide; FI, Ferrite Isolator; PCVA, Precision Calibrated Variable Attenuator; CWM, Cavity Wave Meter; DC (3 db), 3-db Multihole Directional Coupler; TX, Tunable Crystal Mount; ST, Stub Tuner; H, Transmitting and Receiving Horns.

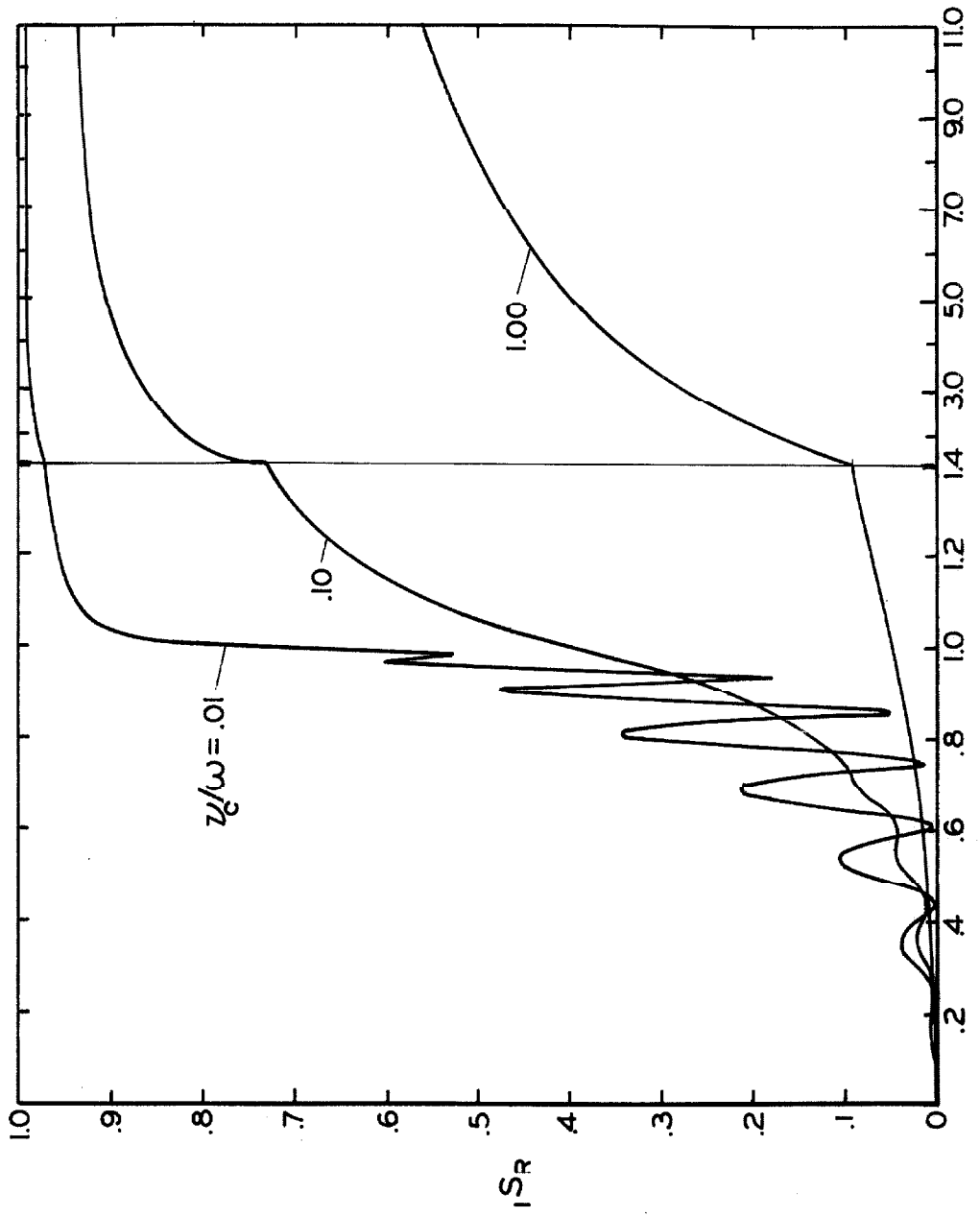

FIG. 12 REFLECTION FROM A PLANE SLAB OF IONIZED GAS
$m = 4$, $\omega = (2\pi)(24 \times 10^9)$

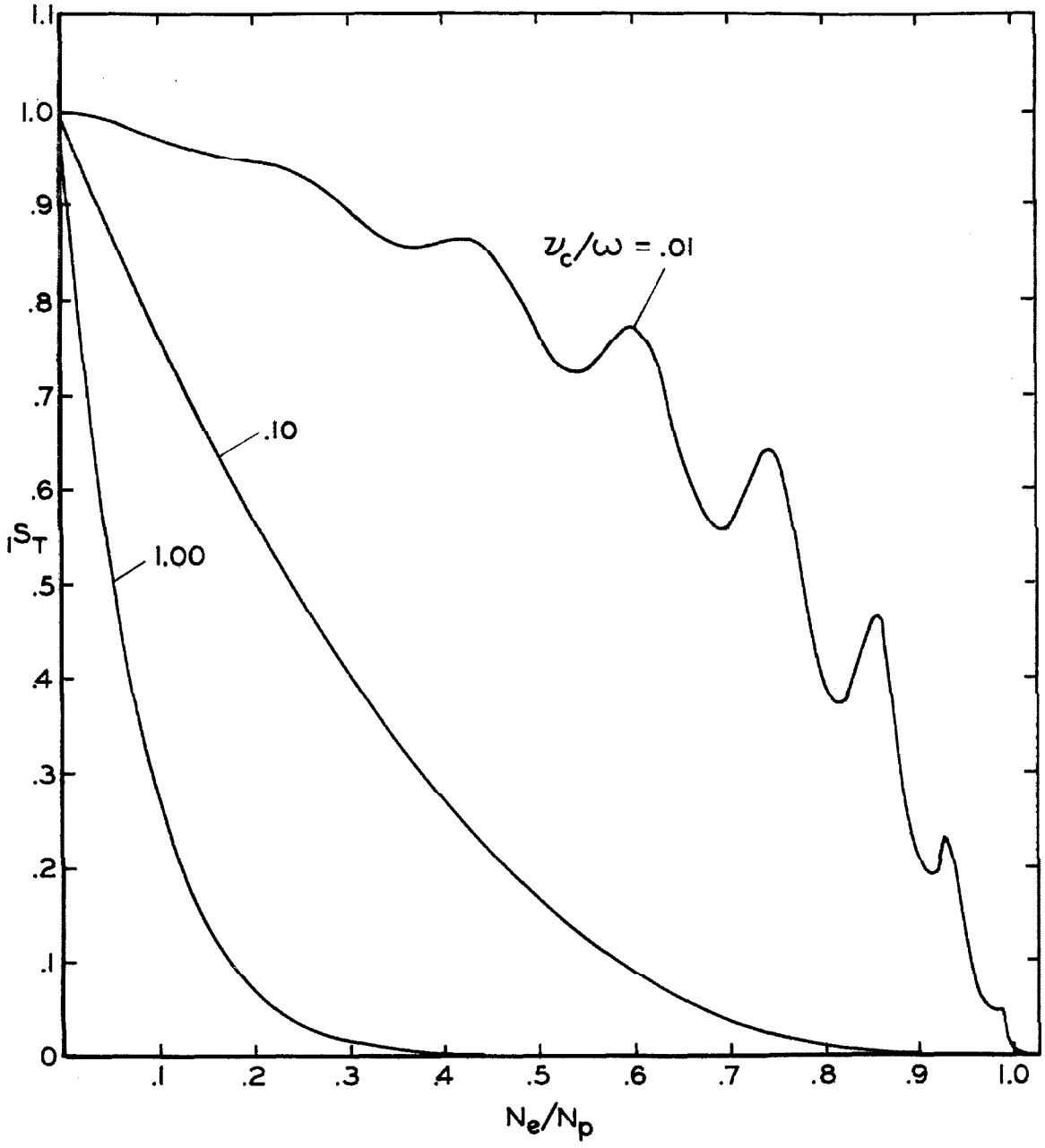

FIG. 13 TRANSMISSION THROUGH A PLANE SLAB OF IONIZED GAS, $m = 4$, $\omega = (2\pi)(24 \times 10^9)$

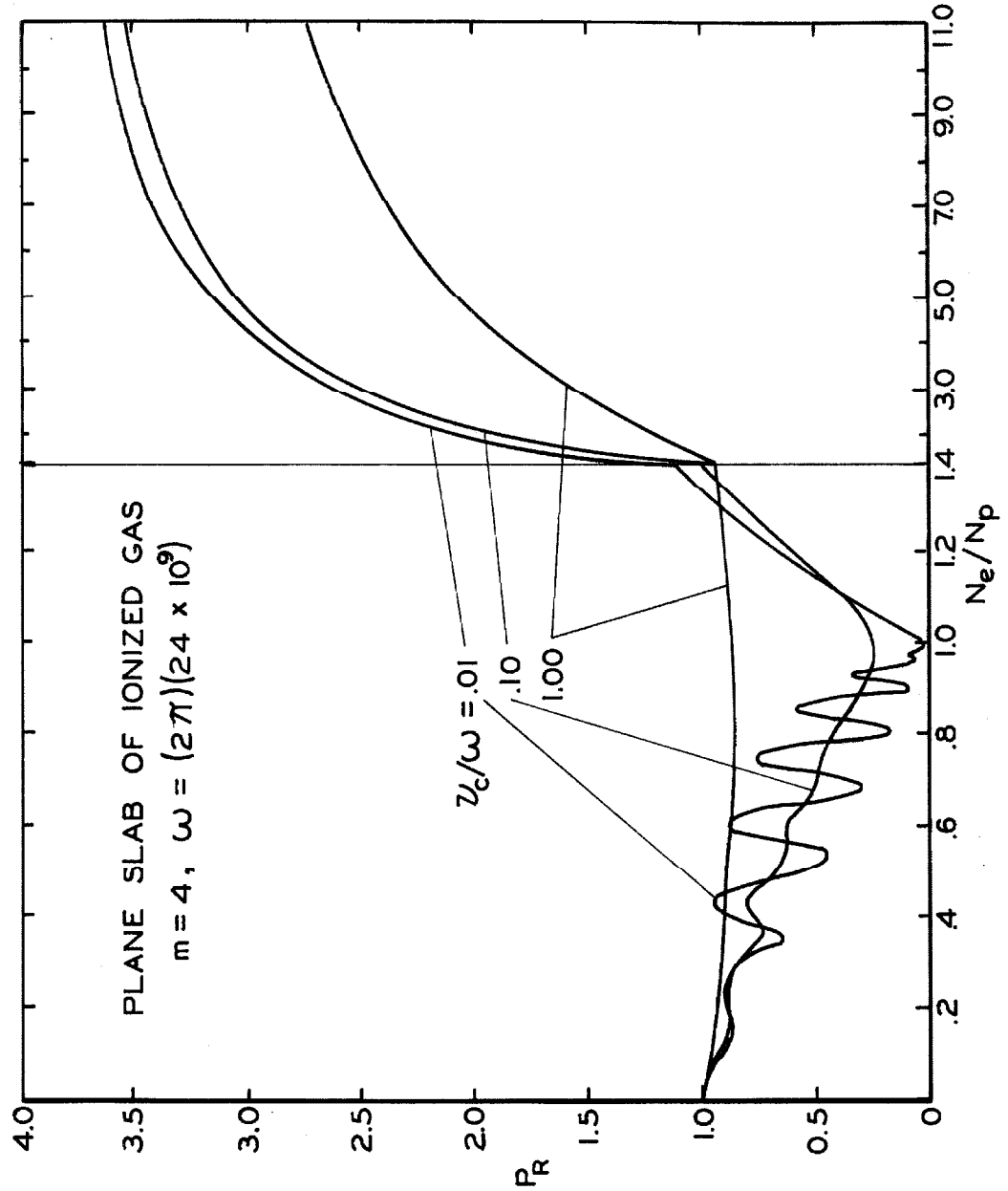

FIG. 14 REFLECTED PHASE MEASURABLE $P_R = 1 + {}_1S_R - 2\sqrt{{}_1S_R}\cos\phi_r$

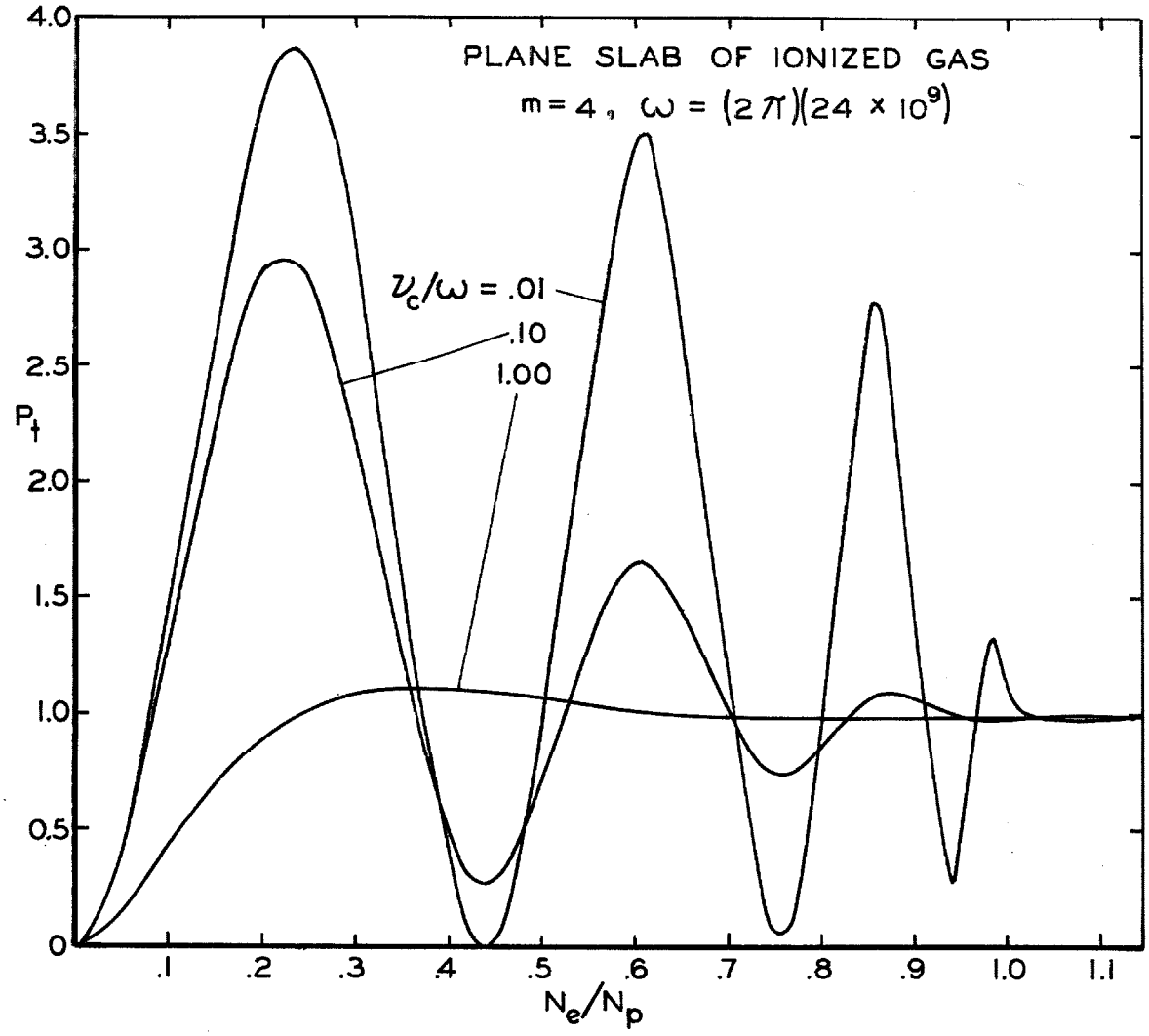

FIG. 15 TRANSMITTED PHASE MEASURABLE

$$P_t = 1 + {}_1S_t - 2\sqrt{{}_1S_t}\cos\phi_t$$

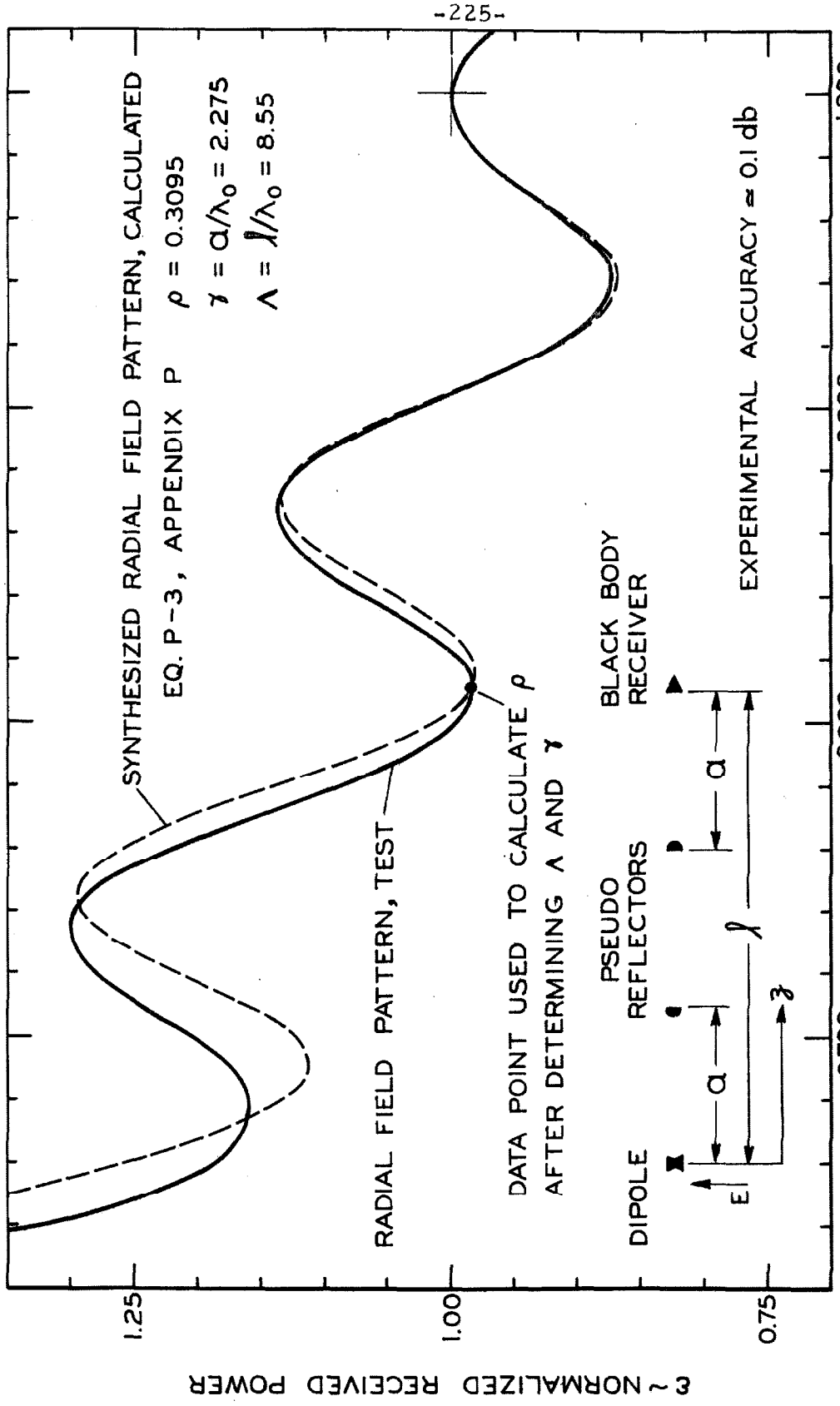

FIG. 16 COMPARISON OF EXPERIMENTAL & SYNTHESIZED RADIAL FIELD PATTERNS

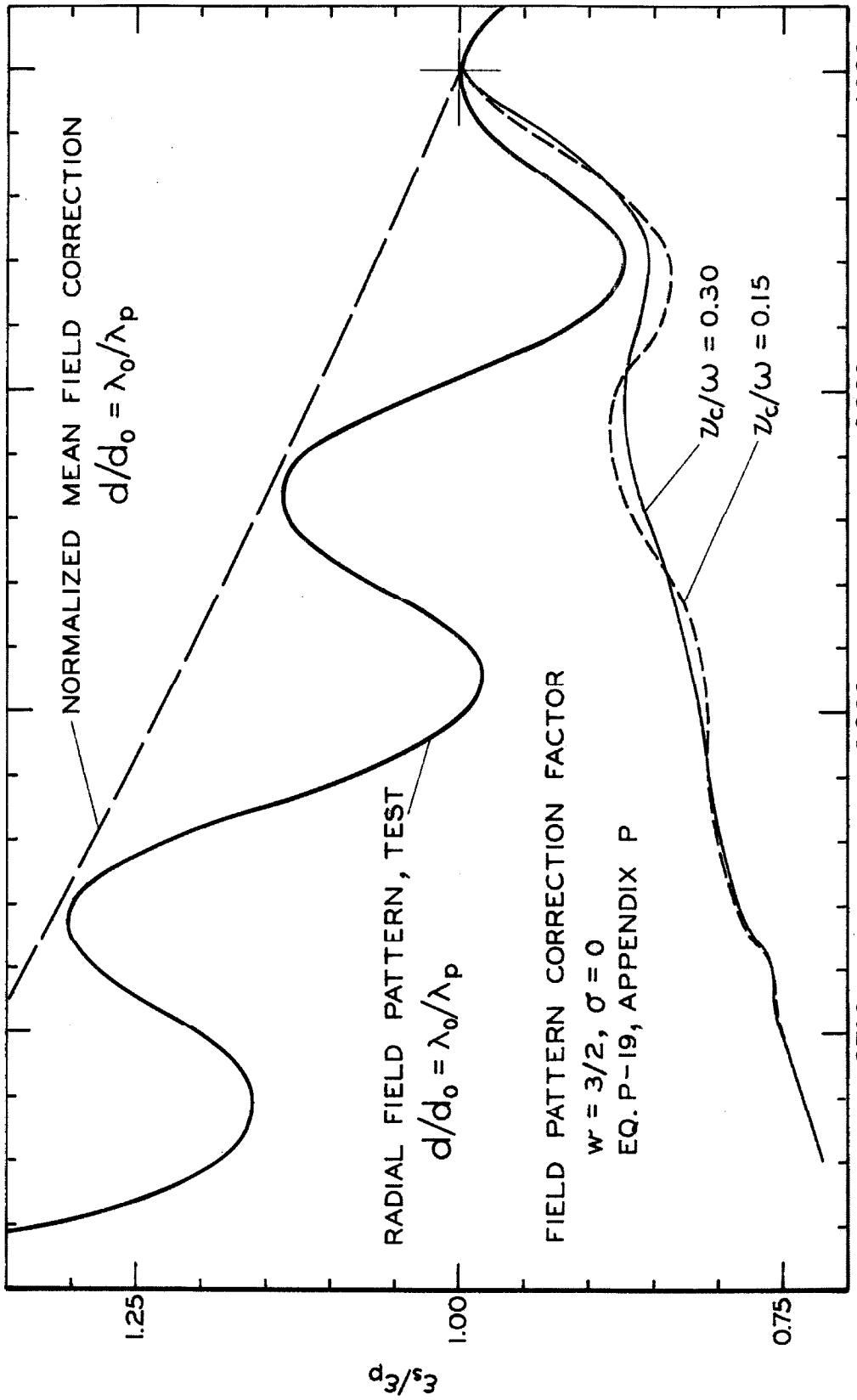

FIG. 17 COMPARISON OF FIELD CORRECTION FUNCTIONS

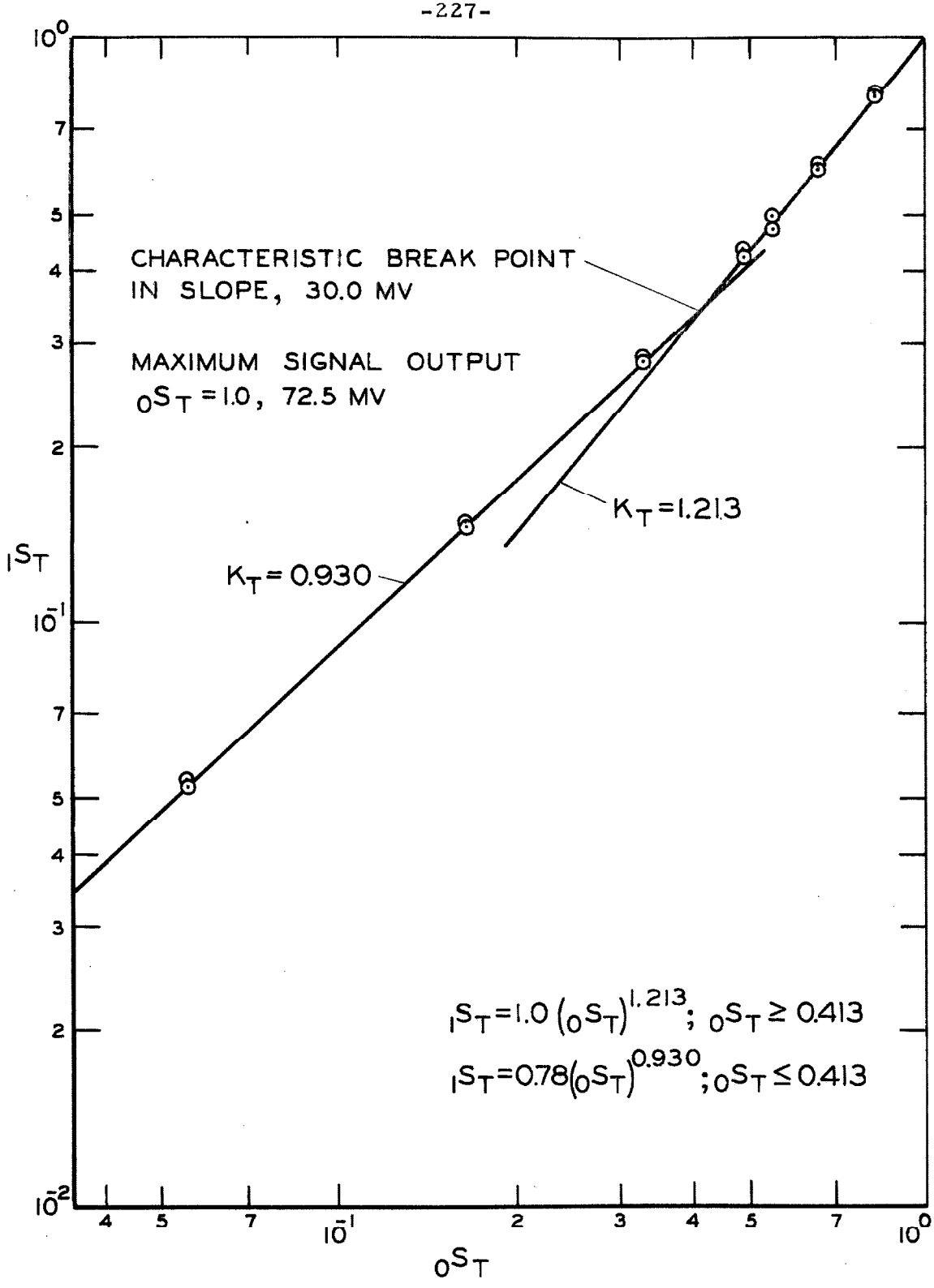

FIG. 18 RECIEVER CRYSTAL CALIBRATION (RUN NO. 945)

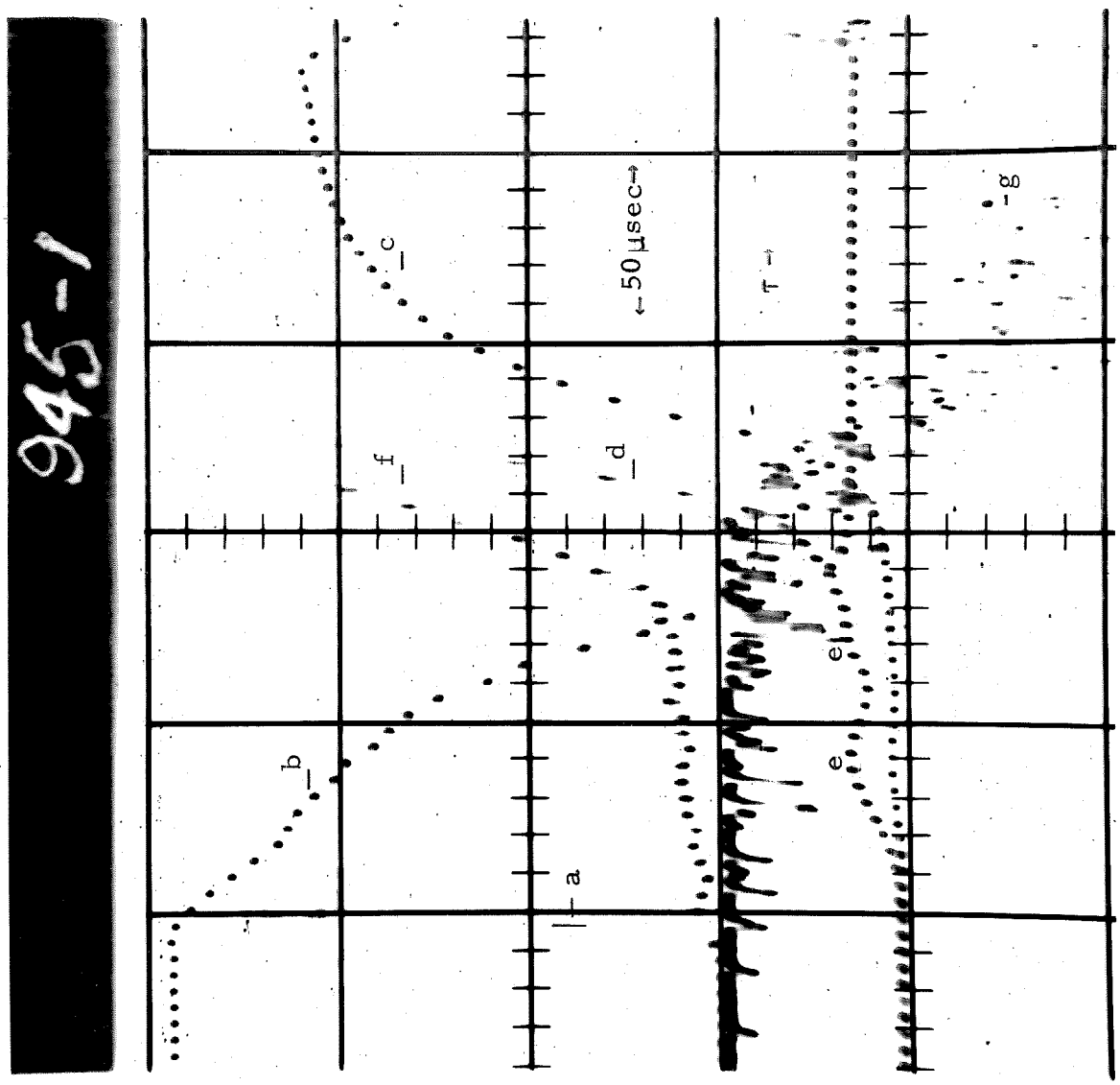

Fig. 19. Photographic Enlargement of Typical Microwave and Luminosity Data. (a) Estimated Shock Position, (b) Transmitted Signal, (c) Reflected Signal, (d) 5 Times Amplified Reflected Signal, (e) "Bumps," (f) Unfiltered Luminosity, (g) Filtered Luminosity.

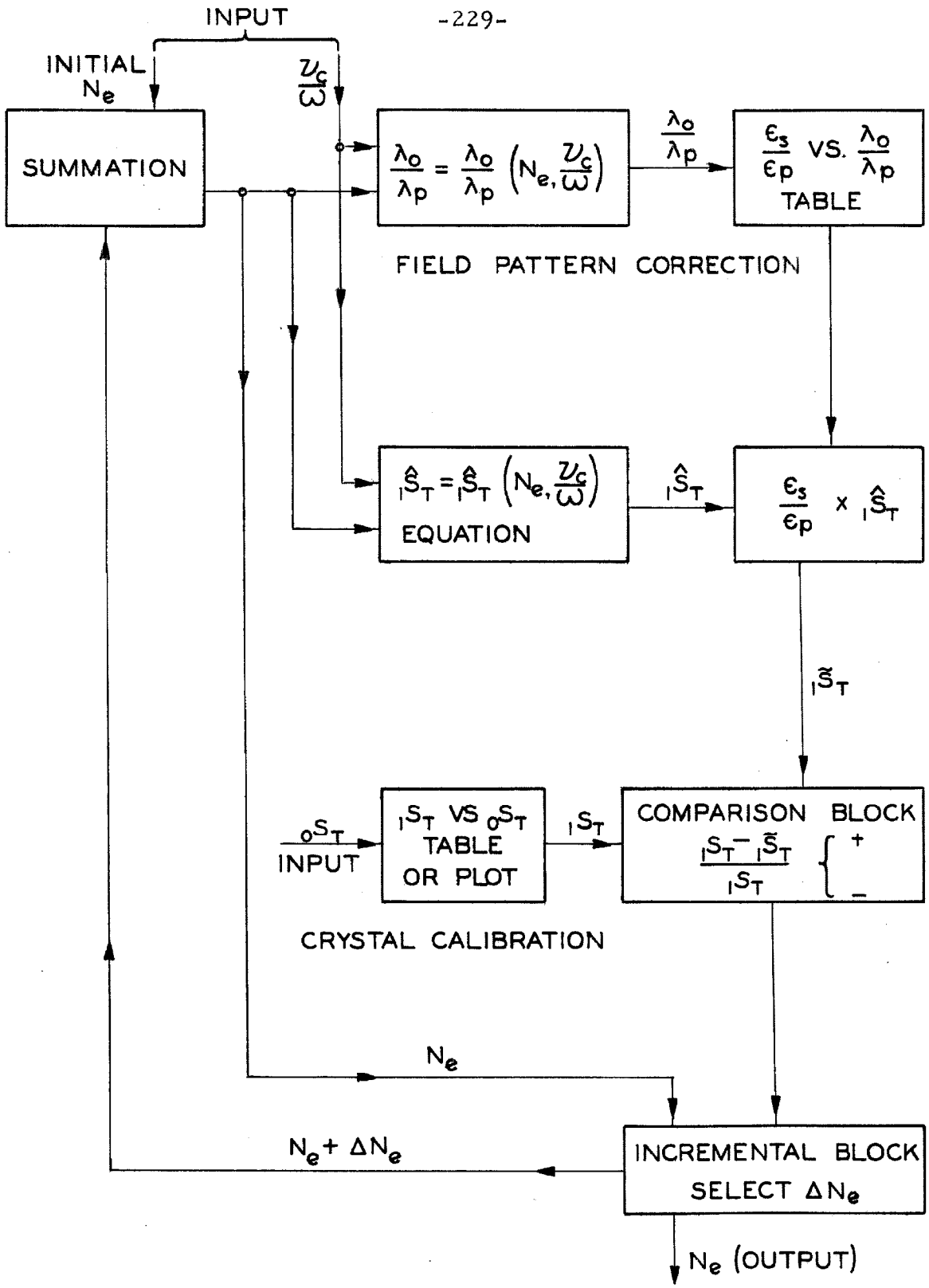

FIG. 20 BLOCK DIAGRAM OF PLASMA II DATA REDUCTION COMPUTER PROGRAM

RUN NO.945 PURE ARGON F.C.T.430

INPUT PARAMETERS

W = 0.1507964E 12
M = 0.4000000E 01
LAMBDA(SUB C) = 0.1249135E 01

TABLE VALUES FOR KTAL CALIBRATION

OST	1.00000	0.82800	0.66200	0.55100	0.49600	0.33100	0.16600	0.05510
1ST	1.00000	0.79400	0.60300	0.48600	0.42900	0.28000	0.14700	0.05370

INDEX	T2(0)	T2	VC/W	NE	R2	THETA T	THETA R	LAMBDA O/P (F)	IND. PAR.
945	0.9750E 00	0.9820E 00	0.8000E-01	0.6504E 11	0.2653E-06	0.1293E-01	0.9997E 00	0.9955E 00 16	0.9000E 01 0
945	0.9500E 00	0.9637E 00	0.8000E-01	0.1314E 12	0.4342E-05	0.5236E-01	0.9984E 00	0.9908E 00 31	0.2700E 02 0
945	0.9250E 00	0.9479E 00	0.8000E-01	0.1889E 12	0.1811E-04	0.1073E-00	0.9960E 00	0.9868E 00 22	0.3800E 02 0
945	0.9000E 00	0.9324E 00	0.8000E-01	0.2458E 12	0.5042E-04	0.1798E-00	0.9921E 00	0.9828E 00 26	0.5000E 02 0
945	0.8750E 00	0.9160E 00	0.8000E-01	0.3065E 12	0.1171E-03	0.2758E-00	0.9862E 00	0.9785E 00 20	0.6100E 02 0
945	0.8500E 00	0.8981E 00	0.8000E-01	0.3732E 12	0.2437E-03	0.4020E-00	0.9776E 00	0.9737E 00 29	0.7300E 02 0
945	0.8250E 00	0.8798E 00	0.8000E-01	0.4418E 12	0.4479E-03	0.5521E 00	0.9665E 00	0.9688E 00 32	0.9600E 02 0
945	0.8000E 00	0.8608E 00	0.8000E-01	0.5134E 12	0.7520E-03	0.7277E 00	0.9531E 00	0.9636E 00 22	0.1190E 03 0
945	0.7500E 00	0.8158E 00	0.8000E-01	0.6851E 12	0.1847E-02	0.1207E 01	0.9180E 00	0.9512E 00 13	0.1510E 03 0
945	0.7000E 00	0.7540E 00	0.8000E-01	0.9287E 12	0.3663E-02	0.1940E 01	0.8845E 00	0.9332E 00 27	0.1780E 03 0
945	0.6500E 00	0.6783E 00	0.8000E-01	0.1247E 13	0.3791E-02	0.2753E 01	0.9048E 00	0.9092E 00 19	0.2090E 03 0
945	0.6000E 00	0.6166E 00	0.8000E-01	0.1525E 13	0.1390E-02	0.3107E 01	0.9454E 00	0.8877E 00 25	0.2240E 07 0
945	0.5500E 00	0.5632E 00	0.8000E-01	0.1768E 13	0.1246E-02	0.3044E 01	0.9334E 00	0.8685E 00 24	0.2360E 03 0
945	0.5000E 00	0.5121E 00	0.8000E-01	0.1997E 13	0.6303E-02	0.2667E 01	0.8622E 00	0.8500E 00 23	0.2510E 03 0
945	0.4500E-00	0.4654E-00	0.8000E-01	0.2210E 13	0.1462E-01	0.2116E 01	0.7780E 00	0.8323E 00 25	0.2630E 03 0
945	0.4000E-00	0.4174E-00	0.8000E-01	0.2449E 13	0.2195E-01	0.1411E 01	0.7272E 00	0.8122E 00 20	0.2710E 03 0
945	0.3000E-00	0.3223E-00	0.8000E-01	0.3017E 13	0.1054E-01	0.2412E-00	0.8181E 00	0.7621E 00 30	0.2900E 03 0
945	0.2000E-00	0.2310E-00	0.8000E-01	0.3560E 13	0.3553E-01	0.6938E 00	0.6598E 00	0.7111E 00 24	0.3210E 03 0
945	0.1000E-00	0.1336E-00	0.8000E-01	0.4342E 13	0.3901E-01	0.1856E 01	0.6499E 00	0.6306E 00 30	0.3400E 03 0

Fig. 21. Reproduction of a Typical Example of IBM Plasma II Program Output Format.

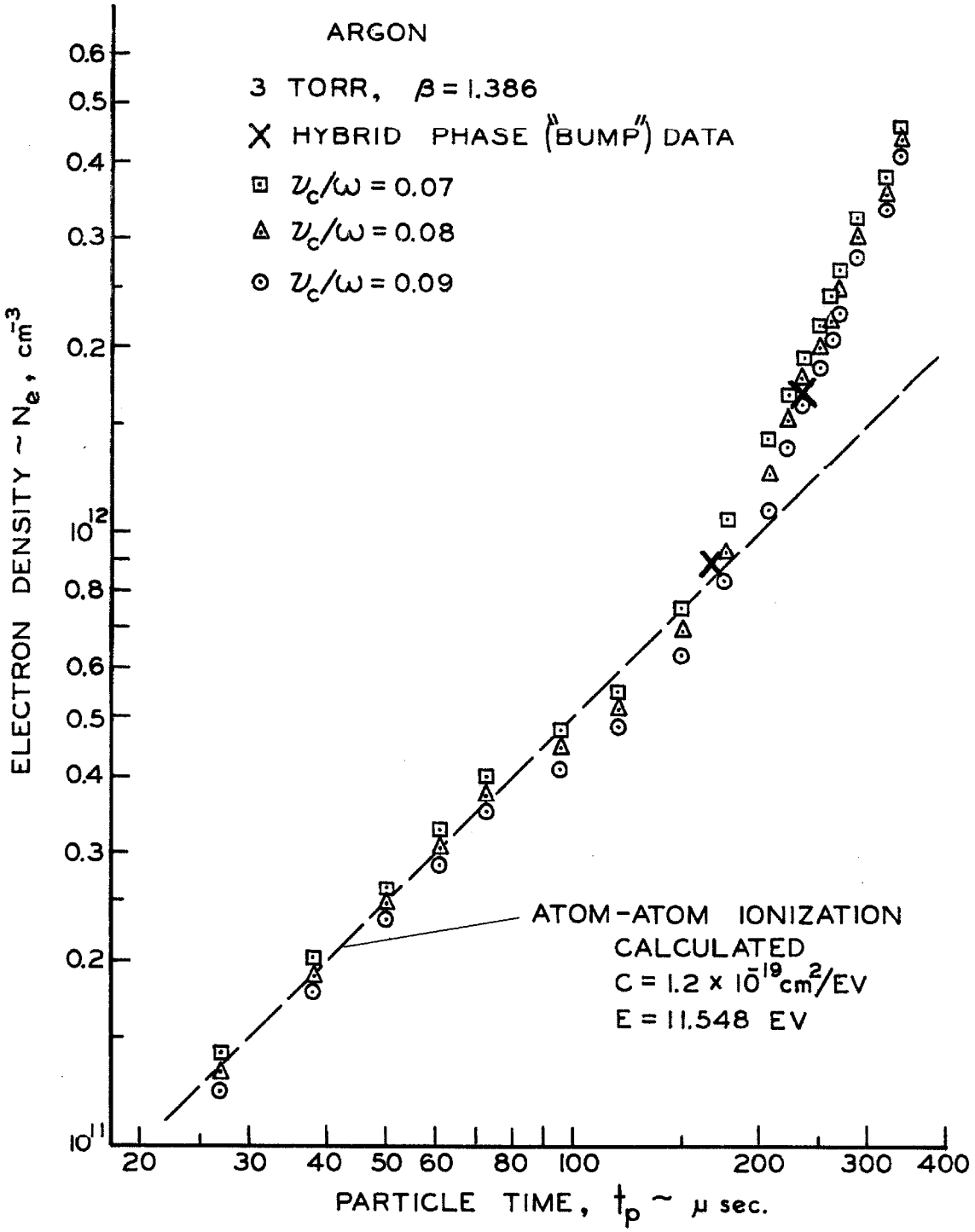

FIG. 22 ELECTRON DENSITY VS. PARTICLE TIME, RUN NO. 945

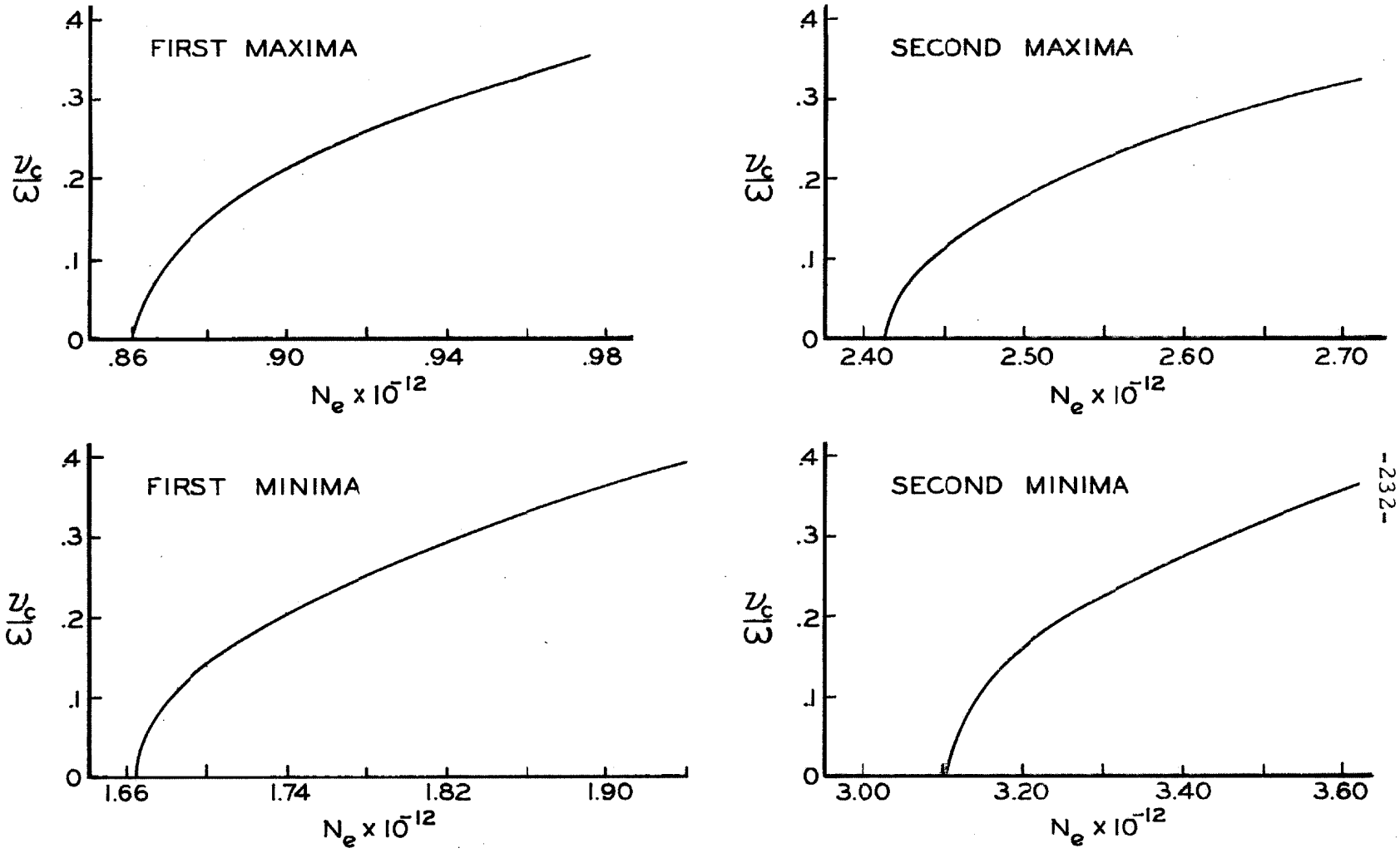

FIG. 23 HYBRID PHASE ("BUMP") EXTREMA, $m=4$, $\omega = 2\pi \times 24 \times 10^9$

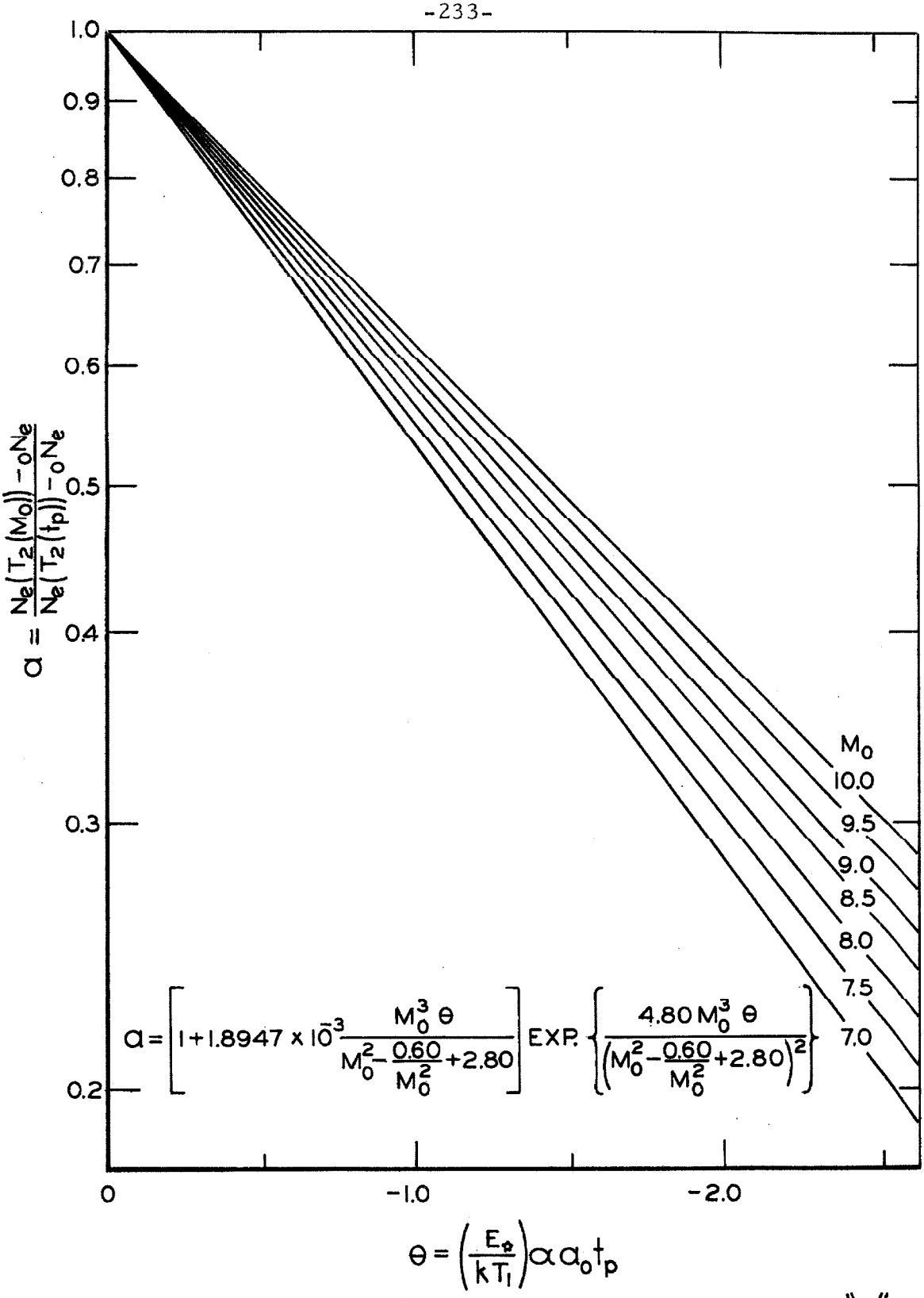

FIG. 24 SHOCK ATTENUATION CORRECTION FACTOR "a" VS. NON-DIMENSIONALIZED PARTICLE TIME "θ"

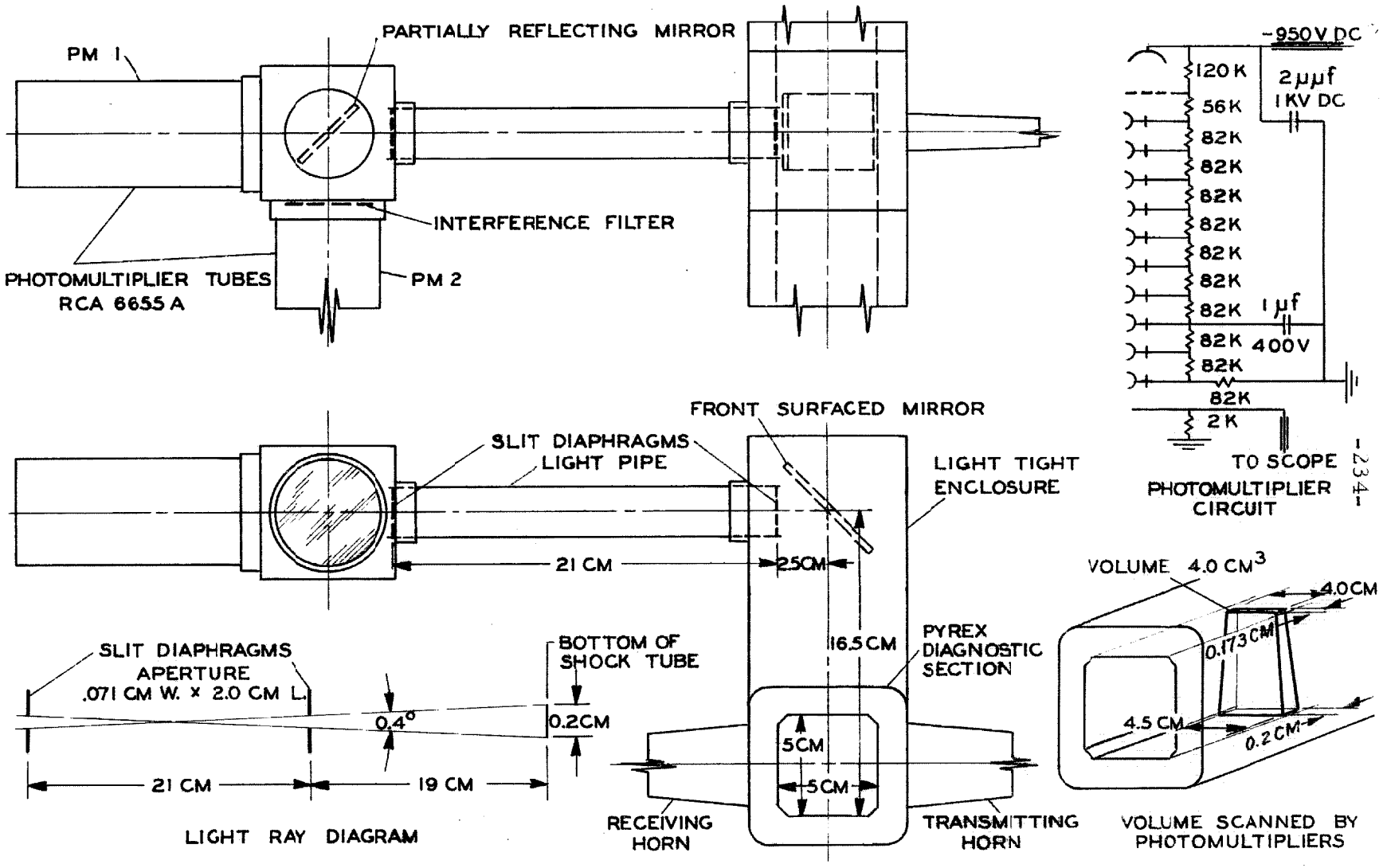

FIG. 25 DETAILS OF VISIBLE LUMINOSITY MONITORING SYSTEM

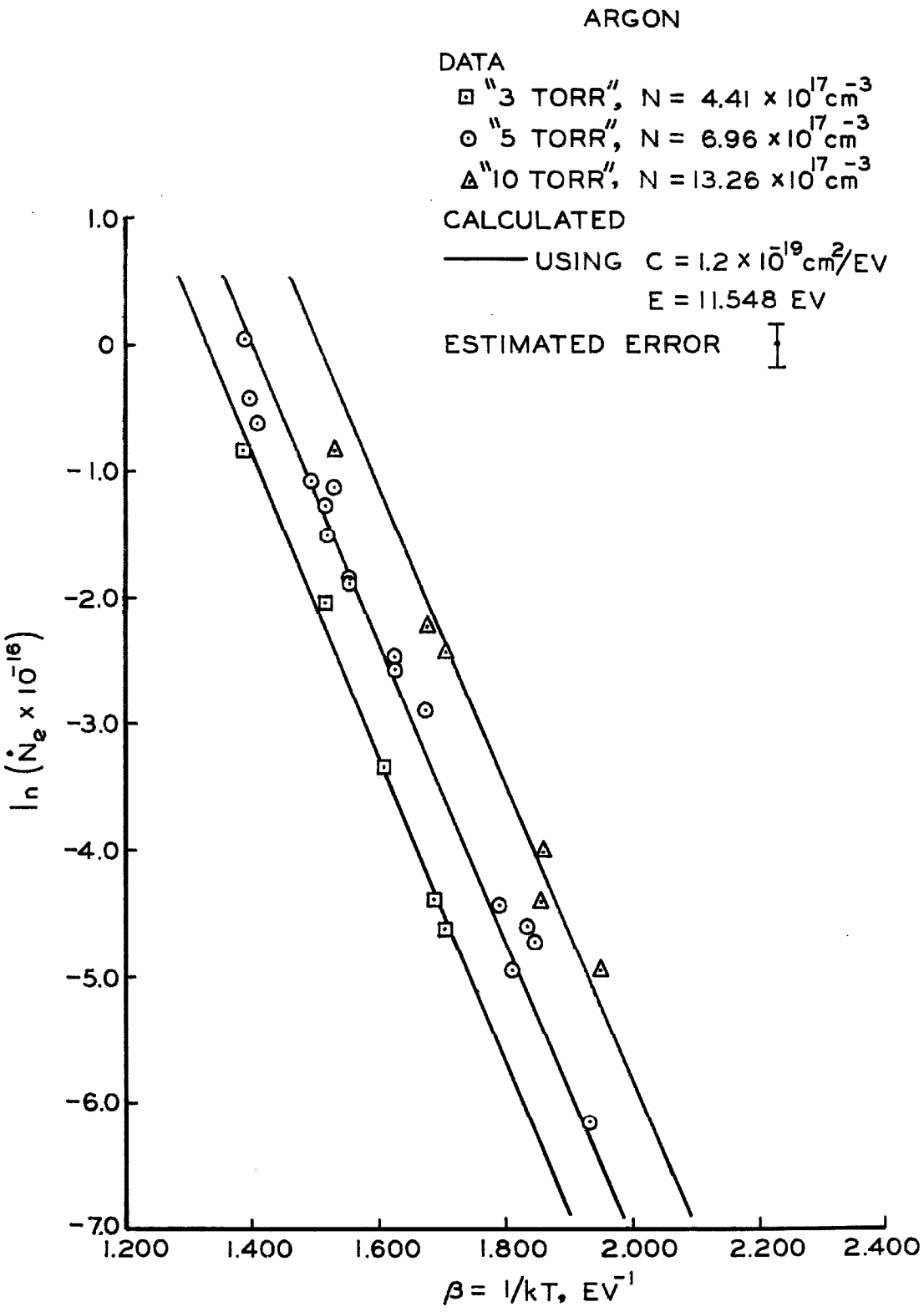

FIG. 26 ARRHENIUS PLOT FOR IONIZATION OF ARGON

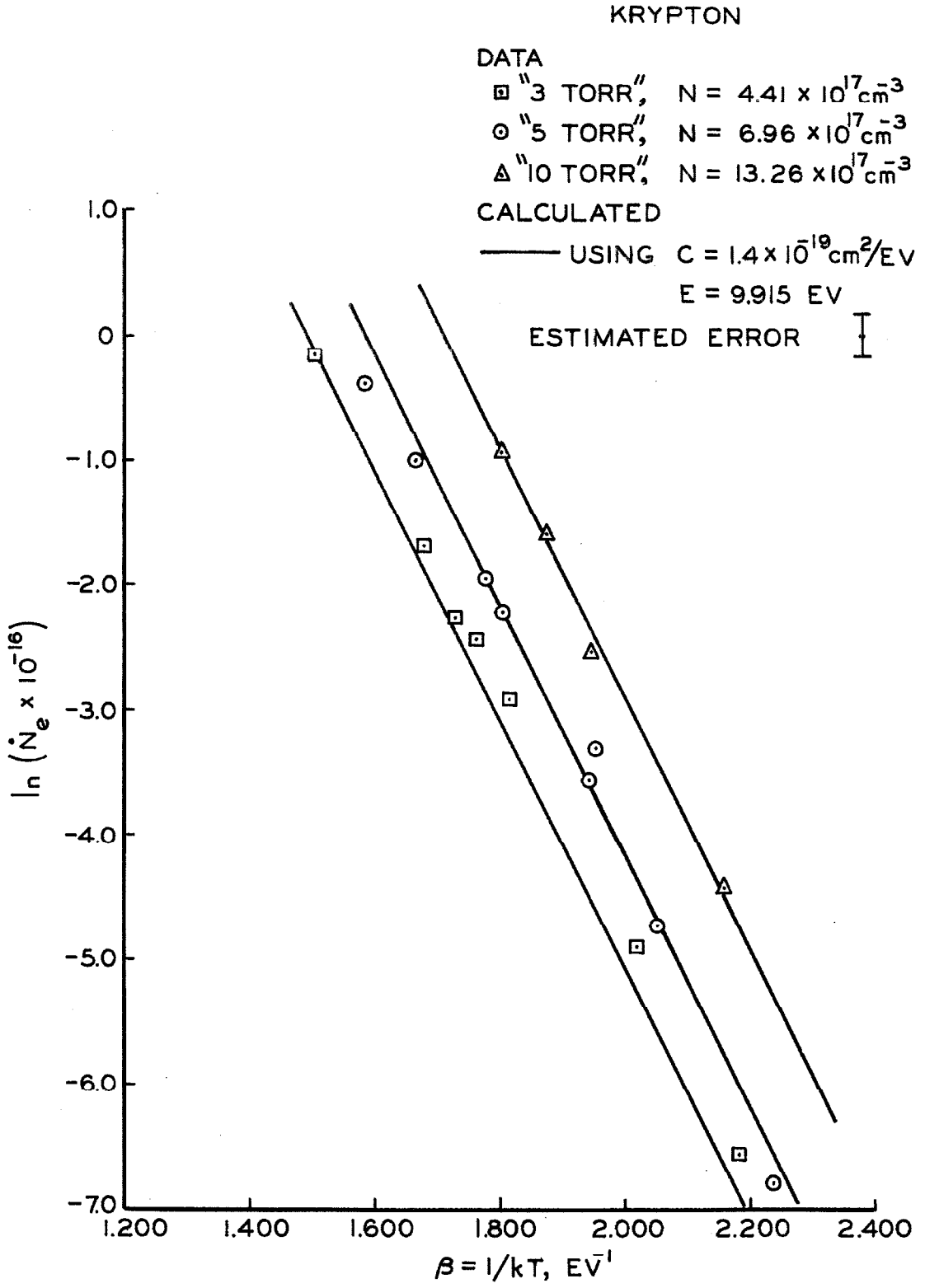

FIG. 27 ARRHENIUS PLOT FOR IONIZATION OF KRYPTON

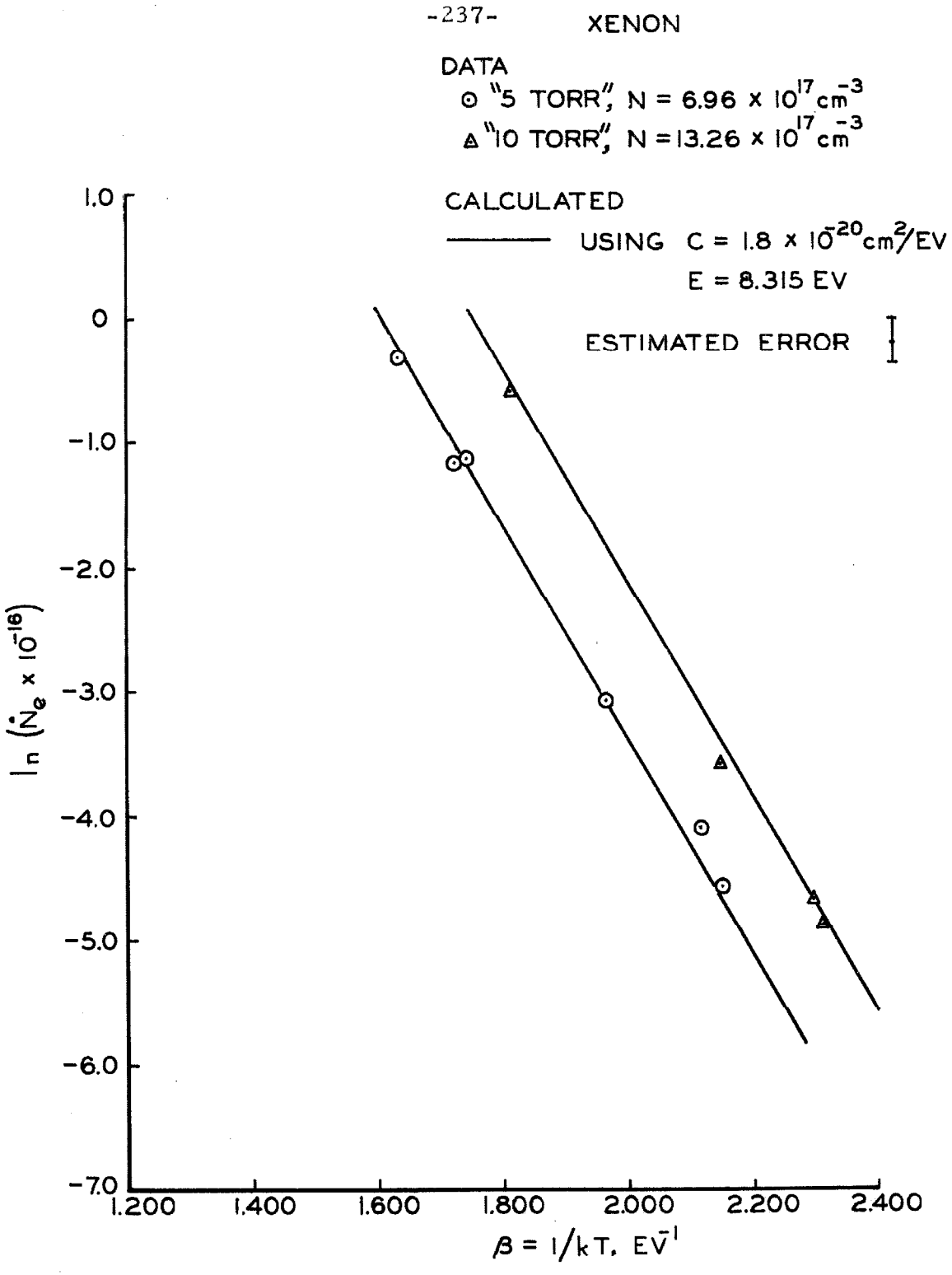

FIG. 28 ARRHENIUS PLOT FOR IONIZATION OF XENON

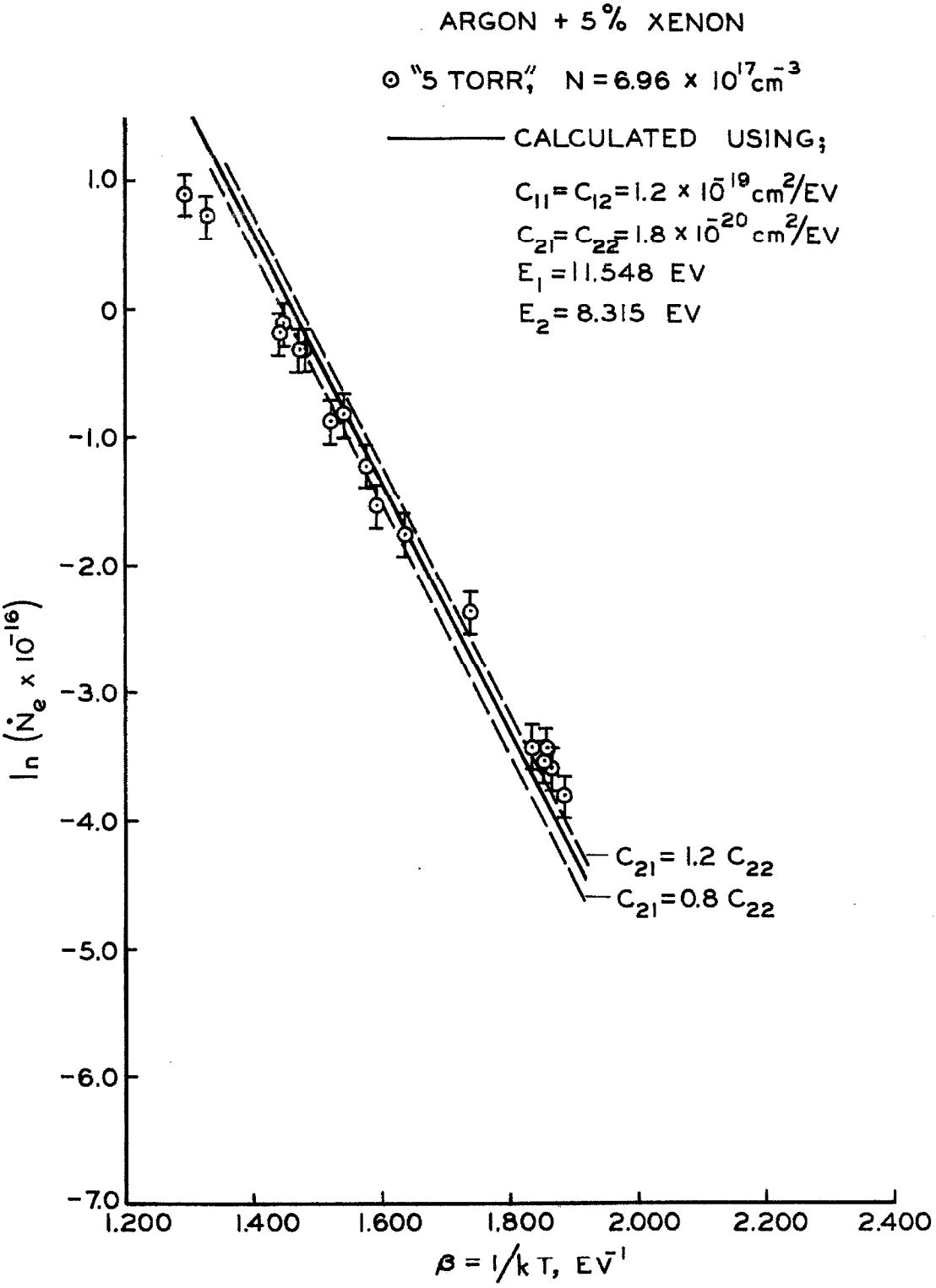

FIG. 29 ARRHENIUS PLOT FOR IONIZATION OF ARGON + 5% XENON

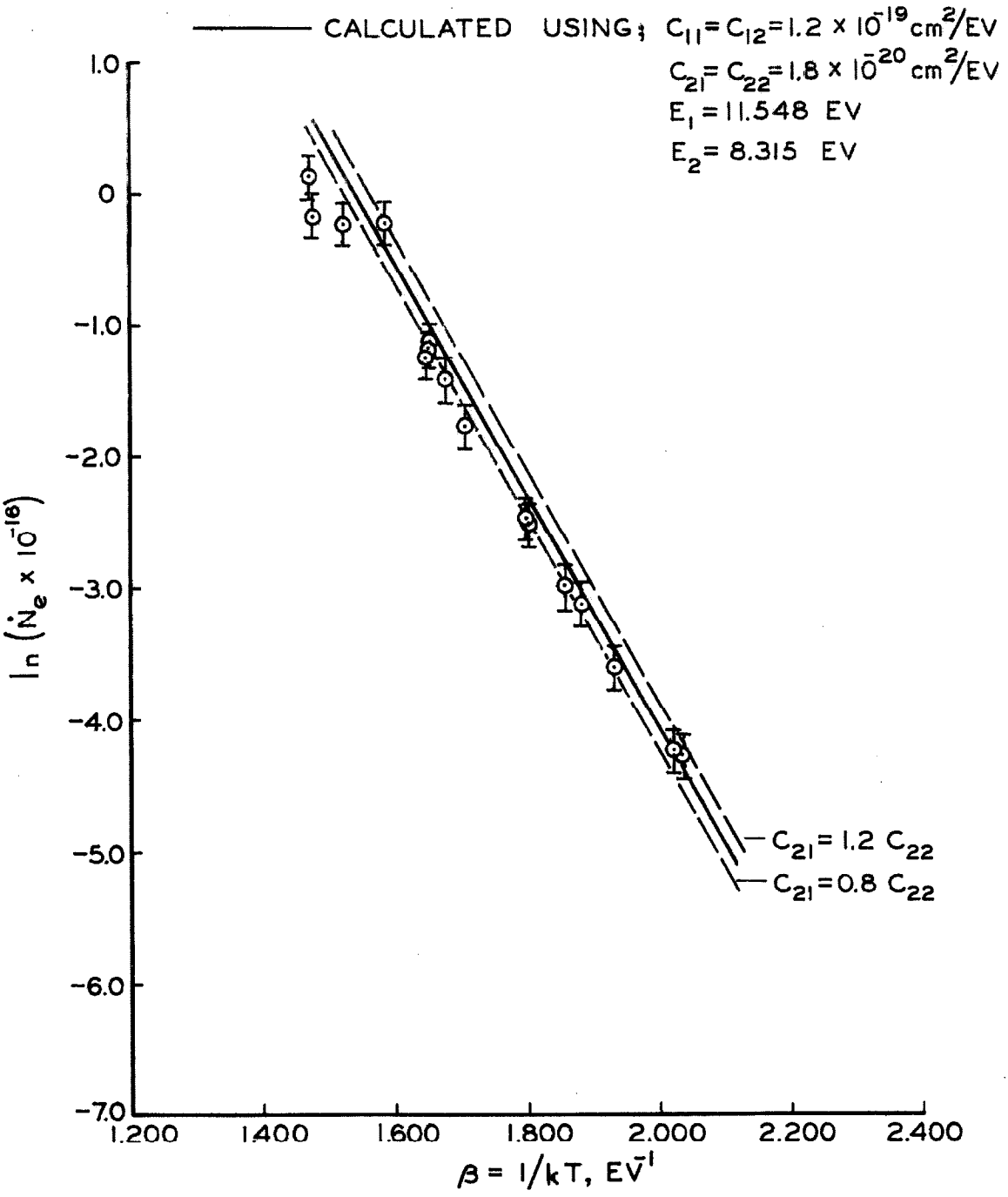

FIG. 30 ARRHENIUS PLOT FOR IONIZATION OF ARGON + 20% XENON

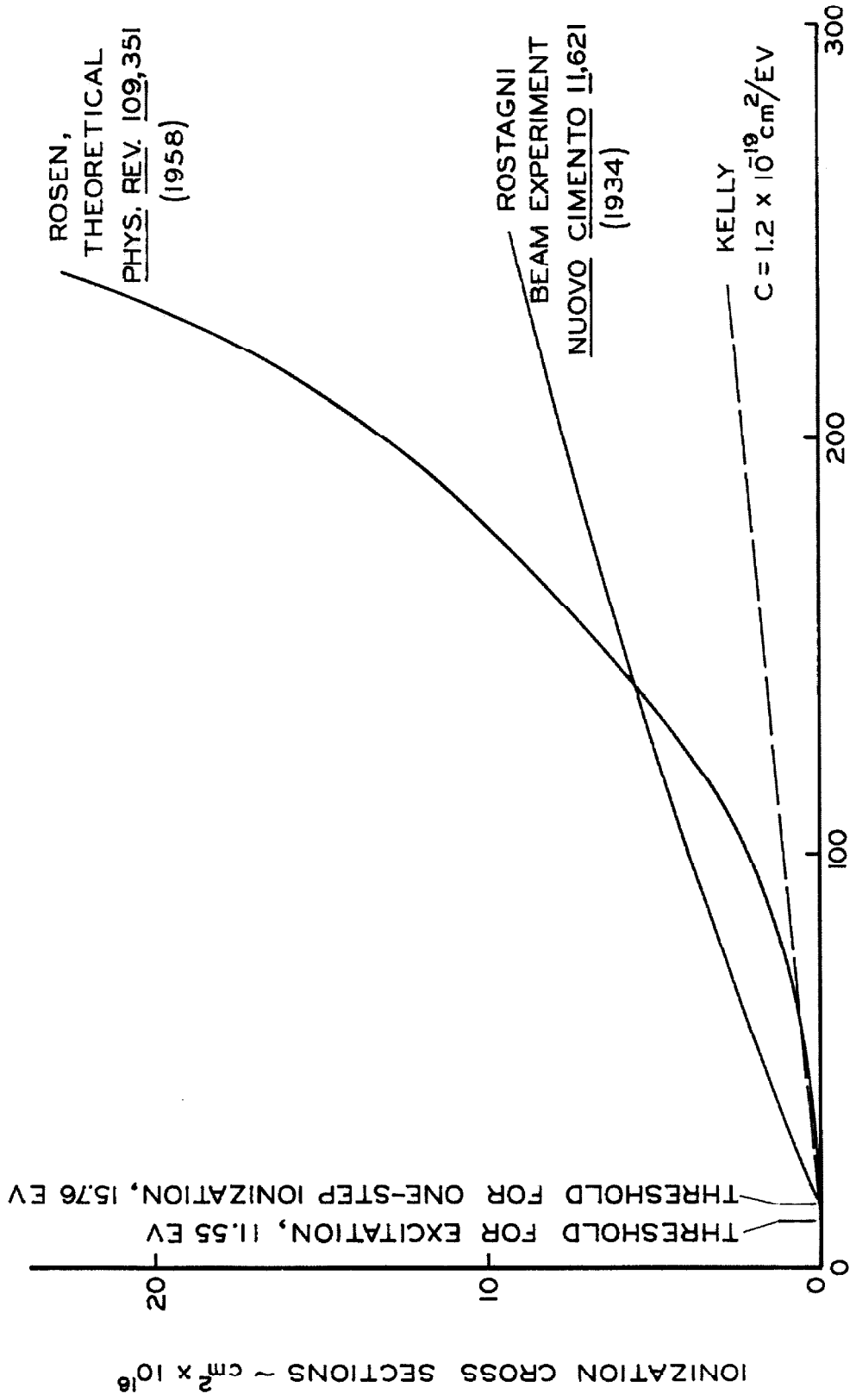

FIG. 31 COMPARISON OF IONIZATION CROSS SECTIONS FOR ARGON

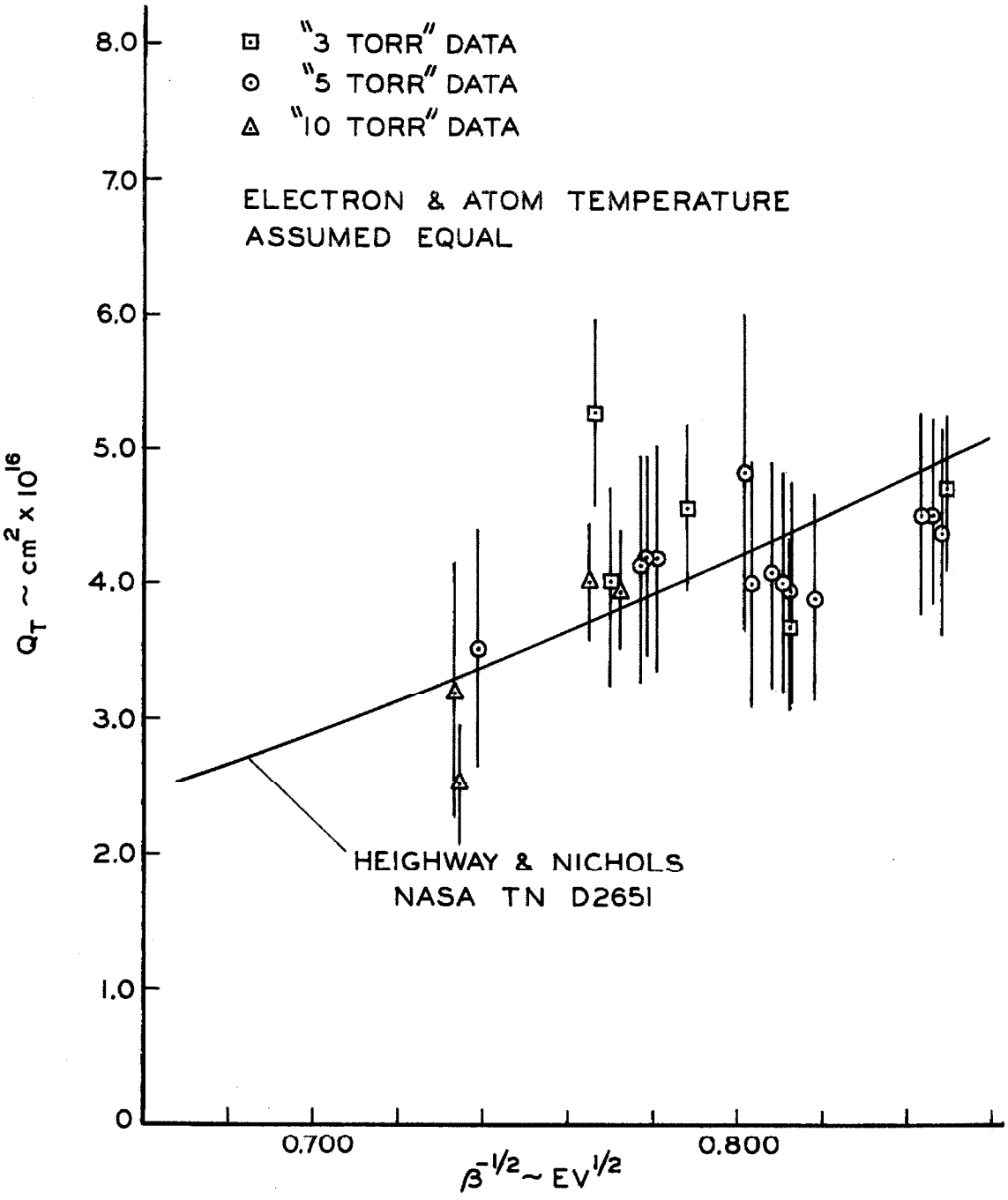

FIG. 32 Q_T VS. $\beta^{-1/2}$ FOR ARGON

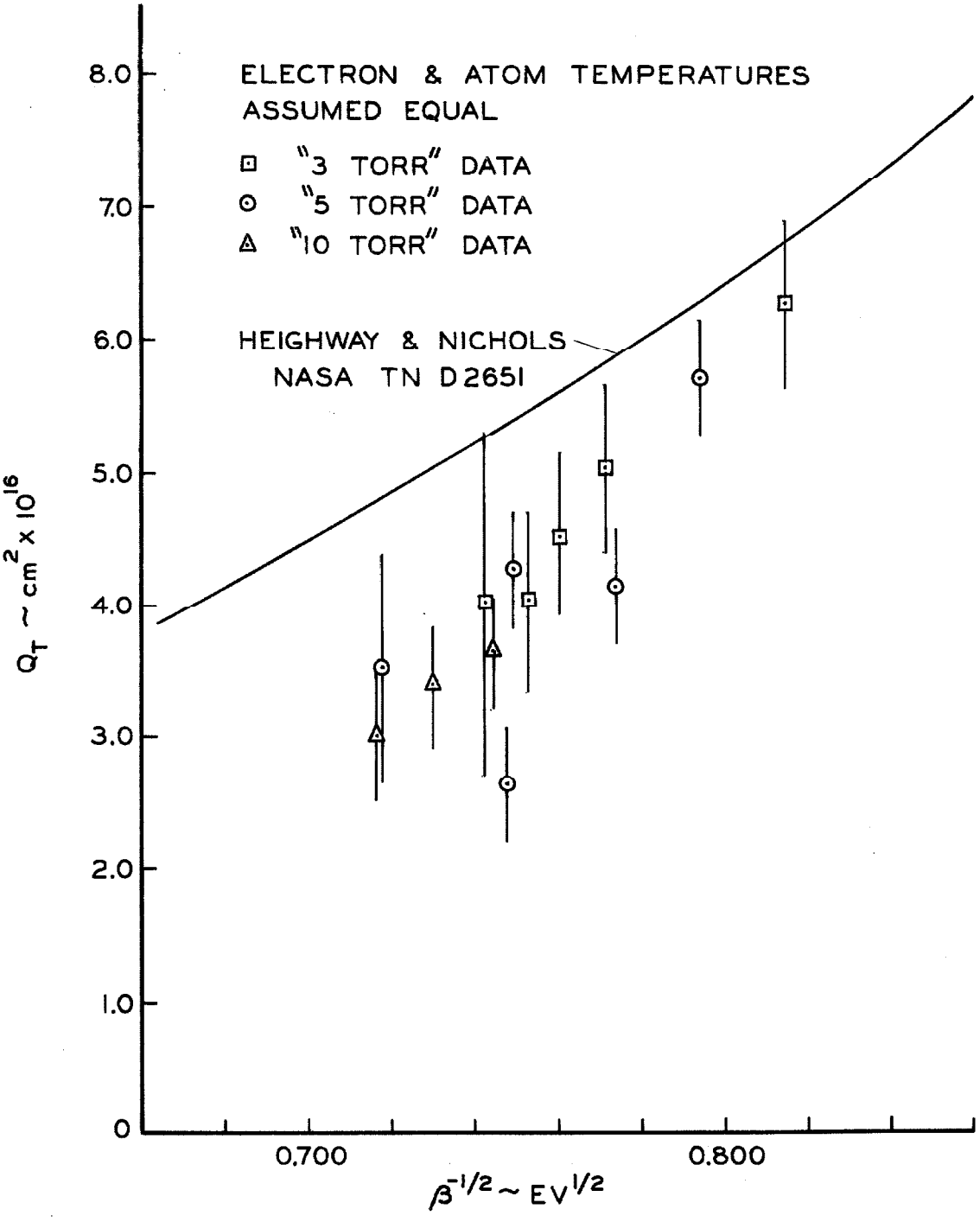

FIG. 33 Q_T VS. $\beta^{-1/2}$ FOR KRYPTON

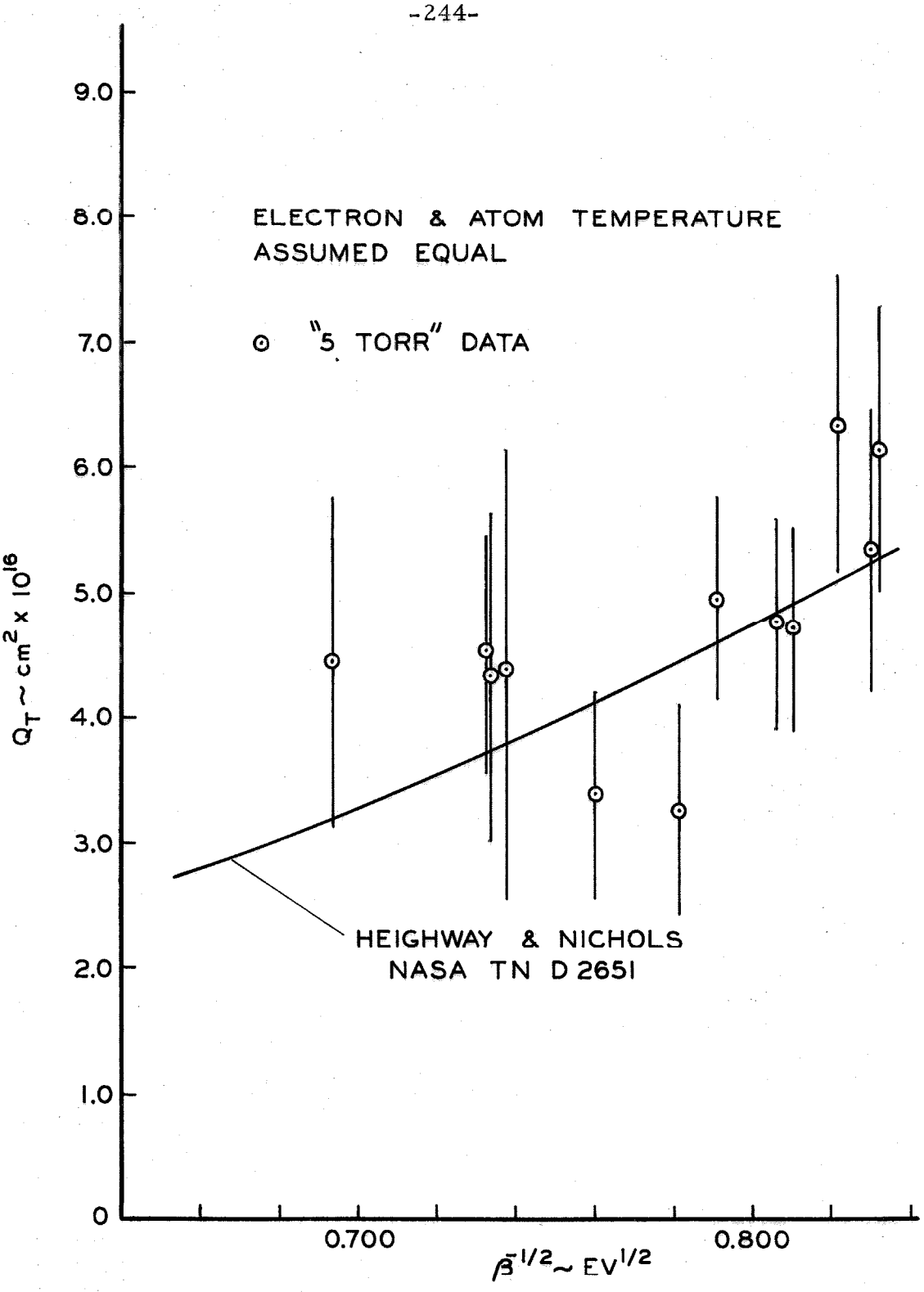

FIG. 35 Q_T VS. $\bar{\beta}^{1/2}$ FOR ARGON + 5% XENON

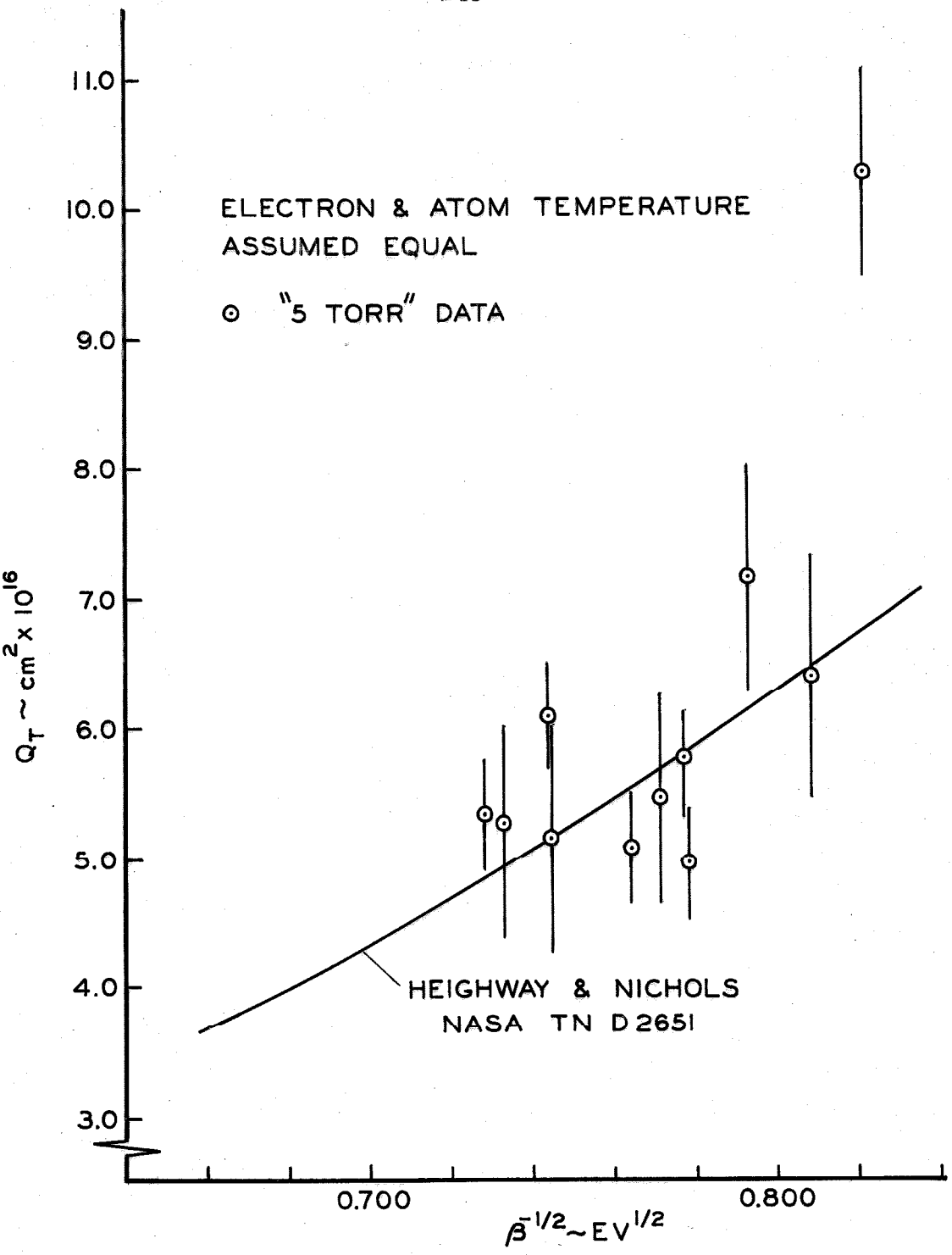

FIG. 36 Q_T VS. $\beta^{-1/2}$ FOR ARGON + 20 % XENON

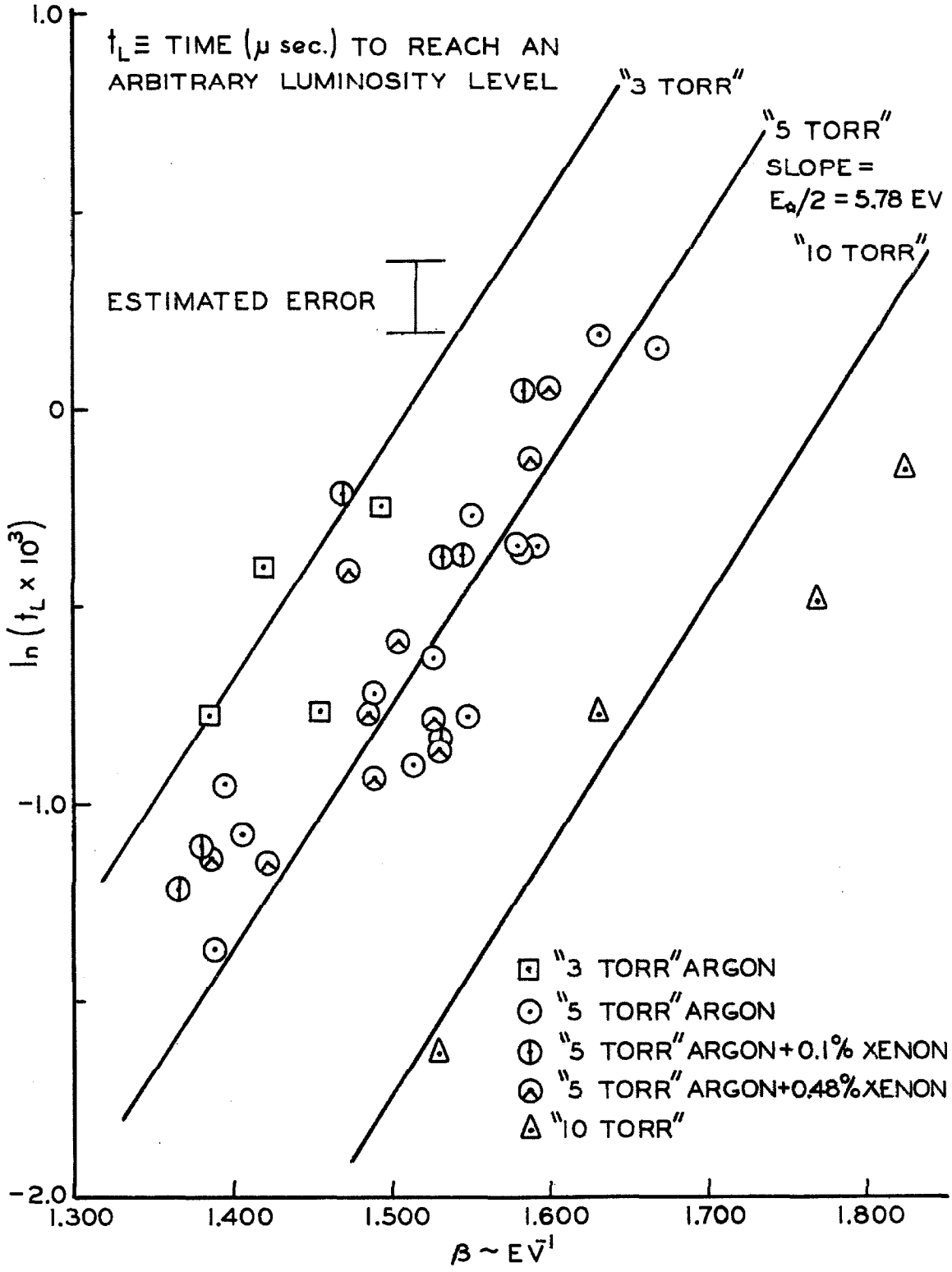

FIG. 37 LUMINOSITY DATA, $\ln(t_L \times 10^3)$ VS. β

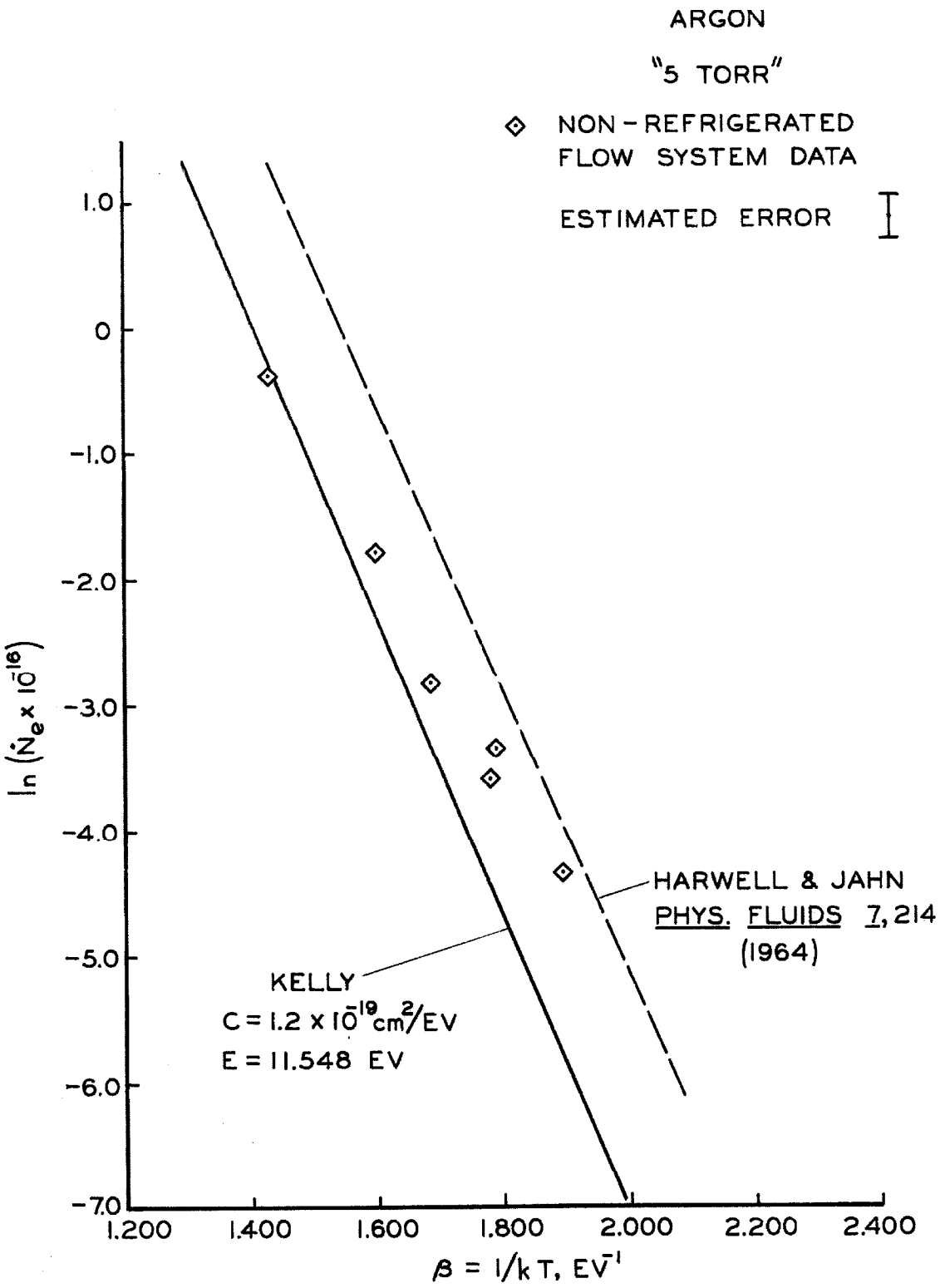

FIG. 38 ARRHENIUS PLOT FOR NON-REFRIGERATED FLOW SYSTEM ~ ARGON

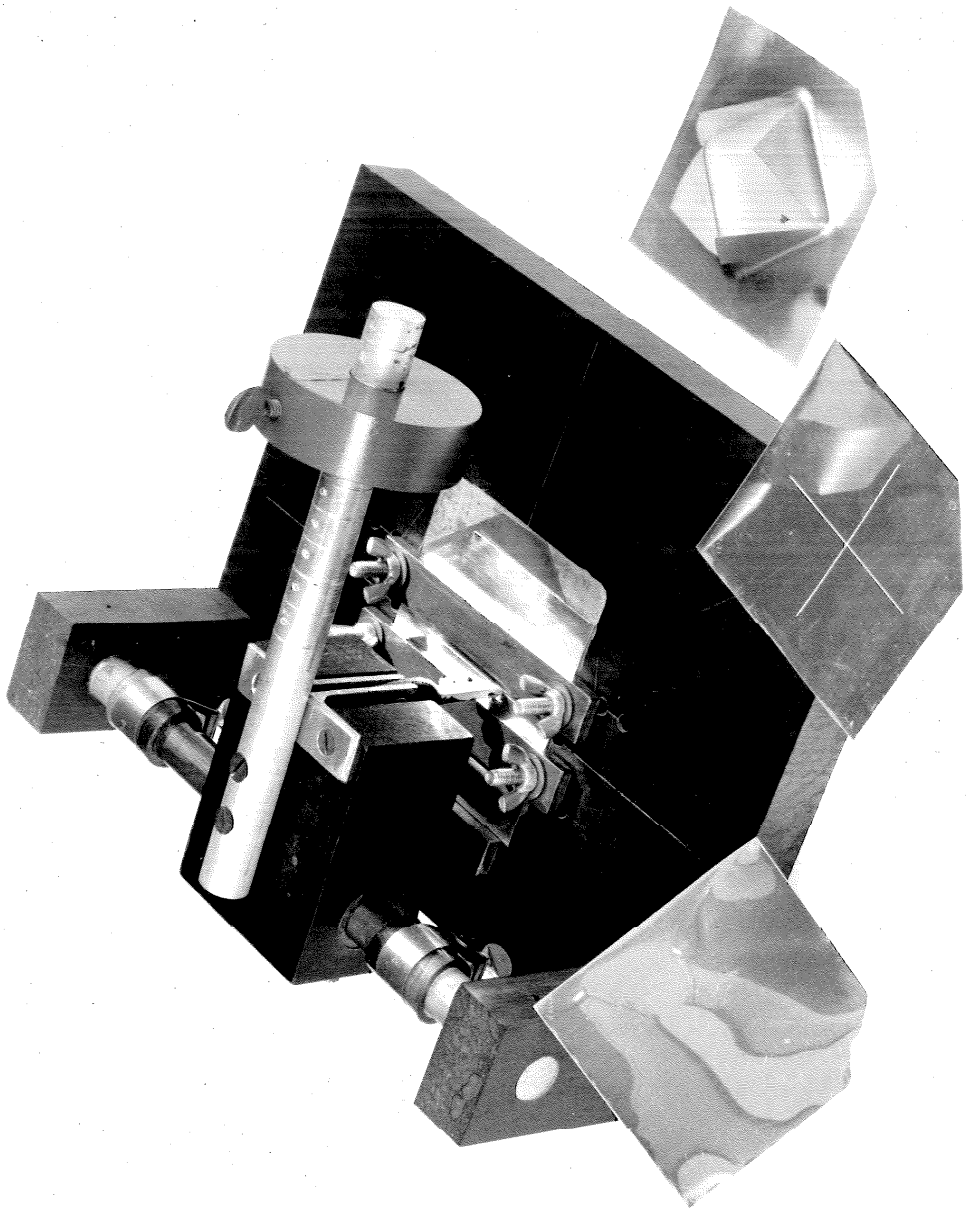

Fig. 39. Shock Tube Diaphragm Scorer.